The University of Nottingham

UNITED KINGDOM · CHINA · MALAYSIA

Seismic Soil-Structure Interaction In Performance-Based Design

by

Yang Lu BEng, MSc

Thesis submitted to The University of Nottingham for the degree of Doctor of Philosophy

Faculty of Engineering

Department of Civil Engineering

June, 2016

Dedication

This thesis is dedicated to my parents for their love,
support and encouragement.

Abstract

Soil-Structure Interaction (SSI) procedures for performance-based seismic design of building structures have been in existence in design guidelines and provisions for decades. However, several issues still remain regarding the application of these procedures to inelastic multi-storey buildings. Three main issues are identified and investigated in this research.

Firstly, the gap between code-specified design response spectra and base shear demands of inelastic flexible-base multi-storey buildings is bridged by introducing a strength reduction factor R_{F} and a Multi-Degree-Of-Freedom (MDOF) modification factor R_{M}. The strength reduction factor R_{F}, derived based on the combined (and similar) effects of SSI and structural yielding, allows base shear demands of a flexible-base yielding Single-Degree-Of-Freedom (SDOF) structure to be calculated directly from code design response spectra. The MDOF modification factor R_{M} links base shear demand of a MDOF structure to that of its SDOF counterpart.

Secondly, the effect of frequency content of ground motions on elastic and inelastic flexible-base buildings located on very soft soil profiles is examined. Results showed that normalising the equivalent period of a SSI system T_{ssi} by the corresponding predominant periods resulted in more rational spectra for seismic design purposes. In the elastic response spectra, T_{ssi} is normalised by the spectrum predominant period T_{P} corresponding to the peak ordinate of a 5% damped elastic acceleration spectrum, while for nonlinear structures T_{ssi} should be normalised by the predominant period of the ground motion, T_{g}, at which the relative velocity spectrum reaches its maximum value.

It is shown that an actual SSI system can be replaced by an equivalent fixed-base SDOF (EFSDOF) oscillator having a natural period of T_{ssi}, a viscous damping ratio ξ_{ssi} and a global ductility ratio of μ_{ssi}. The EFSDOF oscillator performed well for linear systems while, in general, overestimated ductility reduction factor R_μ of SSI systems with high initial damping ratio, which consequently led to an underestimation of inelastic displacement ratio C_μ.

The two issues stated above were addressed by results of a large number of response-history analyses performed using a simplified SSI model where the foundation response was assumed to be linearly elastic and frequency-dependent. The soil-foundation model, developed on the basis of the cone theory, has been verified to be a reliable tool for simulating dynamic soil-foundation interaction.

Finally, in order to take into account foundation nonlinearity in preliminary seismic design of building structures, a simplified nonlinear sway-rocking model was developed. The proposed model is intended to capture the nonlinear load-displacement response of shallow foundations during strong earthquake events where foundation bearing capacity is fully mobilised. Emphasis is given to heavily-loaded structures resting on a saturated clay half-space. The variation of soil stiffness and strength with depth, referred to as soil non-homogeneity, is considered in the model. Although independent springs are utilised for each of the swaying and rocking motions, coupling between these motions is taken into account by expressing the load-displacement relations as functions of the factor of safety against vertical bearing capacity failure (FS_{V}) and the moment-to-shear ratio (M/H). The simplified model is calibrated and validated against results from a series of static push-over and dynamic analyses performed using a more rigorous finite-difference numerical model. Despite some limitations of the current implementation, the concept of this model gives engineers more degrees of freedom in defining their own model components, providing a good balance between simplicity, flexibility and accuracy.

Acknowledgements

The completion of the research in this thesis would not have been possible without the support of many individuals to whom I would like to express my sincere gratitude.

First and foremost, I would like to thank my supervisors, Dr. Iman Hajirasouliha and Dr. Alec Marshall, for the continuous support of my Ph.D study and research. Thanks to Dr. Iman Hajirasouliha for leading me into an exciting field of research, for his motivation, enthusiasm, and contributions of time and guidance to make my Ph.D. experience stimulating. I thank Dr. Alec Marshall for his infinite patience, insightful advice, and mostly his support and encouragement during the most difficult time of my study. My sincere thanks also goes to Dr. Charles Heron for offering me inspirational discussions, helpful comments and thoughtful advices during the research.

My special thanks goes to my examiners Professor Ioannis Anastasopoulos and Dr. Luis Neves, for their patience in reading the thesis, for their kindness during the Ph.D viva voce and the constructive comments and suggestions.

I would like to thank all my friends and colleagues at the University of Nottingham for their constant support in both my life and research. I gratefully acknowledge the financial support from 'Dean of Engineering Research Scholarship for International Excellence' provided by the Faculty of Engineering at the University of Nottingham.

Lastly, I am deeply indebted to my parents. Their love and support provided me the energy to attain my study.

Contents

List of Figures

List of Tables

Nomenclature

Roman Symbols

a_0	structure-to-soil stiffness ratio
h_{tot}	total height of a building
h_{eff}	effective height of a building subjected to seismic excitations
k_{in}	initial foundation stiffness
k_{V}	coefficient of subgrade reaction
$\overline{k}$	foundation impedance function
m_{f}	foundation mass
m_{s}	storey mass of a building
$\overline{m}$	structure-to-soil mass ratio
$\overline{m}_{\mathrm{f}}$	structure-to-foundation mass ratio
r	equivalent radius of a foundation
s	slenderness ratio of a building
s_{u}	soil undrained shear strength
s_{u0}	soil undrained shear strength at ground level
u_{g}	ground displacement
u_{h}	foundation horizontal translation
u_{ssi}	displacement of the structural mass in a SSI system relative to the ground
u_{50}	foundation displacement at which 50% of bearing force is mobilised in monotonic loading
w	foundation settlement
A	foundation area

B	bulk modulus
C_{h}	high-frequency foundation radiation damping coefficient for horizontal response
C_{r}	linear range of a foundation force-displacement backbone curve
C_{s}	seismic response coefficient
C_{μ}	inelastic displacement ratio
C_{θ}	high-frequency foundation radiation damping coefficient for rocking response
D	foundation diameter
FS_{V}	Safety factor of foundation against vertical loading
G_{cyc}	cyclic shear modulus
G_{sec}	secant shear modulus
H_{c}	foundation shear capacity under combined loading
H_{u}	foundation shear capacity under pure sliding
$\overline{H}$	effective height of a building corresponding to its first mode of vibration
J_{f}	mass moment of inertia of a foundation
J_{s}	storey mass moment of inertia of a building
K_{h}	static horizontal stiffness of a foundation resting on an elastic homogeneous half-space
K_{v}	staticvertical stiffness of a foundation resting on an elastic homogeneous half-space
K_{θ}	static rocking stiffness of a foundation resting on an elastic homogeneous half-space
M_{c}	foundation moment capacity under combined loading
M_{u}	foundation moment capacity under pure rocking
ΔM_{θ}	trapped soil mass in the cone model to account for soil in-compressibility
M_{φ}	mass moment of inertia taking into account frequency dependence of foundation rocking
R_{d}	deformation response factor

R_{F}	strength reduction factor due to SSI and yielding
R_{M}	MDOF modification factor
R_{μ}	ductility reduction factor
Sa	spectral acceleration
Sd	spectral displacement
$\mathrm{S_{DS}}$	peak spectral ordinate of a design accelearion spectrum
T_0	characteristic period of a design acceleration spectrum
T_{g}	predominant period corresponding to the peak ordinate of an elastic relative velocity spectrum
T_{s}	fundamental period of a building in its fixed-base state
T_{ssi}	equivalent natural period of a SSI system
T_{P}	predominant period corresponding to the peak ordinate of a 5% damped elastic acceleration spectrum
V	base shear
V_{p}	dilatational wave velocity
V_{s}	shear wave velocity
$V_{\mathrm{s,30}}$	average shear wave velocity of the top 30 meters of a site
V_{u}	foundation bearing capacity under pure downward vertical translation
V_{y}	base shear at yield

Greek Symbols

α_{h}	dynamic modifier for foundation horizontal stiffness
α_{θ}	dynamic modifier for foundation rocking stiffness
α_{k}	modification factor for foundation stiffness as a function of soil heterogeneity and vertical factor of safety
α_{ξ}	correction factor for constant-ductility spectra
γ	shear strain
γ_{cyc}	cyclic shear strain
θ	foundation rotation

κ	soil stiffness modulus/undrained shear strength gradient with depth
Λ	heterogeneity index of a soil deposit
μ_{s}	structural ductility ratio
μ_{ssi}	global ductility ratio of a SSI system
ν	Poisson's ratio
ξ_{f}	foundation damping factor
ξ_{g}	soil damping ratio
ξ_{ssi}	effective damping ratio of a SSI system
ρ	soil mass density
τ	shear stress
χ	modification factor for the purely elastic foundation stiffness
ω_{s}	lowest Eigenfrequency of a building in its fixed-base state
ω_{ssi}	equivalent circular frenqucy of a SSI system
$\overline{\omega}$	dimensionless frequency
φ	rotational degree of freedom in the cone model to account for frequency dependence

Abbreviations

ADRS	Acceleration-Displacement Response Spectrum
ATC	Applied Technology Council
BNRS	Bi-normalised Response Spectrum
EFSDOF	Equivalent Fixed-base Single-Degree-Of-Freedom
EOM	Equations of Motion
FEM	Finite-Element Method
FFM	Free-Field Motion
FFT	Fast Fourier Transform
FIM	Foundation Input Motion
IFFT	Inverse Fast Fourier Transform
II	Inertial Interaction

KI	Kinematic Interaction
MDOF	Multi-Degree-Of-Freedom
NSR	Nonlinear Sway-Rocking
NEHRP	National Earthquake Hazard Reduction Program
OCR	Overconsolidation Ratio
PGA	Peak Ground Acceleration
PGD	Peak Ground Displacement
PRA	Peak Response Acceleration
PI	Plastic Index
RRS	Ratio of Response Spectra
SD	Standard Deviation
SDOF	Single-Degree-Of-Freedom
TF	Transfer Function

Chapter 1

Introduction

1.1 Research motivation

Soil-Structure Interaction (SSI) may have a significant effect on seismic response of buildings. In recent years, implementation of SSI procedures has found its way into seismic design provisions on the basis of replacing the whole SSI system with an equivalent fixed-base Single-Degree-Of-Freedom (EFSDOF) oscillator. However, current design guidelines are insufficient to capture more realistic SSI phenomena for the reasons that follow.

Firstly, either a force-based (e.g., ASCE, 2010) or a displacement-based (e.g., ASCE, 2013) procedure is based on a SDOF structure representative of the fundamental mode of vibration of a Multi-Degree-Of-Freedom (MDOF) building. Current seismic codes apply modification factors to design procedures for SDOF systems so that they can be used for MDOF buildings. The effect of SSI on these factors is still an area of uncertainty.

Secondly, design codes usually adopt an elastic pseudo-acceleration spectrum having a constant portion spanning over the low to intermediate period range and a descending segment in the long period range. This spectral shape is determined through smoothing the averaged response spectrum derived for a number of earth-

quake ground motions. It is generally believed that SSI results in a lower frequency of vibration and a higher damping compared with the case without SSI. The combined period lengthening and added damping effects in most cases lead to a reduced base shear demand according to the stated spectral shape.

In reality, however, peaks in response spectra occur at various periods of vibration. This peak response is more prominent for softer soil conditions where greater period lengthening effects are expected. In this sense, if the natural period of a structure in its fixed-base state is lower than the site characteristic period (corresponding to which an acceleration response spectrum attains its maximum ordinate), an increased base shear demand could be induced as a result of an increase in period.

The discrepancy between the code-specified and real response spectra stems from an unreasonable averaging process. The smoothed elastic design spectral shapes are usually defined by different soil types which are classified mainly according to the mean value of shear wave velocity over the top tens of meters (e.g., 30m) of a site. A range of site characteristic periods in the ratio of 1 to 4 is possible within a single soil site class (Ziotopoulou and Gazetas, 2010). Averaging response spectra with peaks at separated periods eliminates the peak response and consequently contributes to an approximately constant segment in the averaged spectrum. The fact that soft soil sites amplify the long-period components of an input motion seems to result in an increased range of the flat portion (i.e., constant acceleration segment) of such a spectrum for softer soil sites, which however is opposite to the reality where the response spectra for soft soil profiles have a sharp rather than flat shape.

Thirdly, modern seismic provisions employ an EFSDOF oscillator which approximates an actual SSI system having a SDOF superstructure. The so-called 'replacement oscillator approach' is based on the selection of a natural period and a damping ratio for the stated oscillator so that its resonant frequency and corresponding pseudo-acceleration are equal to those of the actual SSI system. This approach has also been extended to include hysteretic actions in inelastic structures. However, the effectiveness claimed for the approach has not been convincingly demonstrated (e.g., Ghannad and Ahmadnia, 2002b; Avilés and Pérez-Rocha, 2003). In other words,

the replacement oscillator approach may not necessarily provide a reliable solution to an SSI problem.

Finally, current code-specified seismic foundation design procedures discourage the acceptance of a foundation as a source of hysteretic energy dissipation (e.g., CEN, 1998). However, soil yielding is unavoidable during strong shaking and incorporation of foundation non-linearity into SSI systems remains a task for performance-based design in earthquake geotechnical engineering. It becomes increasingly important for both structural and geotechnical engineers to identify not only the individual but also the combined effect of structural and foundation 'hinges' on performance of seismically-excited structures and foundations.

1.2 Aims and objectives

The aim of this research is to develop practical procedures and simplified models for performance-based design of soil-structure interaction in earthquake engineering. The following objectives are laid down for the research study:

- Implement a simplified and reliable soil-structure interaction model for parametric study of soil-structure interaction.
- Investigate the effect of SSI on seismic response of elastic and inelastic structures supported on compliant foundations.
- Improve the current performance-based design procedures for SSI, with emphasis on force reduction and MDOF modification factors in the force-based design framework.
- Evaluate the performance of the equivalent fixed-base SDOF oscillator.
- Explore the effect of frequency content of ground motions on design spectra and coefficients considering SSI.

- Develop a simplified SSI model that is able to capture nonlinear foundation response.

- Calibrate and validate the proposed model against a detailed finite-different model.

1.3 Structure of the thesis

This thesis consists of eight chapters. Chapter 1 gives the motivation, aims and objectives of the research as well as the outline of the thesis. Chapter 2 presents the fundamentals of a dynamic SSI problem. SSI procedures in current seismic design provisions and guidelines are also reviewed. Chapter 3 provides a comprehensive review of the commonly used SSI models in engineering practice. Emphasis is given to geotechnical components. Chapter 4 focuses on implementing a simplified SSI model in computer code. The equations of motion and solution techniques for linear and nonlinear problems are described. The concept of an equivalent fixed-base SDOF oscillator for SSI analysis is also introduced. Chapter 5 proposes a practical performance-based approach for design of inelastic flexible-base multi-storey buildings. Chapter 6 highlights the effect of frequency content of ground motions on seismic design of buildings located on very soft soil deposits. Chapter 7 develops a nonlinear sway-rocking model for seismic assessment of buildings on mat foundations. Conclusions and suggestions are finally drawn in Chapter 8.

Chapter 2

Fundamentals of dynamic soil-structure interaction

2.1 Introduction

Conventional evaluations of seismic response of building structures assume that a structure is rigidly supported (i.e., a 'fixed-base' condition), which is a crude assumption since in many situations, buildings are founded on deformable soils (i.e., a 'flexible-base' condition). Introduction of soil flexibility modifies the seismic structural behaviour in comparison with the fixed-base condition. This chapter reviews the fundamentals of dynamic soil-structure interaction. First, a comparison of dynamic response of fixed-base and flexible-base structures is provided, followed by an introduction of common approaches to dynamic SSI. A review of SSI procedures in current seismic design provisions and guidelines is also given.

2.2 Dynamic response of fixed-base and flexible-base structures

Wolf (1985) illustrated the salient features of soil-structure interaction in Figure 2.1 by comparing the seismic response of a structure founded on rock with that of the identical structure with a rigid base (including the base-mat and the side walls) embedded in soil. The incident seismic waves with horizontal motions (represented by solid arrows) propagate vertically though the rock towards the structure with the magnitudes of the motions measured by the lengths of the solid arrows. Point A at the free surface of the rock is used as a reference point in which the motion is compared with those in other points.

For the structure built on rock (which can be regarded approximately as a fixed-base condition), the motions at points A and B are practically identical and equal to the wave-induced horizontal motion. Therefore, the motion recorded at the reference point A can be applied directly to the base of the structure. If the lateral structural stiffness is high, the input motion at the base would lead to horizontal accelerations that are constant over the height of the structure. Consequently, a transverse shear force and an overturning moment will develop at the base. Since the rock is very stiff, the horizontal shear force and rocking moment would hardly cause any additional deformation in the surrounding ground. As a result, the rigid foundation is 'bonded' to the rock and moves in phase with the horizontal motion in the rock.

On the other hand, the structure embedded in the soil exhibits a distinctly different dynamic response when compared to the structure on rock. This difference is mainly attributed to the fact that the motion at the base centre (i.e., point O) deviates from that at the reference point A due to the following three phenomena.

Firstly, the so-called 'free-field' motion, which corresponds to the motion of the site without presence of any structures and excavations, is modified. As depicted in Figure 2.1(c), the soft soil layer overlying the rock reduces the motion in point C, denoted as $\ddot{u}_g$, which would be identical to the motion in the reference point A if there were no soil on top of the rock (see Figure 2.1(b)). The wave propagation through

the soil layer subjects the soil particles to vibration, resulting in an amplification or attenuation of the free-field motion. Depending on the frequency content of excitations, the motion is usually amplified. Consequently, motions in points D and E denoted by $\ddot{u}_{g,b}$, which would lie on the soil-structure interface once the structure is built, differ from that in point C in Figure 2.1(c). The calculations of free-field motion require a site response analysis. Secondly, constructing the rigid

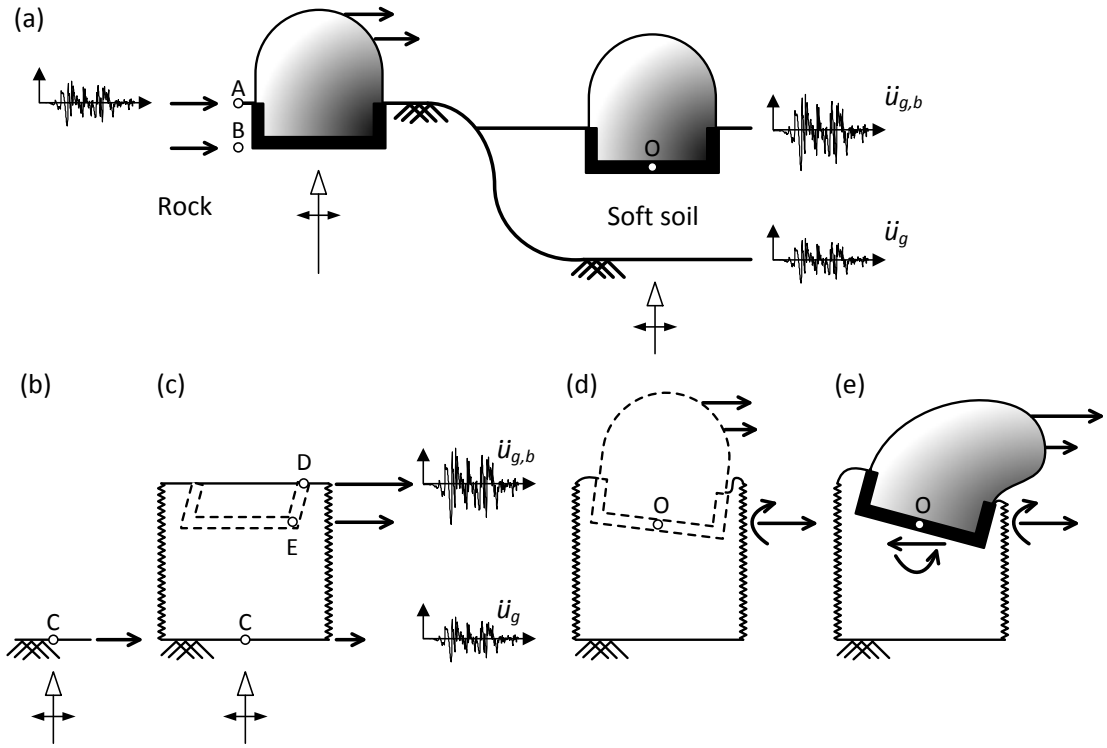

Figure 2.1: Seismic response of structures founded on rock and on soil. (a) Sites; (b) outcropping rock; (c) free field; (d) kinematic interaction; (e) inertial interaction (after Wolf, 1985).

foundation in the soil modifies the motion at its base, which may experience some average swaying displacement and an additional rocking motion (Figure 2.1(d)). The combined swaying and rocking response would lead to a variation of lateral acceleration with the height of the stiff superstructure. This phenomenon is mainly a result of the stiffness contrast between the foundation and the surrounding soil and occurs even when the foundation is mass-less, in which case it is referred to as 'Kinematic Interaction' (KI) (see Section 2.2.1).

Thirdly, the transverse shear force and the overturning moment resulting from the

inertial forces will cause additional deformation in the soil, which in turn modifies the input motion in point O at the base centre (Figure 2.1(e)). This interaction phenomenon between the excited structure and its adjacent soil is termed 'Inertial Interaction' (II) (see Section 2.2.2).

2.2.1 Kinematic interaction

The kinematic interaction effect is the direct result from the stiffness contrast between the soil and the foundation. In the free field where a structure is absent, the soil particles follow the pattern of motion induced by wave propagation. Suppose that a foundation, resting on or embedded in the soil, is so stiff that it cannot conform to the free-field displacement pattern; a deviation of foundation motion from the free-field motion will be caused, even if the foundation is mass-less.

Figure 2.2 illustrates cases where the kinematic interaction phenomenon prevails. Note that in all graphs, foundations are assumed to have no mass and dotted curves represent the free-field motions. Figure 2.2(a) shows an embedded pile subjected to shear waves, the amplitude of which increases while propagating vertically upward through the soil. On the one hand, the flexural stiffness of the pile prevents it from following the free-field motion, tending to modify the soil displacements (compared to the free-field displacements) in the vicinity of the pile shaft. On the other hand, the movement of the soil around the pile generates bending moments, which may pose a threat to the stability of the pile.

Figures 2.2(b) and (c) compare the effect of frequency components of a motion on response of a mass-less embedded foundation. When subjected to a high-frequency motion that varies horizontally (Figure 2.2(b)), the 'kinematic forces' exerted on the foundation cancel out, leaving the foundation 'unaffected' by the wave motion. On the contrary, excited by a lower-frequency motion (Figure 2.2(c)), the foundation tends to rock and translate, giving rise to a 'foundation input motion' which is made up of a swaying and rocking component, even though the free-field motion is purely horizontal.

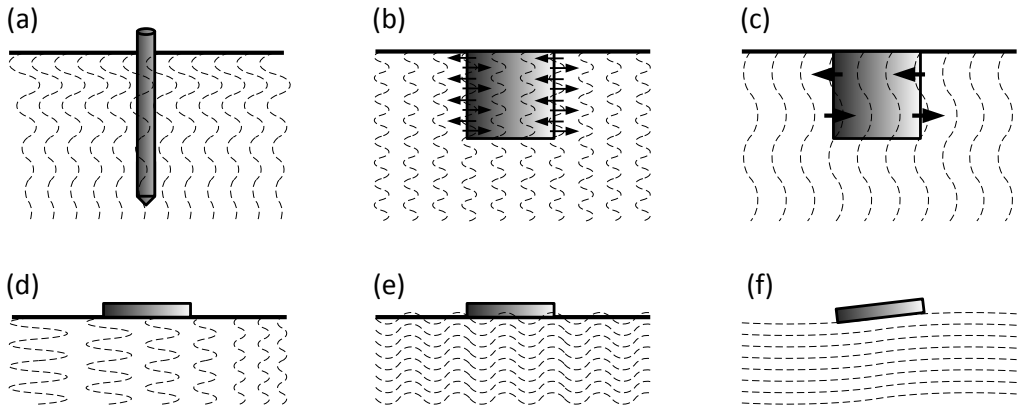

Figure 2.2: Kinematic interaction effect for shallow and deep foundations.

Although kinematic interaction is more common with embedded foundations, especially for deep foundations; there are cases where this effect is also significant for surface foundations. An example is illustrated in Figure 2.2(d) where the in-plane stiffness of a surface foundation does not allow it to follow the displacement pattern in the underlying soil. In addition, Figures 2.2(e) and (f) again demonstrate that excitation frequency has a significant effect on the foundation response, which is similar to the explanations given by reference to Figures 2.2(b) and (c).

In general, the way kinematic interaction affects the foundation behaviour depends on the predominant wavelength relative to the dimensions of the foundation. For high-frequency motions whose wavelengths are considerably small relative to the characteristic dimension of the foundation, the contribution to foundation response from these motions is almost negligible (with reference to Figures 2.2(a), (b) and (e)). In this sense, the foundation can be visualised as a high-period-pass (i.e. low-frequency-pass) filter applied to the high-frequency components of the free-field motions (ATC, 2005). This filtering effect is more pronounced for short-period structures (which are affected mainly by high-frequency motions), leading to a large reduction of seismic demands for these structures.

When foundation dimensions are comparable to the wavelength, kinematic interaction will tend to alter the modes of vibration of the foundation (with reference to Figures 2.2(c) and (f)). If, however, the characteristic foundation dimension becomes sufficiently small compared to the wavelength, the kinematic interaction effect can reasonably be ignored.

The phenomenon displayed in Figure 2.2(d) is referred to as the 'base-slab averaging effect', which is also predominant at low periods. It should be mentioned that kinematic interaction is not present in all problems. For example, if the surface foundations shown in Figures 2.2(d), (e) and (f) are subjected to the seismic waves described in Figures 2.2(a), (b) or (c), kinematic interaction will not occur.

2.2.2 Inertial interaction

In an inertial interaction, the superstructure is 'activated' by the foundation input motion and inertial forces are developed within the structure. Two important features arising from this interaction are discussed below.

Firstly, the inertia-induced transverse shear force and overturning moment developed at the base of the foundation cause deformation in the soil in addition to that due to the free-field motion. The deformation magnitude is controlled by the amplitude of vibration and the compliance of the soil. Introduction of deformable soil beneath the foundation makes the whole SSI system more flexible, and thus, more prone to longer-period components of a ground motion.

Secondly, the excited foundation acts as a finite source of vibration that emits waves propagating though the soil towards infinity. For an embedded shallow foundation, the swaying response (with swaying displacement denoted by 'u_{h}') shown in Figure 2.3(a) generates P-waves (i.e., dilatational waves denoted by 'P') and S-waves (i.e., shear waves denoted by 'S') respectively through compression/extension (at the vertical interfaces) and friction (at the horizontal interface) between the foundation and the adjacent soil. In the rocking mode of vibration (with angle of rotation denoted by 'θ' in Figure 2.3(b)), P-waves arise mainly from compressive stresses transmitted from the foundation base to the underlying soil.

Two main types of wave energy dissipation are involved in inertial interaction. The first energy dissipation is a result of the geometric attenuation during the wave propagation where an expansion of the wave front from a point source occurs. This mechanism is usually called 'radiation damping', since foundation vibration radiates

waves into the soil medium. The other mechanism corresponds to the nonlinear soil behaviour and is called 'hysteretic damping'. If foundation uplift is allowed, the impact of the foundation onto the soil and concomitant vertical oscillatory motion dissipate part of the kinetic energy imparted on the foundation (Adamidis et al., 2014).

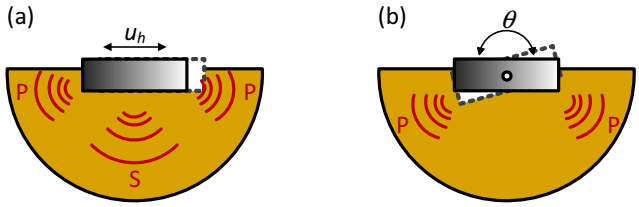

Figure 2.3: Foundation vibration of (a) swaying mode and (b) rocking mode in inertial interaction dissipates wave energy into the surrounding soil domain.

To summarise, two main features of inertial interaction are, respectively, lengthening of the vibration period and introducing radiation damping and soil hysteretic damping into the vibrating system.

2.3 Approaches to dynamic SSI

2.3.1 Direct approach

The most 'rigorous' way of solving a dynamic SSI problem may be using a 'direct approach', which involves modelling the entire soil-structure system in the time domain, accounting for spatial variation of soil properties, material and geometric nonlinearities, wave propagation complexities and careful treatment of interface and boundary conditions. The direct approaches are usually performed by using the Finite-Element Method (FEM) where the whole SSI system is modelled and analysed in a single step. The Equations of Motion (EOM) for an SSI Finite-Element model can be written as:

$$[M]\{\ddot{u}\} + [k]\{u\} = -[M]\{\ddot{u}_g\} \tag{2.1}$$

where $[M]$ and $[k]$ are respectively mass and stiffness matrices, $\{u\}$ is a displacement vector corresponding to the degrees of freedom of the internal nodes within the SSI

model, and $\{u_g\}$ is the input displacement vector for the nodes which usually lie at the bottom of the model.

Although the direct approach is able to treat the soil and the structure with equal rigour, it usually requires a great computational effort and is not easy to put into practice. In the preliminary design stage, practical engineers are more accustomed to a 'substructure' approach which will be described in the following section.

2.3.2 Substructure approach

The substructure method is also called a 'multi-step approach' where an SSI problem is solved by combining solutions from the previously stated kinematic and inertial interaction phenomena, as illustrated in Figure 2.4.

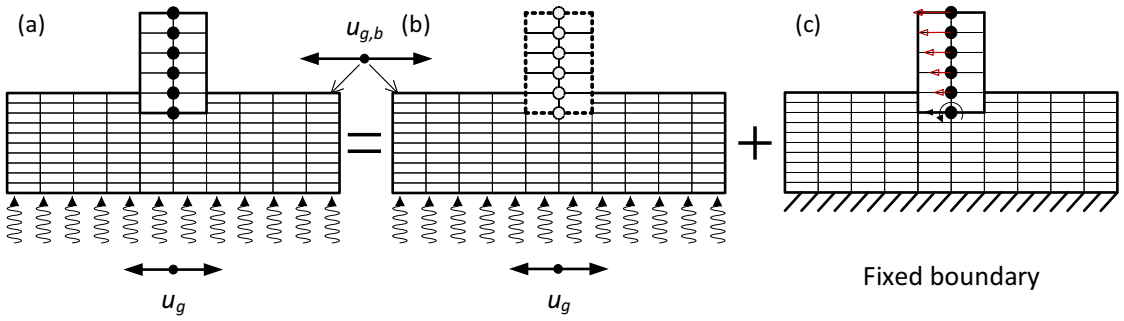

Figure 2.4: The analysis of (a) an SSI problem can be broken down into (b) a kinematic interaction analysis and (c) an inertial interaction analysis.

In the kinematic interaction analysis (Figure 2.4(b)), seismic excitations are applied to the bottom of the SSI model where the structure and foundation are assumed to have stiffness but no mass. The EOM for kinematic interaction can be written as:

$$[M_{\text{soil}}]\{\ddot{u}_{\text{KI}}\} + [k]\{u_{\text{KI}}\} = -[M_{\text{soil}}]\{\ddot{u}_{\text{g}}\} \tag{2.2}$$

where $[M_{\text{soil}}]$ is the mass matrix in which the entries corresponding to the structure and the foundation are zero and the subscript KI denotes kinematic interaction.

Mathematically, the EOM for inertial interaction can be extracted from the total EOM (Equation (2.1)) by subtracting those for the kinematic interaction (Equation

(2.2)):

$$[M]\{\ddot{u}_{\mathrm{II}}\} + [k]\{u_{\mathrm{II}}\} = -[M_{\mathrm{structure}}]\{\ddot{u}_{\mathrm{g}} + \ddot{u}_{\mathrm{KI}}\} \tag{2.3}$$

where $\{u_{\mathrm{II}}\} = \{u\} - \{u_{\mathrm{KI}}\}$ is the inertial interaction component of the displacement vector $\{u\}$, and $[M_{\mathrm{structure}}] = [M] - [M_{\mathrm{soil}}]$ is the mass matrix where the 'soil' entries are equal to zero.

Note that for the degrees of freedom corresponding to the structure-foundation system, $\{u_{\mathrm{KI}}\} + \{u_{\mathrm{g}}\}$ is reduced to the foundation input motion. In particular, for a surface foundation subjected to coherent vertically propagating shear waves, $\{u_{\mathrm{KI}}\} + \{u_{\mathrm{g}}\}$ at the foundation level is equal to $\{u_{\mathrm{g,b}}\}$ which is the motion at the ground surface in the free field.

From a practical structural engineer's point of view, to simplify an SSI analysis, the soil medium is usually replaced by the so-called 'impedance function' that captures the stiffness and damping characteristics of the soil-foundation interaction when subject to vibration at various frequencies. These frequency-dependent impedance functions are physically represented by springs with a complex-valued stiffness. In this case, the procedures presented in Figure 2.4 can utilise a even simpler SSI model, as illustrated in Figure 2.5 which involves three steps (Kramer and Stewart, 2004). (1) Calculate the foundation input motion which depends on the stiffness and geometry of the foundation and the soil. (2) Evaluate the impedance function which, for a simple case of a rigid foundation, is a function of elastic soil properties (e.g., stiffness and Poisson's ratio), soil stratigraphy, foundation geometry and vibrating frequency. (3) Perform dynamic analysis on the flexible-base structure subjected to the foundation input motion.

It is clear in this section that the solution of kinematic interaction is the effective foundation input motion. Inertial interaction solves the response of the SSI system where the structure (including foundation) is excited by the foundation input motion and interacts with the surrounding soil. The total response of the system is thus the sum of responses obtained from both interaction analyses.

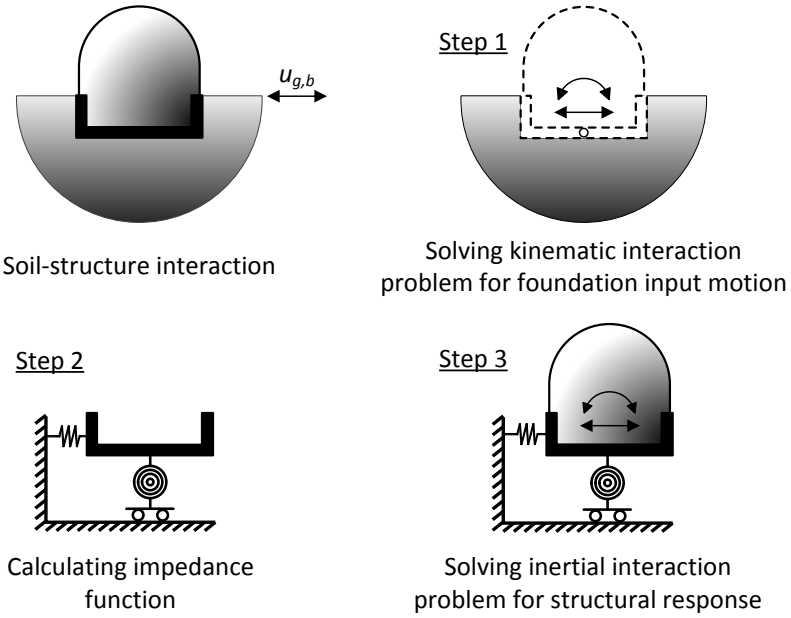

Figure 2.5: Substructure approach to an SSI problem utilising impedance function (after Kramer and Stewart, 2004).

2.3.3 Time domain analysis

Since the EOM are formulated in the time domain, the most general approach for solving these equations is a response history analysis. A number of numerical integration methods are available for obtaining incremental solutions at each time step. A nonlinear SSI analysis should be performed in the time domain where iterations may be required to solve the equilibrium equations. This requires a huge computational effort for a problem having a large number of degrees of freedom.

2.3.4 Frequency domain analysis

Due to the frequency-dependent nature of the impedance function, a frequency domain analysis is best suited for the substructure approach described in Figure 2.5. Before an analysis can be performed in the frequency domain, the raw time-varying data is separated, through a Fourier Transform (FT), into a series of harmonic components, each with a specific phase angle and amplitude as well as a unique frequency. The response is then calculated independently at individual frequencies.

The frequency responses can eventually be translated back into the time domain by using the Inverse Fourier Transform (IFT). This class of analysis only applies to linear (including equivalent-linear) systems where true nonlinearity is excluded, and therefore, the frequency domain analysis is not able to predict residual deformation.

2.4 SSI in seismic design guidelines

Soil-structure interaction was first introduced in the U.S. ATC-3 report (ATC, 1978), *Tentative provisions for the development of the seismic regulations for buildings*, which is the predecessor of the National Earthquake Hazard Reduction Program (NEHRP) seismic provisions. The simple procedures for SSI in ATC-3 suggest that a reduced design base shear (compared with the fixed-base value) should be adopted. This beneficial effect of SSI is part of the reason why SSI provisions serve as optional design considerations and have never been integrated into building codes. The fact that code practice is reluctant to accept SSI design procedures is also due to the uncertainties in the SSI effect, which is still controversial.

2.4.1 Eurocode

Although no specific design methods are proposed, Eurocode 8 (CEN, 2004) gives qualitative description of SSI effects in its Annex D and recognises the following situations where SSI effects might be detrimental and should be considered in design:

- structures where P-δ (2nd order) effects play a significant role;
- structures with massive or deep-seated foundations, such as bridge piers, offshore caissons, and silos;
- slender tall structures, such as towers and chimneys;
- structures supported on very soft soils, with average shear wave velocity less than 100 m/s.

For piled foundations, Annex C provides the pile-head stiffness that can be used for SSI calculations.

2.4.2 U.S. standards and design guidlines

SSI provisions currently exist in several important U.S. seismic design standards (e.g., ATC, 2005; BSSC, 2009; ASCE, 2010; ATC, 2012; ASCE, 2013). The following presents simplified SSI procedures that have been implemented in existing force-based and displacement-based design for building structures in these standards.

2.4.2.1 Force-based procedures

The *NEHRP Recommended Seismic Provisions for New Buildings and Other Structures* (BSSC, 2009) adopts a force-based design methodology which integrates SSI into the equivalent lateral force procedure and is also provided in Chapter 19 of ASCE (2010), *Minimum design loads for buildings and other structures*.

ASCE (2010) neglects the effect of kinematic interaction and deals with the period lengthening and modified damping resulting from inertial interaction. The inertial effect on design seismic spectrum is illustrated in Figure 2.6. The reduction of base shear V is calculated as:

$$\Delta V = \left[C_{\mathrm{s}} - C_{\mathrm{s,ssi}} \left(\frac{\xi_{\mathrm{s}}}{\xi_{\mathrm{ssi}}} \right)^{0.4} \right] \overline{W} \leq 0.3 C_{\mathrm{s}} \overline{W} \tag{2.4}$$

where C_{s} is a seismic response coefficient (i.e., the design pseudo-acceleration Sa normalised by the acceleration of gravity g) of a system having a period of vibration T and a damping ratio ξ. The subscript 'ssi' denotes an SSI system. For fixed-base systems (denoted by using subscript 's'), the damping ratio, defined as a fraction of critical damping, is usually taken as 5%. $\overline{W}$ is the effective seismic weight of the superstructure, usually taken as 70% of the total seismic weight. For structures supported on mat foundations that are resting on the ground surface or shallowly embedded in the soil where the effect of contact between the side walls and soil is

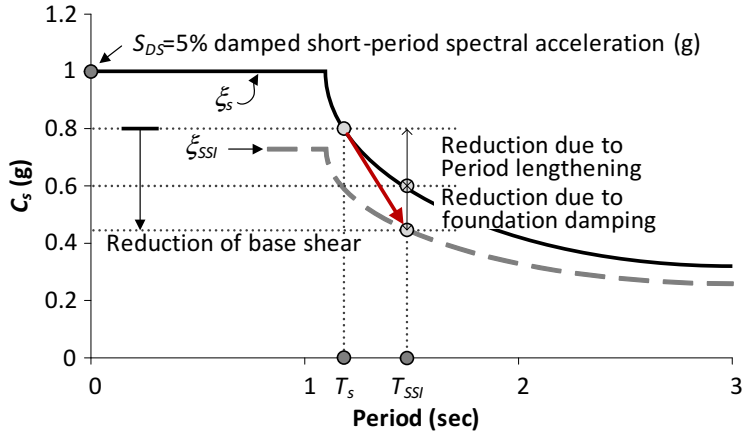

Figure 2.6: Schematic showing effects of period lengthening and foundation damping on design spectral ordinates for linear SSI systems.

deemed insignificant, the effective period of the flexible-base structure $T_{\rm ssi}$ can be evaluated from an adapted form of Veletsos and Meek (1974):

$$T_{\rm ssi} = T\sqrt{1+\frac{25\alpha R_{\rm h}\overline{h}}{V_{\rm s}^2 T_{\rm s}^2}\left(1+\frac{1.12R_{\rm h}\overline{h}^2}{\alpha_\theta R_\theta^3}\right)} \tag{2.5}$$

where

α=the relative weight density of the structure and the soil defined by:

$$\alpha = \frac{\overline{W}}{\gamma A\overline{h}} \tag{2.6}$$

$R_{\rm h}$ and R_θ=characteristic foundation lengths defined by:

$$R_{\rm h} = \sqrt{\frac{A}{\pi}} \qquad\qquad R_\theta = \sqrt[4]{\frac{4I}{\pi}} \tag{2.7}$$

where

A=the area of the load-carrying foundation.

$\overline{h}$=the effective height of the structure, taken as 0.7 times the total height (for multi-storey structures) except for structures where the gravity load is effectively concentrated at a single level (e.g., for one-storey structures) in which case $\overline{h}$ is taken as the height to that level.

I=the in-plane static moment of inertia of the load-carrying foundation about a centroidal axis normal to the direction in which the structure is analysed.

α_θ=dynamic foundation stiffness modifier for the rocking motion as determined from Table 2.1.

V_s=shear wave velocity.

T_s=fundamental period of the structure in its 'fixed-base' state.

Table 2.1: Values of α_θ (ASCE, 2010)

R_θ/V_sT_s	α_θ
<0.05	1.0
0.15	0.85
0.35	0.7
0.5	0.6

The effective damping of the flexible-base structure is calculated as:

$$\xi_{ssi} = \xi_f + \frac{\xi_s}{\left(\frac{T_{ssi}}{T_s}\right)^3} \tag{2.8}$$

where ξ_f is the foundation damping factor that can be evaluated from Figure 2.7.

BSSC (2009) and ASCE (2010) take into account the strain-dependent foundation stiffness and damping factor by relating them to the peak spectral ordinate S_{DS} (shown in Figure 2.6) corresponding to the short-period value on a 5% damped design acceleration spectrum.

Note that the graphical solutions in Figure 2.7 are derived by using the Veletsos and Nair (1975) damping expression as a function of the period lengthening ratio T_{ssi}/T_s, peak spectral acceleration S_{DS}, and structural slenderness ratio $\overline{h}/r$. The equivalent foundation radius r is determined by:

$$r = \begin{cases} R_h, & \text{if } \dfrac{\overline{h}}{L} \leq 0.5. \\ R_\theta, & \text{if } \dfrac{\overline{h}}{L} \geq 1. \end{cases} \tag{2.9}$$

where L is the overall length of the side of the foundation in the direction being analysed.

For intermediate values of S_{DS} between 0.1 and 0.2, and values of $\overline{h}/L$ between 0.5 and 1; the values of ξ_f and r can be calculated by linear interpolation. ASCE (2010)

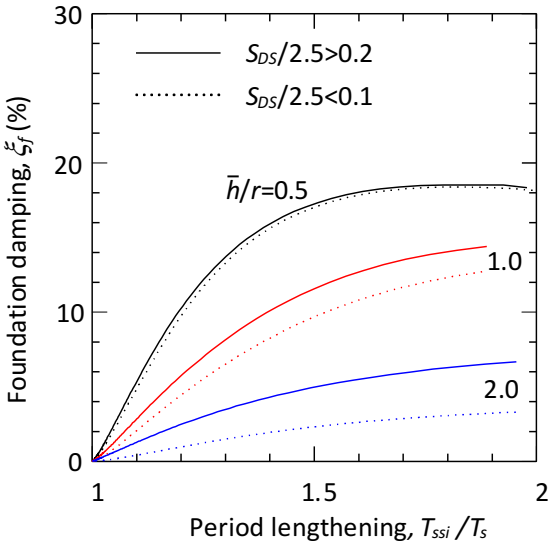

Figure 2.7: Foundation damping factor specified in ASCE (2010).

requires that the effective damping of an SSI system ξ_{ssi} calculated by Equation (2.8) should neither exceed 20% nor be less than the fixed-base value 5%. Considering that the design spectrum has a constant and descending segment over a wide range of periods, the force-based procedures seem always to reduce base shear.

Implementation of SSI in modal analysis is also allowed, with similar procedures to the equivalent lateral load analysis but only applied to the fundamental mode of response. Since higher-mode responses are essentially unaffected by SSI (e.g., Bielak, 1976), the contributions of higher modes are calculated based on the fixed-base assumption.

The stated SSI procedures for determining the design base shear are appropriate for linear SSI systems where yielding is excluded. Seismic codes encourage nonlinear hysteretic action to occur in structural members to dissipate earthquake energy through permanent deformation. In its Chapter 12, ASCE (2010) gives a simple expression for the seismic response coefficient that takes into account the inelastic structural behaviour:

$$C_{\text{s}} = \frac{\text{S}_{\text{DS}}}{\left(\frac{R}{I}\right)} \tag{2.10}$$

where R is a response modification factor that accounts for the ductility of a building and reduces the base shear accordingly; and I is an important factor, which for

common buildings usually equals one. As noted by Crouse (2002), existing R factors may already reflect the beneficial effects of SSI, and modifying the base shear to account for both SSI and ductility may be unconservative in some cases. This was confirmed by Ghannad and Jahankhah (2007) who showed that using the R factors derived based on the fixed-base assumption for SSI systems led to a higher ductility demand (than the target value).

2.4.2.2 Displacement-based procedures

U.S. seismic provisions for existing buildings are based on nonlinear static (pushover) procedures. A variety of pushover methods are readily available, such as: Capacity Spectrum Method (ATC, 1996), Coefficient Method (BSSC, 2000), Improved Coefficient (Displacement Modification) Method and Linearisation Method (ATC, 2005). SSI procedures have been implemented in the latter two methods in ATC (2005) which were then revised into ASCE (2013).

A displacement-based procedure requires two important components: a capacity curve (or a pushover curve) and a design response spectrum (or a demand spectrum), both plotted in an Spectral acceleration (Sa) versus Spectral displacement (Sd), or ADRS format.

The capacity curve can be derived from an incremental pushover analysis where an MDOF building-foundation-soil system (in its gravitational equilibrium) is subject to a static lateral load pattern. The whole system is pushed monotonically until a target displacement (usually evaluated at the roof level) is reached (see Figure 2.8). The cumulative lateral load H, which is statically equal to the mobilised base shear, could be plotted against the roof displacement Δ to reflect the level of inelasticity in the structure.

The seismic structural performance is assessed by combining the capacity curve with a seismic demand spectrum in the ADRS form. This requires the MDOF system to be transformed to an equivalent SDOF structure (the fundamental mode of vibration of the MDOF system is usually selected for this purpose). In order to

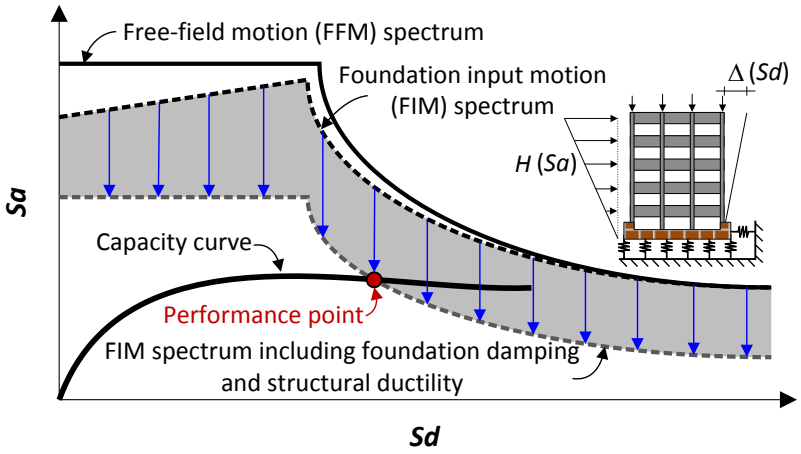

Figure 2.8: Schematic showing SSI effects on displacement-based method for assessing nonlinear structural performance.

account for inelastic structural response, the demand spectrum, without considering SSI effects, should be reduced from its elastic counterpart. Either an equivalent elastic spectrum (derived for an equivalent viscous damping ratio that relates to the expected inelasticity level) or an inelastic spectrum (which explicitly accounts for structural inelasticity through the response modification factor R) can be used as the demand spectrum. The effects of SSI on the demand spectrum are quantified by ASCE (2013) through reductions of demands in kinematic and inertial interaction phenomena which will be addressed in the following.

Theoretically, the foundation input motion (FIM) can be evaluated in kinematic interaction by means of a number of transfer functions expressed as frequency-dependent ratios of the Fourier amplitudes of FIM to those of the free-field motion (FFM). ASCE (2013) recommends that a reduced response spectrum can be used to account for kinematic interaction. This is based on the similarity between the transfer function ordinates (i.e., the amplitude ratios of FIM/FFM) and the response spectral ratios of FIM/FFM at frequencies lower than 5Hz (Veletsos and Prasad, 1989). The ratio of response spectra (RRS) is specified for base-slab averaging ($\mathrm{RRS_{bsa}}$) and embedment ($\mathrm{RRS_e}$) effects (see Section 2.2.1 for explanations of both effects) but the total reduction of FFM spectral ordinate is not permmited to be greater than 50% (i.e., $\mathrm{RRS}=\mathrm{RRS_{bsa}} \times \mathrm{RRS_e} \geq 0.5$).

For vertically propagating waves, the transfer function, and thus $\mathrm{RRS_{bsa}}$ is calculated

by:

$$\mathrm{RRS_{bsa}} = 0.25 + 0.75 \left\{ \frac{1}{b_0^2} \left[1 - \exp(-2b_0^2) \mathrm{B_{bsa}} \right] \right\}^{1/2} \tag{2.11}$$

where

$$\mathrm{B_{bsa}} = \begin{cases} 1 + b_0^2 + b_0^4 + \dfrac{b_0^6}{2} + \dfrac{b_0^8}{4} + \dfrac{b_0^{10}}{12}, & \text{if } b_0 \leq 1. \\ \exp(2b_0^2) \left[\dfrac{1}{\sqrt{\pi} b_0} \left(1 - \dfrac{1}{16 b_0^2} \right) \right], & \text{if } b_0 > 1. \end{cases} \tag{2.12}$$

$$b_0 = 0.0001 \left(\frac{2\pi b_\mathrm{e}}{T} \right) \tag{2.13}$$

T=fundamental period of the flexible-base building T_{ssi} which shall not be taken as less than 0.2sec when used in Equation (2.13). The low-period cutoff 0.2sec is determined in accordance with the previously stated frequency of 5Hz in order that RRS correlates well with the transfer function.
b_e=$\sqrt{A} \leq$ 260ft is the effective foundation size in feet.

The RRS factor for embedment, $\mathrm{RRS_e}$ is determined by Equation (2.14):

$$\mathrm{RRS_e} = 0.25 + 0.75 \cos \left(\frac{2\pi e}{T V_\mathrm{s}} \right) \geq 0.50 \tag{2.14}$$

where e is foundation embedment depth in feet.

ASCE (2013) specifies the following situations where reductions due to kinematic interaction effect is not allowed:

1. Structures having floor and roof diaphragms classified as flexible where reductions are not permitted for base-slab averaging effect, i.e., $\mathrm{RRS_{bsa}} = 1$;

2. Structures located on firm rock sites (e.g., site classes A and B in Table 4.3) where reductions are not permitted for embedment effect, i.e., $\mathrm{RRS_e} = 1$;

3. Structures located on soft clay sites (e.g., site class E in Table 4.3) where reductions are not permitted for both effects, i.e., RRS = 1;

4. Structures with foundation components that are not laterally connected where reductions are not permitted for both effects, i.e., RRS = 1.

In ATC (2005) and hence ASCE (2013), the reduced seismic demand spectrum is evaluated for an equivalent viscous damping ratio (Equation (2.15)) due to the combined effect of SSI and structural yielding in inertial interaction.

$$\xi_0 = \xi_\mathrm{f} + \frac{\xi_\mathrm{s}}{\left(\frac{T_\mathrm{ssi,eff}}{T_\mathrm{s,eff}}\right)^3} \leq 20\% \tag{2.15}$$

where ξ_f is the foundation damping ratio that can be estimated from Figure 2.7, $T_\mathrm{ssi,eff}/T_\mathrm{s,eff}$ is the effective period lengthening ratio evaluated at maximum post-yield displacement:

$$\frac{T_\mathrm{ssi,eff}}{T_{s,\mathrm{eff}}} = \left\{1 + \frac{1}{\mu}\left[\left(\frac{T_\mathrm{ssi}}{T_\mathrm{s}}\right)^2 - 1\right]\right\}^{0.5} \tag{2.16}$$

where $T_\mathrm{ssi}/T_\mathrm{s}$ is the period lengthening of linear SSI systems as determined by Equation (2.5), μ is a ductility factor that measures the degree of nonlinearity due to yielding in structures.

When reducing an elastic design spectrum from its 5% damped counterpart, a damping coefficient B, as a function of the effective viscous damping ξ_0, is introduced. The reduced demand spectrum is obtained by dividing the 5% damped spectrum by B.

2.5 Summary

Structures supported by deformable soil exhibit different dynamic response compared to their fixed-base conditions. This difference arises from kinematic interaction and inertial interaction. The former interaction phenomenon results in a deviation of the foundation input motion from the free-field motion whereas the latter usually leads to a higher period of vibration and damping for an SSI system. Although a direct method serves as a rigorous approach to SSI, design standards usually adopt a substructure approach which combines the solutions derived from the two interaction analyses.

Chapter 3

Review of commonly used models for seismic SSI problems

3.1 Introduction

This chapter elaborates the previously stated direct and substructure approaches (see Section 2.3) through a review of available models that are commonly used in seismic analysis of soil-structure interaction problems. Domain-type models are widely used in research as a direct approach while spring-type models are more favoured by engineers as a simple tool for assessing seismic performance of buildings and foundations in inertial interaction. In this chapter, a comprehensive review of the model components is provided. Emphasis is given to geotechnical components since existing structural models are well-developed. Strengths and limitations of these models are also addressed.

3.2 Domain-type models

Domain-type models are usually used to handle problems where an arbitrary shaped body with complicated material behaviour is subjected to complex dynamic loading conditions. The material is often idealised as a continuum having an infinite number of degrees of freedom. In order to solve such a problem, the whole domain needs to be discretised into a number of sub-domains with a finite number of degrees of freedom. The discretisation can be achieved by using either a Finite Element Method or a Finite Difference Method. Figure 3.1 illustrates a direct SSI analysis performed using a finite-difference code FLAC^{3D}. More information of modelling issues on FLAC^{3D} will be provided in Chapter 7.

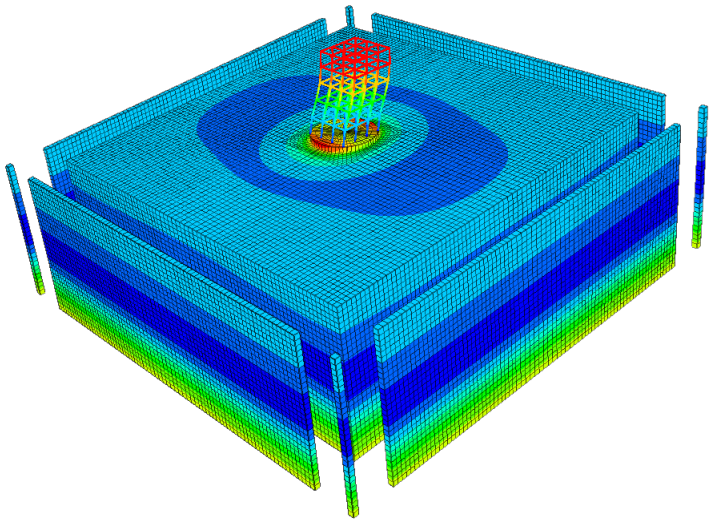

Figure 3.1: Application of finite-difference technique to direct soil-structure interaction analysis by using the numerical code FLAC^{3D}.

Apart from numerical computational techniques, two main issues should be given careful consideration. The first issue relates to the description of soil behaviour, which is usually achieved by means of mathematical constitutive formulations (constitutive models). The second issue concerns a site response analysis which deals with dynamic loading and boundary conditions, spatial variation of material properties in a soil deposit and wave propagation through the soil profile. These two issues are discussed in detail in following subsections.

3.2.1 Dynamic soil behaviour

In earthquake events, a soil element within a site is subjected to a variation of stress during passage of seismic waves. Consider upward propagating waves through a water saturated soil profile. Ishihara (1996) demonstrated that dilatational (compressional) waves induce almost a pure isotropic stress state in saturated soils with deviator stress components being practically negligible. Since wave-induced compressive stress is transmitted though pore water without changing the effective stress carried by the soil skeleton, the effect of compressional waves on ground stability is insignificant. On the other hand, in response to shearing of soil skeleton, pore water increases in pressure and attempts to flow out to low-pressure zones, which in an undrained condition leads to build-up of pore water pressure and an accompanying reduction of effective stress. Therefore, shear stress induced by propagation of shear waves is the main focus of a geotechnical earthquake engineering problem.

In the laboratory, it is possible to perform an undrained cyclic simple shear test to reproduce the seismic response of saturated soil subjected to one-dimensional shear waves, as sketched in Figure 3.2(a). Experimental results are very similar to those depicted in Figures 3.2(b)-(d) in terms of shear stress (τ) versus shear strain (γ). The steady-state cyclic soil response is characterised by a hysteresis loop illustrated in Figure 3.2(b). A secant shear modulus $G_{\text{sec}} = G_{\text{cyc}}$, defined as the slope of the line connecting the tips of the hysteresis loop, is usually used to measure the shear resistance of a soil element in response to a shear deformation $\gamma_{textupcyc}$. The area enclosed by the loop represents the energy dissipated during a cycle, which can be quantified mathematically by a damping ratio defined as:

$$\xi_{\text{g}} = \frac{\Delta E}{4\pi E} \tag{3.1}$$

where ΔE is the energy dissipated within a cycle and E is an equivalent maximum elastic energy stored during the cycle. Experimental results have shown that the secant shear modulus and damping ratio is mainly a function of cyclic strain amplitude. At very small strain level, the secant modulus G_{cyc} is close to the purely elastic counterpart G_{max}.

Figure 3.2(c) shows a reduction of the secant shear modulus with increasing the cyclic shear strain amplitude. This relationship can be described by a 'backbone curve' joining the tips of hysteresis loops achieved under various strain amplitudes. Even under a constant shear strain amplitude, the hysteresis loop grows flatter with increasing the number of cycles n, as illustrated in Figure 3.2(d), especially at large strain levels. For saturated soils, increasing number of cycles is usually accompanied by a degradation of strength and stiffness, thereby leading to a degraded backbone curve. The degradation of the shear modulus for sands is also influenced by void ratio and effective confining stress; for clays, it is affected by plastic index (PI) and overconsolidation ratio (OCR).

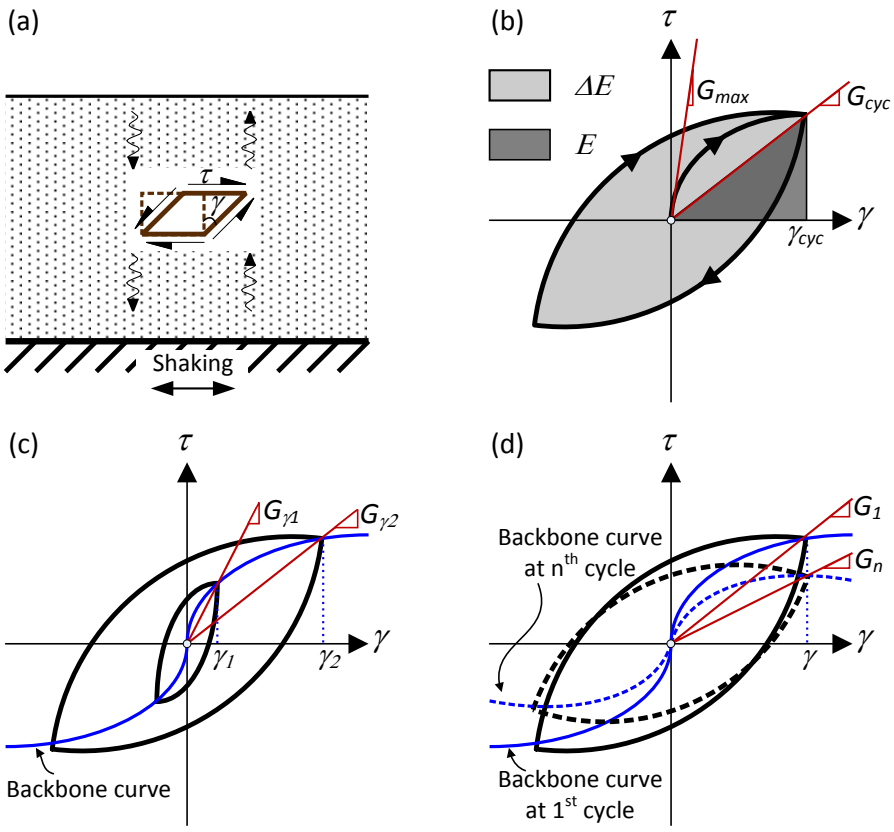

Figure 3.2: Cyclic response of (a) a soil element at a site subjected to shear waves, characterised by (b) a hysteresis loop which is affected by (c) cyclic strain amplitude and (d) number of cycles.

The dependence of shear modulus and damping on cyclic shear amplitude can alternatively be described by a pair of dimensionless curves, sketched in Figure 3.3,

which was first proposed by Seed and Idriss (1970).

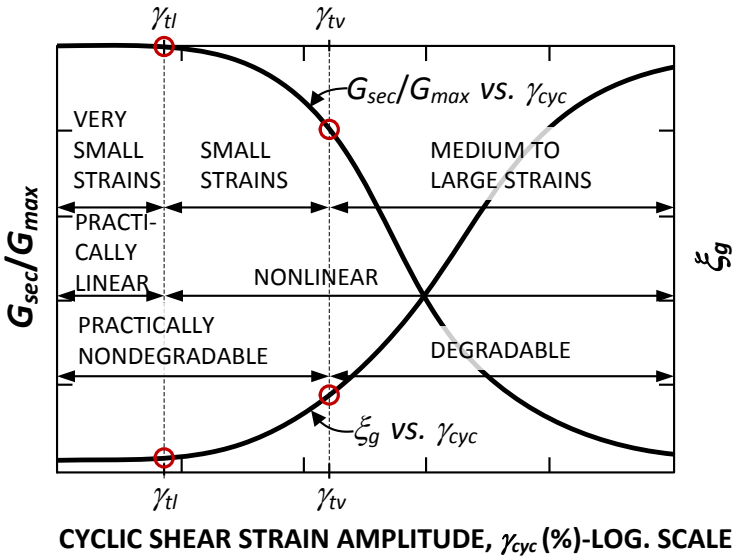

Figure 3.3: Dimensionless backbone and damping curves with various strain amplitude for saturated soils (after Vucetic, 1994).

Vucetic (1994) showed that these dimensionless curves are widely used in research and practice because (1) both normalised shear modulus and damping ratio are not significantly affected by the effective consolidation stress and OCR; and (2) the strain-dependent secant shear modulus can be readily determined from its very small-strain values G_{max} which is usually calculated from the field-measured shear wave velocity V_s by:

$$G_{\max} = \rho V_s^2 \tag{3.2}$$

where ρ is the density of soil mass. A large number of studies have been devoted to determining G_{sec}/G_{max} and ξ_g vs. γ_{cyc} (e.g., Seed and Idriss, 1970; Hardin and Drnevich, 1972; Lee and Finn, 1978; Seed et al., 1986; Sun et al., 1988; Ishibashi and Zhang, 1993; Zhang et al., 2005; Oztoprak and Bolton, 2013). These dimensionless modulus and damping curves gave rise to an 'equivalent-linear' method which has been widely used in geotechnical earthquake engineering to simulate true nonlinear soil behaviour, especially in ground response analyses. The limitation of the equivalent-linear method is its inability to capture irrecoverable deformation due to large strains, in which case a nonlinear model is required. A simple criterion for

determining whether a linear, an equivalent-linear or a nonlinear model should be adopted is based on the so-called cyclic threshold shear strains, as marked on the curves in Figure 3.3. The elastic cyclic threshold shear strain γ_{tl} may be considered as the boundary between the linear and the nonlinear soil behaviour whereas the volumetric threshold strain γ_{tv} is the critical strain for the onset of irrecoverable deformations. Both threshold strains increase with PI, as presented in Figure 3.4.

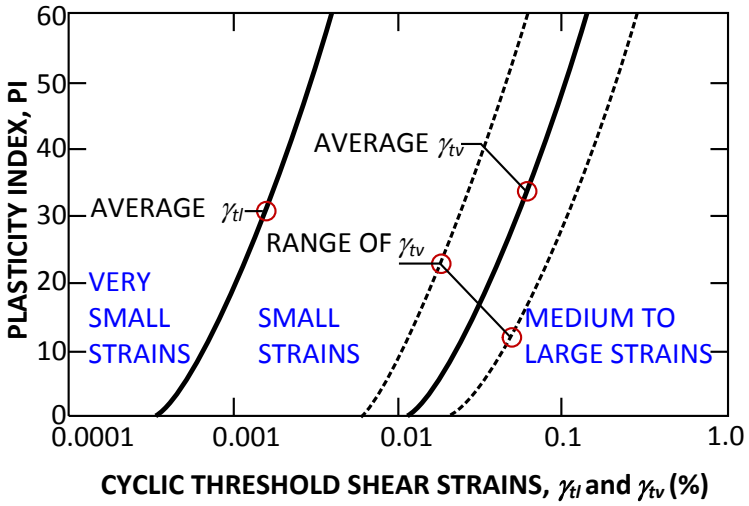

Figure 3.4: Variation of threshold cyclic shear strains γ_{tl} and γ_{tv} with plasticity index PI (after Vucetic, 1994).

In the regime of very small strains, a linear model may be adequate to capture the soil stress-strain relation. If an isotropic material property is assumed, two independent material parameters are required for such a model. These can be a combination of any two parameters of shear modulus G, bulk modulus B and Poisson's ratio ν. In the small strain range where soils do not exhibit severe degradation, the equivalent linear model could be adopted. This method is based on a total stress analysis, with an equivalent shear modulus and viscous damping ratio representing respectively shear resistance and energy loss. Soil nonlinearity is approximated by using the shear modulus degradation curve and damping curve as shown in Figure 3.3. Since both shear modulus and damping ratio are dependent on the calculated strains, an iterative procedure is required so that these properties are compatible with the induced strain levels.

When modelling moderate to large strain behaviour, a nonlinear model is required. Common nonlinear models in engineering practice range from simple cyclic stress-strain relations to advanced elasto-plastic models capable of estimating soil responses under complex three dimensional loading conditions.

Simple nonlinear cyclic stress-strain relations are described by backbone cures, illustrated in Figures 3.2 and 3.3, and a set of rules that define the subsequent unloading and reloading behaviour. Masing and extended Masing rules (Masing, 1926; Pyke, 1979; Vucetic, 1990) are widely adopted to characterise the unloading-reloading soil response and are described as follows (Figure 3.5):

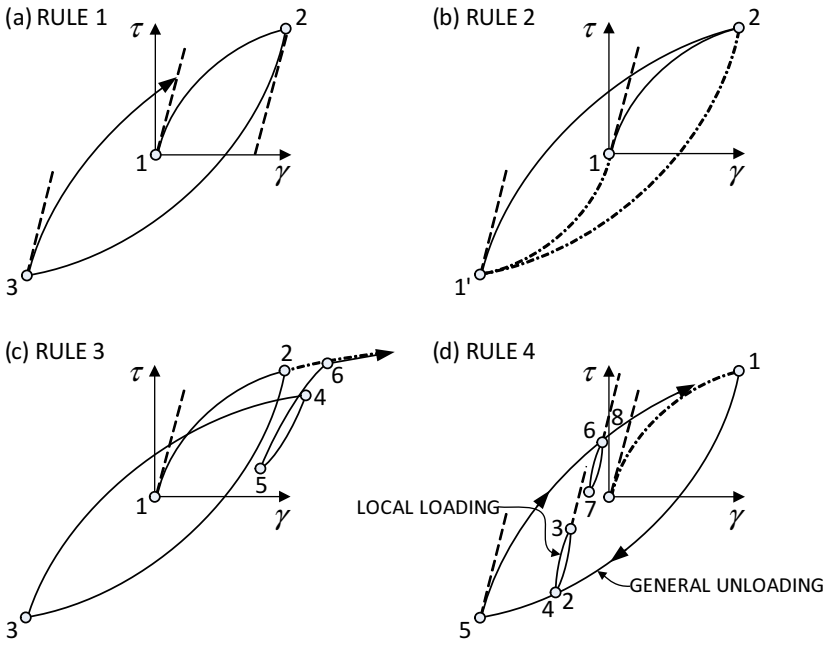

Figure 3.5: Masing and extended Masing rules (after Stewart et al., 2008).

1. The shear modulus upon each loading reversal is equal to the initial tangent modulus of the backbone curve.

2. The unloading or reloading curves have the same shape as that of the initial loading curve, but scaled by a factor of two.

3. The unloading or reloading curves should follow the backbone curve if the maximum past strain is exceeded when intersecting the backbone curve.

4. If an unloading or loading curve intersects the previous unloading or loading curve, the stress-strain relation follows the previous curve.

Although the use of simple backbone relations with Masing rules provides an appealing alternative to the equivalent-linear approximation of nonlinear soil behaviour, it has the following drawbacks (Pyke, 1979; Pyke, 2004). Firstly, by matching the analytical modulus degradation curve to that obtained from experimental cyclic shear tests, the measured damping ratios (when applying Masing rules) are much higher than the lab test results at moderate and large strains. Secondly, the experimental hysteresis loops are not strictly symmetric under constant cyclic shear strains.

Advanced elasto-plastic constitutive models are able to capture complex soil response under various loading conditions. Two widely used models in this class are respectively based on multi-surface plasticity (e.g., Mroz, 1967; Iwan, 1967; Prévost, 1977) and bounding surface plasticity (e.g., Dafalias and Popov, 1975; Krieg, 1975). These models appear frequently in research-based studies but are scarcely used in engineering practice, due to the difficulty in measuring model parameters and expertise required in running nonlinear dynamic analyses (Pecker, 2008).

3.2.2 Site response analysis

When using a domain-type model in earthquake engineering analysis, it is important to ensure that the input motions, boundary conditions and wave propagation characteristics are appropriately captured.

3.2.2.1 Boundary conditions

In dynamic SSI problems where the size of a structure is very small compared to the underlying soil medium, the fixed/roller boundaries (e.g., used in static problems) should be placed at a sufficient distance from the structure to exclude the effects of reflected waves on structural response. However, increasing the size of the soil domain may cause an increase in the number of elements required for modelling,

resulting in a higher computational cost.

Alternatively, special artificial boundaries can be used to prevent/reduce the wave reflection. These boundaries are also called 'quiet boundaries' which either absorb wave energy (e.g., Lysmer and Kuhlemeyer, 1969; Lysmer and Waas, 1972) or let incident waves 'transmit' through them (e.g., Smith, 1974; Lindman, 1975; Zienkiewicz et al., 1983). Kausel (1988) demonstrated that these boundaries were mathematically equivalent. Comparative studies on different types of boundaries used in dynamic analysis showed that the viscous boundary utilising simple physical dashpots provided a good balance between effectiveness and efficiency (e.g., Roesset and Ettouney, 1977; Wolf, 1986).

Lysmer and Kuhlemeyer (1969) proposed that dashpots attached independently to boundary in the normal and shear directions can be used to absorb incident waves. These dashpots provide viscous normal and shear forces, denoted respectively by σ and τ, given by:

$$\sigma = -\rho V_{\mathrm{p}} v_{\mathrm{n}} \qquad \tau = -\rho V_{\mathrm{s}} v_{\mathrm{s}} \tag{3.3}$$

where V_{p} and V_{s} are respectively dilatational and shear wave velocities, v_{n} and v_{s} are respectively normal and tangential components of the velocity at the boundary. This method proves almost perfect for cases where the angle of incidence of the body waves relative to the viscous boundary is greater than thirty degrees while some reflection occurs at lower angles. Moreover, it is easy to implement in engineering practice for solving dynamic problems. However, in order to apply these boundaries to nonlinear soils, the geo-static stress and strain states should be satisfied before a dynamic analysis is performed.

In seismic analysis with site motions represented by vertically propagating plane waves, regardless of the presence of a structure, the lateral boundaries at the sides of the soil model should remain as the free-field condition. The free-field motion can be enforced on some free-field elements that are connected to the main soil model at its lateral boundaries by dashpots (which are operated as those of a quiet boundary) to produce a non-reflecting boundary condition (Cundall et al., 1980).

Another concern with the boundary condition is the application of seismic input. For a shallow soil layer resting on a relatively rigid rock mass shown in Figure 2.4, a time-varying motion recorded on the surface of the rock mass may be applied to the base of the soil layer. However, for a compliant base simulation, the seismic input and the corresponding boundary condition should be treated with care. There are several cases where a compliant base is preferable to be adopted. One example is a practical SSI problem involving a deep soil profile, which can be truncated in modelling to reduce computational cost. Another common example may be a simulation that requires a soil medium to be modelled as a half-space when validating analytical solutions in an elasto-dynamic problem. In these cases, a truncation of the soil medium is necessary while the region outside the modelled soil domain can be replaced by quiet boundaries. When using viscous dashpots to develop a quiet boundary at the base of the soil model, the seismic input should be applied as a stress or force history to the surface or node of the elements that are directly connected to the quiet boundary.

3.2.2.2 Seismic input motion

If an 'uncorrected' (raw) acceleration or velocity record is used as a time history for seismic analysis, several issues could arise. One prominent issue is that integration of the acceleration/velocity data over the recorded duration of motion may not be zero, which consequently leads to unrealistic continuing velocity/residual displacement after shaking. A baseline correction process (see Boore, 2001; Boore and Bommer, 2005) could be performed to correct the acceleration record in order that both final velocity and displacement reduce to zero.

Sometimes the design earthquake ground motions are recorded at the surface of the free field whereas the input motion is usually specified at the base of a domain-type model. A process is required to determine the input motion so that it recovers to the target ground motion. Such a process by which a base input motion is calculated from the target ground motion can be performed through a deconvolution analysis. One dimensional wave propagation problems usually adopt a linear/equivalent-linear

deconvolution on the basis of the use of transfer functions. These transfer functions are ratios of the response at certain depths of a soil profile to that at the free surface and are usually frequency dependent. In order to calculate an input response history, first the ground motion should be expanded into its Fourier series. Then each term in the Fourier series is multiplied by the corresponding transfer function to obtain the Fourier series of the input motion. The input time-varying motion is finally computed through an inverse Fourier transform (Kramer, 1996). An equivalent-linear approach to deconvolution can be realised using a widely used computer program for seismic response analysis called SHAKE (Schnabel et al., 1972).

For numerical analysis of wave propagation, the size of an element should satisfy the following condition so that numerical distortion of transmitting waves is avoided (Kuhlemeyer and Lysmer, 1973):

$$\Delta l \leq \frac{\lambda}{10} \sim \frac{\lambda}{8} \tag{3.4}$$

where Δl is the spatial element size and λ is the wavelength associated with the highest frequency component that contains appreciable energy. It is clear in Equation (3.4) that frequency content of a ground motion controls the allowable maximum size of an element of a domain-type model. Acceleration records containing higher frequency components require a finer spatial mesh and consequently a more expensive computation. Silva (1988) showed that up to 75% of the power (87% of the amplitude) of a ground motion is due to vertically propagating shear waves at frequencies less than 15 Hz. The rest of the energy is carried by scattered waves and P-waves. In this sense, a 15Hz low-pass filter can be applied to the ground motion to remove high frequency components. Alternatively, one may look at the power spectral density of the motion and determine the frequency (up to which most of the power is preserved) of the low-pass filter.

3.3 Spring-type models

For practicing engineers, it is desirable to have a model, which is simpler than the domain-type model, that is still able to capture the most important features

of a vibrating foundation-soil system so as to provide reliable information for design of the superstructure. Simplifying assumptions are made in order to develop such models. For example, the foundation is usually assumed to be rigid so that only the responses at a point representative of the foundation (e.g., the base centre of a surface foundation) are necessary to be calculated. The soil compliance can be represented by coupled/uncoupled springs, whose stiffness is either constant, or frequency/deformation-dependent. This section reviews several simplified foundation-soil interaction models that are popular in engineering practice, with their strengths and limitations summarised.

3.3.1 Foundation impedance function

A foundation impedance function characterises the dynamic force-displacement relationship of a massless foundation (in a specific mode of vibration) resting on or embedded in an elastic soil medium. It varies with foundation stiffness, geometry and soil stratigraphy.

For a structure built on a surface foundation bonded to a homogeneous isotropic elastic soil half-space illustrated in Figure 3.6(a), when subject to a vertically propagating shear wave, the motions of the (massless) foundation may be determined by using a simplified model (Figure 3.6(b)) which replaces the soil half-space with a sway and rocking foundation impedance (coupling between the sway and rocking motions for a surface foundation is usually negligible) and responds to the free-field horizontal ground shaking. Mathematically, each of the impedance functions is complex-valued with its real and imaginary parts modelled respectively by a spring and a dashpot, arranged in parallel (Figure 3.6(c)):

$$\overline{k}_j(\omega) = k_j(\omega) + i\omega c_j(\omega) \tag{3.5}$$

where $\overline{k}_j(\omega)$ is a complex-valued impedance function that relates the generalised foundation forces F (e.g., base shear and moment) to the corresponding displacements u (e.g., translation and rotation) and depends on the circular frequency of vibration ω; j=h, θ denote respectively the sway and rocking modes of vibration;

$k_j(\omega)$ is the stiffness of the spring; $c_j(\omega)$ is the viscous damping coefficient of the dashpot; and i is the imaginary unity satisfying $i^2 = -1$.

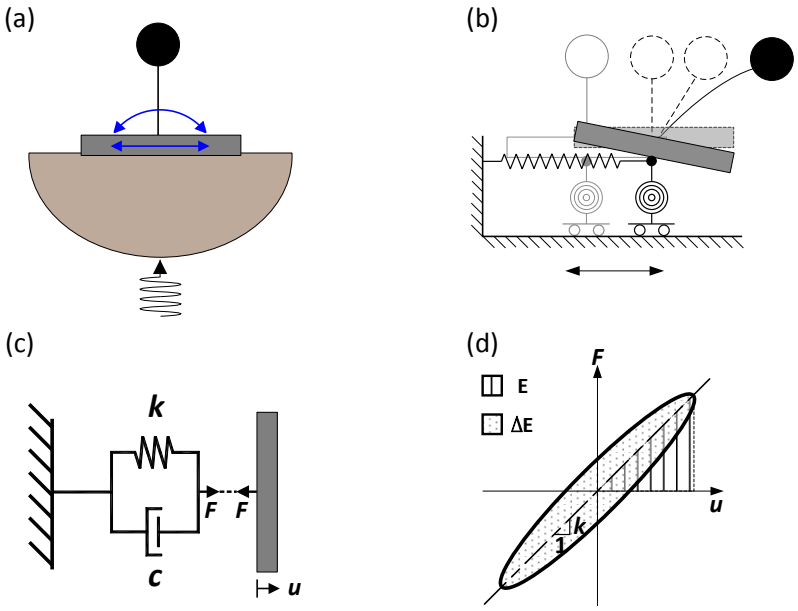

Figure 3.6: (a) vibration of a laterally excited structure supported by a surface foundation on an elastic soil half-space; (b) the soil half-space is replaced by a sway and a rocking impedance function; (c) each of the impedance functions can be represented physically by a spring and dashpot placed in parallel; (d) the steady-state response of a foundation impedance exhibits a hysteresis loop.

The steady-state harmonic force-displacement response of the configuration shown in Figure 3.6(c) is depicted in Figure 3.6(d), which is very similar to the stress-strain loop illustrated in Figure 3.2(b). The energy dissipated during one force-displacement cycle ΔE equals the area enclosed by the loop:

$$\Delta E = \pi c(\omega)\omega u^2(\omega) \tag{3.6}$$

where $u(\omega)$ is the displacement amplitude associated with the frequency ω. The maximum elastic energy stored in one cycle E is given by:

$$E = \frac{1}{2}k(\omega)u^2(\omega) \tag{3.7}$$

The damping ratio ξ is obtained by substituting Equations (3.6) and (3.7) into Equation (3.1):

$$\xi = \frac{\omega c(\omega)}{2k(\omega)} \tag{3.8}$$

This foundation damping ratio, valid when $k(\omega) > 0$, includes contributions from both wave radiation and soil nonlinearity.

Since a zero-frequency stiffness corresponds to a static foundation stiffness, a frequency dependent term may be extracted from $k_j(\omega)$ and written explicitly as a dynamic modifier (stiffness coefficient) α_j to the static stiffness K_j:

$$k_j(\omega) = \alpha_j(\overline{\omega},\, \nu,\, \xi_{\mathrm{g}})K_j \tag{3.9}$$

where ν is the Poisson's ratio of the homogeneous soil medium; ξ_{g} is the hysteretic soil damping ratio given by Equation (3.1); for a circular surface foundation, a dimensionless frequency $\overline{\omega}$ and the static foundation stiffness K_j are expressed as (Poulos and Davis, 1974):

$$\overline{\omega} = \frac{\omega r}{V_{\mathrm{s}}} \tag{3.10}$$

$$K_{\mathrm{h}} = \frac{8Gr}{2-\nu} \tag{3.11}$$

$$K_{\theta} = \frac{8Gr^3}{3(1-\nu)} \tag{3.12}$$

where r is the radius of the foundation, G is the shear modulus of the homogeneous soil medium.

Impedance functions for rigid circular foundations resting on a homogeneous and isotropic elastic half-space were derived by Luco and Westmann (1971) and Veletsos and Wei (1971). The effects of foundation shape, flexibility, embedment and soil non-homogeneity with depth have been accounted for through experimental or numerical techniques (e.g, Kausel et al., 1974; Bielak, 1974; Elsabee and Morray, 1977; Iguchi and Luco, 1982; Dobry and Gazetas, 1986; Apsel and Luco, 1987; Liou and Huang, 1994).

Figure 3.7 presents the frequency-dependent sway and rocking foundation impedance functions obtained using the closed form expressions proposed by Veletsos and Verbič (1973). These expressions were derived based on the assumption that only a portion of the half-space represented by a semi-infinite truncated cone (see details in Section 3.3.2) is effective in transmitting the energy imparted to the circular surface

foundation (Meek and Veletsos, 1973). Modifications to the cone expressions were empirically made to match the rigorous half-space solutions obtained by Veletsos and Wei (1971) (Verbič and Veletsos, 1972). Graphical solutions of the impedance functions illustrated in Figure 3.7 show the variation of stiffness and damping of a disk bonded to an undrained soil half-space (ν=0.5), with and without soil hysteretic damping (ξ_g=0, 0.05), with frequency of vibration. It is clear in Figure 3.7 that inclusion of soil material damping reduces the stiffness coefficient while increasing the foundation damping. For the rocking motion, the stiffness coefficient α_θ decreases with increasing frequency of vibration, and α_θ may have negative values.

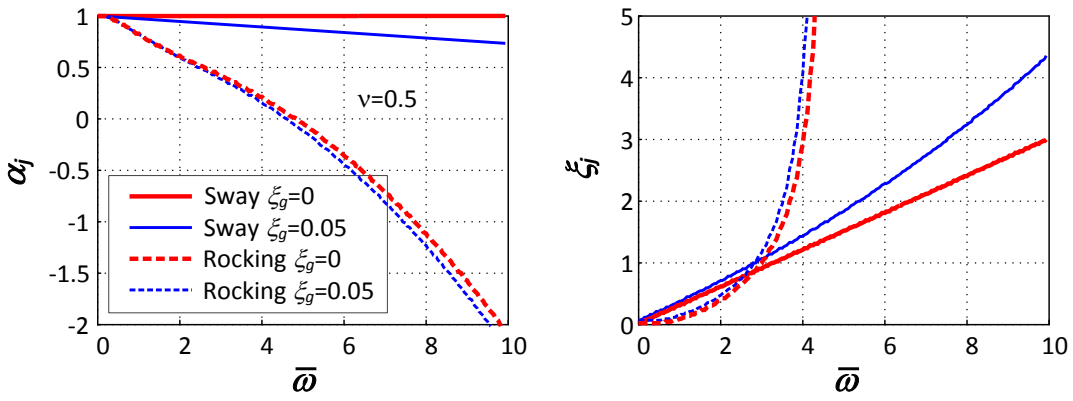

Figure 3.7: Variation of stiffness coefficient and damping of circular surface foundation with vibration of frequency (results are based on Veletsos and Verbič (1973)).

Although impedance functions are able to characterise the frequency response of the foundation force-displacement relationships, their application in seismic soil-structure interaction analyses require the performance of Fourier/Inverse Fourier transform. Nonlinear behaviour of the structure is not permitted in these analyses.

3.3.2 Discrete-element model based on cone theory

Structural engineers prefer to use simplified lumped-element models assembled by constant masses, springs and dashpots representing the effects of inertia, stiffness and damping, respectively. A prominent advantage of such a model over the impedance functions is the frequency-independence of each model element, which

enables the model to be analysed in the time domain where structural nonlinearity can be accounted for.

This section presents a simplified lumped-element model based on the cone theory, which was first introduced by Ehlers (1942) and then extended by Meek and Veletsos (1973), Meek and Wolf (1992a), Meek and Wolf (1992b), and Meek and Wolf (1994a). The basic idea of this theory is to replace the soil medium with a truncated cone for each foundation motion, as depicted in Figure 3.8 where the comma denotes the ordinary derivative. A 'plane sections remain plane' postulation is adopted so that the complex three-dimensional elasticity is substituted by a simple approximate one-dimensional description.

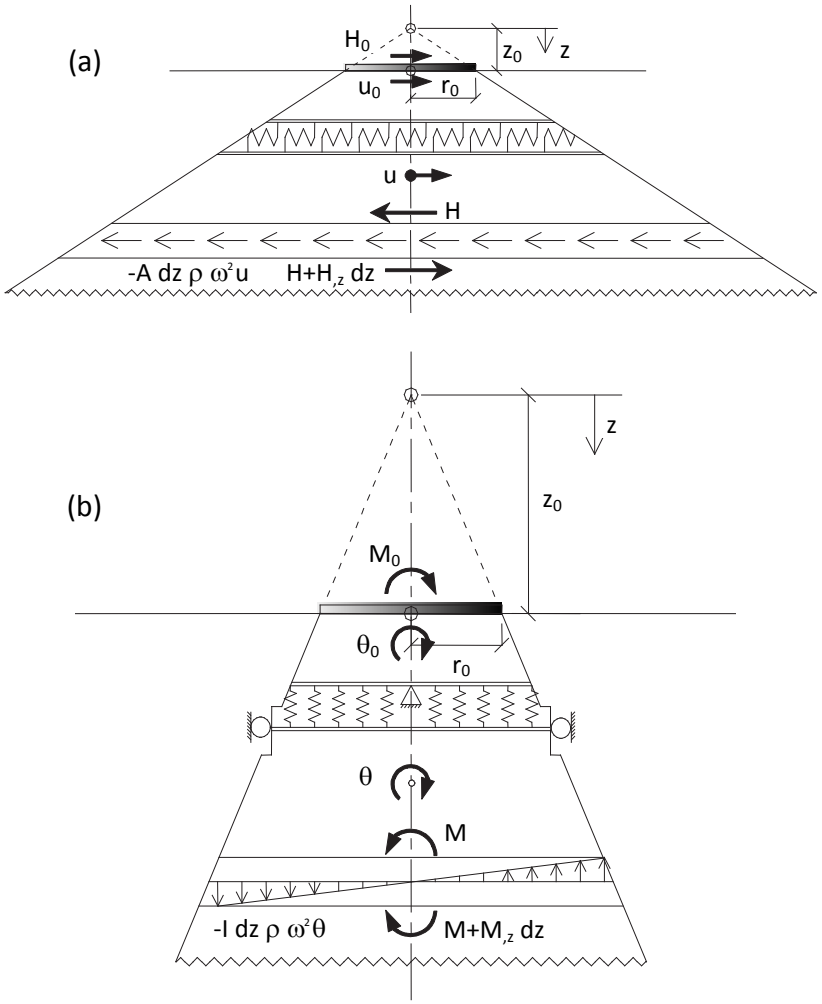

Figure 3.8: Truncated semi-infinite cones and equilibrium of infinitesimal element for (a) horizontal motion with shear distortion and (b) rocking motion with rotational axial distortion (after Wolf and Deeks, 2004).

By equating the static stiffness of the cone to that of the foundation on a half-space, the aspect ratio z_0/r_0 can be determined. The dynamic force-displacement relationships of the foundation are developed by solving the equations of motion of an infinitesimal element within the cones. The portion of the half-space outside the cone is disregarded. Mathematical details of the derivations of the dynamic foundation force-displacement relationships are presented in Wolf (1994).

With reference to the notations in Figure 3.8, cone solutions of the sway and rocking foundation force-displacement relationships are formulated in the time domain and are shown respectively by Equations (3.13) and (3.14).

$$H_0(t) = K_{\mathrm{h}} u_0(t) + C_{\mathrm{h}} \dot{u}_0(t) \tag{3.13}$$

$$M_0 = K_\theta \theta_0(t) + C_\theta \dot{\theta}_0(t) + \Delta M_\theta \ddot{\theta}_0(t) - \int_0^t h(t-\tau) C_\theta \dot{\theta}_0(\tau) d\tau \tag{3.14}$$

where K_{h} and K_θ are given by Equations (3.11) and (3.12), C_{h} and C_θ are viscous damping coefficients calculated by:

$$C_{\mathrm{h}} = \rho V_{\mathrm{s}} A_0 \qquad\qquad C_\theta = \rho V I_0 \tag{3.15}$$

where ρ is the soil mass density; A_0 and I_0 are area and centroidal moment of inertia of the circular foundation; V_{s} is the shear wave velocity, whereas V equals the dilatational wave velocity V_{p} for $\nu \leq 1/3$, and V_0=$2V_{\mathrm{s}}$ for $1/3 < \nu \leq 1/2$. In Equation (3.14),

$$\Delta M_\theta = \begin{cases} 0, & \text{if } \nu \leq 1/3. \\ 0.3\pi \left(\nu - \dfrac{1}{3}\right) \rho r_0^5, & \text{if } 1/3 < \nu \leq 1/2. \end{cases} \tag{3.16}$$

and the last term with a negative sign is a convolution integral performed with the rotational velocity $\dot{\theta}_0$ where $h(t)$ is a unit-impulse response function defined by:

$$h(t) = \begin{cases} 0, & \text{if } t < 0. \\ \dfrac{V}{z_0} \exp(-\dfrac{V_0}{z_0} t), & \text{if } t \geq 0. \end{cases} \tag{3.17}$$

ΔM_θ is associated with trapped soil beneath the foundation, which for nearly incompressible soil ($\nu \rightarrow 1/2$) moves as a rigid body in phase with the foundation (Wolf,

1994); the convolution integral is used to tune the frequency-dependent response of the massless foundation-soil system. The low-frequency response is governed by the static stiffness K_θ whereas the high-frequency response is dominated by the dashpot coefficient C_θ.

Soil hysteretic damping can be accounted for by applying the correspondence principle (Bland, 1960) which requires each of the elastic constants (stiffness modulus) to be multiplied by a complex factor $1 + 2i\xi_g$. Meek and Wolf (1994b) presents a discrete-element model, sketched in Figure 3.9, which is not only capable of incorporating soil material damping but also able to accommodate rigorously the convolution integral embedded in the moment-rotation relationship. The mass moment of inertia M_φ added to the degree of freedom φ is calculated by:

$$M_\varphi = \frac{9}{128}(1-\nu)\pi^2\rho r^5\left(\frac{V_p}{V_s}\right)^2 \tag{3.18}$$

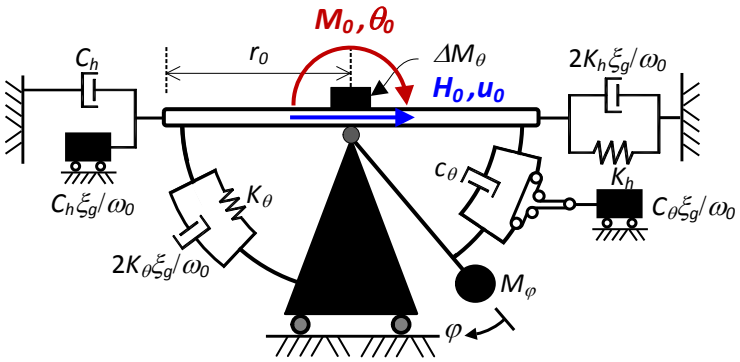

Figure 3.9: Discrete-element sway-rocking model based on the cone theory (after Wolf, 1994).

Application of the corresponding principle to the mathematical dynamic foundation force-displacement relationships is physically equivalent to augmenting each of the original spring and dashpot respectively by an additional spring and mass, connected in parallel, as shown in Figure 3.9. Utilising a Voigt theory of viscoelasticity, the soil material damping ratio ξ_g exhibits its exact value only at the frequency of vibration ω=ω_0. For practical application of the model, it is usually assumed that ω_0 equals the fundamental circular frequency of the vibrating system of interest.

The strength of the presented discrete-element model is its rigorous treatment of

the cone theory that approximates the foundation vibration analysis for a half-space problem. The model components with constant coefficients have clear physical meanings and are best suited for time domain analysis where nonlinear structural behaviour is permitted. Although the cone theory is based on a number of simplifying assumptions, its accuracy has been proved against rigorous half-space solutions to be sufficient in practical applications (Wolf, 1994). The limitations of the discrete-element cone model are as follows. Firstly, the model is not able to capture the plastic (irrecoverable) deformation in the soil medium. As a result, the residual foundation displacements may not be reflected. Secondly, the assumption that the foundation is perfectly bonded to the ground surface may not be appropriate for light slender structures built on sandy soil with large load eccentricity during strong shaking, in which case temporary separation of the foundation and the soil could occur.

3.3.3 Beam on Winkler foundation model

Although SSI procedures in most current seismic standards and provisions (see Section 2.4) are based on linear (equivalent-linear) soil behaviour while attributing all nonlinearities to plastic hinging in structural components, these guidelines also take into account possible nonlinearity arising from foundation-soil interaction in design considerations for foundations. A Winkler-based model is often used in practice for seismic design of foundations.

In general, apart from plastic hinges in structural components, two main types of nonlinearity are common in strong shaking events. As is illustrated in Figure 3.10(a), if no tensile stress is allowed to develop in the soil medium, severe rocking motion may lead to uplift at one side of the foundation, which in the meantime increases the bearing pressure beneath the other side of the foundation. The uplifting phenomenon, associated with a geometric nonlinearity, reduces the contact area between the foundation and the underlying soil, resulting in progressive loss of stiffness of the system. The increase in foundation bearing pressure may give rise to yielding of soil (material nonlinearity). Another possible nonlinear mechanism is

the sliding of the foundation over the ground surface caused when frictional capacity of the foundation-soil interface is exceeded.

In Figure 3.10(b), the whole system is represented by a Winkler model containing a number of closely placed vertical springs that are used to account for the coupled vertical and rocking modes of vibration. A horizontal spring is used to model the swaying response of the foundation. In order to capture the partial separation between the foundation and soil, each of the spring consists of a gap element as depicted in Figure 3.10(c). Energy dissipation due to radiation damping and soil plasticity can be described respectively by a dashpot and an elasto-plastic element.

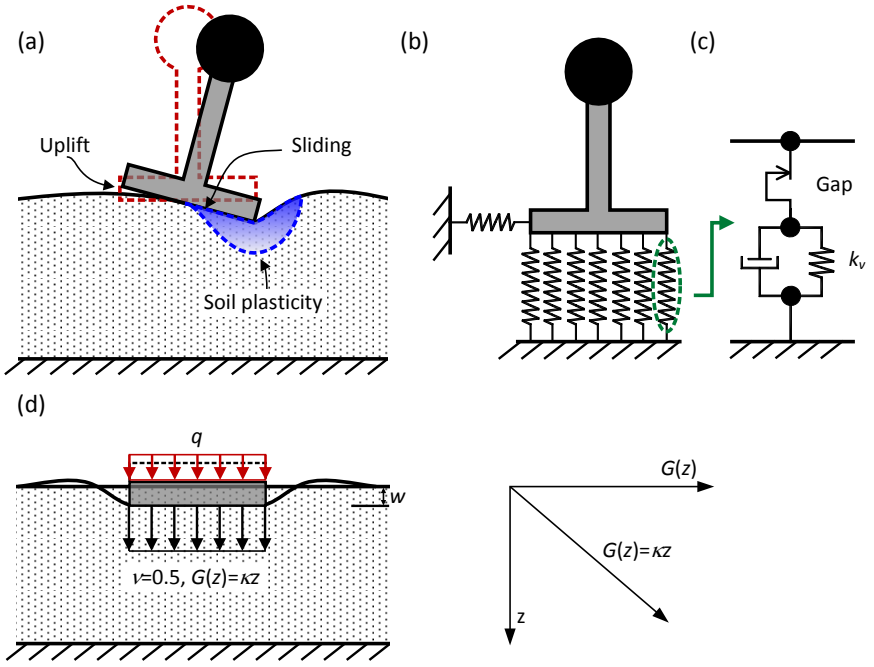

Figure 3.10: (a) Soil-structure interaction system with different types of nonlinearities. (b) Foundation stiffness and strength are characterised by Winkler springs. (c) Each of the springs consists of a gap element to capture loss of contact between the foundation and soil. (d) Uniform bearing pressure beneath a vertically loaded foundation resting on an incompressible soil medium with shear modulus (which equals zero at the ground surface) increasing linearly with depth.

Calibration of the spring stiffness k_{V} is usually done by matching the global vertical

foundation stiffness for the actual system to that of the Winkler model. A variety of foundation pressure distributions can be assumed, and the simplest one is the uniform distribution, which is valid for a foundation resting on an elastic incompressible half-space with Poisson's ratio $\nu = 0.5$ and shear modulus that is zero at ground level and increases linearly with depth at a gradient κ, as illustrated in Figure 3.10(d) (Gibson, 1967). The vertical spring stiffness k_{V}, also called a 'coefficient of subgrade reaction' is defined as the ratio of the pressure q to the corresponding settelment w:

$$k_{\mathrm{V}} = \frac{q}{w} = 2\kappa \tag{3.19}$$

For the case of a homogeneous half-space however, the assumption of a uniform stress distribution due to a settlement of w does not comply with the elastic solution. Figure 3.11(a) shows a smooth strip foundation resting on an elastic uniform half-space. The contact pressure distributions due to a pure vertical load and a rocking moment are illustrated respectively in Figures 3.11(b) and (c) (Borowicka, 1939; Muskhelishvili, 1966). The pressure is much higher at both ends of the foundation, tending to infinity at $|x/b| = 1$. If a constant k_{V} is used to match the global vertical foundation stiffness K_{V}, the global rocking stiffness K_θ will be underestimated.

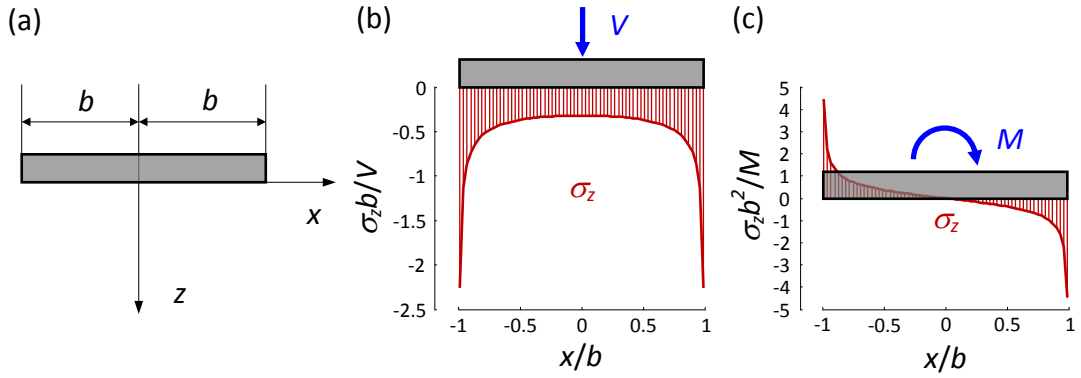

Figure 3.11: (a) Smooth strip foundation resting on an elastic homogeneous half-space. (b) Contact pressure distribution due to a vertical load V (per unit length). (c) Contact pressure distribution due to a moment M (per unit length).

In order to tune the Winkler model to approximately match both the global vertical and rocking stiffnesses from elastic solutions (Gazetas, 1991), ASCE (2013) suggests

that a footing (length× width=$L \times B$) be divided into two regions with stiffer vertical springs placed in the end regions (L_{end}=$B/6$), as illustrated in Figure 3.12. The stiffness per unit length in these end zones is based on the vertical stiffness of a $B \times B/6$ isolated footing. The stiffness per unit length in the middle zone is equivalent to that of an infinitely long strip footing.

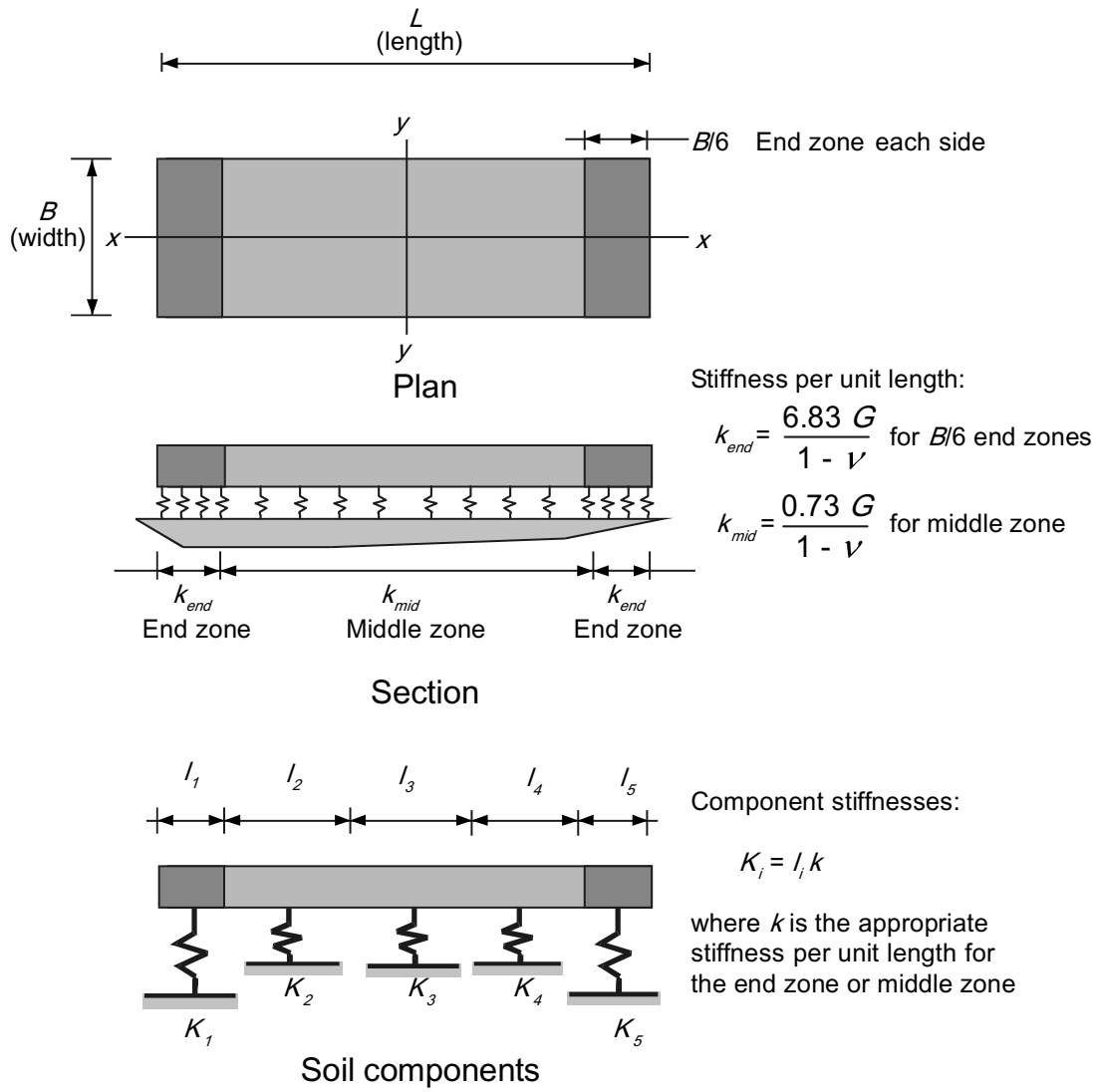

Figure 3.12: Bed of Winkler-spring model for shallow strip footings in ASCE (2013).

Alternative methods to approximate the analytical global vertical and rocking foundation stiffnesses have been proposed by Harden et al. (2005), Houlsby et al. (2005), Pender et al. (2006), and Apostolou (2011).

On the other hand, for the same strip foundation, shown in Figure 3.11(a), lying

on a homogeneous undrained clay half-space, a uniform distribution of the spring capacity, obtained by matching the global foundation bearing capacity due to a pure vertical load V_u, is sufficient to capture the foundation failure due to a combined vertical load and rocking moment. The failure envelope for the coupled vertical-rocking motions is described by:

$$\frac{M_c}{V_u b} = \frac{V_c}{V_u} - \left(\frac{V_c}{V_u}\right)^2 \tag{3.20}$$

where M_c and V_c are respectively moment and vertical load when foundation bearing capacity is fully mobilised. Equation (3.20) was analytically derived by Meyerhof (1953), Allotey and El Naggar (2003), and Gajan et al. (2005), and confirmed by Gourvenec (2007b) and Gazetas et al. (2013) through finite element modelling.

A limitation of the Winkler model shown in Figure 3.10(b) is the lack of coupling between the horizontal and vertical/rocking motions. For example, the capacity of the horizontal spring is usually set equal to the shear (frictional) capacity H_u of the foundation when it is in full contact with the underlying soil. However, the mobilisable 'shear strength' of the foundation due to combined vertical-horizontal-moment loading is generally lower than H_u. Moreover, the gradual loss of contact between the foundation and soil due to uplift (geometric nonlinearity) decreases the shear capacity. To overcome this limitation, Houlsby et al. (2005) employed a generalised Winkler model where normal and shear components of traction on the base of the foundation were treated within a plasticity-based framework, as shown in Figure 3.13.

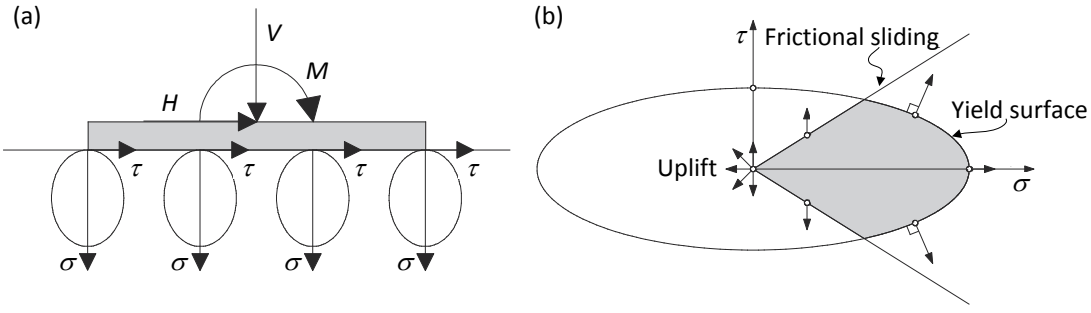

Figure 3.13: (a) Generalised Winkler model with pointwise behaviour characterised by plasticity-based σ-τ interaction diagram. (b) Yield surfaces and flow for each point at the base of the foundation. (Houlsby et al., 2005).

Although the Houlsby et al. (2005) model is Winkler-based, strictly speaking, it falls into the category of a macro-element model rather than a conventional spring-type model. The following section provides a brief review of the macro-element models.

3.4 Macro-element model

The concept of a macro-element representation of the foundation-soil interaction arises from the similarity between the macroscopic foundation force-displacement relationships and the stress-strain relationships of a soil element. Within a framework of plasticity, the yield surface of a soil element is replaced by a failure envelope in the generalised V-H-M space. An example of such an envelope is shown in Figure 3.14 for a circular foundation lying on sand under combined planar loading (Houlsby and Cassidy, 2002).

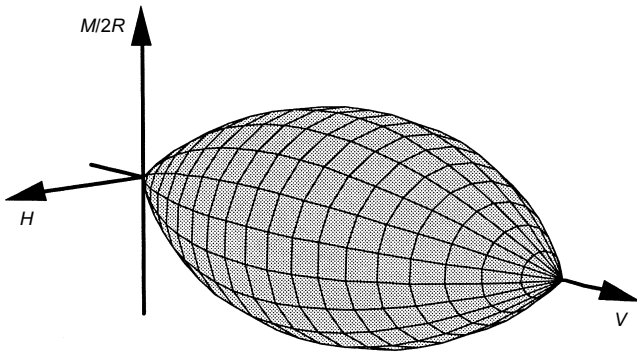

Figure 3.14: Shape of the failure envelope for a circular foundation of a radius R resting on sand. (Houlsby and Cassidy, 2002).

In the context of earthquake engineering applications, Paolucci (1997) was the first to introduce a macro-element model for simulating the seismic behaviour of a strip foundation on sand, utilising a V-H-M failure envelope proposed by Nova and Montrasio (1991). This model was based on an elastic perfectly plastic foundation force-displacement relationship where the foundation-soil system behaved quasi-elastically within the failure envelope, while infinite plastic flow occurred whenever the force state of the foundation resided on the failure envelope. The plastic foundation displacements are calculated from a non-associated flow rule whereas uplift behaviour

was disregarded in Paolucci (1997).

Cremer et al. (2001) proposed a macro element for nonlinear dynamic soil structure interaction analysis of a strip foundation resting on clay. Their model consists of two sub-models that simulate both soil plasticity and foundation uplift, previously shown in Figure 3.10(a). These two sub-models were built separately but coupled. The plasticity model reproduced continuous yielding of the foundation by defining a loading surface (yield surface) that evolves in the V-H-M towards the failure envelope under a monotonic loading. Compared with the Paolucci (1997) model which exhibits a bi-linear hysteretic response under strong cyclic loading, the Cremer et al. (2001) model is able to capture the gradual variation of foundation (tangent) stiffness during the loading/unloading cycles, which could arise from geometrical expansion/contraction of the plastic zone, even if a soil element follows elastic perfectly plastic behaviour. The Houlsby et al. (2005) model shown in Figure 3.13 is also able to model the gradual change of foundation stiffness due to yielding. Actually, integration of the pointwise response along the foundation gives rise to a multiple-surface model in the V-H-M space. Gajan and Kutter (2009) developed a Contact Interface Model by keeping track of the geometry of the soil surface beneath the footing as well as the kinematics of the footing-soil system including moving contact areas and gaps. The variation of foundation stiffness was determined based on the bounding surface plasticity theory. Macro-element models combine the features of both domain and spring-type models (i.e., coupling and efficiency). However, this macro element for practical engineers remains a 'black box' where the multi-yield (and sometimes multi-mechanism) complexity makes it difficult to be implemented into computer codes.

3.5 Summary

Common models for simulating foundation vibration were reviewed in this chapter. The domain-type models are able to handle complex geometry and loading in two and three-dimensional engineering problems. A variety of material constitutive re-

lations are available. The boundary conditions and dynamic input motions should be treated with care. Spring-type models are efficient practical tools assembled by independent elements with clear physical meanings. The plasticity-based macro-element models combine the features of domain-type and spring-type models. Users can choose the models of interest according to their strengths and limitations.

Chapter 4

Numerical and analytical modelling of dynamic SSI

4.1 Introduction

This chapter focuses on obtaining the dynamic response of soil structure interaction systems. Several methods are presented to solve such a problem for an input seismic motion. Multi-storey buildings are represented by Multi-Degree-Of-Freedom (MDOF) shear-beam models. Both impedance functions (see Section 3.3.1) and cone models (see Section 3.3.2) are employed to simulate the dynamic foundation-soil interaction. Fourier and inverse Fourier transforms are performed when using the frequency-dependent impedance functions while the equations of motion for cone models are solved using numerical integration techniques. For the simplest case, the MDOF shear-beam building reduces to a SDOF oscillator, as commonly adopted to derive seismic response spectra. In this case, a fixed-base oscillator is introduced to approximate the response of the flexible-base SDOF structure. The methods described in this chapter are the basis for analysis in the following two chapters.

4.2 SSI models and equations of motion

In a preliminary seismic design stage, building structures are often simplified into equivalent MDOF models. Shear-building models are one such simplified model that have been widely used to study the seismic response of multi-storey buildings. This type of model, despite some drawbacks, is adopted herein due to its capability of capturing both nonlinear behaviour and higher mode effects without compromising the computational effort (e.g., Diaz et al., 1994; Takewaki, 1998). All parameters required to define a shear-building model corresponding to a full-frame model can be determined by performing a single pushover analysis (Hajirasouliha and Doostan, 2010). A typical shear-building model is illustrated in Figure 4.1 where each floor is idealised as a lumped mass connected by springs that only experience shear deformations when subjected to lateral forces.

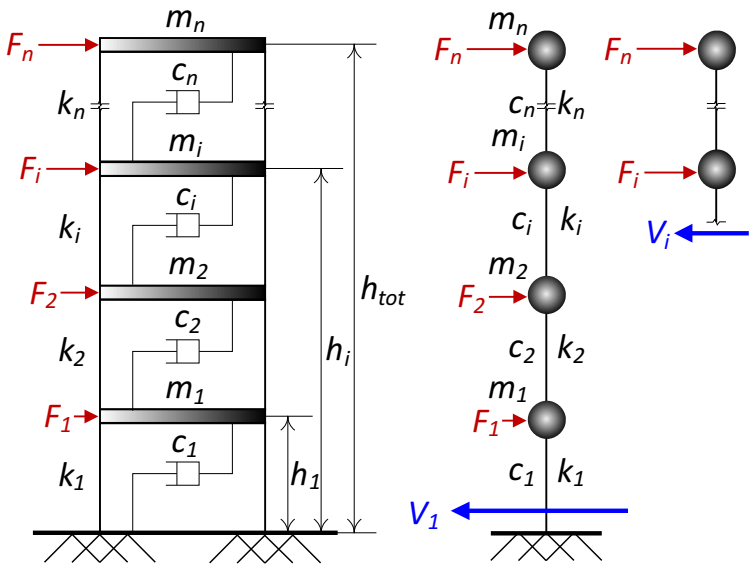

Figure 4.1: Typical shear-building model fixed in its base.

In shear-building models, the lateral strength (and stiffness) of each floor is assumed proportional to the corresponding storey shear force V_i which can be obtained by enforcing force equilibrium with an applied equivalent lateral force pattern. The lateral seismic force distributions in most building codes (e.g., IBC, 2012) follow a pattern which is similar to the first-mode deflected shape of lumped MDOF elastic

systems. In general, the design lateral force F_i at storey i can be expressed as:

$$F_i = \frac{w_i h_i^k}{\sum_{j=1}^{n} w_j h_j^k} V \tag{4.1}$$

where V ($= V_1$ in Figure 4.1) is the total design base shear; w_i and h_i are the effective weight and height of the floor at level i from the ground, respectively; n is the number of storeys; and the exponent k, as a function of the building's fundamental period (T_s), is mainly used to take into account higher mode effects (Hajirasouliha and Pilakoutas, 2012). To compare the effect of lateral force distribution on the seismic response of MDOF structures, six different patterns are considered in this study, as depicted in Figure 4.2. Table 4.1 presents the k values in accordance with each force pattern.

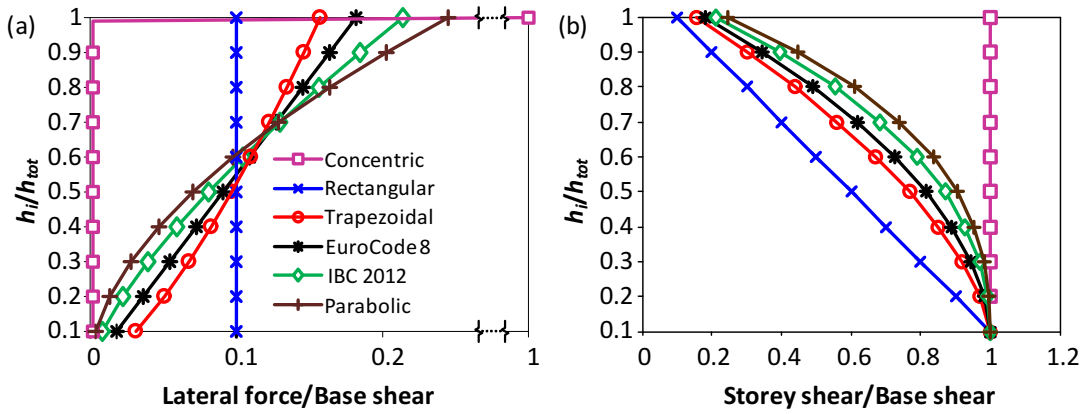

Figure 4.2: Seismic lateral force and storey shear distributions adopted in this study (curves plotted for T_s=1.0sec).

According to ASCE (2010), the fundamental period of an MDOF structure in its fixed-base condition can be approximated by using the following formula:

$$T_s = C_t h_{tot}^x \tag{4.2}$$

where h_{tot} is the total height of the MDOF structure, while the coefficients C_t and x are related to the type of the structural system, as presented in Table 4.2.

A complete soil-structure model is illustrated in Figure 4.3(a) where a multi-storey shear frame is built on a rigid foundation that rests on a soil half-space, subjected to

the horizontal component of a seismic motion. It is assumed the horizontal motion is caused by a coherent shear wave that propagates vertically. In this case, kinematic interaction would not occur and the free-field ground motion, denoted by u_g, can directly be applied to the foundation (see Section 2.2.1). The complete SSI model can be represented by simplified models through transforming the shear frame into an equivalent MDOF structure and replacing the soil half-space by either the impedance functions (Figure 4.3(b)) described in Section 3.3.1 or the discrete-element model (Figure 4.3(c)) based on the cone theory (see Section 3.3.2). To simplify the analysis, it is assumed that the building and foundation are axisymmetric. The effective radii r of each floor and foundation are determined by Equation (2.9) and their moments of inertia are calculated by:

$$J_i = \frac{m_i r^2}{4} \tag{4.3}$$

Table 4.1: Lateral load patterns determined by the exponent k

Lateral load pattern	Exponent k
Concentric	N/A (A single load applied at roof)
Rectangular	0
Trapezoidal	$0.5+0.2T_s$
Eurocode 8	1
IBC-2012	1, if T_s <0.5sec 2, if $T_s > 2.5$sec $1 + 0.5(T_s - 0.5)$, other T_s
Parabolic	$1+0.8T_s$

Table 4.2: Values of C_t and x for different structural systems according to ASCE (2010)

Structural Type	C_t	x
1 Steel moment-resisting frames	0.0724	0.8
2 Concrete moment-resisting frames	0.0466	0.9
3 Steel braced frames	0.0731	0.75
4 All other structural systems	0.0488	0.75

The following presents the equations of motion for the soil structure interaction system shown in Figure 4.3. Notations for the parameters used in the equations are consistent with those illustrated in Figures 3.9 and 4.3, unless stated otherwise. The subscripts 'imp' and 'con' are used to denote quantities associated with the soil impedance model (Figure 4.3(b)) and the cone model (Figure 4.3(c)) respectively. The governing equation can be written in the following matrix form:

$$[M]\{\ddot{u}\} + [C]\{\dot{u}\} + [K]\{u\} = -[M]\{R\}\ddot{u}_{\mathrm{g}} \tag{4.4}$$

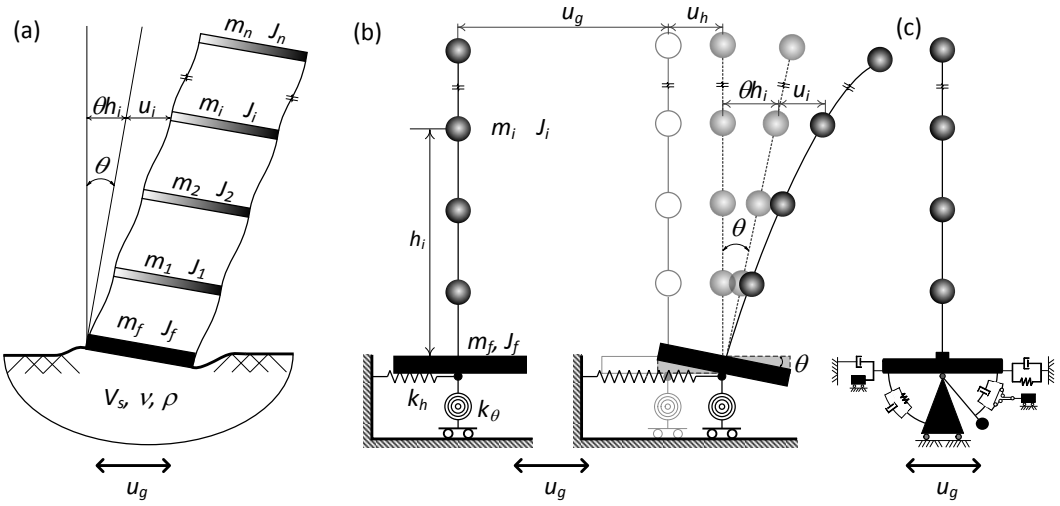

Figure 4.3: Soil-structure interaction models: (a) multi-storey shear frame resting on a soil half-space, (b) equivalent MDOF structure supported by soil impedance functions, (c) soil half-space replaced by the cone-based discrete-element model.

The mass matrix $[M]$ in general can be expressed as:

$$[M] = \left[\begin{array}{c|c} M_{\mathrm{s}} & M_{\mathrm{sf}} \\ \hline M_{\mathrm{sf}}^T & M_{\mathrm{f}} \end{array}\right] \tag{4.5}$$

where

$$[M_{\mathrm{s}}] = \begin{bmatrix} m_n & & & \\ & \ddots & & \\ & & m_2 & \\ \text{Sym.} & & & m_1 \end{bmatrix} \tag{4.6}$$

$$[M_{\text{sf,con}}] = \left[\begin{array}{c|c} M_{\text{sf,imp}} & 0 \end{array}\right] \tag{4.7}$$

in which

$$[M_{\text{sf,imp}}] = \begin{bmatrix} m_n & m_n h_n \\ \vdots & \vdots \\ m_2 & m_2 h_2 \\ m_1 & m_1 h_1 \end{bmatrix} \tag{4.8}$$

$$[M_{\text{f,con}}] = \left[\begin{array}{c|c} M_{\text{f,imp}} & 0 \\ \hline 0 & 0 \end{array}\right] + \begin{bmatrix} \frac{\xi_{\text{g}} c_{\text{h}}}{\omega_0} & 0 & 0 \\ & \Delta M_\theta + \frac{\xi_{\text{g}} c_\theta}{\omega_0} & -\frac{\xi_{\text{g}} c_\theta}{\omega_0} \\ \text{Sym.} & & M_\varphi + \frac{\xi_{\text{g}} c_\theta}{\omega_0} \end{bmatrix} \tag{4.9}$$

in which

$$[M_{\text{f,imp}}] = \begin{bmatrix} m_{\text{f}} + \sum_{i=1}^{n} m_i & \sum_{i=1}^{n} m_i h_i \\ \text{Sym.} & J_{\text{f}} + \sum_{i=1}^{n} J_i + \sum_{i=1}^{n} m_i h_i^2 \end{bmatrix} \tag{4.10}$$

The stiffness matrix $[K]$ is given by:

$$[K] = \left[\begin{array}{c|c} K_{\text{s}} & 0 \\ \hline 0 & K_{\text{f}} \end{array}\right] \tag{4.11}$$

where

$$[K_{\text{s}}] = \begin{bmatrix} k_n & -k_n & & \\ & \ddots & \ddots & \\ & & k_2 + k_3 & -k_2 \\ \text{Sym.} & & & k_1 + k_2 \end{bmatrix} \tag{4.12}$$

$$[K_{\text{f,con}}] = \left[\begin{array}{c|c} K_{\text{f,imp}} & 0 \\ \hline 0 & 0 \end{array}\right] \tag{4.13}$$

in which

$$[K_{\text{f,imp}}] = \begin{bmatrix} k_{\text{h}} & 0 \\ \text{Sym.} & k_\theta \end{bmatrix} \tag{4.14}$$

where k_{h} and k_θ are frequency-dependent 'stiffnesses' given by Equation (3.5) for the impedance model; while for the cone model, they are equal to the static foundation

stiffnesses according to Equations (3.11) and (3.12). The damping coefficient matrix $[C]$ is calculated according to:

$$[C] = \left[\begin{array}{c|c} C_{\mathrm{s}} & 0 \\ \hline 0 & C_{\mathrm{f}} \end{array}\right] \tag{4.15}$$

where the natural damping in the building in its fixed-base is specified by using the Rayleigh damping formulation:

$$[C_{\mathrm{s}}] = \alpha[M_{\mathrm{s}}] + \beta[K_{\mathrm{s}}] \tag{4.16}$$

where the values of α and β are determined in order that a damping ratio of 5% is assigned to the first mode (of the rigid-base vibrating building) and to the mode at which the cumulative mass participation exceeds 95%.

$$[C_{\mathrm{f,con}}] = \left[\begin{array}{c|c} C_{\mathrm{f,imp}} & 0 \\ \hline 0 & 0 \end{array}\right] + \begin{bmatrix} \frac{2\xi_{\mathrm{g}} k_{\mathrm{h}}}{\omega_0} & 0 & 0 \\ & \frac{2\xi_{\mathrm{g}} k_{\theta}}{\omega_0} & -c_{\theta} \\ \text{Sym.} & & c_{\theta} \end{bmatrix} \tag{4.17}$$

in which

$$[C_{\mathrm{f,imp}}] = \begin{bmatrix} c_{\mathrm{h}} & 0 \\ \text{Sym.} & c_{\theta} \end{bmatrix} \tag{4.18}$$

Similar to k_{h} and k_{θ}, c_{h} and c_{θ} are frequency-dependent for the impedance model; while for the cone model, they are equal to the high-frequency damping coefficients according to Equation (3.15).

The displacement vectors u and influence coefficient vectors R are defined as:

$$\{u_{\mathrm{con}}\} = [u_n, \cdots, u_2, u_1, u_{\mathrm{h}}, \theta, \varphi]^T \qquad \{R_{\mathrm{con}}\} = [0, \cdots, 0, 0, 0, 1, 0, 0]^T \tag{4.19}$$

$$\{u_{imp}\} = [u_n, \cdots, u_2, u_1, u_{\mathrm{h}}, \theta]^T \qquad \{R_{imp}\} = [0, \cdots, 0, 0, 0, 1, 0]^T \tag{4.20}$$

where $u_1 \sim u_n$ are structural distortions (excluding rigid-body movements of the foundation) of the n-DOF building illustrated in Figure 4.3; u_{h}, θ are foundation sway and rocking displacements, corresponding to u_0, θ_0 respectively in Figure 3.9; φ is the DOF of the moment of inertia M_{φ} which is also shown in Figure 3.9.

4.3 Influencing parameters

Past studies showed that a dynamic SSI problem could be defined by using the following dimensionless parameters (e.g., Veletsos and Nair, 1975; Wolf, 1994; Ghannad and Jahankhah, 2007; Ganjavi and Hao, 2014):

1. Structure-to-soil stiffness ratio a_0:

$$a_0 = \frac{\omega_s \overline{H}}{V_s} \tag{4.21}$$

where ω_s is the lowest Eigenfrequency (corresponding to the fundamental period T_s=$2\pi/\omega_s$) of the superstructure in its fixed-base condition and $\overline{H}$ is the corresponding height given by:

$$\overline{H} = \frac{\sum_{i=1}^{n} m_i \phi_{i1} h_i}{\sum_{i=1}^{n} m_i \phi_{i1}} \tag{4.22}$$

in which ϕ_{i1} is the amplitude at the i^{th} storey in the fundamental mode of vibration of the superstructure fixed at its base (see Figure 4.1). For practical purposes, the first-mode amplitude profile for common buildings is usually assumed to be an inverted triangle, thus $\overline{H}$=$0.7h_{\text{tot}}$ can be adopted.

2. Slenderness ratio of the superstructure s calculated as the ratio of structural height $\overline{H}$ to the radius of the foundation r:

$$s = \frac{\overline{H}}{r} \tag{4.23}$$

3. Structure-to-soil mass ratio $\overline{m}$:

$$\overline{m} = \frac{\sum_{i=1}^{n} m_i}{\rho h_{\text{tot}} r^2} \tag{4.24}$$

where ρ is the mass density of the soil.

4. Structure-to-foundation mass ratio $\overline{m}_f$=$m_f/\sum_{i=1}^{n} m_i$.

5. Poisson's ratio of the soil ν.

6. Damping ratio in the structure without damage ξ_s, and in the soil ξ_g.

7. Maximum inter-storey ductility ratio μ defined for any storey i in the Figure 4.3 as:

$$\mu_i = \frac{\Delta u_{i,\max}}{\Delta u_{i,y}} \tag{4.25}$$

where $\Delta u_{i,\max}$ is the maximum inter-storey distortion (i.e., $(u_i - u_{i-1})_{\max}$) whereas $\Delta u_{i,y}$ is the inter-storey distortion at the onset of yielding in the i^{th} storey.

The practical range of the a_0 values can be determined by Equations (4.2) and (4.21) for various soil sites that are classified into different groups according to the average shear wave velocity of the top 30 meters of the sites $V_{s,30}$ (See Table 4.3).

Table 4.3: Site soil classifications according to IBC (2012)

Site class	Soil profile name	$V_{s,30}$(m/s)	ν
A	Hard rock	>1500	N/A
B	Rock	760-1500	N/A
C	Very dense soil/soft rock	360-760	0.33
D	Stiff soil	180-360	0.40
E	Soft soil	<180	0.50

Figure 4.4 illustrates the practical range of a_0 for various types of multi-storey buildings located on different site classes according to IBC (2012). To cover a wide range of SSI conditions, the abscissa in Figure 4.4 starts at 90 m/s representing the average value of site class E, and ends at 1500 m/s which represents a fixed-base condition for common buildings located on site class A.

It is seen from Figure 4.4 that, for a given shear wave velocity, a greater a_0 value is always expected for tall buildings. While the maximum value of a_0 for frame structures is about 2, it is shown that a_0 can increase to up to 3 for other structural systems.

ATC (2005) suggests that for conventional building structures, $\overline{m}$ ranges approxi-

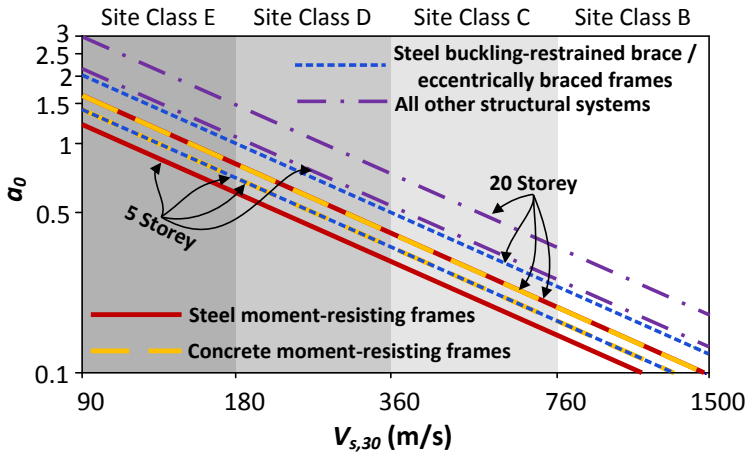

Figure 4.4: Practical range of a_0 for various types of structures located on different soil sites according to IBC (2012).

mately from 0.3∼0.6. In this study, representative values of $\overline{m}$=0.5 and $\overline{m}_{\mathrm{f}}$=0.1 are used. The values of soil Poisson's ratio according to different soil conditions are also presented in Table 4.3. The damping ratios for modelling buildings and soil are both assumed to be 5%. The stated values are consistent with Ghannad and Jahankhah (2007) and Ganjavi and Hao (2014).

4.4 Frequency response analysis

Soil-structure interaction analysis is performed in the frequency domain in this section. For the simplest case, a SDOF structure supported by foundation springs is first considered, as shown in Figure 4.5(a). It is reasonable to assume that the harmonic response of the SSI system is qualitatively similar to that of a fixed-base oscillator. Furthermore, it may be possible to use an Equivalent Fixed-base SDOF (EFSDOF) oscillator (Figure 4.5(b)) to quantitatively capture the harmonic response of the SSI system, especially its dominant mode of vibration.

Rather than formulating the equations of motion (EOM) of the SSI system with respect to the structural distortion, as done in Equations (4.19) and (4.20), it is more convenient to write the equations with respect to the displacement of the mass relative to the ground, i.e., u_{ssi} shown in Figure 4.5. In this case, there is a one-to-one

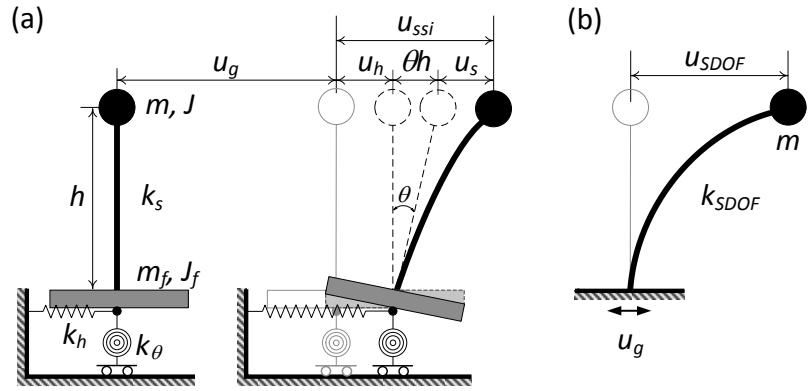

Figure 4.5: (a) SDOF structure supported on a compliant base. (b) Equivalent Fixed-base SDOF (EFSDOF) oscillator.

correspondence between u_{ssi} and u_{SDOF}. The equivalent natural circular frequency ω_{ssi} and effective damping ratio ξ_{ssi} of the SSI system, which respectively equal to those (ω_{SDOF} and ξ_{SDOF}) of the EFSDOF can be determined through principles of structural dynamics as follows. The resonant response of the SDOF oscillator shown in Figure 4.5(b) can be characterised by means of a 'deformation response factor' R_{d} given by (Chopra, 2012):

$$R_{\text{d}} = \frac{U_{\text{SDOF,r}}}{U_{\text{static}}} = \frac{U_{\text{SDOF,r}}}{\dfrac{m\ddot{U}_{\text{g}}}{k_{\text{SDOF}}}} = \boxed{\frac{\omega_{\text{SDOF}}^2 U_{\text{SDOF,r}}}{\ddot{U}_{\text{g}}} = \frac{1}{2\xi_{\text{SDOF}}\sqrt{1-\xi_{\text{SDOF}}^2}}} \tag{4.26}$$

where U_{static} is the maximum static deformation of the oscillator, under a horizontal force $m\ddot{U}_{\text{g}}$, with $\ddot{U}_{\text{g}}$ representing the amplitude of the harmonic ground acceleration; $U_{\text{SDOF,r}}$ is the deformation amplitude of the oscillator in its steady-state vibration at resonance. The natural circular frequency ω_{SDOF} of the oscillator is related to the resonant frequency of vibration ω_{r} by (Chopra, 2012):

$$\omega_{\text{SDOF}} = \frac{\omega_{\text{r}}}{\sqrt{1-2\xi_{\text{SDOF}}^2}} \tag{4.27}$$

ω_{SDOF} and ξ_{SDOF} are solved by Equations (4.26) and (4.27). According to the discussion stated above, the EOM for the impedance model and the cone model are

then respectively given, with respect to u_{ssi}, by:

$$\begin{bmatrix} m & 0 & 0 \\ & m_{\text{f}} & 0 \\ \text{Sym.} & & J + J_{\text{f}} \end{bmatrix} \begin{Bmatrix} \ddot{u}_{\text{ssi}} \\ \ddot{u}_{\text{h}} \\ \ddot{\theta} \end{Bmatrix} + \begin{bmatrix} c_{\text{s}} & -c_{\text{s}} & -c_{\text{s}}h \\ & c_{\text{h}} + c_{\text{s}} & c_{\text{s}}h \\ \text{Sym.} & & c_{\text{s}}h^2 + c_\theta \end{bmatrix} \begin{Bmatrix} \dot{u}_{\text{ssi}} \\ \dot{u}_{\text{h}} \\ \dot{\theta} \end{Bmatrix} + \begin{bmatrix} k_{\text{s}} & -k_{\text{s}} & -k_{\text{s}}h \\ & k_{\text{h}} + k_{\text{s}} & k_{\text{s}}h \\ \text{Sym.} & & k_{\text{s}}h^2 + k_\theta \end{bmatrix} \begin{Bmatrix} u_{\text{ssi}} \\ u_{\text{h}} \\ \theta \end{Bmatrix} = - \begin{Bmatrix} m \\ m_{\text{f}} \\ 0 \end{Bmatrix} \ddot{u}_{\text{g}} \tag{4.28}$$

and

$$\begin{bmatrix} m & 0 & 0 & 0 \\ & m_{\text{f}} + \dfrac{\xi_{\text{g}} c_{\text{h}}}{\omega_0} & 0 & 0 \\ & & J + J_{\text{f}} + \Delta M_\theta + \dfrac{\xi_{\text{g}} c_\theta}{\omega_0} & -\dfrac{\xi_{\text{g}} c_\theta}{\omega_0} \\ \text{Sym.} & & & M_\varphi + \dfrac{\xi_{\text{g}} c_\theta}{\omega_0} \end{bmatrix} \begin{Bmatrix} \ddot{u}_{\text{ssi}} \\ \ddot{u}_{\text{h}} \\ \ddot{\theta} \\ \ddot{\varphi} \end{Bmatrix} + \begin{bmatrix} c_{\text{s}} & -c_{\text{s}} & -c_{\text{s}}h & 0 \\ & c_{\text{h}} + c_{\text{s}} + \dfrac{2\xi_{\text{g}} k_{\text{h}}}{\omega_0} & c_{\text{s}}h & 0 \\ & & c_{\text{s}}h^2 + c_\theta + \dfrac{2\xi_{\text{g}} k_\theta}{\omega_0} & -c_\theta \\ \text{Sym.} & & -c_\theta & c_\theta \end{bmatrix} \begin{Bmatrix} \dot{u}_{\text{ssi}} \\ \dot{u}_{\text{h}} \\ \dot{\theta} \\ \dot{\varphi} \end{Bmatrix} + \begin{bmatrix} k_{\text{s}} & -k_{\text{s}} & -k_{\text{s}}h & 0 \\ & k_{\text{h}} + k_{\text{s}} & k_{\text{s}}h & 0 \\ & & k_{\text{s}}h^2 + k_\theta & 0 \\ \text{Sym.} & & & 0 \end{bmatrix} \begin{Bmatrix} u_{\text{ssi}} \\ u_{\text{h}} \\ \theta \\ \varphi \end{Bmatrix} = - \begin{Bmatrix} m \\ m_{\text{f}} + \dfrac{\xi_{\text{g}} c_{\text{h}}}{\omega_0} \\ 0 \\ 0 \end{Bmatrix} \ddot{u}_{\text{g}} \tag{4.29}$$

where $c_{\text{s}} = 2\xi_{\text{s}}\sqrt{mk_{\text{s}}}$ is the damping coefficient of the superstructure with ξ_{s} denoting its corresponding damping ratio. For harmonic excitations, Equations (4.28) and (4.29) can be generalised as:

$$\left(-\omega^2[M] + i\omega[C] + [K]\right)\{U\} = -[M]\{R\}\ddot{U}_{\text{g}} \tag{4.30}$$

where ω is the frequency of vibration; i is the imaginary unity; $\{U\}$ is the displacement amplitude vector; the first two entries of the influence coefficient vector $\{R\}$ equal unity while the rest of the entries are all zero. The displacement amplitudes

are solved by:

$$\{U\} = -\left(-\omega^2[M] + i\omega[C] + [K]\right)^{-1}[M]\{R\}\ddot{U}_{\mathrm{g}} \tag{4.31}$$

The frequency response of a SDOF structure mounted on a saturated soft clay (ν=0.5) is presented in Figure 4.6 for the 'radiation damping only' condition. Results obtained using both impedance and cone models compare well within the range of frequency considered. By setting the resonant response of an EFSDOF to that of the actual SSI system, Equations (4.26) and (4.27) can be written as:

$$\frac{\omega_{\mathrm{ssi}}^2 U_{\mathrm{ssi,r}}}{\ddot{U}_{\mathrm{g}}} = \boxed{\frac{\omega_{\mathrm{s}}^2 U_{\mathrm{ssi,r}}}{\ddot{U}_{\mathrm{g}}}\left(\frac{\omega_{\mathrm{ssi}}}{\omega_{\mathrm{s}}}\right)^2 = \frac{1}{2\xi_{\mathrm{ssi}}\sqrt{1-\xi_{\mathrm{ssi}}^2}}} \tag{4.32}$$

$$\omega_{\mathrm{ssi}} = \frac{\omega_r}{\sqrt{1-2\xi_{\mathrm{ssi}}^2}} \tag{4.33}$$

With Equations (4.32) and (4.33) as well as the resonant coordinates in Figure 4.6, the equivalent natural frequency ω_{ssi} and damping ratio ξ_{ssi} are determined.

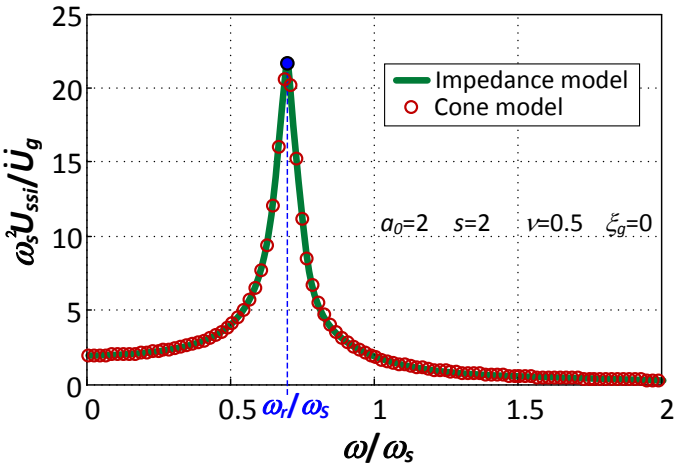

Figure 4.6: Comparison of the frequency response of a flexible-base SDOF structure.

Alternatively, Maravas et al. (2007; 2008; 2014) developed exact solutions of ω_{ssi} and ξ_{ssi} based on the following summation rule (with reference to Figure 4.5):

$$\frac{1}{k_{\mathrm{ssi}}} = \frac{1}{k_{\mathrm{h}}} + \frac{1}{k_\theta}\left(\frac{h}{r}\right)^2 + \frac{1}{k_{\mathrm{s}}} \tag{4.34}$$

where the stiffnesses are all assumed to be complex-valued while k_{ssi}, k_{h} and k_θ are frequency-dependent. In general, a complex-valued stiffness can be obtained by

modifying the elastic constants through the correspondence principle (see Section 3.3.2):

$$k_{\mathrm{h}} = (\alpha_{\mathrm{h}} K_{\mathrm{h}} - m_{\mathrm{f}}\omega^2)(1 + 2i\xi) \tag{4.35}$$

$$k_{\theta} = (\alpha_{\theta} K_{\theta} - J_{\mathrm{f}}\omega^2)(1 + 2i\xi) \tag{4.36}$$

where i is the imaginary unity, ξ is the damping ratio, α is the dynamic modifier applied to the static stiffness K (Equations (3.11) and (3.12)). Substituting these complex-valued stiffnesses into Equation (4.34), the following expressions are obtained:

$$\omega_{\mathrm{ssi}} = \sqrt{\frac{\Lambda}{1 + 4\xi_{\mathrm{ssi}}^2}} \tag{4.37}$$

$$\xi_{\mathrm{ssi}} = \Lambda \left[\frac{\xi_{\mathrm{h}}}{\omega_{\mathrm{h}}^2(1 + 4\xi_{\mathrm{h}}^2)} + \frac{\xi_{\theta}}{\omega_{\theta}^2(1 + 4\xi_{\theta}^2)} + \frac{\xi_{s}}{\omega_{\mathrm{s}}^2(1 + 4\xi_{\mathrm{s}}^2)} \right] \tag{4.38}$$

where Λ is given by:

$$\Lambda = \left[\frac{1}{\omega_{\mathrm{h}}^2(1 + 4\xi_{\mathrm{h}}^2)} + \frac{1}{\omega_{\theta}^2(1 + 4\xi_{\theta}^2)} + \frac{1}{\omega_{\mathrm{s}}^2(1 + 4\xi_{\mathrm{s}}^2)} \right]^{-1} \tag{4.39}$$

in which

$$\omega_{\mathrm{h}} = \sqrt{\frac{\alpha_{\mathrm{h}} K_{\mathrm{h}} - m_{\mathrm{f}}\omega^2}{m}} \quad \omega_{\theta} = \sqrt{\frac{\alpha_{\theta} K_{\theta} - J_{\mathrm{f}}\omega^2}{mh^2}} \quad \omega_{\mathrm{s}} = \sqrt{\frac{k_{\mathrm{s}}}{m}} \tag{4.40}$$

Figure 4.7 illustrates the equivalent period T_{ssi} (as a lengthening ratio with respect to the period of the structure in its fixed-base condition T_{s}) and damping ratio ξ_{ssi} as functions of the structure-to-soil stiffness ratio a_0 and the slenderness ratio s for two values of soil Poisson's ratio ν=0.33, 0.5. Veletsos and Verbič (1973) impedance models and cone models (where ω_0=ω) are both used with Equations (4.32) and (4.33) while Veletsos and Verbič (1973) impedance functions are also adopted in Equations (4.37) and (4.38) derived by Maravas et al. (2014). In the latter case, due to the frequency dependence of the impedance, data shown in Figure 3 are obtained iteratively (by increasing the frequency of vibration ω) until ω is equal to ω_{ssi}, within an acceptable tolerance. It should be mentioned that the Maravas et al. (2014) method inherently assumes that the structural damping is frequency independent. If viscous damping is used, as is done in this study, the damping ratios ξ_{s} in Equations (4.38) and (4.39) should be multiplied by $\omega_{\mathrm{s}}/\omega$.

It is seen from Figure 4.7 that in general, three sets of results (especially the period lengthening ratio) are very similar. Taking the solutions obtained by Equations (4.32) and (4.33) with the impedance models as the reference answer, cone models perform better for a saturated soil condition than for a lower value of soil Poisson's ratio, which is consistent with Wolf (1994). It is also clear that flexible-base slender buildings (e.g., s=4) always have a greater period lengthening and a lower effective damping when compared with short squatty structures (e.g., s=1). Softer soil conditions (i.e. higher a_0 values) also lead to greater period lengthening and higher effective damping ratios for less slender structures. For SSI systems with slender superstructures, an increase in the structure-to-soil stiffness ratio a_0 can significantly increases the period lengthening, while it has a negligible influence on the effective damping ratio.

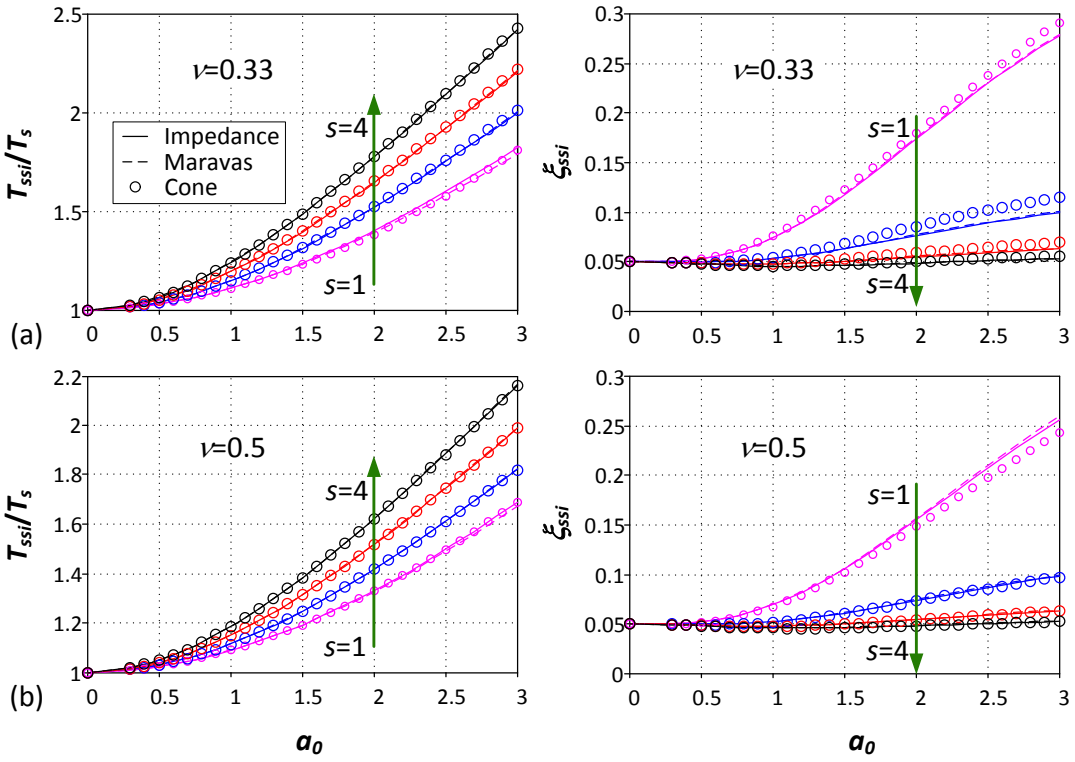

Figure 4.7: Comparison of equivalent period and damping ratio obtained by various methods considering ξ_g=0.05 for (a) ν=0.33, and (b) ν=0.5.

The EFSDOF oscillator will be extended to account for inelastic structural behaviours in Chapter 6, with its accuracy in response to seismic excitations assessed by comparisons with results for the corresponding actual SSI system.

Figures 4.8 and 4.9 show the response of a 10-storey building resting on a sandy soil (a_0=1, ν=0.33) and a saturated clay (a_0=3, ν=0.5) respectively. The superstructure is designed according to the IBC (2012) lateral load distribution and is based on the following parameters, s=3, $\overline{m}$=0.5, $\overline{m}_f$=0.1, ξ_s=ξ_g=0.05. The total mass of the structure is evenly distributed along the height and each storey height is assumed to be three metres. Both impedance and cone models are used and excellent agreement is observed between the results obtained by using the two models.

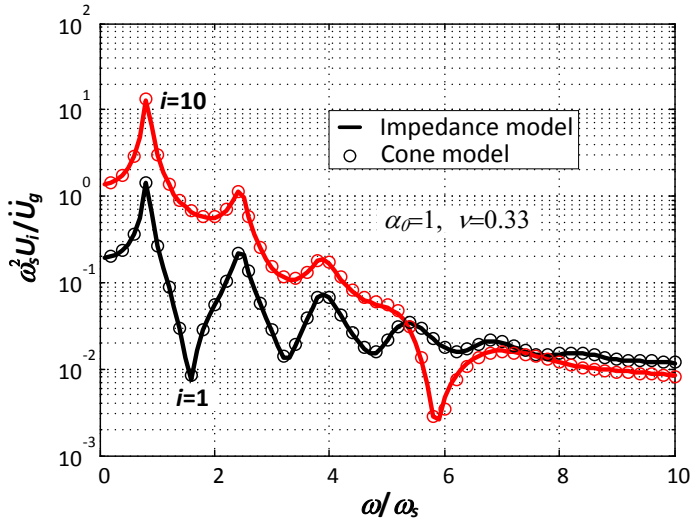

Figure 4.8: Frequency response of a flexible-base 10-storey building considering ν=0.33 and a_0=1.

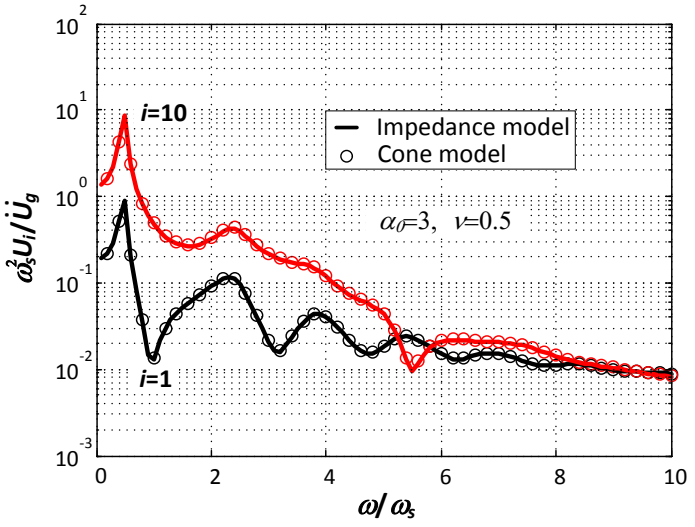

Figure 4.9: Frequency response of a flexible-base 10-storey building considering ν=0.5 and a_0=3.

4.5 Seismic response analysis

The most general approach for seismic response analysis of SSI problems is to solve Equation (4.4) in the time domain by numerical integration techniques of which two widely used methods are central difference method and Newmark's method. However, the frequency-dependent nature of the impedance functions requires the analysis to be performed in the frequency domain. In this case, Fourier analysis can be used to transform a time-varying motion into a series of simple harmonic motions and vice versa. These are done through Fast Fourier Transform (FFT) and Inverse Fast Fourier Transform (IFFT) algorithms that are readily available in many computer codes. In this section, Fourier analysis is performed to evaluate the seismic response of structures supported by foundation impedance functions while direct numerical integration techniques are adopted for solving SSI problems where the soil-foundation system is modelled with cone models.

4.5.1 Fourier analysis of SSI with impedance functions

In earthquake engineering problems, a ground motion is usually recorded at closely spaced discrete intervals of time, and thus is described by a finite number of data points. Consider for example a ground acceleration time history $\ddot{u}_g$ containing n time-acceleration pairs sampled at a constant interval Δt. By expanding the number of $\ddot{u}_g$ to N where $N \geq n$ is a power of 2 and filling the $(n+1)^{\text{th}}$ to the N^{th} $\ddot{u}_g$ with zero, each of the ground acceleration points can be expressed through the discrete inverse Fourier transform by:

$$\ddot{u}_g(t_p) = \sum_{q=0}^{N-1} \ddot{U}_g(\omega_q) e^{i(2\pi qp/N)} \qquad p = 0, 1, 2, \cdots, N-1 \tag{4.41}$$

where $t_p = p\Delta t$ is the time point, ω_q=$2\pi q/(N\Delta t)$ is the frequency point, i is the imaginary unity, and $\ddot{U}_g(\omega_q)$ is the Fourier coefficient given by the Fourier transform as:

$$\ddot{U}_g(\omega_q) = \frac{1}{N} \sum_{p=0}^{N-1} \ddot{u}_g(t_p) e^{-i(2\pi qp/N)} \qquad q = 0, 1, 2, \cdots, N-1 \tag{4.42}$$

Now the frequency response Equation (4.31) can be written as:

$$\{U\} = \{H\}\ddot{U}_g(\omega_q) \quad \{\dot{U}\} = i\omega_q\{U\} \quad \{\ddot{U}\} = -\omega_q^2\{U\} \tag{4.43}$$

where H is called transfer function (ground acceleration to relative displacement) expressed as:

$$\{H\} = -\left(-\omega_q^2[M] + i\omega_q[C] + [K]\right)^{-1}[M]\{R\} \tag{4.44}$$

The process by which a response history is obtained due to a specific ground motion is broken down into the following steps (with reference to Figure 4.10) :

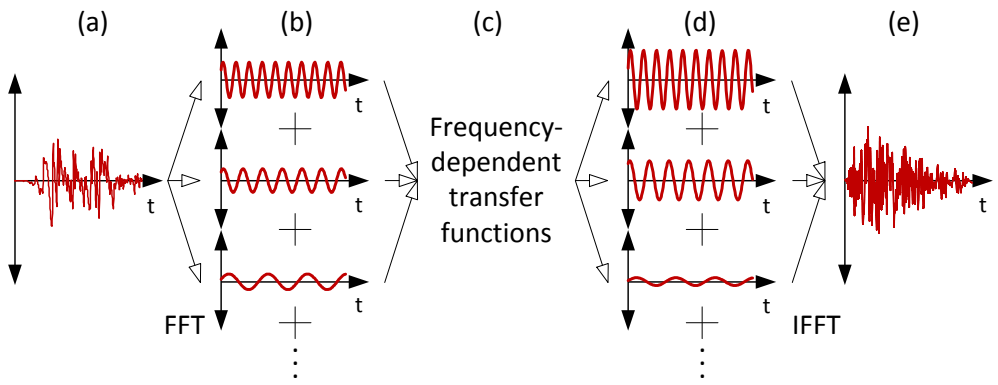

Figure 4.10: Fourier analysis used to solve response history of a building subjected to a ground motion: (a) ground motion time history; (b) time-varying ground motion split into simple harmonic motions through FFT; (c) evaluation of frequency response by means of transfer functions; (d) summation of the harmonic responses through IFFT to obtain the response history; (e) time-varying response of the building.

- Evaluate the Fourier coefficients of the ground motion (Equation (4.42)) by means of Fast Fourier Transform (FFT).
- Calculate the Transfer Function (TF) H according to Equation (4.44).
- Determine the harmonic responses (i.e., displacement, velocity and acceleration) of the building according to Equation (4.43).
- Estimate the response history of the building using the Inverse Fast Fourier Transform (IFFT) according to Equation (4.41).

4.5.2 Numerical integration of EOM

Although Fourier analysis is able to handle the frequency-dependent characteristics of the dynamic foundation stiffness, it is based on superposition of simple responses, which restricts the analysis to linear systems. To tackle a nonlinear problem, time-stepping methods are preferable, and the equation of motion (Equation (4.4)) is more convenient to be written as:

$$[M]\{\ddot{u}\} + [C]\{\dot{u}\} + \{F_{\mathrm{s}}\} = \{P\} = -[M]\{R\}\ddot{u}_{\mathrm{g}} \tag{4.45}$$

where $\{F_{\mathrm{s}}\}$ is a resisting force vector given by $\{F_{\mathrm{s}}\}$=$[K]\{u\}$ for linear systems. $\{P\}$ is an 'applied force' vector which is known when ground acceleration $\ddot{u}_{\mathrm{g}}$ is provided. $\ddot{u}_{\mathrm{g}}$ is often given by a discrete values $\ddot{u}_{gi}$=$\ddot{u}_{\mathrm{g}}(t_i)$, with the time interval:

$$\Delta t_i = t_{i+1} - t_i \tag{4.46}$$

The response is determined at the discrete time instants t_i by the following relation:

$$[M]\{\ddot{u}_i\} + [C]\{\dot{u}_i\} + \{F_{\mathrm{s}(i)}\} = \{P_i\} \tag{4.47}$$

Solving such a relation requires information from the previous time instant (i.e., at time t_{i-1}). Given the initial conditions, solutions for the next step can be obtained through numerical integration techniques. Stepping from time i to $i+1$ by using the same integration methods, responses at each time instant are successively calculated. Two common integration techniques are introduced to relate solutions between successive steps in what follows.

4.5.2.1 Central difference method

Expanding a displacement u at respectively $t_i+\Delta t$ and $t_i-\Delta t$ (assuming a constant time step Δt) using Taylor series, the following relations are obtained:

$$u(t_i + \Delta t) = u(t_i) + \frac{\Delta t}{1!}\dot{u}(t_i) + \frac{(\Delta t)^2}{2!}\ddot{u}(t_i) + \frac{(\Delta t)^3}{3!}\dddot{u}(t_i) + \cdots \tag{4.48}$$

$$u(t_i - \Delta t) = u(t_i) - \frac{\Delta t}{1!}\dot{u}(t_i) + \frac{(\Delta t)^2}{2!}\ddot{u}(t_i) - \frac{(\Delta t)^3}{3!}\dddot{u}(t_i) + \cdots \tag{4.49}$$

Subtracting Equation (4.49) from Equation (4.48) gives:

$$\dot{u}(t_i) = \frac{u(t_i + \Delta t) - u(t_i - \Delta t)}{2\Delta t} + \mathcal{O}((\Delta t)^2) \tag{4.50}$$

Adding Equation (4.49) to Equation (4.48) yields:

$$\ddot{u}(t_i) = \frac{u(t_i + \Delta t_i) - 2u(t_i) + u(t_i - \Delta t)}{(\Delta t)^2} + \mathcal{O}((\Delta t)^2) \tag{4.51}$$

Ignoring the higher order terms in Equations (4.50) and (4.51), the velocity and acceleration are approximated by:

$$\dot{u}_i \simeq \frac{u_{i+1} - u_{i-1}}{2\Delta t} \quad \ddot{u}_i \simeq \frac{u_{i+1} - 2u_i + u_{i-1}}{(\Delta t)^2} \tag{4.52}$$

Substitute Equation (4.52) into Equation (4.47) and rearrange:

$$\left(\frac{[M]}{(\Delta t)^2} + \frac{[C]}{2\Delta t}\right)\{u_{i+1}\} = \{P_i\} - \{F_{s(i)}\} - \frac{2[M]}{(\Delta t)^2}\{u_i\} - \left(\frac{[M]}{(\Delta t)^2} - \frac{[C]}{2\Delta t}\right)\{u_{i-1}\} \tag{4.53}$$

Let i=0 denote the initial condition, eliminating u_{i+1} in Equation (4.52) gives:

$$u_{-1} = u_0 - \Delta t\dot{u}_0 + \frac{(\Delta t)^2}{2}\ddot{u}_0 \tag{4.54}$$

Response can thus be solved using Equation (4.53) by stepping from $i = 0$ to $n - 1$ (considering n steps). An advantage of this method is that the response at the $(i+1)^{\text{th}}$ step is explicitly determined from the EOM at the i^{th} step and no iteration is required. Performing the central difference method requires a sufficiently small time step to guarantee the stability of analysis and accuracy of results, which is impractical for systems having a large number of DOFs. For the simplified SSI models considered in this study, this method can be proved efficient.

4.5.2.2 Newmark's method

Newmark (1959) developed a family of step-by-step integration methods through the following approximating expressions:

$$u(t_i + \Delta t) \simeq u(t_i) + \frac{\Delta t}{1!}\dot{u}(t_i) + \frac{(\Delta t)^2}{2!}\ddot{u}(t_i) + \beta(\Delta t)^3\dddot{u}(t_i) \tag{4.55}$$

$$\dot{u}(t_i + \Delta t) \simeq \dot{u}(t_i) + \frac{\Delta t}{1!}\ddot{u}(t_i) + \gamma(\Delta t)^2\dddot{u}(t_i) \tag{4.56}$$

These expressions are derived based on the corresponding Taylor series by replacing β for 1/3! and γ for 1/2!, respectively, and ignoring the higher order terms. If the third derivative of displacement with respect to time is linearised by:

$$\dddot{u}(t_i) = \frac{\ddot{u}(t_i + \Delta t) - \ddot{u}(t_i)}{\Delta t} \tag{4.57}$$

Substituting Equation (4.57) into Equations (4.55) and (4.56) gives:

$$u_{i+1} \simeq u_i + \Delta t \dot{u}_i + (0.5 - \beta)(\Delta t)^2 \ddot{u}_i + \beta(\Delta t)^2 \ddot{u}_{i+1} \tag{4.58}$$

$$\dot{u}_{i+1} \simeq \dot{u}_i + (1 - \gamma)\Delta t \ddot{u}_i + \gamma \Delta t \ddot{u}_{i+1} \tag{4.59}$$

The parameters γ and β describe the variation of acceleration over a time step and determine the stability and accuracy of the method. A value of γ=0.5 and a range of $1/6 \leq \beta \leq 1/4$ are normally used to ensure the stability of solution (Chopra, 2012). Specially, β=1/4 and 1/6 are respectively corresponding to an average acceleration and a linear acceleration that varies over a time step.

From Equation (4.58), $\ddot{u}_{i+1}$ can be expressed as:

$$\ddot{u}_{i+1} = \frac{1}{\beta(\Delta t)^2}(u_{i+1} - u_i) - \frac{1}{\beta \Delta t}\dot{u}_i - \left(\frac{1}{2\beta} - 1\right)\ddot{u}_i \tag{4.60}$$

Substituting Equation (4.60) into Equations (4.59) gives:

$$\dot{u}_{i+1} = \frac{\gamma}{\beta \Delta t}(u_{i+1} - u_i) + \left(1 - \frac{1}{\beta}\right)\dot{u}_i + \Delta t \left(1 - \frac{1}{2\beta}\right)\ddot{u}_i \tag{4.61}$$

Substituting Equations (4.60) and (4.61) into Equation (4.47) for the dynamic equilibrium at time $i+1$, $\{u_{i+1}\}$ can be solved. Noting that apart from $\{u_{i+1}\}$, $\{F_{s(i+1)}\}$ needs to be determined as well, equilibrium at time $i+1$ may be solved iteratively. For linear systems whose $\{F_{s(i+1)}\}=[K]\{u_{i+1}\}$, $\{u_{i+1}\}$ can be extracted from $\{F_{s(i+1)}\}$, leaving the only unknown $\{u_{i+1}\}$ in the equilibrium that could be solved without iterations.

However, if the resisting force F_s is an implicit nonlinear function of the imposed deformation u, iteration is required, and the Newmark's method becomes implicit. The following presents a Newton-Raphson iteration scheme through a simple example that solves a displacement u of a SDOF system due to a given static force P.

The equilibrium condition for the problem is simply:

$$F_{\mathrm{s}}(u) = P \tag{4.62}$$

Expanding the resisting force F_{s}^{j+1} at $j+1^{\mathrm{th}}$ iteration by Taylor series with respect to the associated displacement u^{i+1} yields:

$$F_{\mathrm{s}}^{j+1} = F_{\mathrm{s}}^{j} + \frac{\Delta u^{j}}{1!} F_{\mathrm{s,u}}^{j} + \frac{(\Delta u^{j})^{2}}{2!} F_{\mathrm{s,uu}}^{j} + \cdots \tag{4.63}$$

where $F_{\mathrm{s,u}}^{j}$ and $F_{\mathrm{s,uu}}^{j}$ are respectively first and second derivatives of F_{s} with respect to u determined at the end of the j^{th} iteration. If u^{j} is close to the solution, Δu^{j} tends to be very small. Ignoring the second and higher order terms in Equation (4.63) gives:

$$F_{\mathrm{s}}^{j+1} \simeq F_{\mathrm{s}}^{j} + R^{j} = P \tag{4.64}$$

where the residual force

$$R^{j} = \Delta u^{j} F_{\mathrm{s,u}}^{j} = k_{T}^{j} \Delta u^{j} \tag{4.65}$$

where k_{T}^{j} is the tangent stiffness at u^{j}. A new and improved estimate of the displacement is calculated as:

$$u^{j+1} = u^{j} + \Delta u^{j} \tag{4.66}$$

With this new displacement and past response history, the resisting force and tangent stiffness for the next iteration can be calculated according to the nonlinear force-displacement relationship. Equations (4.64), (4.65) and (4.66) are then iterated until a convergence criterion is achieved. To avoid calculation of the tangent stiffness for each iteration, the initial stiffness at the end of the last converged time step can be used for all iterations within the current time step. This iteration scheme is called the modified Newton-Raphson method. Both iteration procedures are illustrated in Figure 4.11.

It is convenient to apply the Newton-Raphson method explained above for a dynamic SDOF system. For such a one-dimensional problem, all quantities in Equation (4.47) for time $i+1$ are scalar:

$$\hat{F}_{\mathrm{s}(i+1)} = P_{i+1} \tag{4.67}$$

where

$$\hat{F}_{\mathrm{s}(i+1)} = m\ddot{u}_{i+1} + c\dot{u}_{i+1} + F_{\mathrm{s}(i+1)} \tag{4.68}$$

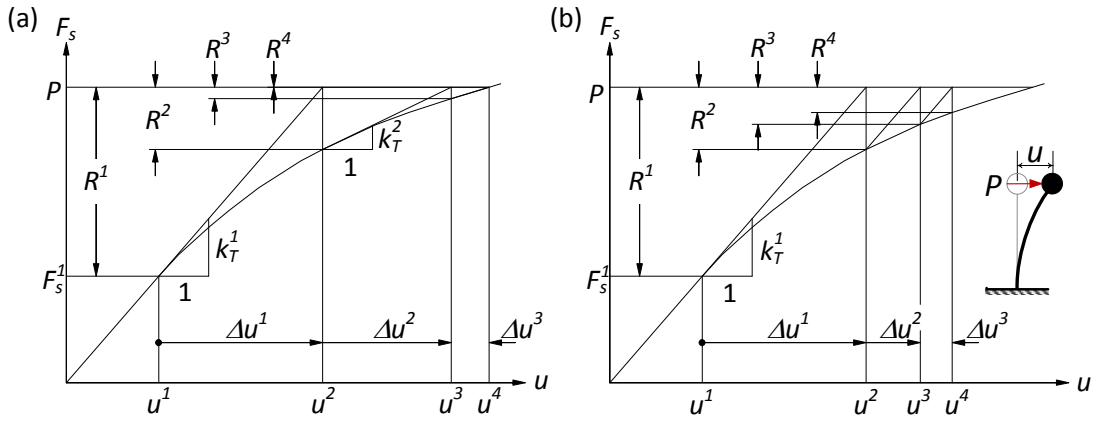

Figure 4.11: Iterative scheme within a time step for a nonlinear system: (a) Newton-Raphson method; (b) Modified Newton-Raphson method (after Chopra, 2012).

Similar to Equations (4.64) and (4.65), the following expression can be obtained:

$$\hat{F}^{j+1}_{\mathrm{s}(i+1)} \simeq \hat{F}^{j}_{\mathrm{s}(i+1)} + \hat{F}_{\mathrm{s},u_{i+1}} \Delta u^j = P_{i+1} \tag{4.69}$$

where the equivalent tangent stiffness is given by:

$$\hat{k}^j_{T(i+1)} \equiv \hat{F}_{\mathrm{s},u_{i+1}} = m\ddot{u}_{,u_{i+1}} + c\dot{u}_{,u_{i+1}} + F_{\mathrm{s},u_{i+1}} \tag{4.70}$$

where the derivatives on the right-hand side of Equation (4.70) can be derived from Equations (4.60) and (4.61) as:

$$\ddot{u}_{,u_{i+1}} = \frac{1}{\beta(\Delta t)^2} \qquad \dot{u}_{,u_{i+1}} = \frac{\gamma}{\beta \Delta t} \tag{4.71}$$

Substituting Equation (4.71) into Equation (4.70) gives:

$$\hat{k}^j_{T(i+1)} = m\frac{1}{\beta(\Delta t)^2} + c\frac{\gamma}{\beta \Delta t} + k^j_{T(i+1)} \tag{4.72}$$

From Equation (4.64), the residual force at the j^{th} iteration within the $(i+1)^{\text{th}}$ time step is calculated by:

$$\hat{R}^j_{i+1} = P_{i+1} - \hat{F}^j_{i+1} \tag{4.73}$$

Substituting Equations (4.60) and (4.61) into Equation (4.68), $\hat{F}^j_{i+1}$ in Equation (4.73) is expressed as:

$$\begin{aligned}\hat{F}^j_{i+1} = F^j_{i+1} + \left(m\frac{1}{\beta(\Delta t)^2} + c\frac{\gamma}{\beta \Delta t}\right)\left(u^j_{i+1} - u_i\right) - \left[m\frac{1}{\beta \Delta t} + c\left(\frac{\gamma}{\beta} - 1\right)\right]\dot{u}_i \\ - \left[m\left(\frac{1}{2\beta} - 1\right) + c\Delta t\left(\frac{\gamma}{2\beta} - 1\right)\right]\ddot{u}_i\end{aligned} \tag{4.74}$$

The iteration procedures are very similar to those in solving the static problem, with merely replacing R, F_{s} and k_T by $\hat{R}$, $\hat{F}_{\mathrm{s}}$ and $\hat{k_T}$, respectively. For MDOF systems, the mass, stiffness, and damping coefficient are written in matrix forms while the force and displacement appear as vectors.

4.5.3 Seismic response history analysis of SSI systems

The Fourier analysis, central difference method and Newmark's method described in the previous subsections were implemented in MATLAB (2011). To compare seismic response of buildings obtained by these methods, the Loma Prieta earthquake (1989), 0° horizontal component of the ground motion recorded by the station Foster City - APEEL 1 ($V_{\mathrm{s},30}$=116.4m/s), was used as shown in Figure 4.12.

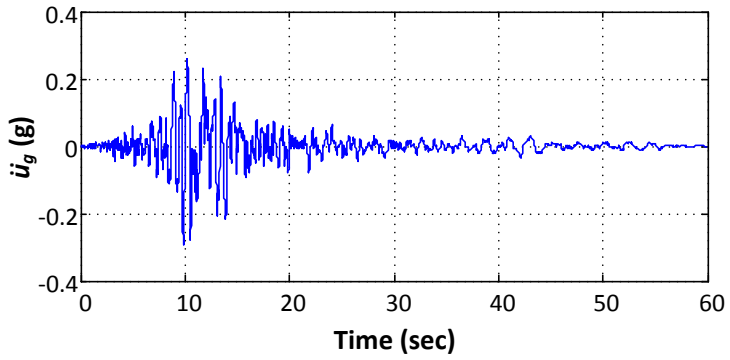

Figure 4.12: Ground acceleration time history of the Loma Prieta earthquake (1989), recorded at the station Foster City - APEEL 1.

The original ground acceleration data was based on a constant time interval Δt=0.005 seconds. In order to use a smaller time step in the analysis, the data were resampled over a shorter time interval by means of a linear interpolation.

Eight different SSI systems were adopted in the comparison study, with their properties listed in Table 4.4. The site soil was assumed to possess a Poisson's ratio ν=0.5 given such a low shear wave velocity. For each of the soil-SDOF structure systems (i.e., number of storeys n=1), a corresponding EFSDOF oscillator was introduced. The linear properties of the EFSDOF oscillators (i.e., T_{ssi} and ξ_{ssi}) were calculated

according to Equations (4.32) and (4.33). For the flexible-base MDOF structures (M1-M4), the EFSDOF oscillators were not relevant. Yielding was allowed only in the structural components and perfect plasticity was assumed for each storey when yielding occurs. In this context, the capacity of the EFSDOF oscillator is equal to the base shear strength of the corresponding flexible-base SDOF structure. For all nonlinear systems considered in Table 4.4, it was assumed that for each storey, the lateral strength f_y was 1/2000 of its lateral stiffness k. The height-wise stiffness and strength distributions were determined according to the IBC (2012) design lateral load pattern.

Table 4.4: Properties of SSI systems used in the comparison study.

Index	n	a_0	s	T_s	u_{yi} (m)	T_{ssi}/T_s	T_{ssi} (sec)	ξ_{ssi} (%)
S1	1	3	4	1.5	∞	2.16	3.24	5.25
S2	1	3	4	1.5	0.0005	2.16	3.24	5.25
S3	1	3	1	0.3	∞	1.69	0.51	25.64
S4	1	3	1	0.3	0.0005	1.69	0.51	25.64
M1	5	1.5	1.5	0.56	∞	-	-	-
M2	5	1.5	1.5	0.56	0.0005	-	-	-
M3	10	2	2	0.94	∞	-	-	-
M4	10	2	2	0.94	0.0005	-	-	-

For linear systems, results from Fourier analysis (see Section 4.4) utilising Veletsos and Verbič (1973) impedance functions were taken as the 'exact' solutions. The Fourier and inverse Fourier transforms were performed on the basis of a time interval Δt=0.005 seconds. When solving the SSI problems in the time domain, the cone models were used. Both Newmark's method and central difference method were adopted for integrating the EOM numerically and operated respectively at a time step of Δt=0.005 seconds and Δt=0.001 seconds. The average acceleration assumption (i.e., β=0.25, γ=0.5) was employed when using Newmark's approach. Since the cone models were analysed in the time domain, the reference frequency ω_0 was set to the equivalent natural period of the SSI system.

For all data shown in Figures 4.13 to 4.18, the Newmark's method and central

difference method almost lead to the same results. Although the central difference method used a smaller size of time step which was one fifth of that in the Newmark's method, it was much faster, especially in solving nonlinear problems, due to the fact that it is an explicit method.

Figure 4.13(a) shows the structural distortion (shear deformation of the structure) time history obtained by using various methods. Generally, the three methods yield similar results for the linear soil-SDOF structure system S1. Although results obtained from the numerical integration techniques do not completely agree with the 'exact' solution produced by the Fourier analysis; the peak values, which are important in methods based on response spectra, are practically identical. In Figure 4.13(b), the displacements of the structural mass relative to the ground u_{ssi} are compared. The EFSDOF oscillator gives an excellent estimation of the results. Noting that u_{ssi} is due to a combined effect of structural distortion, foundation swaying and rocking, the contribution from structural distortion could be only twenty percent.

For the nonlinear system S2, comparisons in Figure 4.14 confirm that results from various methods are practically the same. It is interesting to note that u_{ssi} of the yielding system S2, which is almost identical to the structural distortion, can be smaller than that in the linear system S1.

Figure 4.15 shows good agreement between results from different methods for the linear system S3. However, for its nonlinear counterpart S4, the EFSDOF oscillator underestimates u_{ssi}, leading to a peak value of u_{ssi} which is less than half of that of the actual SSI system, as illustrated in Figure 4.16(b). The trend that the yielding system has a smaller u_{ssi} compared to the linear system (compare results in Figures 4.13 and 4.14) is reversed for systems S3 and S4.

For the flexible-base MDOF structures, comparisons in Figures 4.17 to 4.18 demonstrate that the numerical integration methods are capable of solving both linear and nonlinear SSI problems involving MDOF superstructures.

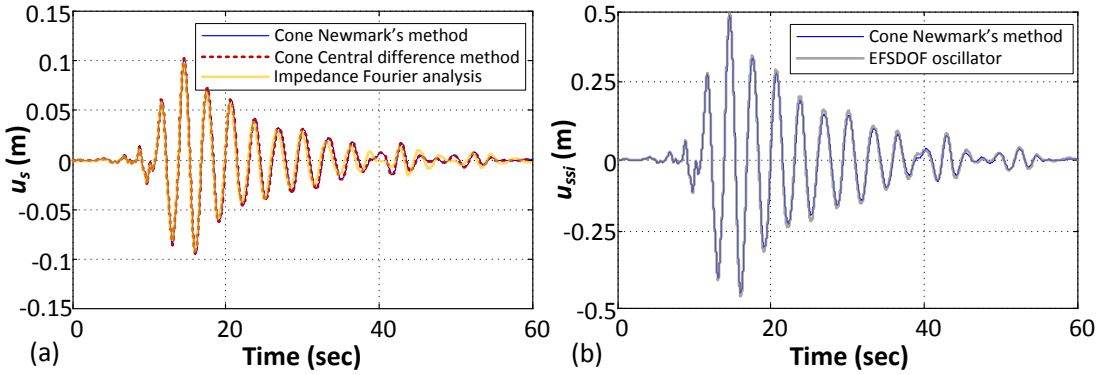

Figure 4.13: Comparison of (a) structural distortion time history and (b) structural displacement (relative to ground) time history obtained using various methods for linear system S1.

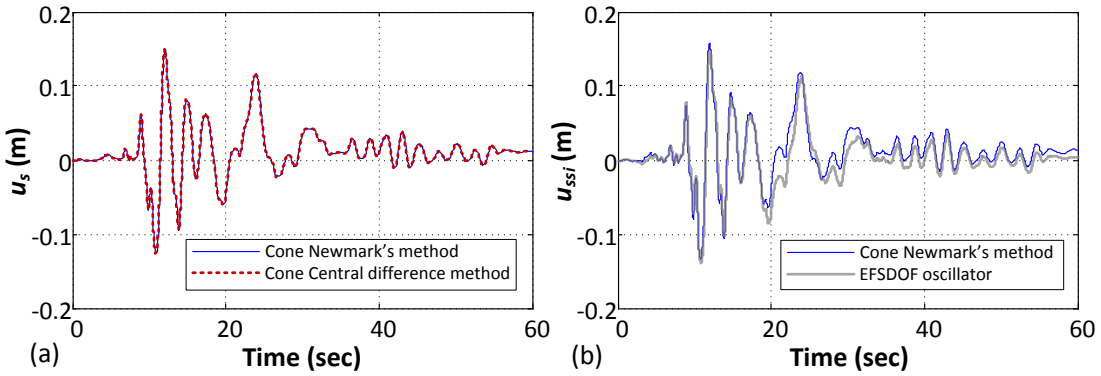

Figure 4.14: Comparison of (a) structural distortion time history and (b) structural displacement (relative to ground) time history obtained using various methods for nonlinear system S2.

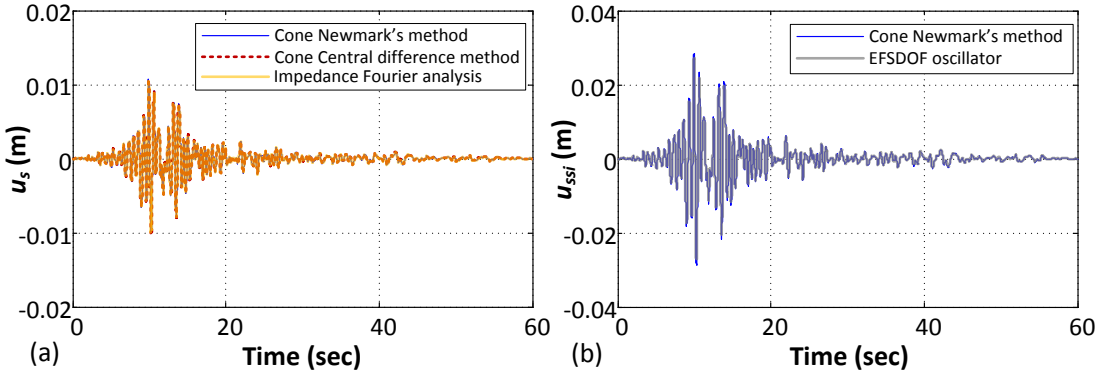

Figure 4.15: Comparison of (a) structural distortion time history and (b) structural displacement (relative to ground) time history obtained using various methods for linear system S3.

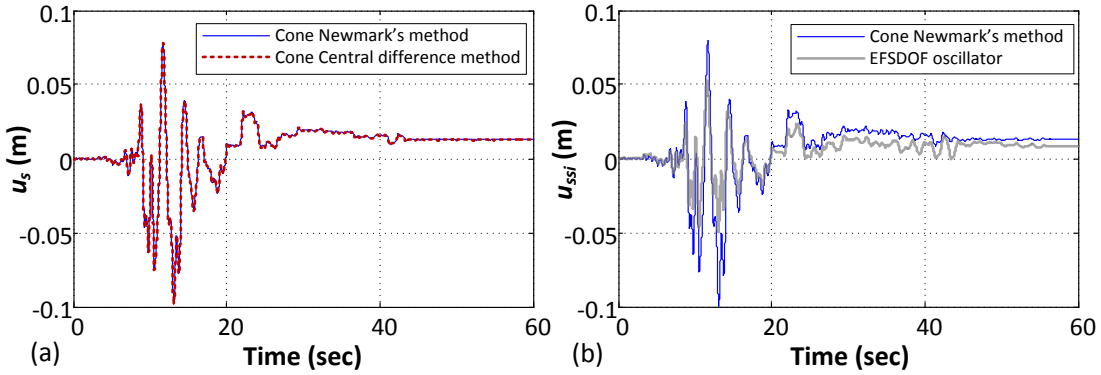

Figure 4.16: Comparison of (a) structural distortion time history and (b) structural displacement (relative to ground) time history obtained using various methods for nonlinear system S4.

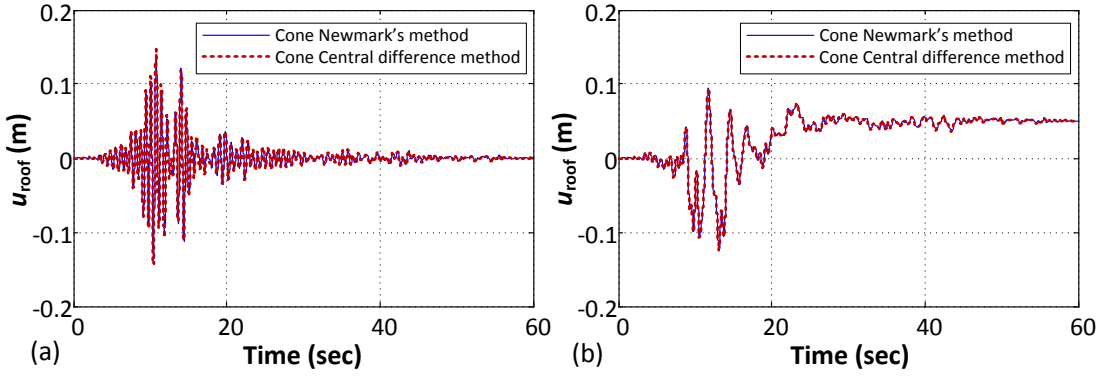

Figure 4.17: Comparison of roof displacement (relative to ground) time history obtained using various methods for (a) linear system M1 and (b) nonlinear system M2.

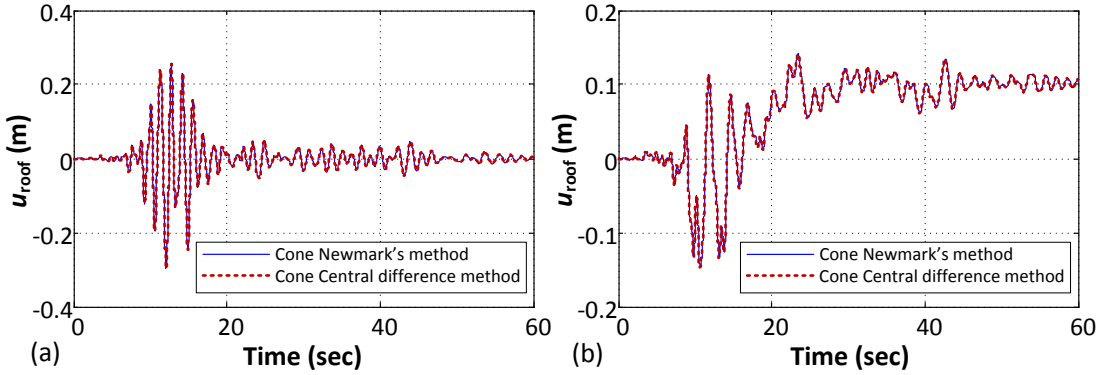

Figure 4.18: Comparison of roof displacement (relative to ground) time history obtained using various methods for (a) linear system M3 and (b) nonlinear system M4.

It should be mentioned that results presented in this subsection only show several possible situations of an SSI problem. In fact, the performance of an SSI system not only depends on the dynamic properties of the system, but also relates to the characteristics of the ground motion. To gain an insight into how SSI alters the seismic response of a building, a comprehensive parametric study is required. This will be the focus of the following two chapters where a broader view of the effect of SSI on structural behaviour is provided.

4.6 Summary

This chapter describes the procedures for solving a dynamic SSI problem through several methods on two SSI models. In order to simplify the analysis, the superstructures are represented by shear-building models where each storey is assumed to have only shear deformation. Under this assumption, a n-storey structure can be simplified into a n-DOF shear-building. Both impedance models and cone models introduced in the previous chapter are used to simulate the dynamic soil-foundation behaviour. The EOM are formulated in both frequency and time domains.

Due to the frequency-dependent nature of the impedance functions, the impedance models are required to be used in the frequency domain whereas the cone models enable the analysis to be performed in either frequency or time domain. An Equivalent Fixed-base SDOF (EFSDOF) oscillator is introduced to estimate the dynamic response of the corresponding actual SSI system. The properties of the EFSDOF are selected on the basis of setting its resonant response and corresponding frequency to those of the actual SSI system.

It is demonstrated that an SSI problem can be defined by using a number of dimensionless parameters. The frequency response of single and multi-storey SSI systems obtained by both impedance and cone models are well compared. In order to solve the response of an SSI system due to a seismic ground motion, three methods are introduced and compared. The Fourier analysis, although limited to linear systems, is able to transform the data between time and frequency domain, making the

impedance models most suitable for this type of analysis. The Newmark's method and central difference method are capable of integrating the EOM numerically. For the simplified SSI models used in this study, all these three methods yield practically the same results.

Chapter 5

Performance-based design of inelastic multi-storey buildings considering SSI

5.1 Introduction

This chapter aims to improve the current design procedures for SSI, presented in Section (2.4), by solving two problems. The first problem concerns the lack of link between the existing ductility reduction factor R_μ and SSI in the force-based design while the second problem relates to the gap in design of flexible-base multi-storey structures from the response spectra for their corresponding SDOF systems. Both problems are solved by introducing a practical performance-based design approach, which utilises interaction-dependent force reduction and MDOF modification factors that could be directly applied to response spectra available in building codes. These factors are derived from results obtained through a series of comprehensive parametric studies. Note that soil is treated in this chapter as an equivalent-linear material of which true nonlinearity and failure are excluded.

5.2 Modelling and analysis considerations

Nonlinear analyses are required in the following sections, and for this purpose, the cone models are combined with the shear-building models to simulate the interaction between soil and overlying structures (Figure 5.1). In cone models, the soil hysteretic damping ξ_g should be specified at the reference circular frequency ω_0 (see Figure 3.9). For SDOF structures, ω_0 can be calculated by Equation (4.37) while for MDOF structures, ω_0 equals the lowest Eigen-frequency of the SSI system ω_{ssi}, which is solved iteratively by increasing the frequency of vibration ω until both frequencies are equal within 0.1 percent.

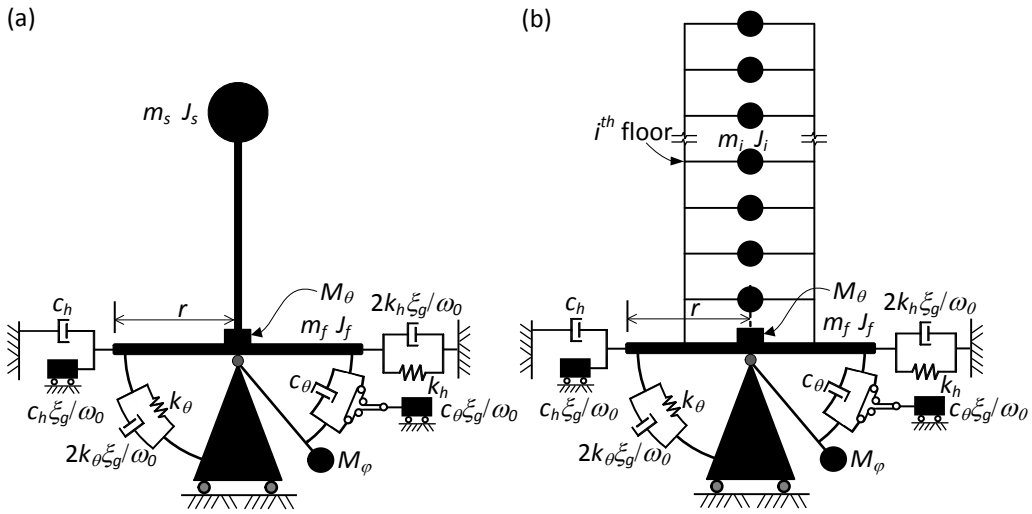

Figure 5.1: Soil structure interaction models for (a) a SDOF structure and (b) a multi-storey structure.

Since the aim of this chapter is to develop a practical design method for flexible-base inelastic MDOF structures on the basis of code-specified response spectra, three sets of spectrum-compatible synthetic earthquakes were generated using the SIMQKE program (Gasparini and Vanmarcke, 1976), to represent the IBC-2012 design response spectra corresponding to soil classes C, D and E (see Table 4.3). Site classes A and B are disregarded because they correspond approximately to the 'fixed-base condition'. Each set of the synthetic earthquakes consists of fifteen seismic excitations with a Peak Ground Acceleration (PGA) of 0.4g. It is shown in Figure 5.2 that the average acceleration response spectrum of synthetic earthquakes

in each set compares very well with its corresponding IBC-2012 design spectrum. The characteristic periods of the design ground motions T_0 are also marked in Figure 5.2. These periods represent the transition points from acceleration-controlled to the velocity-controlled segment of 5% damped design spectra.

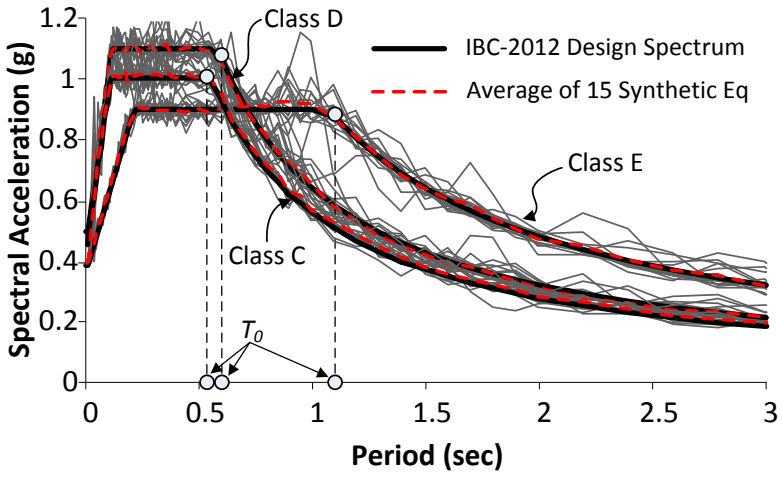

Figure 5.2: Comparison of mean response spectra of 15 synthetic earthquakes for site classes C, D and E.

In order to control the inelastic level of a building or a structural component, the ductility ratio μ is used. The concept of ductility is explained in Figure 5.3. For each storey of a building, the actual response is linear under low force magnitudes and becomes nonlinear once the first significant yielding occurs (i.e., when mobilised shear strength equals F_s). With increasing the force level, the storey structural components successively mobilise their full strengths until the overall strength (F_u) is fully mobilised, leading to large deformations. Alternatively, the curves in Figure 5.3 can be used to describe the global response of a building, for example, showing its base shear (V) versus roof displacement.

For design purposes, the design base shear V_d usually corresponds to the formation of the first plastic hinge (i.e., V_d=F_s). As shown in Figure 5.3, V_d is reduced firstly from its linear elastic counterpart V_e due to inelastic action. The amount of reduction is controlled by a ductility reduction factor R_μ defined as:

$$R_\mu = \frac{V_e}{F_u} \tag{5.1}$$

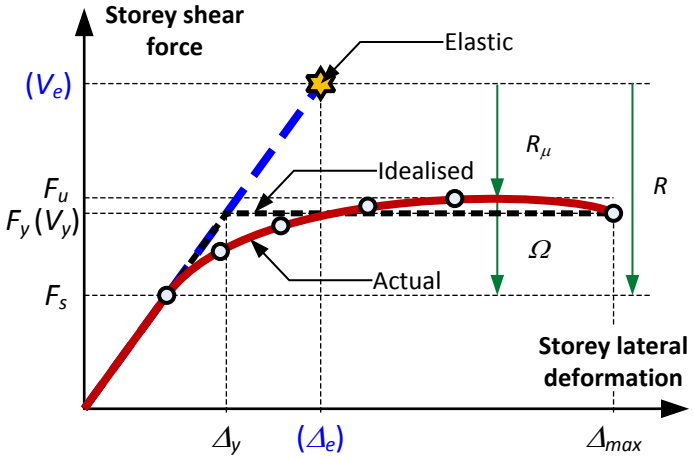

Figure 5.3: Elastic and inelastic force-deformation relationship.

Further reduction of V_{d} is due to the strength reserve at the onset of the first significant yielding. To describe this reduction, a structural over-strength factor is defined:

$$\Omega = \frac{F_{\mathrm{u}}}{F_{\mathrm{s}}} \tag{5.2}$$

The total force reduction factor R is therefore expressed as:

$$R = R_{\mu}\Omega \tag{5.3}$$

For the SSI models used in this study, the actual structural response in Figure 5.3 can be idealised by a linearly elastic-perfectly plastic curve. With the assumption of perfect plasticity, the yield force is unique and therefore, $F_{\mathrm{y}}(V_{\mathrm{y}})$=$F_{\mathrm{s}}$=$F_{\mathrm{u}}$, which leads to:

$$R = R_{\mu} = \frac{V_{\mathrm{e}}}{V_{\mathrm{y}}} = \frac{\Delta_{\mathrm{e}}}{\Delta_{\mathrm{y}}} \tag{5.4}$$

where Δ_{e} is the design maximum deformation of an elastic structure whereas Δ_{y} is the yield deformation of a degraded structure.

The ductility factor (or ductility ratio) μ is defined for the degraded structure as the ratio of the maximum deformation Δ_{max} to that at yielding Δ_{y}:

$$\mu = \frac{\Delta_{\mathrm{max}}}{\Delta_{\mathrm{y}}} \tag{5.5}$$

To relate the global maximum deformation of a yielding structure to that in its elastic condition, an inelastic displacement ratio is usually adopted:

$$C_{\mu} = \frac{\Delta_{\mathrm{max}}}{\Delta_{\mathrm{e}}} \tag{5.6}$$

From Equations (5.4), (5.5) and (5.6), the following relation is obatained:

$$C_\mu = \frac{\mu}{R_\mu} \tag{5.7}$$

The inelastic displacement ratio C_μ is a key parameter in the displacement Coefficient Method for simplified nonlinear static procedure in BSSC (2000) and ATC (2005).

For multi-storey structures, Equation (5.5) corresponds essentially to a storey ductility ratio (see Equation (4.25)) that could be a key index for seismic performance assessment (e.g., Nassar and Krawinkler, 1991; Krawinkler and Nassar, 1992; Ghobarah et al., 1999; Santa-Ana and Miranda, 2000; Moghaddam and Mohammadi, 2001).

It should be mentioned that the ductility ratio μ depends strongly on the definitions of 'deformation'. In fact, deformation in an entire SSI system results from the flexibility of both structural and geotechnical components. In this chapter, the ductility ratio is determined on the basis of the inter-storey distortions that are exclusive of rigid-body foundation movements, and therefore, directly reflect the damage in structures.

The term 'ductility demand', which will be used in the following analyses in this chapter to control the degrees of structural nonlinearity, refers to the maximum value of the ductility ratio throughout an earthquake. For multi-storey buildings, 'ductility demand' corresponds to the maximum value of the storey ductility ratio throughout an earthquake. When ductility demand is less than one, according to Equation (5.5), the maximum deformation is no greater than the yielding deformation, and the corresponding system remains elastic.

In order to achieve a target ductility demand μ_t, iterations are required on the total strength demand F_{tot} (defined as the maximum value of the sum of the storey strengths i.e., $\sum V_i$ with reference to Figure 4.1) while maintaining the initial pattern of the strength distribution. The procedures to calculate the total strength demand for a prescribed ductility demand are presented in Figure 5.4. It should be noted

that storey ductility does not increase monotonically when reducing the strength, which means that there could be more than one strength demand satisfying a given ductility demand. In this case, only the highest strength should be considered.

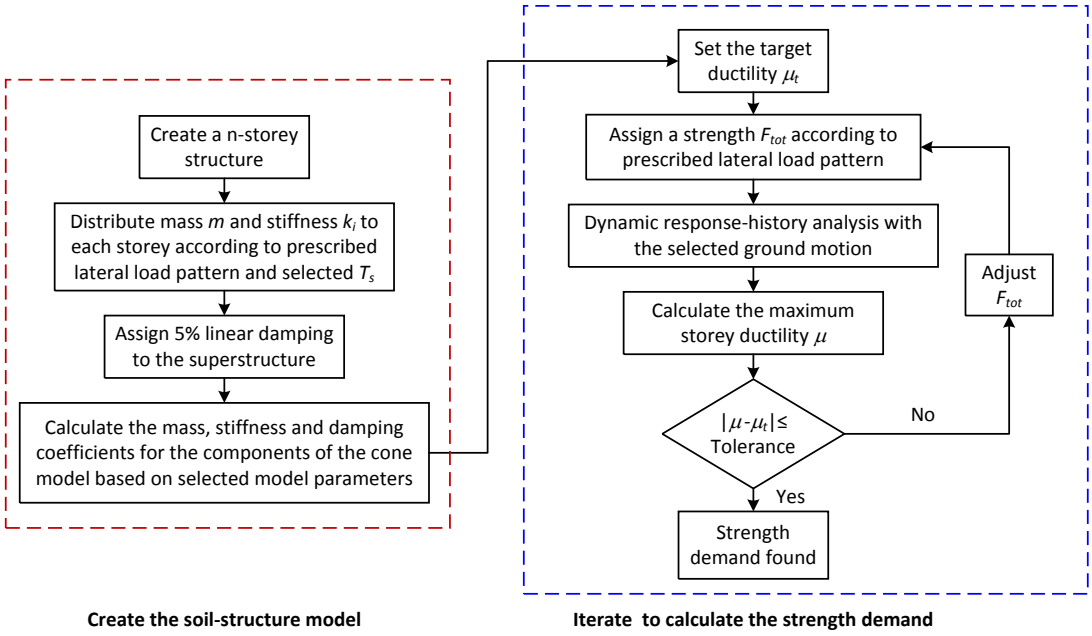

Figure 5.4: Procedures for calculation of strength demand for a target ductility demand.

To investigate the sensitivity of structural strength demand to the influencing parameters introduced in Section (4.3), buildings having various fixed-base fundamental periods T_s, number of storeys n, slenderness ratios s and inelastic levels μ were subjected to the code spectrum-compatible synthetic earthquakes, considering different structure-to-soil stiffness ratios a_0. The values of soil Poisson's ratio were selected in accordance with the site class, as presented in Table 4.3. The mean response of the structures is obtained by averaging the results for each set of synthetic records representing a specific site class. The following parameters were kept constant, $\overline{m}$=0.5, $\overline{m}_f$=0.1, ξ_s=ξ_g=0.05.

5.3 Effect of SSI on seismic response of SDOF structures

This section shows the effect of SSI on base shear demands of SDOF structures V_{SDOF} for different structural ductility demands. An example is given in Figure 5.5 for structures located on soil site class E. The abscissas represent the natural periods of the SDOF structures in their fixed-base state while the ordinates are corresponding base shear demands normalised by the product of structural mass and PGA (in 'g'). Data in Figure 5.5 are averaged results from the fifteen earthquakes for soil site class E (i.e., very soft soil profile). Again, a_0=0 represents exactly the rigid-base condition while increasing the a_0 value leads to softer soil conditions.

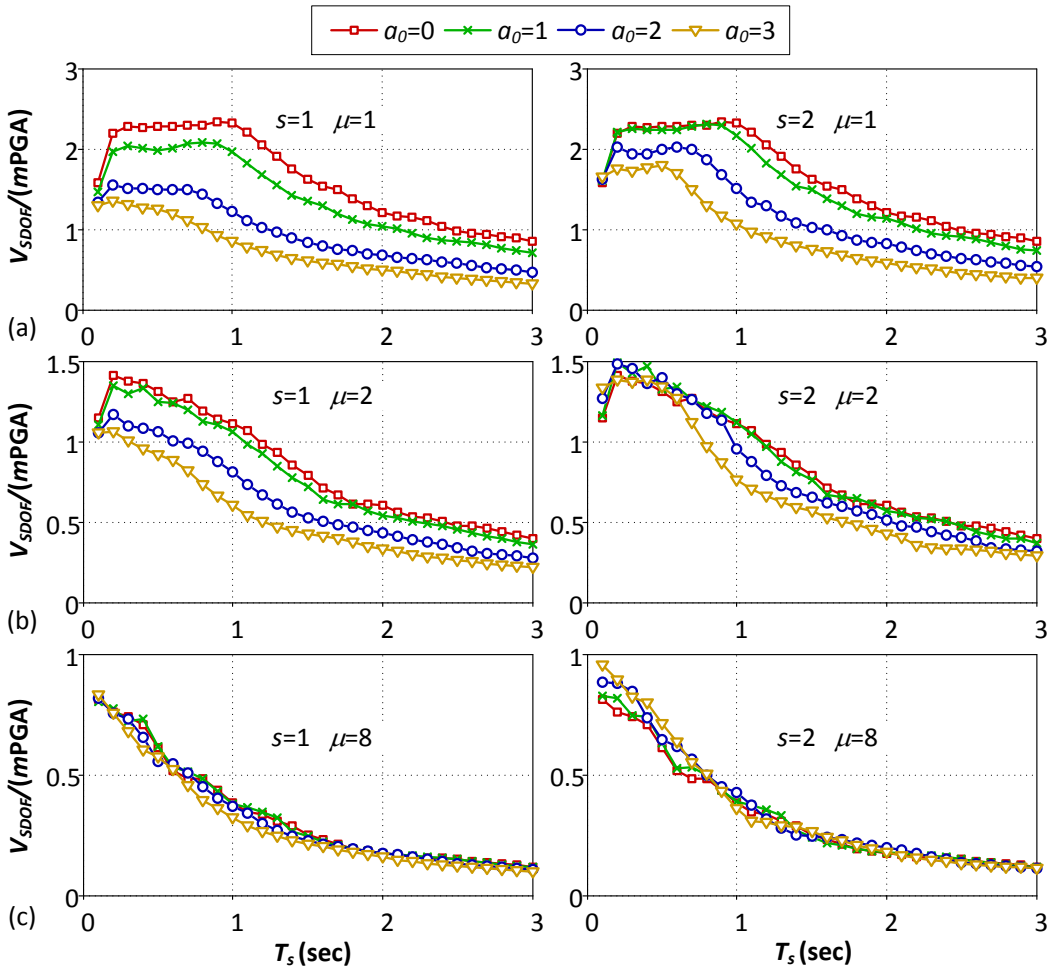

Figure 5.5: Effect of structure-to-soil stiffness ratio a_0 on base shear demands of SDOF structures located on site class E.

Consider the data for fixed-base systems as the reference for results. It is observed that the way a_0 affects V_{SDOF} is significantly influenced by the structural ductility demands. For linear and slightly nonlinear systems, in general, considering SSI results in a reduction of base shear from the fixed-base values. It is observed that the reduction is up to 65% for linear elastic systems with μ=1, as shown in Figure 5.5(a). The observation implies that considering SSI in the seismic design of buildings with low ductility demands can lead to more cost-effective design solutions with less structural weight. This beneficial effect, however, becomes less prominent for highly nonlinear structures and the difference between the results of fixed-base and flexible-base systems becomes less significant when structures undergo large inelastic deformations (i.e. μ=8). Similar results were obtained by Veletsos and Verbič (1974) and Ghannad and Jahankhah (2007), which can be explained by the fact that the energy dissipated by the soil medium would be negligible compared to that caused by plastic deformations of highly nonlinear structures.

It is also observed that increasing the slenderness ratio for flexible-base short-period structures may result in an increase in their base shear demands. Figure 5.6 provides a better comparison of data for different values of slenderness ratio.

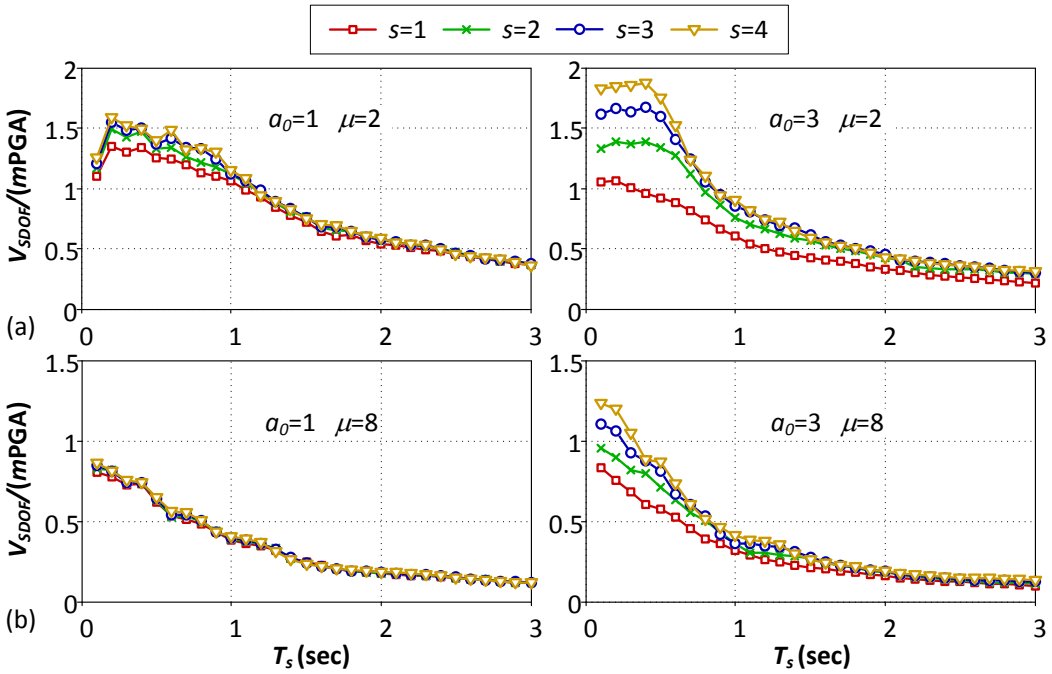

Figure 5.6: Effect of structural slenderness s on base shear demands of SDOF structures located on site class E.

It is shown that the effect of s on base shear demands is insignificant for long-period structures. However, a higher base shear demand may be required for a slender structure than for a squatty structure (both having the same T_s) to achieve an identical ductility demand, in the short-period range. This phenomenon is more obvious for lightly nonlinear structures supported on softer soil profiles. It is suggested that the difference caused by slenderness ratio in the strength demands is mainly attributed to the effective damping of the SSI system ξ_{ssi}, which increases as the slenderness ratio is reduced. As illustrated in Figure 4.7, the variation of damping due to slenderness ratio is more pronounced in systems with higher structure-to-soil stiffness ratio a_0. The effective damping, however, makes a smaller contribution to the total energy dissipation when compared with that provided by large inelastic deformations, as described previously. Results for site classes C and D are presented in Appendix A.1, and they have similar trends as those depicted in Figures 5.5 and 5.6 because of the similarity of the shapes of the corresponding design spectra.

5.4 Strength reduction factor R_F for flexible-base SDOF structures

According to Equation (5.4), the ductility reduction factor is defined as the ratio of the base shear required to maintain elasticity to that required to produce a target ductility demand μ_t. For a fixed-base SDOF oscillator, R_μ is given by:

$$R_\mu = \frac{V(T_s, \mu = 1)}{V(T_s, \mu = \mu_t)} \tag{5.8}$$

Equation (5.8) is based on a hysteretic force-displacement relationship (e.g., elastic-perfectly plastic behaviour) and a constant damping ratio of 5% applied to the elastic response.

Knowing that the base shear demand is also sensitive to a_0 and s (Section 5.3), the ductility reduction factor R_μ could be expressed as:

$$R_\mu = \frac{V(T_s, a_0, s, \mu = 1)}{V(T_s, a_0, s, \mu = \mu_t)} \tag{5.9}$$

It is clear that a_0=0 represents the fixed-base condition where the base shear demand is only a function of T_s and μ. In this condition, Equation (5.9), which seems to be a more general expression for the ductility reduction factor, reduces to Equation (5.8).

Using Equation (5.9), Figure 5.7 compares the ductility reduction factor of SDOF systems for different site classes considering various combinations of a_0, s and μ. Results are averaged values for the 15 synthetic spectrum-compatible earthquakes corresponding to each site class.

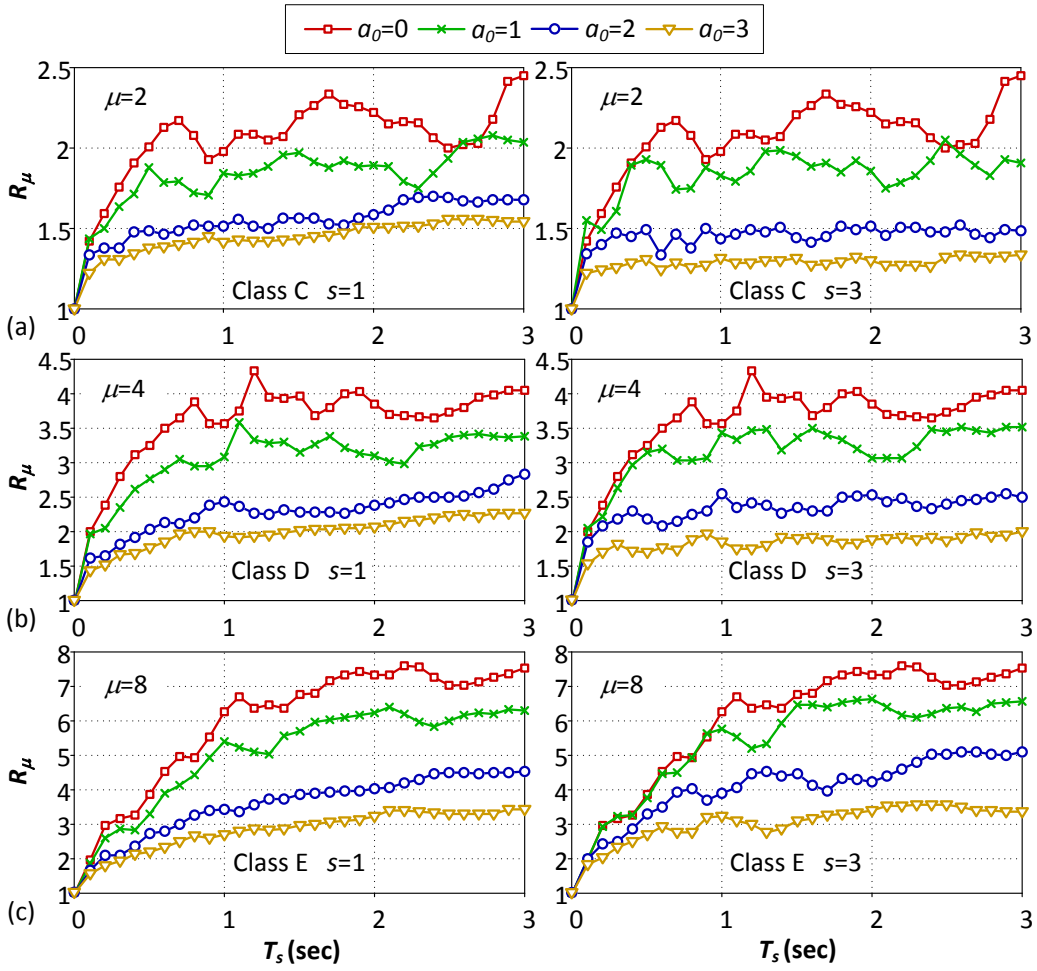

Figure 5.7: Effect of SSI on ductility reduction factor R_μ of SDOF structures located on different site classes.

Generally, an ascending trend is observed for R_μ when increasing the fixed-base natural period T_s, especially in the low period range. This trend, however, is less pronounced in the high period region. For the rigid-base systems (i.e., a_0=0), the

R_μ curves show two distinct segments that are separated by a transition point at a threshold period. The first segment corresponds to a monotonically increasing R_μ with T_s, whereas the second segment exhibits an oscillating R_μ around a maximum value, which is much less affected by T_s. This observation can be well described by a bi-linear approximation of R_μ versus T_s proposed by Vidic et al. (1994), with the threshold period almost equal to the characteristic period T_0.

For flexible-base systems shown in Figure 5.7, the bi-linear approximation of R_μ spectra seems to provide reasonable results, but the threshold periods are considerably lower than T_0, especially for systems with greater a_0 values and higher slenderness ratios. This could be a result of period lengthening due to SSI, which causes the transition points to occur earlier in the spectra, as illustrated in Figure 5.5.

It is observed that the ductility reduction factor R_μ decreases by increasing the a_0 value, which was also reported by Ghannad and Jahankhah (2007), who concluded that using a fixed-base reduction factor to design a flexibly-supported structure is un-conservative.

It should be noted that applying conventional R_μ-T_s relationships for seismic design of flexible-base structures may not be appropriate, since the slenderness ratio can lead to inconsistent results in R_μ spectra. For example, a higher slenderness ratio can either result in a larger (Figure 5.7(c)) or a smaller (Figure 5.7(a, b)) R_μ factor for SSI systems with a_0=2 and 3 in the long period range. This inconsistency can be addressed by presenting the ductility reduction factor in a 'R_μ versus T_{ssi}' format, as shown in Figure 5.8.

It is clear in Figure 5.8(c) that the threshold periods for the 'constant' segments of R_μ curves are well correlated with the characteristic period T_0, at which the intermediate to long-period transition points on elastic base shear demand spectra (Figure 5.8(a)) are well preserved. Moreover, increasing the values of slenderness ratio leads to consistent increase in R_μ values, due to the reduced effective system damping ξ_{ssi}. For structures having a slenderness ratio of s=3, regardless of the a_0 value, their base shear demands are practically the same, provided that their equivalent natural periods are identical. This can be explained by the fact that the

effective damping ratio of an SSI system is very similar to its superstructure with s=3, as shown in Figure 4.7.

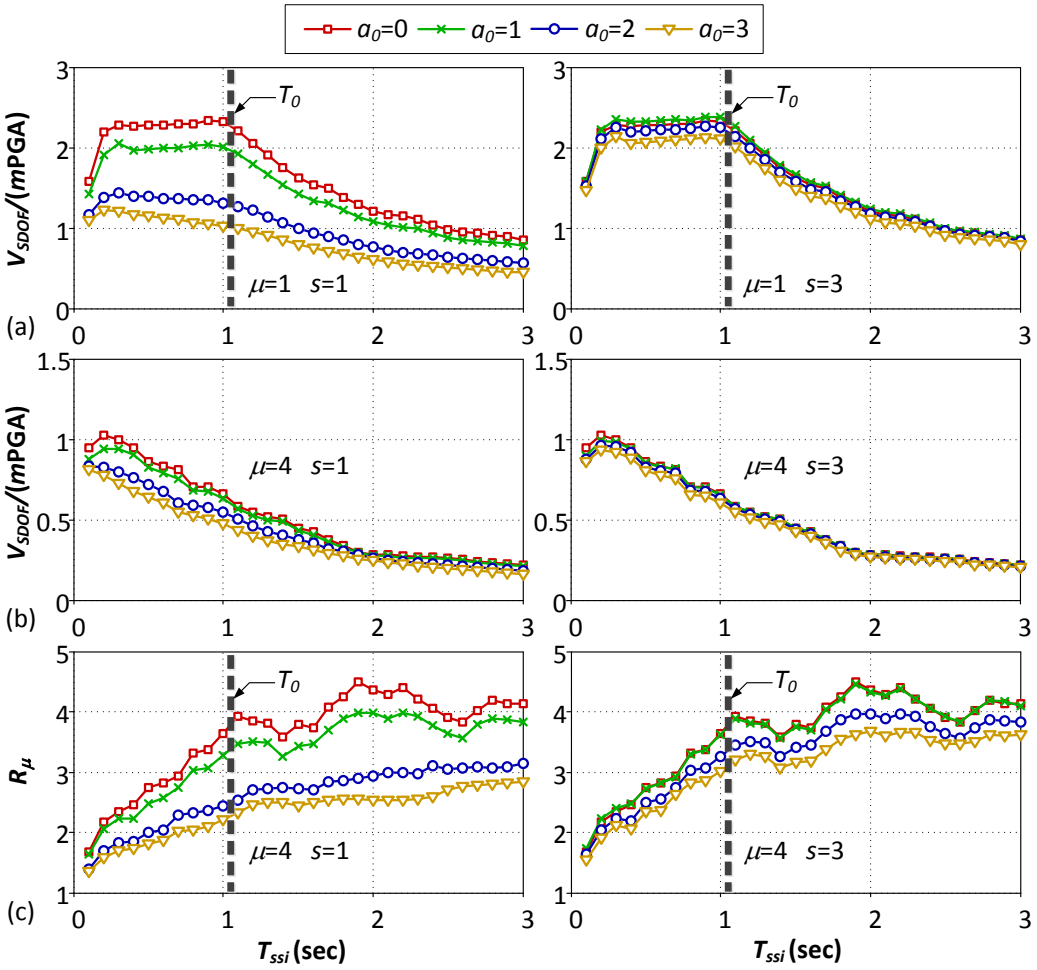

Figure 5.8: Base shear demand and ductility reduction factor against equivalent natural period of SSI systems for site class E.

In this regard, R_μ-$T_{\rm ssi}$ should be a rational basis for developing an SSI-dependent ductility reduction factor. However, in view of developing a more practical approach, a new strength reduction factor $R_{\rm F}$ is suggested in this study to use fixed-base SDOF elastic design spectra (e.g. from seismic design guidelines) for seismic design of non-linear systems.

$$R_{\rm F} = \frac{V(T_{\rm s}, a_0 = 0, \mu = 1)}{V(T_{\rm s}, a_0, s, \mu = \mu_t)} \tag{5.10}$$

Note that if a_0=0, $R_{\rm F}$ corresponds to R_μ for fixed-base structures (whose dynamic responses are not affected by s), which reflects the reduction only attributed to the nonlinear behaviour of the structures; while μ_t=1 leads to a R_μ associated with the

reduction only due to the SSI effects (i.e. inelastic hysteretic behaviour of structure is excluded). Therefore, R_F defined in Equation 5.10 can be interpreted as a strength reduction factor due to the combination of yielding and SSI effects.

Based on the results of more than 100,000 nonlinear dynamic analyses of 7,200 SDOF systems, the following equation is proposed to estimate the strength reduction factor R_F:

$$R_F = \begin{cases} \dfrac{R-1}{T_0} T_s + 1, & \text{for } 0 \le T_s < T_0 \\ R, & \text{for } T_s \ge T_0 \end{cases} \tag{5.11}$$

where R is a function of ductility demand μ, structure-to-soil stiffness ratio a_0, and slenderness ratio s, with its values presented in Table 5.1. Again, T_0 is the characteristic period of the design ground motions as shown in Figure 5.2. The shape of R_F spectra described by Equation 5.11 was originally proposed by Vidic et al. (1994) for design of inelastic fixed-base structures.

Table 5.1: Proposed values for R in Equation (5.10)

R	μ=2				μ=3				μ=4				μ=5			
s	1	2	3	4	1	2	3	4	1	2	3	4	1	2	3	4
Site C																
a_0=0	2.2	2.2	2.2	2.2	3.9	3.9	3.9	3.9	5.4	5.4	5.4	5.4	6.8	6.8	6.8	6.8
a_0=1	2.4	2.2	2.2	2.1	4.1	3.9	3.9	3.9	5.5	5.4	5.3	5.3	6.8	6.7	6.7	6.7
a_0=2	3.2	2.6	2.4	2.5	4.8	4.2	3.9	3.9	6.1	5.6	5.4	5.3	7.4	6.8	6.7	6.6
a_0=3	4.1	3.2	2.9	3.0	5.6	4.5	4.2	4.1	7.0	5.8	5.3	5.2	8.2	7.1	6.5	6.2
Site D																
a_0=0	2.1	2.1	2.1	2.1	3.8	3.8	3.8	3.8	5.3	5.3	5.3	5.3	6.6	6.6	6.6	6.6
a_0=1	2.3	2.3	2.1	2.1	3.9	3.8	3.7	3.7	5.3	5.2	5.2	5.2	6.6	6.5	6.5	6.5
a_0=2	3.0	2.5	2.4	2.4	4.6	4.0	3.	3.7	5.9	5.4	5.2	5.1	7.2	6.7	6.5	6.3
a_0=3	3.9	3.1	2.8	2.8	5.5	4.4	4.0	4.0	6.8	5.7	5.2	5.0	8.0	6.9	6.5	6.2
Site E																
a_0=0	2.2	2.2	2.2	2.2	4.1	4.1	4.1	4.1	5.7	5.7	5.7	5.7	7.1	7.1	7.1	7.1
a_0=1	2.4	2.3	2.2	2.2	4.1	4.0	4.0	4.0	5.7	5.6	5.5	5.5	7.1	7.0	7.0	6.9
a_0=2	3.1	2.6	2.4	2.4	4.7	4.2	4.0	4.0	6.2	5.7	5.5	5.5	7.5	7.0	6.9	6.8
a_0=3	4.0	3.0	2.8	2.8	5.6	4.5	4.2	4.1	7.0	6.0	5.5	5.4	8.2	7.2	6.8	6.5
Average																
a_0=0	2.2	2.2	2.2	2.2	3.9	3.9	3.9	3.9	5.5	5.5	5.5	5.5	6.8	6.8	6.8	6.8
a_0=1	2.4	2.3	2.2	2.1	4.0	3.9	3.9	3.9	5.5	5.4	5.3	5.3	6.8	6.7	6.7	6.7
a_0=2	3.1	2.6	2.4	2.4	4.7	4.1	3.9	3.9	6.1	5.6	5.4	5.3	7.4	6.8	6.7	6.6
a_0=3	4.0	3.1	2.8	2.9	5.6	4.5	4.1	4.1	6.9	5.8	5.3	5.2	8.1	7.1	6.6	6.3

Figures 5.9 to 5.11 compare the mean values of strength reduction factor R_F for

flexible-base SDOF structures obtained from the 15 synthetic earthquakes of each of the three site classes with those calculated according to Equation 5.11. It is shown that the R_{F} versus T_{s} curves follow reasonably closely a bi-linear relationship with the intersection of two linear segments approximately corresponding to the characteristic period of the design spectrum T_0 for each site class. This is one of the benefits of reducing base shear demands directly from the code-based design spectra. Regression analyses were done to obtain best-fit values for R in Equation 5.11, which minimised the sum of the squared residuals over all period points. The residual is defined as the difference between the mean value of R_{F} and that calculated by Equation 5.11 at a period T_{s}.

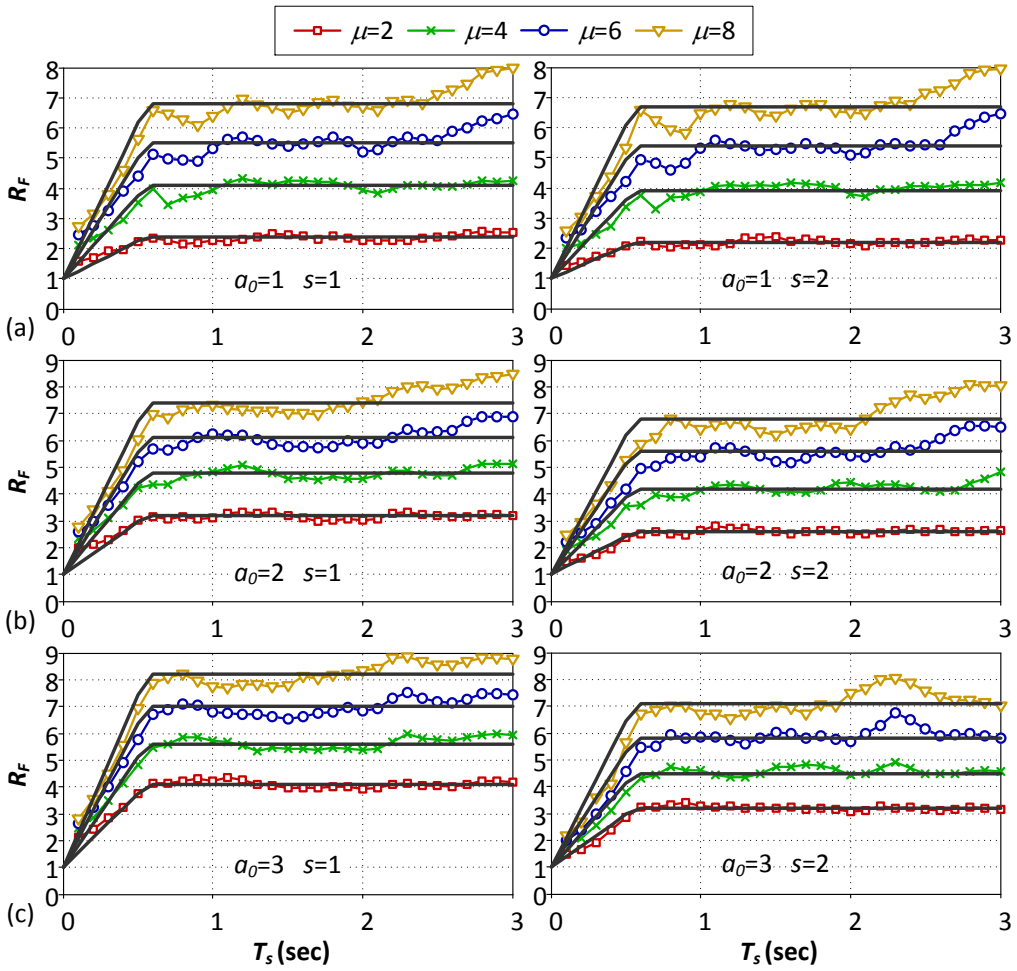

Figure 5.9: Comparison of the mean strength reduction factors R_{F} with those calculated using Equation 5.11 (bi-linear lines) for soil-SDOF structure systems for site class C.

Table 5.1 shows that the R values, in general, are not sensitive to the soil site classes,

especially for lower ductility demands. Therefore, it is suggested that the average R values presented in Table 5.1, which are site-independent, may be used in Equation 5.11. Multi-linear interpolation can be adopted to estimate intermediate values of R for a_0-s-μ combinations that are not included in Table 5.1. As expected, the results indicate that the slenderness ratio of the structure, s, has a negligible effect on R values when the structure-to-soil stiffness ratio a_0 is small (i.e. $a_0 < 1$), and hence the SSI effects are not dominant.

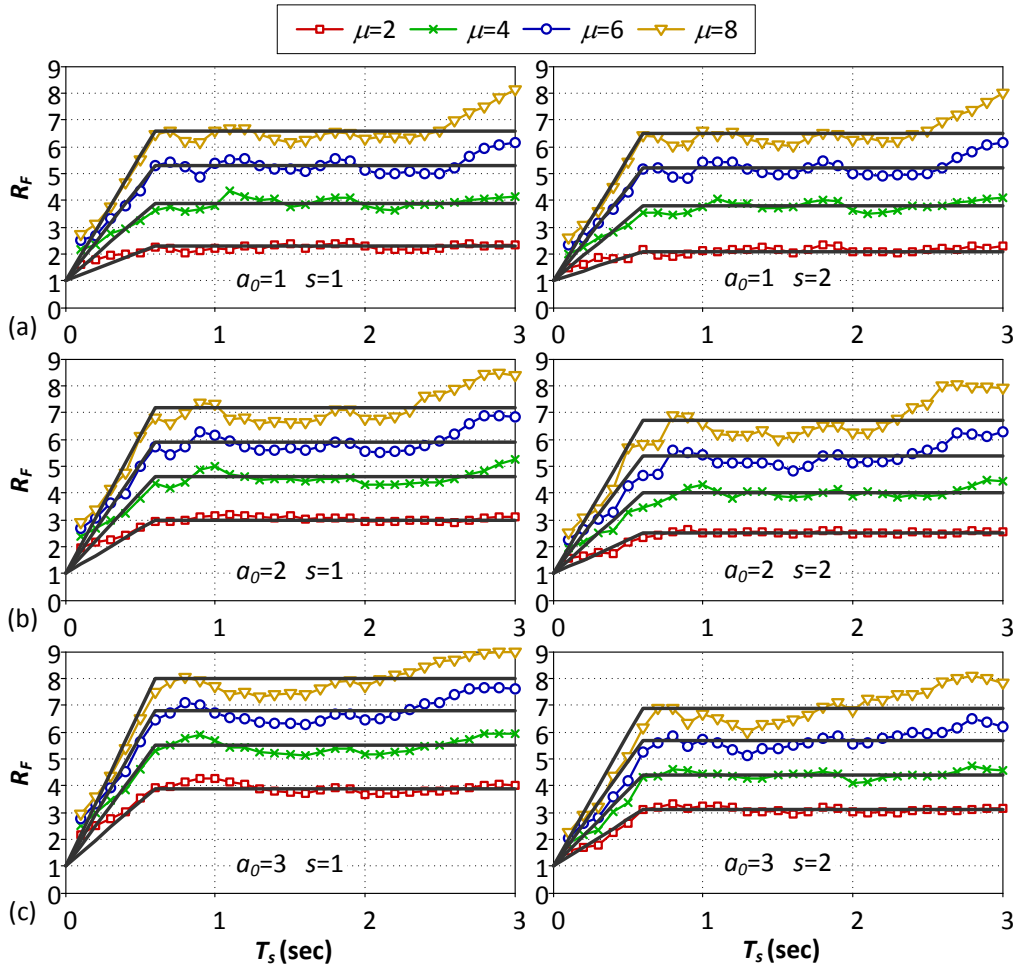

Figure 5.10: Comparison of the mean strength reduction factors R_{F} with those calculated using Equation 5.11 (bi-linear lines) for soil-SDOF structure systems for site class D.

The proposed equation for strength reduction factor R_{F} not only addresses the issues associated with the R_{μ}-T_{s} relationships discussed previously, but also has two prominent advantages. Firstly, it captures the reduction of strength due to the combination of SSI and structural yielding, with the SSI effect being negligible

for structures with high ductility demands. Therefore, the amount of reduction due to SSI in addition to that of yielding is 'seen' by engineers. Secondly, the inelastic strength demand of a flexible-base structure can be directly estimated from the elastic response of its corresponding fixed-base structure through the reduction factor R_{F}. This implies that by using Equation 5.11, the calculation of the base shear demand of flexible-base structures does not require the knowledge of the elastic response spectra derived for SSI systems, which is ideal for practical design purposes.

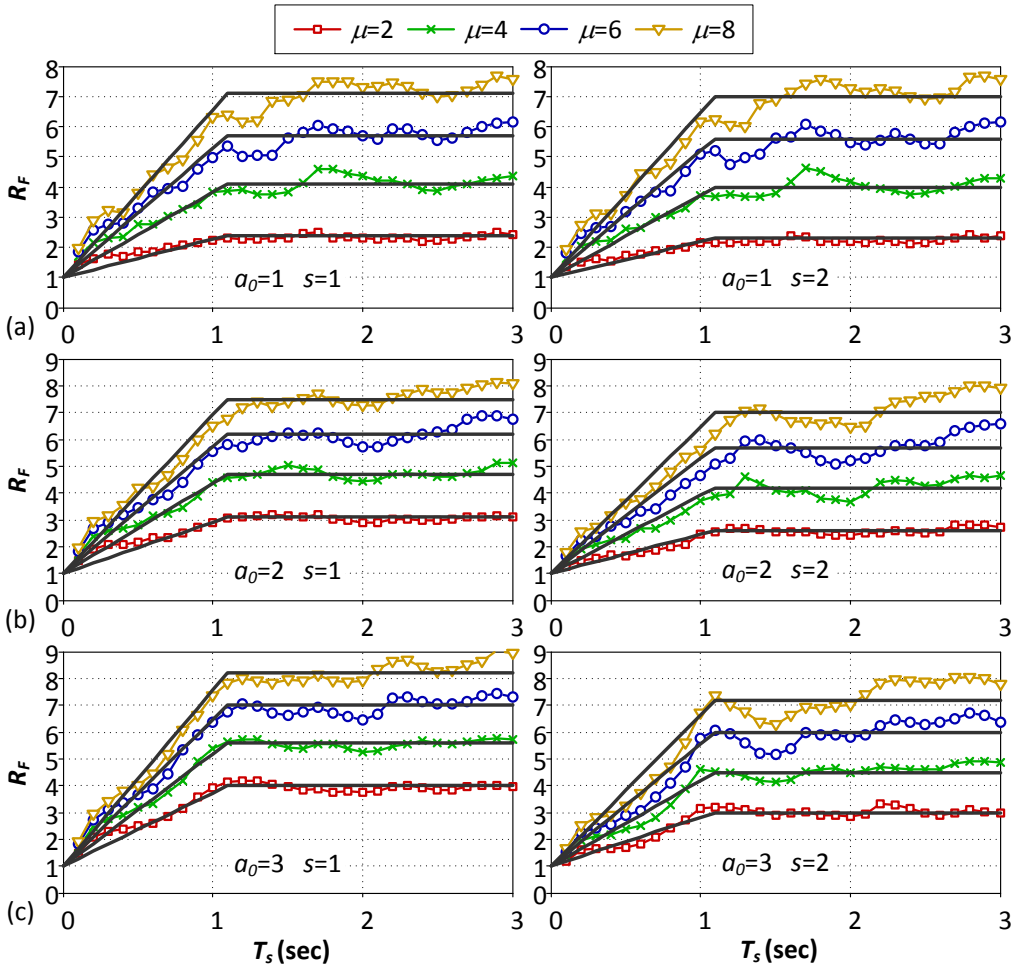

Figure 5.11: Comparison of the mean strength reduction factors R_{F} with those calculated using Equation 5.11 (bi-linear lines) for soil-SDOF structure systems for site class E.

5.5 Effect of SSI on seismic response of MDOF structures

In this section, the effects of lateral seismic design load pattern, structure-to-soil stiffness ratio, structural slenderness and site conditions on the strength-ductility relationship of multi-storey flexible-base buildings are investigated.

The lateral seismic design load pattern can significantly influence the stiffness and strength distributions in multi-storey buildings, and hence the displacement and strength demands under seismic excitations. Figure 5.12 compares the total strength demand F_{tot} of fixed-base (a_0=0) and flexible-base (a_0=3) 10-storey buildings (s=2) designed with different load patterns that were illustrated in Figure 4.2. F_{tot} was calculated by summing the strength demands of all storeys. It is clear from Figure 4.4 that for a typical 10-storey building (a_0 values between 5 and 20-storey limits), a_0=3 corresponds to a soil condition of site class E. Therefore, the results in Figure 5.12 are the average values from the fifteen spectrum-compatible earthquakes corresponding to site Class E. Results for other site classes (see Appendix A.2) showed similar trends to those presented in Figure 5.12. By an analogy with the normalisation of the base shear demand of SDOF structures, the total strength demands of MDOF structures are normalised by the product of the total mass of the structure and PGA. The shaded areas on the graphs in Figure 5.12 represent the practical range of the fundamental period of a 10-storey building with different structural systems calculated using Equation (4.2).

Figure 5.12 shows that the strength demands of the buildings designed according to the concentric and rectangular load patterns are always higher than those corresponding to the other load patterns, especially for lower values of fundamental period. Within the practical range of the fundamental period of a typical 10-storey building (i.e. shaded areas), using the concentric and rectangular load distributions can result in up to 1.68 and 2 times higher strength demands, respectively, compared to code-based load patterns such as IBC-2012 and Eurocode 8. It should be mentioned that this observation is opposite to conclusions made by Ganjavi and

Hao (2012), where the concentric pattern was found to yield the lowest strength demand. The reason for this difference is attributed to different definitions of strength demand used in the two studies. The current study calculated the total strength as the sum of all storey strengths, whereas Ganjavi and Hao (2012) used the base shear strength that corresponds only to the strength of the first storey. The total strength demand that is used in the current study can be considered proportional to the total structural weight of the shear building and is, therefore, a more appropriate parameter to compare the seismic performance of buildings designed according to different lateral load patterns.

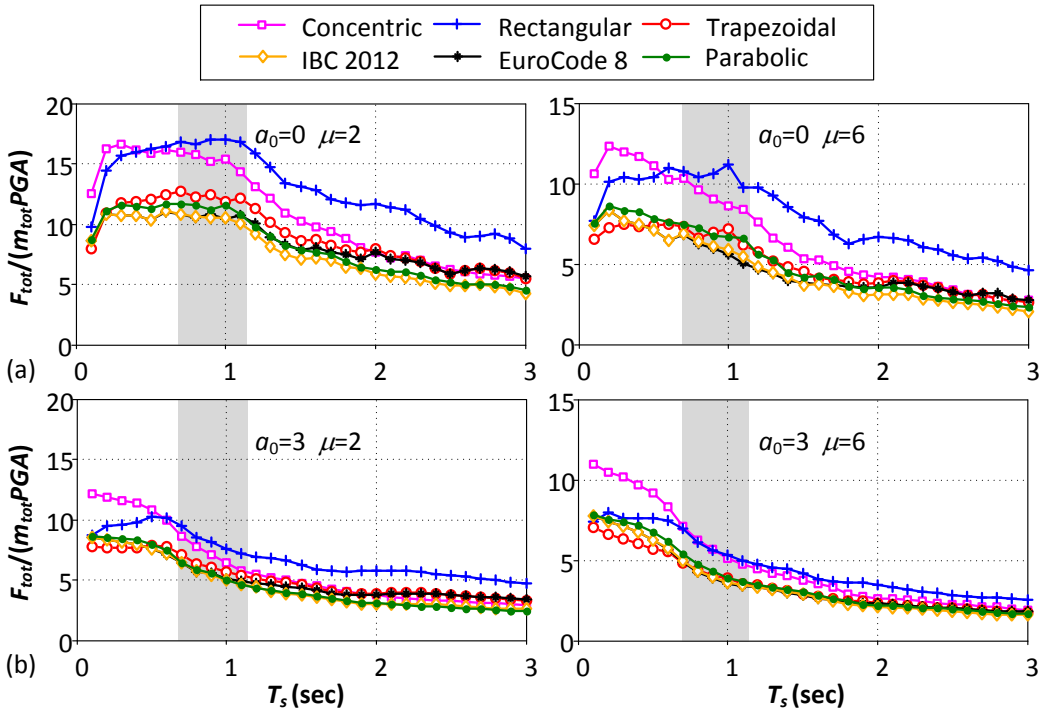

Figure 5.12: Total strength demands of (a) fixed-base and (b) flexible-base 10-storey buildings designed according to different lateral load patterns, Soil Class E, s=2.

Although strength demands corresponding to parabolic, trapezoidal and code-based load patterns are not significantly different, especially for the SSI systems, the trapezoidal lateral load pattern is in general most suitable for seismic design of nonlinear short period flexible-base structures (i.e., requiring minimum total strength to satisfy a target ductility demand) and code-specified design patterns are more appropriate for structures with a fundamental period $T_s > 0.8$sec. This conclusion is in agreement with the results reported by Moghaddam and Hajirasouliha (2006) for

fixed-base shear-buildings subjected to a group of natural earthquake excitations.

Based on the concept of uniform damage distribution, it can be assumed that the uniform distribution of deformation demands is a direct consequence of the optimum use of material (Hajirasouliha and Pilakoutas, 2012). Therefore, the coefficient of variation of storey ductility demands (COVμ) can be used as a performance parameter to evaluate the effectiveness of different lateral load patterns. Figure 5.13 compares the mean COVμ of fixed-base and SSI systems designed according to different load patterns under fifteen spectrum-compatible earthquakes corresponding to site class E. As expected, the concentric and rectangular patterns resulted in a much higher COVμ compared to other load patterns. Within the expected range of periods for 10-storey frames (i.e. shaded areas), the concentric pattern always led to the largest ductility dispersion, while the code patterns provided the most cost-effective design solutions.

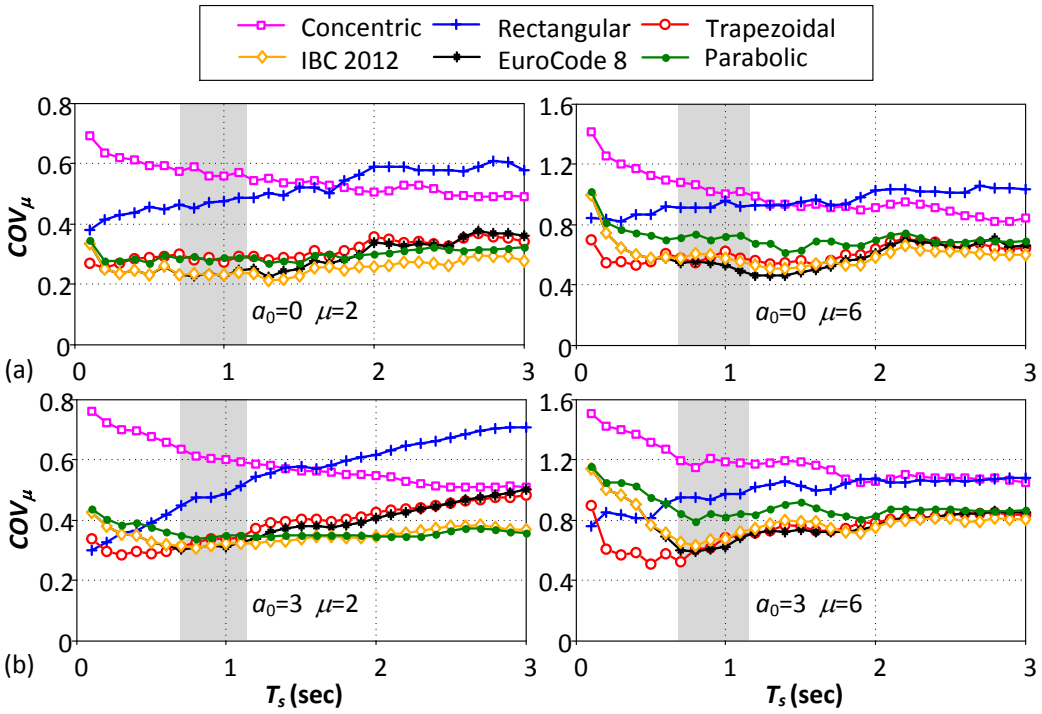

Figure 5.13: Coefficient of variation of storey ductility for (a) fixed-base and (b) flexible-base 10-storey buildings designed according to different lateral load patterns, Soil Class E, s=2.

Figure 5.14 compares the total strength demands of 10-storey buildings, designed

according to the IBC-2012 load pattern, with fundamental periods ranging from 0.1 to 3 sec and target ductility demands μ=2 and 8 for structure-to-soil stiffness ratios a_0=0, 1, 2 and 3. It should be noted that the selected range of the design parameters are only for comparison purposes; some cases do not represent practical scenarios. For example, a value of 3 for a_0 is not suitable for common buildings located on soil site class C (see Figure 4.21).

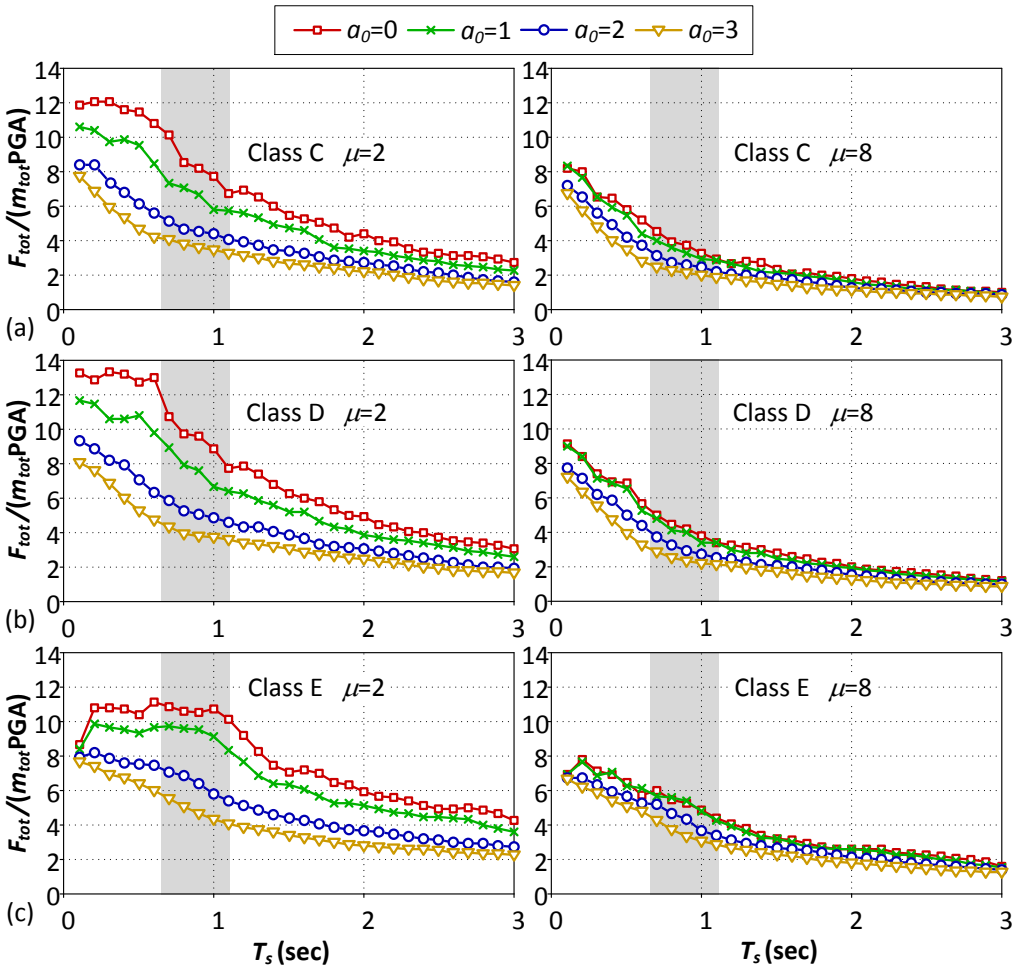

Figure 5.14: Total strength demands of 10-storey structures (s=1) located on (a) class C, (b) class D and (c) class E for μ=2 and 8.

Similar to the data for soil-SDOF structure systems, flexible-base MDOF structures, in general, exhibit reduced total strength demands in comparison with their rigid-base counterparts. The reduction is more substantial for structures designed with a lower ductility demand. Results presented in Figure 5.14 are total strength demands for only squatty 10-storey buildings. However, an increase in structural slenderness ratio was shown to increase the base shear demands of short-period flexible-base

SDOF structures. This effect is also expected for MDOF structures. An example is shown in Figure 5.15 for 10-storey buildings designed according to the IBC-2012 design load pattern.

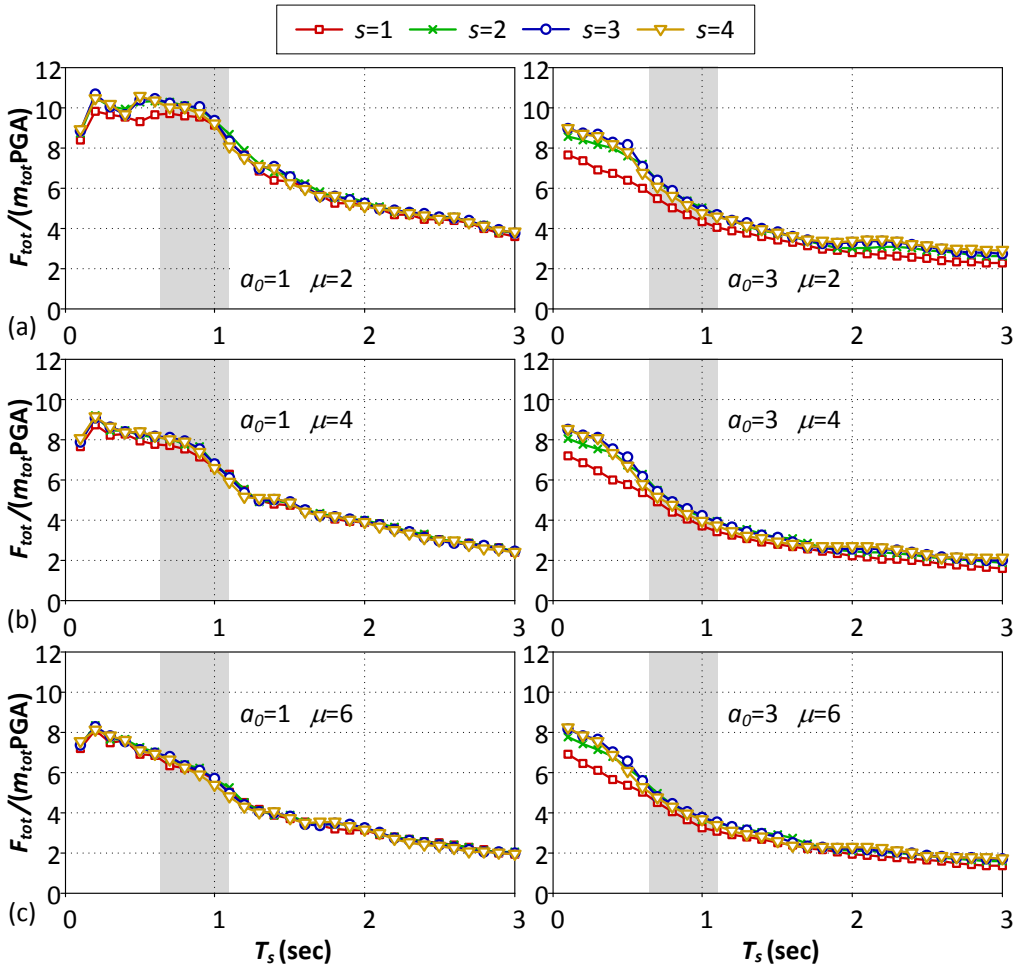

Figure 5.15: Effect of slenderness ratio on total strength demands of 10-storey SSI systems on soil site class E.

Comparing with Figure 5.6, the effect of slenderness ratio on strength demands of yielding flexible-base MDOF structures seems to be less significant than that of the SDOF structures. Within the practical range of T_s for a 10-storey building in its fixed-base state, as shown by the shaded areas, the total strength demand is insensitive to structura slenderness ratio.

5.6 MDOF modification factor R_{M} for flexible-base MDOF structures

In order to use a SDOF design spectrum for MDOF systems, modifications should be made to take into account the higher mode effects. Considering SDOF and MDOF structures with similar structural mass and fundamental period T_{s}, the MDOF modification factor for a flexible-base structure can be defined as:

$$R_{\mathrm{M}} = \frac{V_{\mathrm{SDOF}}(T_{\mathrm{s}}, a_0, s, \mu = \mu_t)}{V_{\mathrm{MDOF}}(T_{\mathrm{s}}, a_0, s, \mu = \mu_t)} \tag{5.12}$$

where $V_{\mathrm{MDOF}}(T_{\mathrm{s}}, a_0, s, \mu = \mu_t)$ is the base shear strength for an MDOF structure to avoid the maximum storey ductility exceeding the target value. Note that when a_0=0, Equation 5.12 is an expression for the fixed-base MDOF modification factor, which was proposed by Nassar and Krawinkler (1991) and has received much attention in the past two decades (e.g., Santa-Ana and Miranda, 2000; Miranda, 1997; Moghaddam and Mohammadi, 2001).

The base shear strength demand of an inelastic flexible-base MDOF structure can be determined from the elastic spectrum for an equivalent fixed-base SDOF system by using Equations 5.10 and 5.12, as follows:

$$V_{\mathrm{MDOF}}(T_{\mathrm{s}}, a_0, s, \mu = \mu_t) = \frac{V_{\mathrm{SDOF}}(T_{\mathrm{s}}, a_0 = 0, \mu = 1)}{R_{\mathrm{F}} R_{\mathrm{M}}} \tag{5.13}$$

It should be mentioned, based on the ductility reduction factor for flexible-base SDOF structures (i.e., Equation (5.9)) Ganjavi and Hao (2012) proposed a similar ductility reduction factor for soil-MDOF structure systems:

$$R_{\mu,MDOF} = \frac{V_{\mathrm{MDOF}}(T_{\mathrm{s}}, a_0, s, \mu = 1)}{V_{\mathrm{MDOF}}(T_{\mathrm{s}}, a_0, s, \mu = \mu_t)} \tag{5.14}$$

Equation (5.14) shows that the base shear demand of a flexible-base nonlinear MDOF structure can be reduced from that of its elastic counterpart by a factor of $R_{\mu,MDOF}$. A simple expression was also provided in Ganjavi and Hao (2014) for $R_{\mu,MDOF}$ as a function of T_{s}, a_0, s and μ. In order to use this expression, the base shear demand of the elastic MDOF structure should be estimated. Ganjavi and Hao (2014) found that considering linear SSI systems, the base shear demands for MDOF

structures could be significantly different from those for the corresponding SDOF structures. However, they did not provide any method for estimating V_{MDOF} of elastic SSI systems. In other words, there is a gap between the design spectrum and base shear demand of flexible-base elastic MDOF structures. $R_{\mu,MDOF}$ is therefore, difficult to be implemented in the existing design methodologies.

To develop an expression for R_{M} that can be calculated according to Equation (5.12), 5, 10, 15 and 20-storey shear buildings are used in the analyses that follow and the effects of structural type and soil site class are also taken into account. The buildings are assumed to be symmetric and represent typical 5-bay structures having a span length of 6 meters. Using a storey height of 3.3 meters, the slenderness ratios corresponding to 5, 10, 15 and 20-storey buildings would be approximately 0.7, 1.4, 2 and 2.7, respectively. The effective foundation radii for swaying and rocking modes were calculated based on Equation (2.7). The fundamental period of the buildings was determined according to Equation (4.2) for the four different ASCE (2010) structural types listed in Table 4.2.

In order to derive a site dependent R_{M}, an averaged shear wave velocity was used to represent each site soil condition, i.e., $V_{\mathrm{s,30}}$=90, 270 and 560m/s for site classes E, D and C, respectively. Therefore, the corresponding a_0 value for an MDOF structure located on a specific soil deposit could be estimated from Figure 4.4. The range of expected a_0 values for different SSI systems is presented in Figure 5.16, which shows higher a_0 values for taller buildings and softer soil conditions. It is observed that frame structures (i.e., type 1-3) have a lower a_0 value compared with other structural systems (i.e., type 4), especially for those located on site class E. Therefore, for better comparison, frame structures are presented as one group in Figure 5.16. It can be noted that the expected a_0 values for typical buildings founded on site class C (average shear wave velocity of 560m/s) are close to zero. This implies that the seismic design of typical multi-storey buildings on site classes A, B and even C (see Table 4.2) could be practically done on the basis of fixed-base structures.

The effect of using different structural types (types 1 to 4 in Table 4.2) on $1/R_{\mathrm{M}}$ is presented in Figure 5.17. It should be noted that shear buildings, in general,

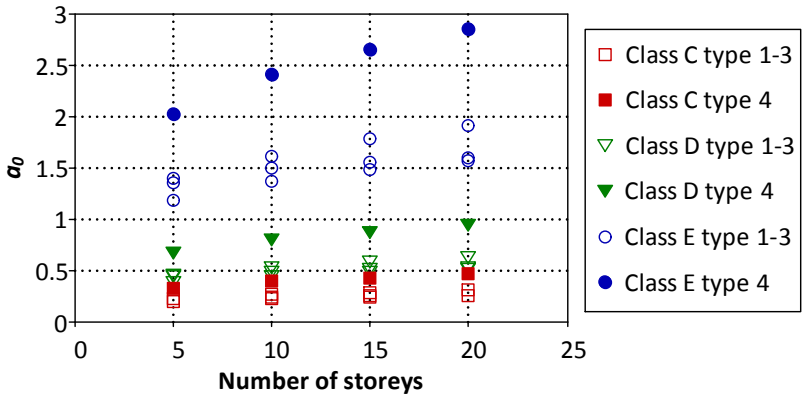

Figure 5.16: Variation of a_0 with number of storeys for different types of structural systems on various site classes.

cannot accurately represent all different structural systems and, therefore, the effect of 'structural type' in this context is attributed mostly to the expected fundamental period of the structures using Equation 4.2. As mentioned previously, according to ASCE (2010), the expected fundamental period of frame structures (types 1-3) is much higher than type 4 structures. Therefore, the results in Figure 5.17 illustrate lower $1/R_{\mathrm{M}}$ values for type 4 structures compared to type 1-3 frame structures.

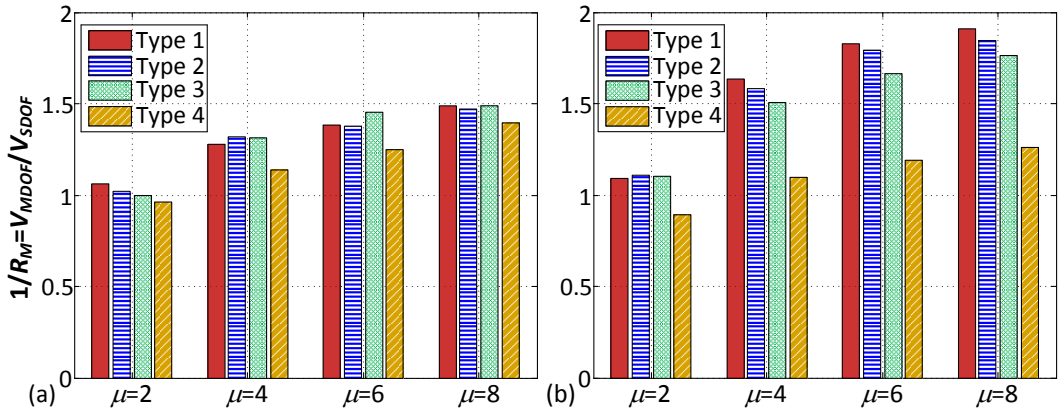

Figure 5.17: Effect of structural type on MDOF modification factor for (a) 10-storey and (b) 15-storey structures located on Site class E.

Results for $1/R_{\mathrm{M}}$ (averaged values for the 15 synthetic earthquakes in each set) are illustrated in Figures 5.18, considering various structural types, numbers of storeys, ductility demands and site classes. Since the values of MDOF modification factor for frame structures are very close to each other (see Figure 5.17), the results were averaged for structural types 1-3. As discussed previously, the effect of SSI is

expected to be pronounced for site class E and insignificant for site class C.

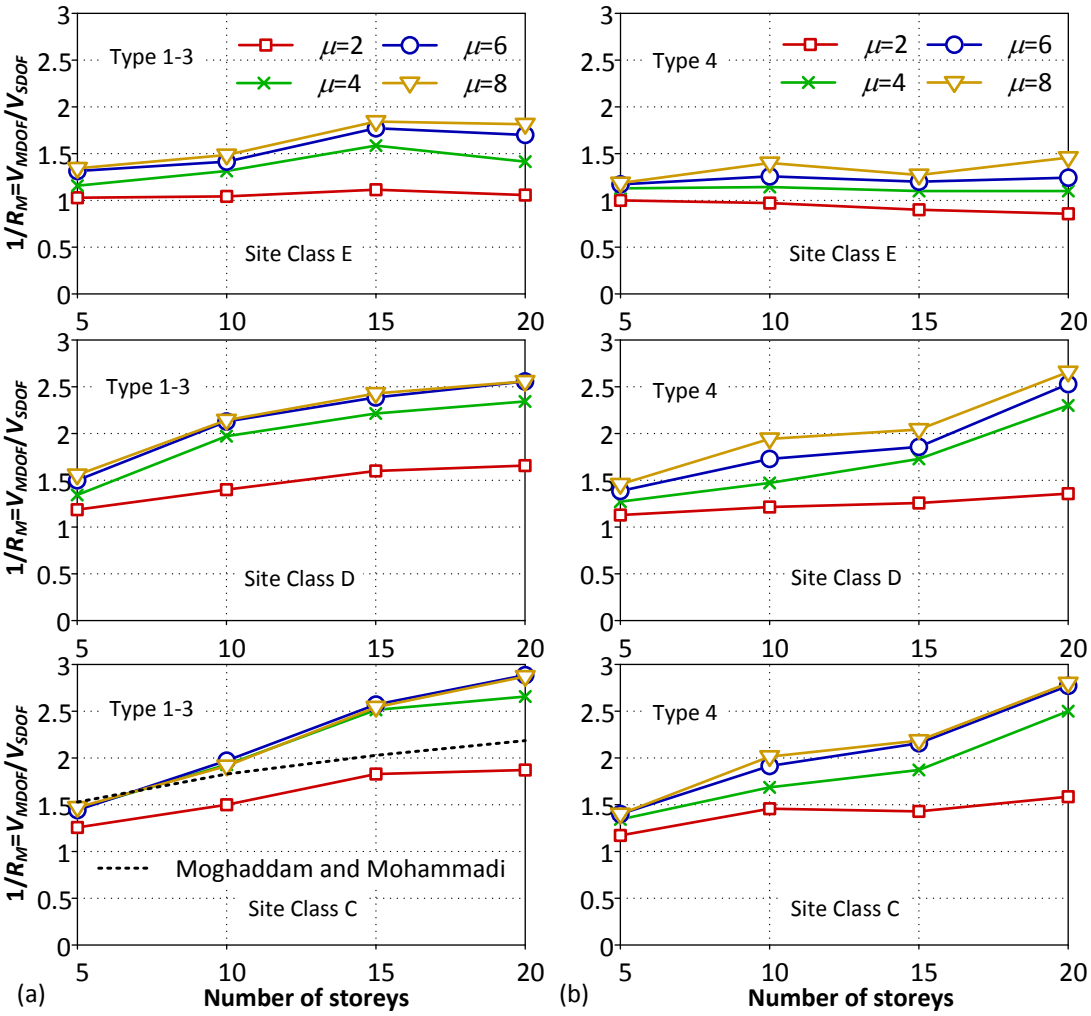

Figure 5.18: Site and interaction-dependent MDOF-to-SDOF base shear strength ratio ($1/R_{\mathrm{M}}$) for (a) frame structures and (b) all other types of structures.

Figure 5.18 shows that, in general, inelastic MDOF structures require a higher base shear strength compared to their SDOF counterparts for the same target ductility demand, especially for tall buildings on stiff soil deposits. This observation is in agreement with findings presented by Santa-Ana and Miranda (2000) for fixed-base structures. The results in Figure 5.18 show a generally higher $1/R_{\mathrm{M}}$ ($=V_{\mathrm{MDOF}}/V_{\mathrm{SDOF}}$) ratio for frame structures and stiff soil conditions than for other structural systems and soft soil profiles. $1/R_{\mathrm{M}}$ curves also exhibit a general increasing trend with increasing ductility demand and number of storeys. Exceptions are observed for site class E where taller structures may have a lower value of $1/R_{\mathrm{M}}$. As foundation soil becomes stiffer, the dependence of $1/R_{\mathrm{M}}$ on ductility demand for

moderately and highly nonlinear structures (μ=4, 6 and 8) is reduced. For example, the results for site class C (very dense soil) in Figure 5.18 show that the effect of ductility demand on $1/R_{\mathrm{M}}$ for structures with μ=6 and 8 is practically negligible. This observation is consistent with the results reported by Moghaddam and Mohammadi (2001), who investigated R_{M} for 5, 10 and 15-storey fixed-base MDOF shear buildings. In their study, R_{M} was found insensitive to ductility demand; a simple expression was suggested for estimating R_{M} as a function of number of storeys, as illustrated in Figure 5.18 for soil class C (with minimum SSI effects). The fact that the RM factor proposed by Moghaddam and Mohammadi (2001) was derived through an averaging process for ductility values μ=2, 4, 6 and 8 is well reflected in this graph, since the results are generally bounded by the high and low-ductility limits used in this study.

The results of this study are used to develop a new practical site and interaction-dependent MDOF modification factor R_{M} for flexible-base structures. Emphasis is given to common frame buildings (types 1-3) according to ASCE (2010). By assessing a variety of curves to obtain the best fit to the results presented in Figure 5.18, the following equation is suggested that is a function of number of storeys, ductility demand and site class:

$$\frac{1}{R_{\mathrm{M}}} = 1 + (n-1)\ln(c\mu^{(0.05-n/1000)}) \tag{5.15}$$

where n is the number of storeys, and c is a soil dependent parameter that is equal to 1.040, 1.027 and 0.982 for site classes C, D and E, respectively.

5.7 Performance-based procedures

The proposed site and interaction-dependent equations to estimate R_{F} and R_{M} modification factors for SSI systems (Equations (5.10) and (5.12) can be obtained based on standard IBC (2012) design spectra for different soil classes and, therefore, can be directly used in practical applications. Here, the following design procedure is suggested for performance-based seismic design of flexible-base structures (with reference to Figure 5.19):

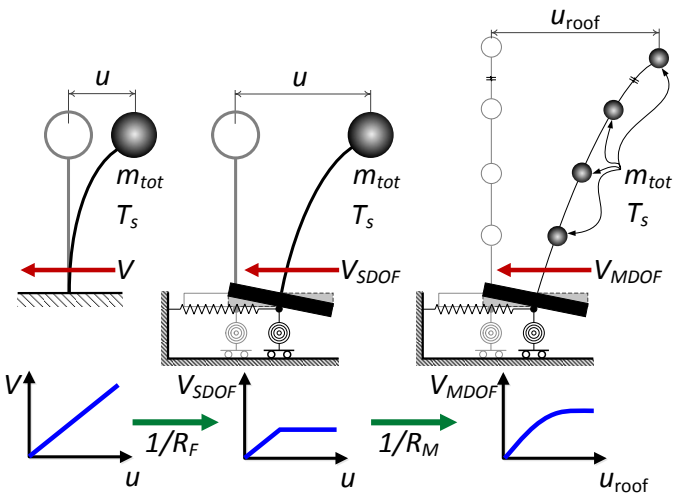

Figure 5.19: Procedures for design of a flexible-base MDOF structure.

Step 1 : The MDOF structure is initially designed based on fixed-base behaviour (i.e. by ignoring the effects of SSI) for gravity and seismic loads according to IBC (2012).

Step 2 : The properties of the representative SDOF structure of the fixed-base MDOF system are then calculated, including the fundamental period T_{s} and slenderness ratio s by using Equations (4.2) and (4.23), respectively. The structure-to-soil stiffness ratio a_0 and characteristic period T_0 are also obtained from Equation (4.21) and Table 4.3, based on the expected shear wave velocity $V_{s,30}$ of the given site class.

Step 3 : The base shear demand of the fixed-base elastic SDOF structure V_{SDOF} is calculated from the elastic design spectrum by using the period T_{s}.

Step 4 : To satisfy the predefined target ductility demand, the design base shear of the inelastic flexible-base MDOF structure is directly calculated from Equation (5.13), where R_{F} and R_{M} are obtained from Equations (5.11) and (5.15), respectively.

Step 5 : The calculated base shear strength is distributed according to the design lateral load pattern used in Step 1, and the MDOF structure is designed based on the new seismic design loads. To achieve more reliable design solutions, the design process can be repeated from Step 2. However, the results of this study

show that, if the initial structure is designed based on code-specified design load patterns, one iteration would be sufficient for practical applications.

5.8 Verification of the proposed procedures

The efficiency of the proposed performance-based design procedure is demonstrated by using several design examples. For this purpose, a number of typical 5, 10, 15 and 20-storey flexible-base buildings with, respectively, fixed-base fundamental periods of 0.61, 1.07, 1.48 and 1.87sec and slenderness ratios of 1, 1.5, 2 and 3 were selected. The a_0 values were calculated based on the assumed shear wave velocities of 90, 270 and 560m/s for site classes E, D and C, respectively. Following the proposed methodology, the buildings were designed for target ductility demands of 2, 4, 6 and 8, and were subsequently subjected to the set of 15 synthetic earthquakes representing the IBC (2012) design spectrum corresponding to the selected site class (see Figure 5.2). The actual ductility demands, averaged for the 15 spectrum-compatible earthquakes in each set, are compared with the target values in Figure 5.20. The comparison shows a very good agreement between the actual and expected ductility demands, which proves the reliability of the proposed design procedure for performance-based design of flexible-base multi-storey buildings.

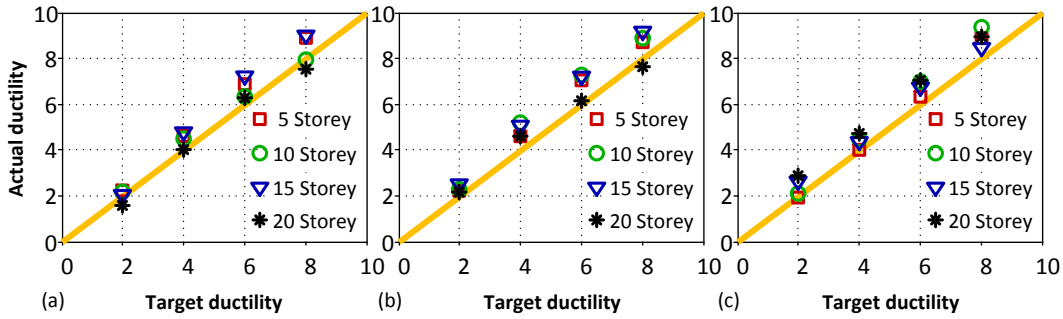

Figure 5.20: Comparison of the actual ductility demands with target ductility ratios for (a) Site Class C, (b) Site Class D, (c) Site Class E.

Admittedly, truly nonlinear soil response up to failure was not taken into account in the proposed design procedures. This chapter is intended to incorporate the effect of soil compliance into design of building structures. Nevertheless, the suggested design

methodology is applicable to practically elastic foundations. The simultaneous effect of soil and structural plasticity will be left for future work.

5.9 Summary

The effects of soil-structure interaction on the strength and ductility demands of single and multi-storey shear buildings were investigated in this chapter. A large number of 1, 5, 10, 15 and 20-storey structures with a wide range of fundamental period, target ductility demand, slenderness ratio and structure-to-soil stiffness ratio were subjected to three sets of synthetic spectrum-compatible earthquakes corresponding to different soil classes. Based on the results, the following conclusions can be drawn:

- Using concentric, rectangular, trapezoidal, parabolic and code-specified design load patterns (IBC (2012) and CEN (2004)) to design flexible-base MDOF structures showed that the code-specified load patterns are, in general, more suitable for long period structures, whereas the trapezoidal pattern provides the most cost-effective design solution for short period flexible-base structures.

- For common building structures with low-to-medium ductility demands under spectrum-compatible earthquakes, increasing structure-to-soil stiffness ratio a_0 can considerably reduce the structural strength demand in comparison to similar fixed-base structures. This implies that for most typical buildings considering SSI in the design process can lead to more cost-effective design solutions with less structural weight.

- To satisfy a target ductility demand for SSI systems with similar fixed-base fundamental periods and structure-to-soil stiffness ratios, the total structural strength increases by increasing the slenderness ratio s, especially in the short period range (i.e., T_s <0.5sec).

- By assessing performance of a large number of SSI systems under spectrum

compatible earthquakes, simple equations were introduced to calculate the site and interaction-dependent MDOF modification factor (R_{M}) and strength reduction factor (R_{F}) for flexible-base structures by taking into account the effects of both SSI and inelastic hysteretic behaviour of the structure.

- Based on the results, a practical performance-based design procedure was proposed to calculate the strength demand of an MDOF flexible-base structure to satisfy a predefined target ductility demand. The reliability and efficiency of the method was demonstrated by using several design examples.

Chapter 6

A more rational design methodology for buildings located on very soft soil profiles

6.1 Introduction

This chapter addresses several issues concerning the seismic design of structures on soft soil profiles by using spectrum-based methods. The problems of the current code-specified design spectra for design of buildings on very soft soil deposits are discussed. One of the main objectives of the chapter is to provide solutions to these problems. This will be done by introducing bi-normalised design spectra for both elastic and inelastic building systems. The concept of a bi-normalised spectrum is based on normalising the natural period of vibration of a system so that the characteristics of the spectrum is well reflected. The other focus of the chapter is on application of the design methodology to soil-structure interaction systems. For this purpose, an efficient approach is proposed, on the basis of extending the equivalent fixed-base SDOF (EFSODF) oscillator developed in Section 4.4 to yielding systems. In addition, the 'errors' between the EFSODF oscillators and corresponding actual SSI systems are identified and corrected.

6.2 Code design spectra for soft soil profiles: problems and remedies

The preliminary design of typical building structures in current seismic design codes and provisions is mainly based on elastic spectrum analysis, where the base shear and displacement demands of yielding systems are estimated by using modification factors such as ductility reduction factor R_μ and inelastic displacement ratio C_μ, as explained in Section 5.2. These code-based design spectra and modification factors are usually derived by averaging the results of response-history analyses performed on simplified building models using a number of earthquake ground motions. It was also shown in previous chapters that the smoothed elastic design spectral shapes are usually defined by different soil types which are classified mainly according to $V_{s,30}$ (e.g., Figure 5.2 and Table 4.3). The fact that soft soil sites amplify the long-period components of an input motion results in an increased range of the flat portion (i.e., constant acceleration segment) of an elastic design spectrum for softer soil sites.

However, numerous studies have shown sharp peaks in response spectra for soft soil profiles rather than a flat shape. This inconsistency between averaged and individual response spectra is illustrated in Figure 6.1 for three different motions (used as free-field ground motions) recorded in the 1989 Loma Prieta earthquake.

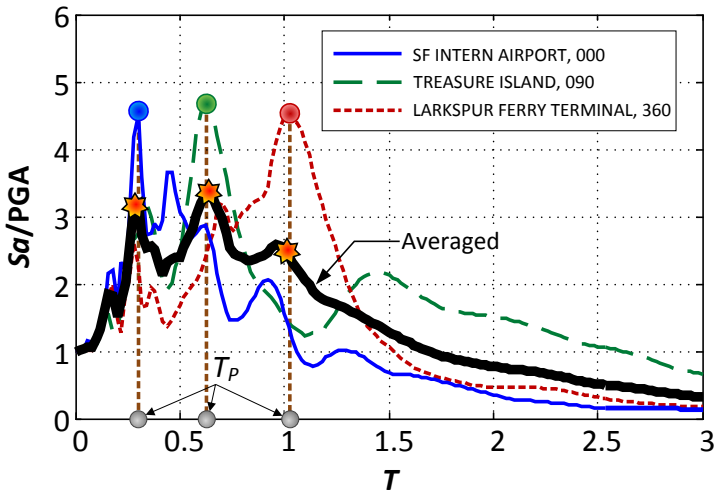

Figure 6.1: Averaging response spectra with peaks at separated periods reduces the peak responses.

It is shown that the response spectra for the three motions exhibit predominant peaks at vastly different periods. Averaging these spectra leads to significantly lower spectral ordinates compared to the individual spectrum. Xu and Xie (2004) and Ziotopoulou and Gazetas (2010) demonstrated that by using an elastic design spectrum in the format of Peak Response Acceleration (PRA) normalised with respect to the Peak Ground Acceleration (PGA) versus period T normalised with respect to the predominant period T_{P} corresponding to the maximum spectral acceleration, the peak of the mean spectrum could be preserved (see Figure 6.2). Moreover, the so-called bi-normalised Response Spectra (BNRS) exhibit much less dependence on soil types and epicentre distance when compared with those currently being adopted in various design codes.

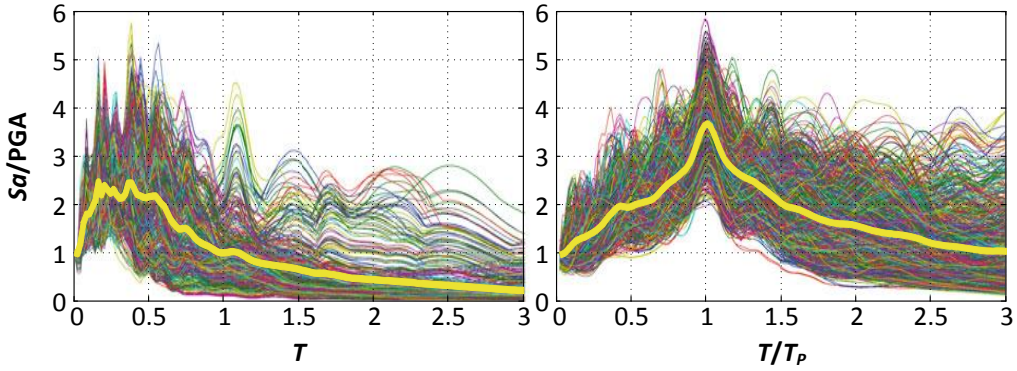

Figure 6.2: Comparison of conventional and bi-normalised response spectra presented in Ziotopoulou and Gazetas (2010).

Studies on inelastic seismic structural demands have also revealed that the inelastic response of structures on very soft soil sites can be significantly different to those corresponding to hard rock or firm sites. The strength and displacement demands of an inelastic system relative to those of an elastic system were strongly dependent on the ratio of the elastic structural period to a predominant period T_{g} (e.g., Miranda, 1993; Ruiz-Garcıa and Miranda, 2006). T_{g} can either be determined at the maximum ordinate of an input energy spectrum Se (5% damped) or the maximum value of the corresponding spectral velocity Sv. Both methods have proved to be valid (see, e.g., Miranda, 1991), as shown in Figure 6.3(a). 'Peaks' and 'valleys' were observed, respectively for the ductility reduction factor and the inelastic displacement ratio spectra, at a period ratio T/T_{g} approximately equal to one. Using 20 ground motions

recorded on very soft soil sites provided in Table 6.1, the averaged ductility reduction factor R_μ and inelastic displacement ratio C_μ for a 5% damped SDOF oscillator are well characterised in Figure 6.3(b).

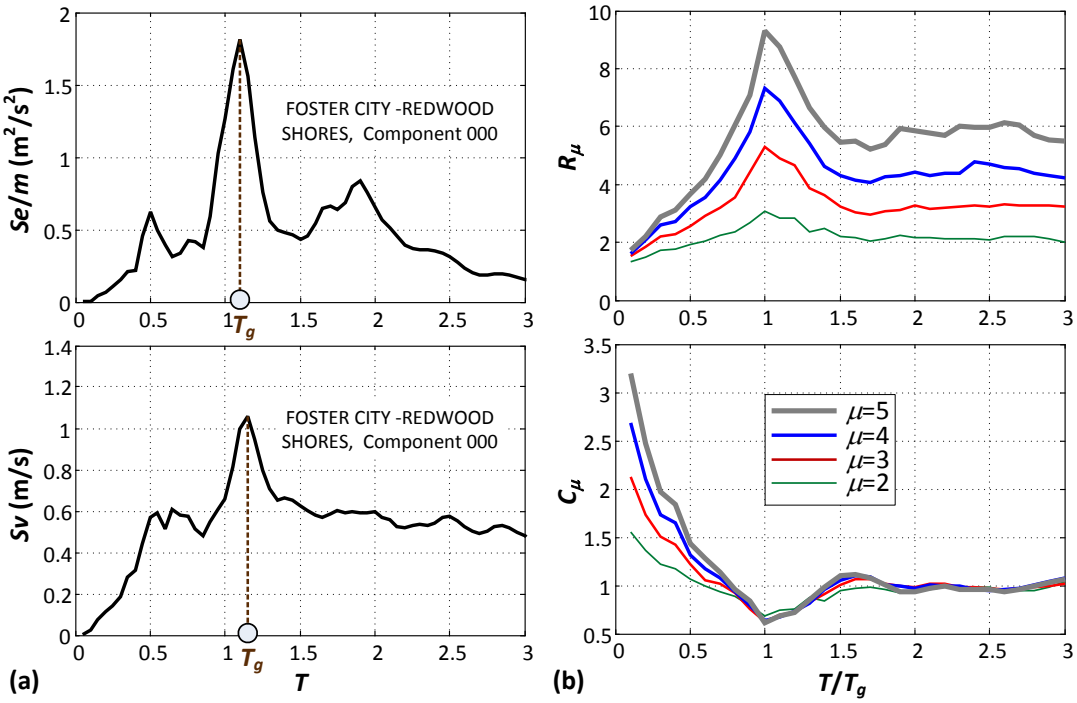

Figure 6.3: (a) Calculation of the predominant period T_g. (b) Normalising period against T_g preserves 'peaks' and 'valleys' of averaged R_μ and C_μ.

6.3 Nonlinear EFSDOF oscillator for estimating seismic response of soil-SDOF structure systems

The concept of using an equivalent fixed-base SDOF oscillator (EFSDOF) to capture the linear response of a soil-SDOF structure system was explained in Section 4.4. In this section, procedures for implementing the EFSDOF in performance-based design of flexible-base buildings are introduced. The EFSDOF oscillator is also extended to account for nonlinear structural response.

Figure 6.4 schematically illustrates how the EFSDOF oscillator approach can be

used to design flexible-base structures. For elastic systems, an SSI system shown in Figure 6.4(a) can be replaced by a fixed-base oscillator with $T_{\rm ssi}$ and $\xi_{\rm ssi}$ (see Figure 4.7) shown in Figures 6.4(b). As a result, the base shear and displacement demands of the flexible-base system can be obtained from a response spectrum derived for fixed-base structures with effective damping ratio $\xi_{\rm ssi}$ and elongated period $T_{\rm ssi}$ (or reduced initial stiffness $k_{\rm ssi}$).

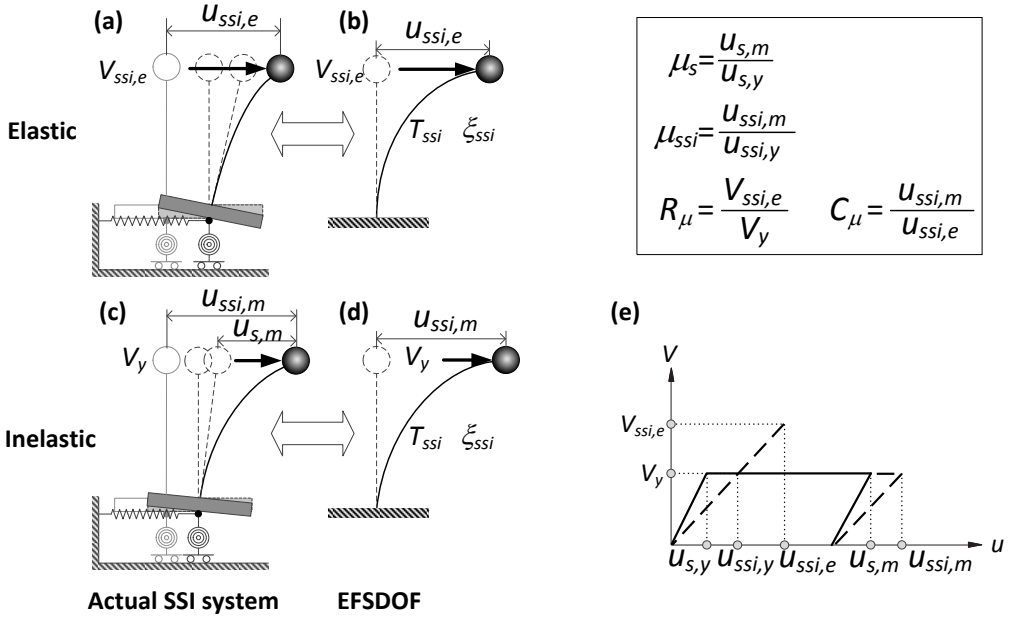

Figure 6.4: Relations between actual SSI systems and corresponding EFSDOF oscillators.

If the superstructure exhibits nonlinear deformations, the maximum seismic lateral force imposed on the structural mass of the SSI system will be equal to the base shear strength $V_{\rm y}$ of the superstructure. To measure the level of inelastic deformations, either the structural ductility demand or a global ductility demand can be used. The structural ductility demand $\mu_{\rm s}$=$u_{\rm s,m}/u_{\rm s,y}$ measures the degree of damage in the superstructure while the global ductility demand, defined as

$$\mu_{\rm ssi} = \frac{u_{\rm ssi,m}}{u_{\rm ssi,y}} \simeq \frac{u_{\rm ssi,m}\omega_{\rm ssi}^2 m}{V_{\rm y}} \tag{6.1}$$

measures the 'deformation' of the SSI system. In Equation (6.1), $u_{\rm ssi,m}$ and $u_{\rm ssi,y}$ are respectively the maximum displacement and yield displacement of the structural mass relative to ground. Based on the assumption that the energy dissipated by yielding of the SSI system (Figure 6.4(c)) is equal to that of the EFSDOF oscillator

(Figure 6.4(d)), the following relation between the global and structural ductility, with reference to Figure 6.4(e), can be obtained (Muller and Keintzel, 1982; Ghannad and Ahmadnia, 2002a; Avilés and Pérez-Rocha, 2003):

$$\mu_{\text{ssi}} = \left(\frac{T_{\text{s}}}{T_{\text{ssi}}}\right)^2 (\mu_{\text{s}} - 1) + 1 \tag{6.2}$$

There are two ways to interpret Equation (6.2): (1) it provides a relationship between the ductility demand of the structure itself and the global ductility demand of the entire SSI system; and (2) it implies that the base shear demand required for the actual flexible-base structure to achieve a ductility demand of μ_{s} is equal to that of the EFSDOF to achieve a ductility demand of μ_{ssi} under an equivalent seismic excitation. The latter interpretation actually signifies that the conventional spectrum-based design methodology for fixed-base structures holds for SSI system, simply by replacing T_{s}, ξ_{s} and μ_{s} with T_{ssi}, ξ_{ssi} and μ_{ssi}, respectively.

Before a EFSDOF oscillator can be implemented in design of an actual SSI system, two issues should be examined. Firstly, the EFSDOF oscillator serves as an approximation of the actual SSI system, its performance should be assessed under possible design scenarios. Secondly, the effect of damping on response spectra and modification factor should be considered, which is especially important when predominant periods are introduced.

It is worth mentioning that Ordaz and Pérez-Rocha (1998) investigated simultaneously the effects of damping ratio and frequency content of ground motion on ductility reduction factor of a SDOF oscillator with initial damping ratio ranging from 2 to 5%. They attributed the dependence of R_μ factor to the corresponding elastic spectral displacement Sd and the expected ductility demand μ:

$$R_\mu = 1 + \left(\frac{D(T, \xi, \mu = 1)}{\text{PGD}}\right)^\beta (\mu - 1) \tag{6.3}$$

where $D(T, \xi, \mu = 1)$ is the elastic spectral relative displacement, PGD is the peak ground displacement; and β, regressed against various ductility values ranging from 1.5 to 8 for different ground motion sets representing soft to firm sites, is expressed as:

$$\beta = 0.388(\mu - 1)^{0.173} \tag{6.4}$$

Note that the effects of initial damping and frequency content of motion are implicitly accounted for by the shape of the elastic displacement spectrum. Equation (6.4) was claimed to be appropriate for a damping ratio ranging between 2 and 10%. It can be seen from Equation (6.4) that the shape of R_μ versus T is similar to that of the elastic relative displacement spectrum. Therefore, the period T_g at which peak R_μ occurs coincides with that corresponding to the maximum spectral displacement.

Based on the concept of ESDOF, Equation (6.4) can be written for a flexible-base structure as:

$$R_{\mu,\mathrm{ssi}} = 1 + \left(\frac{D(T_{\mathrm{ssi}}, \xi_{\mathrm{ssi}}, \mu_{\mathrm{ssi}} = 1)}{\mathrm{PGD}}\right)^{\beta} (\mu_{\mathrm{ssi}} - 1), \quad \beta = 0.388(\mu_{\mathrm{ssi}} - 1)^{0.173} \tag{6.5}$$

More recently, Jarernprasert et al. (2013) proposed a simple formula for estimating the ductility reduction factor of flexible-base structures. Their work is based on a constant base shear demand spectrum corresponding to a mean ductility demand (Jarenprasert et al., 2006). The mean ductility demand μ_{mean} was calculated by averaging values obtained from all ground motions with a prescribed value of base shear V. By progressively reducing the base shear demand, they found that $\log(\mu_{mean})$ varied approximately linearly with $\log(V)$.

The proposed reduction factor R_{μ_s}, as a function of the structural ductility demand μ_s, equivalent natural period T_{ssi} and the period lengthening ratio $T_{\mathrm{ssi}}/T_\mathrm{s}$, was associated with a fictitious spectrum (referred to as the "unreduced spectrum" in Jarernprasert et al. (2013)) which corresponds to the intersections of the fitted straight lines (which approximate $\log(\mu_{mean})$ versus $\log(V)$) and the axis of μ_{mean}=1. The following expression was suggested to relate ductility and its reduction factor:

$$R_{\mu,\mathrm{s}} = (\mu_\mathrm{s}^{n(T_{\mathrm{ssi}})})^{(T_\mathrm{s}/T_{\mathrm{ssi}})} \tag{6.6}$$

where $n(T_{\mathrm{ssi}})$ is an inelastic modification factor of a fixed-base system, with its negative values representing the slopes of the fitted straight lines.

It should be mentioned that Equation (6.6) was derived by varying the values of $T_{\mathrm{ssi}}/T_\mathrm{s}$ from 1 to 1.5 with a constant slenderness ratio of $s \approx 2.5$. Looking back at Figure 4.7, a combination of $T_{\mathrm{ssi}}/T_\mathrm{s}$=1.5 and s=2.5 corresponds approximately to

an a_0 value of 2, which means that the maximum damping ratio of the entire SSI system ξ_{ssi} investigated by Jarernprasert et al. (2013) was less than 10%. However, T_{ssi}/T_s=1.5 could lead to more than 20% of ξ_{ssi} for structures with a slenderness ratio of s=1. Even if the standard requirement that the system damping ratio ξ_{ssi} should never exceed 20% (see Equation (2.15)) is considered, an initial system damping ratio greater than 10% may have a significant effect on the ductility reduction factor. Using Equation (6.6), therefore, should be justified in cases where squatty structures are located on very soft soil deposits ($\xi_{ssi} > 10\%$).

6.4 Bi-normalised response spectra for SSI systems

In this section, the effects of frequency content of ground motion and soil-structure interaction on elastic response spectra are investigated. A total of 20 ground motions recorded on very soft soil profiles are used, as presented in Table 6.1. In design of fixed-base structures, the pseudo-acceleration spectra are often adopted, since they are practically identical to the corresponding actual-acceleration spectra due to the fact that the damping force is usually very small compared with the restoring force for low damping ratios (e.g., 2-5%). However, when using a EFSDOF oscillator, the actual acceleration should be considered for design of base shear of flexible-base structures. This can be shown by the dynamic force equilibrium of the structural mass in the actual SSI system with reference to Figure 4.5:

$$(\ddot{u}_{ssi} + \ddot{u}_g) + 2\omega_s\xi_s\dot{u}_s + \omega_s^2 u_s = 0 \tag{6.7}$$

where the actual acceleration $(\ddot{u}_{ssi} + \ddot{u}_g)$ is very similar to the pseudo acceleration $\omega_s^2 u_s$. Formulating the equation of motion for the EFSDOF oscillator in 4.5 and replacing the subscript 'SDOF' with 'ssi' gives:

$$(\ddot{u}_{ssi} + \ddot{u}_g) + 2\omega_{ssi}\xi_{ssi}\dot{u}_{ssi} + \omega_{ssi}^2 u_{ssi} = 0 \tag{6.8}$$

In fact, in Equation (6.8), the actual acceleration $(\ddot{u}_{ssi} + \ddot{u}_g)$ could be significantly higher than the pseudo acceleration $\omega_{ssi}^2 u_{ssi}$ due to high damping (i.e., large values of ξ_{ssi}).

Table 6.1: Ground motions recorded on very soft soil profiles.

Date	Event name	Magnitude (Ms)	Station	Component (°)	PGAs (cm/s^2)
10/17/89	Loma Prieta	7.1	Foster City (APEEL 1; Redwood Shores)	0	263
				90	278
10/17/89	Loma Prieta	7.1	Larkspur Ferry Terminal	270	135
				360	95
10/17/89	Loma Prieta	7.1	Redwood City (APEEL Array Stn. 2)	43	270
				133	222
10/17/89	Loma Prieta	7.1	Treasure Island (Naval Base Fire Station)	0	112
				90	98
10/17/89	Loma Prieta	7.1	Emeryville, 6363 Christie Ave.	260	255
				350	210
10/17/89	Loma Prieta	7.1	San Francisco, International Airport	0	232
				90	323
10/17/89	Loma Prieta	7.1	Oakland, Outer Harbor Wharf	35	281
				305	266
10/17/89	Loma Prieta	7.1	Oakland, Title and Trust Bldg.	180	191
				270	239
10/17/89	Loma Prieta	7.1	El Centro Array 3, Pine Union School	140	261
				230	217
10/15/79	Imperial Valley	6.8	El Centro Array 3, Pine Union School	140	261
				230	217
04/24/84	Morgan Hill	6.1	Foster City (APEEL 1; Redwood Shores)	40	45
				310	67

Figure 6.5 compares spectral accelerations of actual SSI systems and EFSDOF oscillators. Two SSI systems are considered, with a_0=3, s=4 and a_0=2.5, s=1 representing respectively initial damping ratios of ξ_{ssi}=0.05 and 0.21. The spectral acceleration of the actual SSI systems was obtained by dividing the base shear demand by the mass of the structure (i.e., $V_{\max}/m=\omega_{\text{s}}^2 u_{\text{s,max}}$). As expected, for the highly damped system, using the pseudo acceleration of the EFSDOF oscillator underestimates the potential base shear demands. It is also observed that the spectral predominant period T_{P} is almost unaffected by the initial system damping ratio.

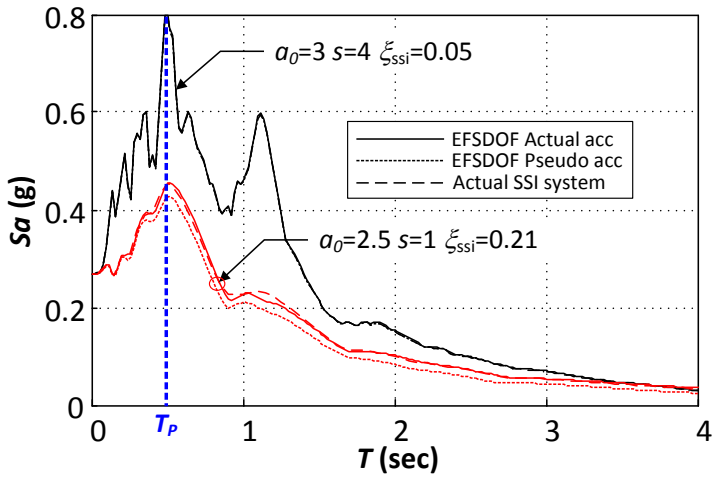

Figure 6.5: Comparison of spectral accelerations of actual SSI systems and EFSDOF oscillators for the 0° component of Loma Prieta earthquake at station Foster City (APEEL 1; Redwood Shores).

The average acceleration response spectra of the 20 selected ground motions (Table 6.1) is calculated for SSI systems with different damping ratios as shown in Figure 6.6. To avoid disregarding the frequency content of the ground motions, the results are also presented by using Bi-Normalised Response Spectrum (BNRS) curves. In Figures 6.6(a) and (b), the solid lines represent the actual SSI systems, whereas the dashed lines are the results obtained using the EFSDOF oscillators. The spectral acceleration (Sa) of an SSI system is again defined as $\omega_s^2 u_{s,max}$, while the spectral (actual) acceleration of the EFSDOF oscillator is obtained based on the response of a fixed-base SDOF system with equivalent damping ratio ξ_{ssi}. To calculate the bi-normalised response spectra, the predominant period T_P was measured for each earthquake record at its maximum spectral ordinate value. Since this period is almost unaffected by the initial damping level in the range of interest (i.e., ξ_{ssi}=5-20%), a value of T_P corresponding to 5% damping was used for all systems.

It is evident from Figure 6.6 that the conventional acceleration response spectra exhibit two subsequent peaks, whereas the BNRS curves reach a distinct peak value at $T_{ssi}/T_P \approx 1$. As discussed earlier, BNRS can provide more reliable results by taking into account the frequency content of the ground motions in the averaging process. The peak spectral ordinates of the BNRS for system damping ratios ξ_{ssi}=0.05, 0.1, 0.16 and 0.21 are respectively 1.22, 1.17, 1.13 and 1.11 times higher than those of

the conventional spectra. It should be noted that, by using more ground motion records, the spectral shape in Figure 6.6(a) would become more similar to those adopted by seismic codes where a flat segment is expected due to averaging and smoothing. In that case, the difference of the peak values between the conventional and bi-normalised spectra would be even more significant (Xu and Xie, 2004; Ziotopoulou and Gazetas, 2010).

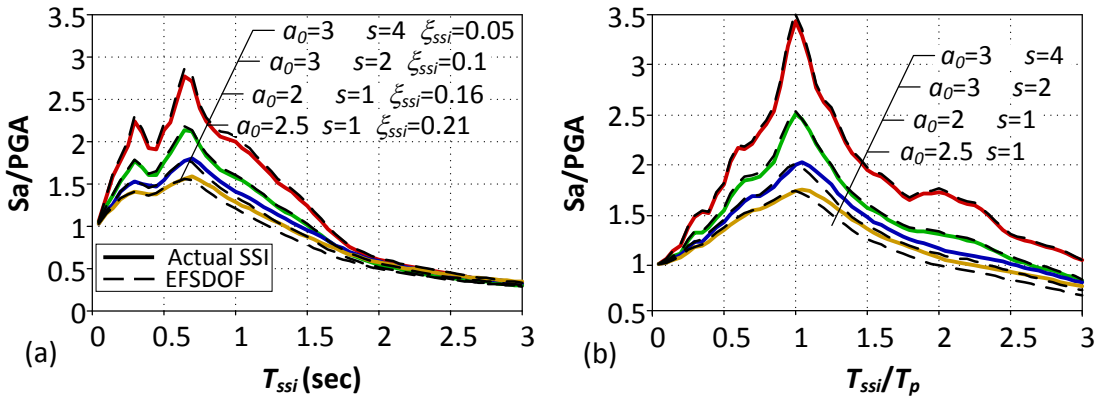

Figure 6.6: Elastic response acceleration spectra of flexible-base structures presented in (a) a conventional format and (b) a bi-normalised format.

It is also observed in Figure 6.6 that for systems with higher initial damping ratios (e.g., a_0=2 or 2.5 and s=1), the performance of the EFSDOF oscillators is not as satisfactory as for systems with lower damping ratios (e.g., a_0=3 and s=2 or 4), when $T_{\rm ssi} > 0.7$sec or $T_{\rm ssi}/T_{\rm P} > 1$. However, despite a maximum underestimation of about 10%, the results indicate that the EFSDOF oscillator can be practically used to predict the acceleration response of an elastic SSI system. As illustrated in Figure 4.7, for buildings having a slenderness ratio of $s \geq 2$ on very soft soil profiles (i.e., $\nu \approx 0.5$), the system damping ratio $\xi_{\rm ssi}$ is always less than about 10%. In other words, the EFSDOF oscillator can be applied to response spectrum analysis of SSI problems with practically no 'errors' for structural slenderness ratios exceeding 2, in comparison with the actual SSI system.

6.5 Ductility reduction factor and inelastic displacement ratio

Ductility reduction factor R_μ and inelastic displacement ratio C_μ, as described in previous sections, are currently used in many performance-based seismic design codes and provisions (ASCE, 2013; CEN, 2004) to estimate the seismic response of fixed-base non-linear structures subjected to earthquake excitations. The effect of SSI on R_μ, associated with the structural ductility demand, was investigated in Section 5.4 by using different values of structure-to-soil stiffness ratio a_0 and slenderness ratio s. Khoshnoudian et al. (2013) proposed a formula for C_R (=C_μ), mainly as a function of T_s (fixed-base structural period), a_0, s and R (=R_μ), to estimate the inelastic distortion of a SDOF structure located on soft soil profiles. In their study, C_R was calculated based on peak displacements excluding the rigid-body swaying and rocking motions of the foundation.

From Section 5.3, the effects of a_0 and s on structural response were shown to be attributed to the effects of T_ssi and ξ_ssi. Therefore, instead of using T_s, a_0, s and μ_s to characterise the properties of an SSI system, the following analyses will be performed by using different values of T_ssi, ξ_ssi and μ_ssi. By doing so, the performance of the EFSDOF oscillator can also be assessed. A number of actual SSI models were created by using various combinations of a_0 and s to achieve effective damping ratios ξ_ssi ranging from 5 to 20%. Correspondingly, the predominant period T_g was measured when the maximum ordinate of the corresponding relative velocity spectrum (for a damping ratio of ξ_ssi) occurred (see Figure 6.3).

Figure 6.7 compares the conventional and normalised R_μ and C_μ spectra derived by using both actual SSI models and EFSDOF oscillators. The a_0 and s values of SSI systems were chosen so that the effective system damping ratio ξ_ssi was approximately equal to 5%, which was then assigned to the EFSDOF oscillators. The results in Figure 6.7 are the averaged R_μ and C_μ spectra obtained for all 20 ground motions and are presented in both conventional and normalised formats. As expected from previous studies, the peaks and valleys are more noticeable by using the normalised

format (Figures 6.7(b) and (d)). For instance, normalised response spectrum curves indicate that, at a period ratio $T_{ssi}/T_g \approx 1$, the peak displacement of an inelastic system is on average smaller than its elastic counterparts (i.e., $C_\mu < 1$) while the ductility reduction factor R_μ is always maximum. This important behaviour is not obvious from the conventional response spectra shown in Figures 6.7(a) and (c).

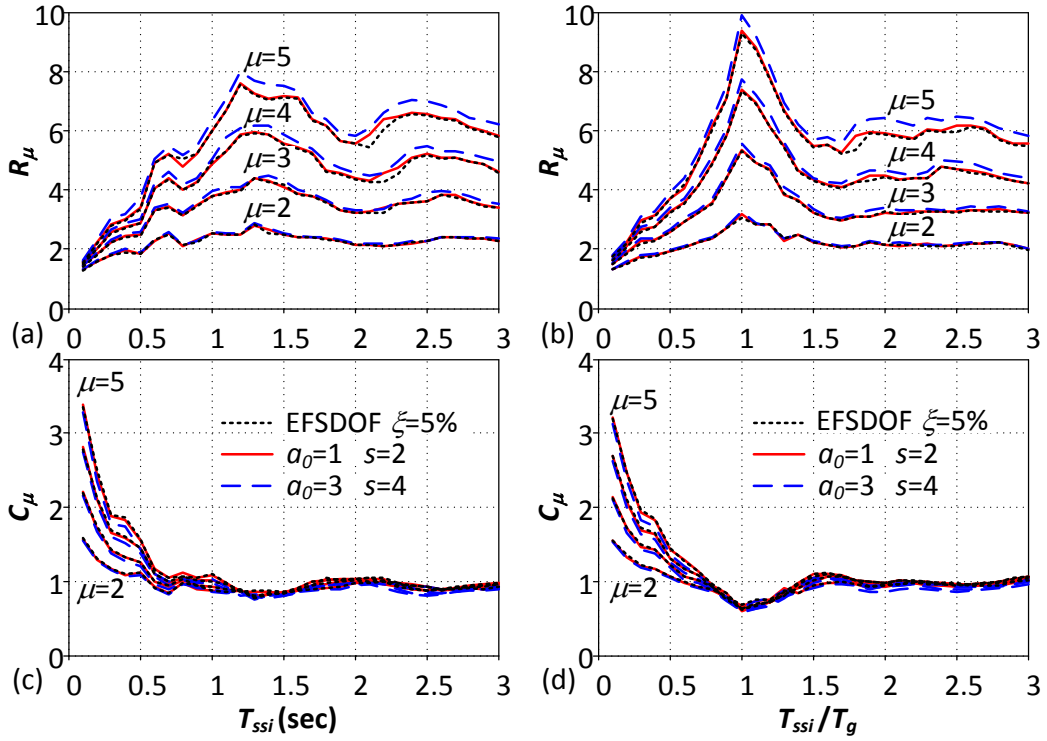

Figure 6.7: Comparison of ductility reduction factor R_μ and inelastic displacement ratio C_μ spectra obtained by using the simplified SSI models and the EFSDOF oscillators having a 5% damping ratio. Spectra are presented in both conventional (a, c) and normalised (b, d) formats.

It is shown in Figure 6.7 that the EFSDOF oscillator is, in general, able to provide a reasonable estimate of R_μ and C_μ for SSI systems. However, for slender structures and very soft soil conditions (e.g., a_0=3, s=4) where period lengthening becomes higher, the EFSDOF oscillator approach slightly underestimates R_μ, which consequently leads to an overestimation of C_μ, especially at higher global ductility demands. Since the EFSDOF oscillator works perfectly well in predicting the elastic response of the SSI system with a_0=3 and s=4 (see Figure 6.6(b)), the underestimation of R_μ could be a result of a higher strength predicted by the oscillator than

that required by the actual SSI system to satisfy a target ductility demand. As will be discussed in the following sections, due to a large period lengthening effect, a global ductility ratio μ_{ssi}=4 for an SSI system with a_0=3 and s=4 corresponds to an unexpectedly high structural ductility ratio $\mu_{\text{s}} > 10$, which is not used in common practice. Therefore, the results for higher global ductility demands are not considered important for practical design purposes.

For a higher effective damping ratio ξ_{ssi}=10%, shown in Figure 6.8, the performance of the EFSDOF oscillator is still excellent. However, in general, R_μ calculated by the EFSDOF oscillator approach is slightly higher than the values for the SSI models. The data in Figure 6.8 also includes results for an SSI system with a larger soil material damping ratio of ξ_{g}=10%, whose R_μ and C_μ are well predicted by the EFSDOF oscillator. Therefore, it can be concluded that the EFSDOF oscillator is a viable substitute for a lightly-to-moderately damped SSI system.

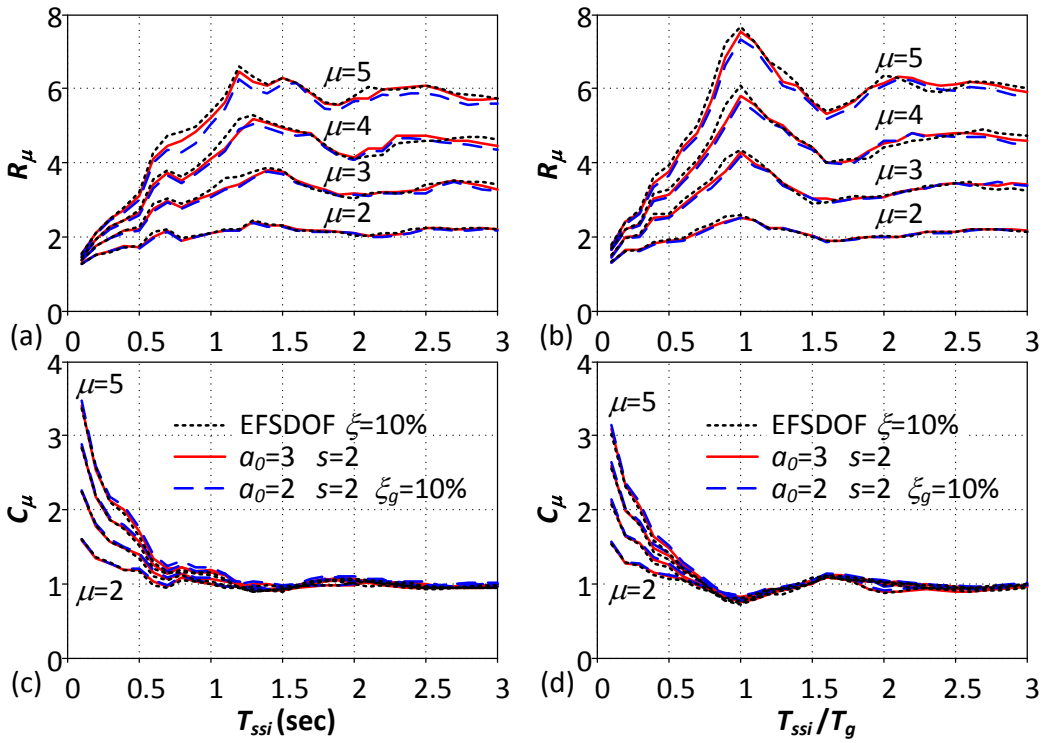

Figure 6.8: Comparison of ductility reduction factor R_μ and inelastic displacement ratio C_μ spectra obtained by using the simplified SSI models and the EFSDOF oscillators having a 10% damping ratio.

Figure 6.9 presents the results for a much higher initial damping ratio μ_{ssi}=20%, which is the upper limit of the overall damping of an SSI system suggested in seismic provisions. It is shown that the EFSDOF oscillators, on average, over-predict the ductility reduction factor R_μ, while they underestimate the inelastic displacement ratio C_μ of the corresponding SSI systems. For the normalised R_μ spectra shown in Figure 6.9(b), this over-prediction, which is up to 26%, is more pronounced when the $T_{\text{ssi}}/T_{\text{g}}$ ratio is smaller than 1.5.

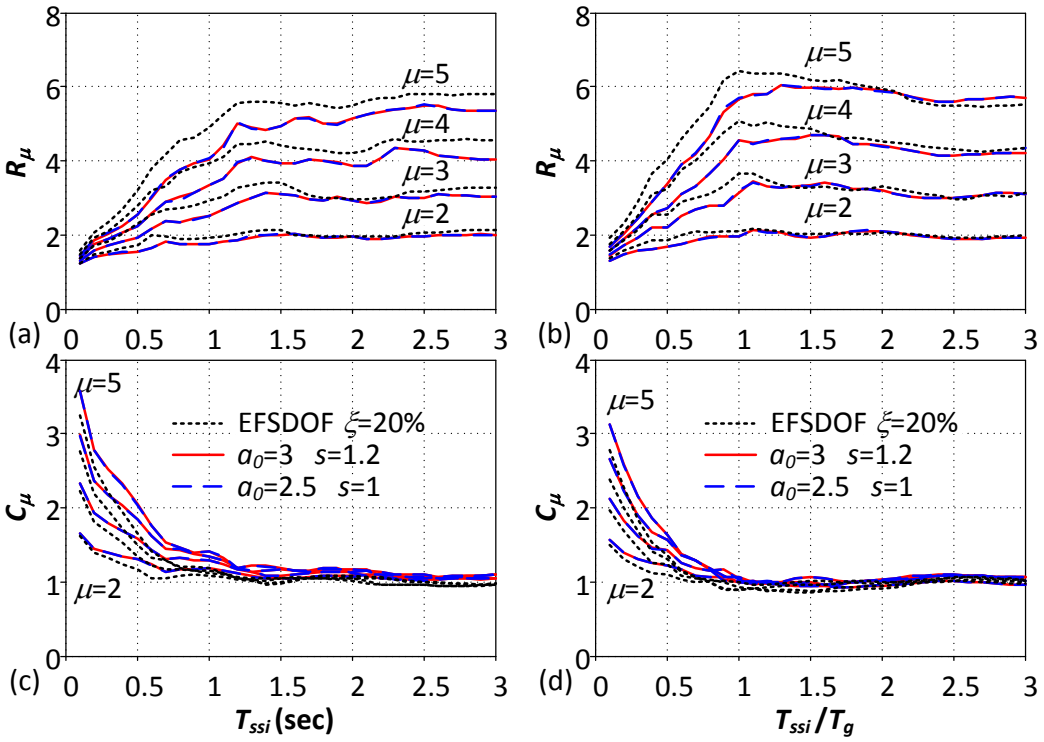

Figure 6.9: Comparison of ductility reduction factor R_μ and inelastic displacement ratio C_μ spectra obtained by using the simplified SSI models and the EFSDOF oscillators having a 20% damping ratio.

It is worth mentioning that although the EFSDOF oscillators are able to predict the peak response at $T_{\text{ssi}}/T_{\text{g}} \approx 1$ in the R_μ spectra shown in Figure 6.9(b), maximum R_μ values for the actual SSI models occur at a normalised period $T_{\text{ssi}}/T_{\text{g}}$ somewhat larger than one. This indicates that for highly damped systems, using T_{g} at which a SDOF oscillator attains its maximum spectral velocity may not be perfect for normalising the T_{ssi} for the actual SSI systems. The results for other values of damping ratio ξ are presented in Appendix B.2.

It can be concluded from the stated observations that the EFSDOF oscillators, over a wide normalised period range, over- and under-estimate, respectively, R_μ and C_μ values for SSI systems with a high initial damping ratio. Therefore, a correction factor can be introduced to improve the predictions of the EFSDOF oscillators for highly damped SSI systems. According to Figure 6.9, emphasis should be given to modifications that improve prediction of R_μ and C_μ by EFSDOF oscillators in the low-to-intermediate normalised period range while maintaining the use of T_g obtained using the EFSDOF oscillator. Note again that for common building structures having a slenderness ratio s greater than 2, the effective system damping ratio is always lower than 10% regardless of a_0 values (see Figure 4.7), which means that the EFSDOF oscillator approach can directly be applied to these structures without any modifications.

To improve the efficiency of EFSDOF oscillators to predict the seismic response of SSI systems, a correction factor α_ξ is defined in this section as the ratio of R_μ predicted by an EFSDOF oscillator ($R_{\mu,\mathrm{EO}}$) to that of an actual SSI system ($R_{\mu,\mathrm{ssi}}$) for a target global ductility demand. According to Equation (5.7), α_ξ can alternatively be expressed as the ratio of C_μ of the SSI model ($C_{\mu,\mathrm{ssi}}$) to that of the EFSDOF oscillator ($C_{\mu,\mathrm{EO}}$):

$$\alpha_\xi(T/T_\mathrm{g},\xi,\mu)=\frac{R_{\mu,\mathrm{EO}}(T/T_\mathrm{g},\xi,\mu)}{R_{\mu,\mathrm{ssi}}(T/T_\mathrm{g},\xi,\mu)}=\frac{C_{\mu,\mathrm{ssi}}(T/T_\mathrm{g},\xi,\mu)}{C_{\mu,\mathrm{EO}}(T/T_\mathrm{g},\xi,\mu)} \tag{6.9}$$

The ductility reduction factor ratios $R_{\mu,\mathrm{EO}}/R_{\mu,\mathrm{ssi}}$ were calculated for each of the SSI systems having ten different initial effective damping ratios varying from 11-20%. Figure 6.10(a) is an example of the results for SSI systems with a global ductility ratio μ_ssi=5. As expected, the correction factor increases with initial system damping level, and the averaged data exhibits, approximately, an ascending, a constant and a descending trend, respectively, in spectral regions $T_\mathrm{ssi}/T_\mathrm{g}<0.4$, $0.4\leq T_\mathrm{ssi}/T_\mathrm{g}<0.9$ and $T_\mathrm{ssi}/T_\mathrm{g}\geq 0.9$. Mean $R_{\mu,\mathrm{EO}}/R_{\mu,\mathrm{ssi}}$ ratios for ductility values from 2 to 5 are compared in Figure 6.10(b), which shows that in general, greater correction factor values should be applied to more ductile systems. Figure 6.10(b) also illustrates the mean α_ξ spectra derived using both ratios of $R_{\mu,\mathrm{EO}}/R_{\mu,\mathrm{ssi}}$ and $C_{\mu,\mathrm{ssi}}/C_{\mu,\mathrm{EO}}$, which are fairly similar and may be approximated by using the following simplified piecewise

expression that is also illustrated in Figure 6.10(b):

$$\alpha_\xi = \begin{cases} \dfrac{m-1}{0.4}\dfrac{T}{T_g}+1, & \dfrac{T}{T_g} \le 0.4 \\ m, & 0.4 < \dfrac{T}{T_g} \le 0.9 \\ \dfrac{m-1}{0.6}\left(1.5-\dfrac{T}{T_g}\right)+1, & 0.9 < \dfrac{T}{T_g} \le 1.5 \\ 1, & \dfrac{T}{T_g} \ge 1.5 \end{cases} \qquad m = \mu^{(0.12\ln\xi+0.3)} \tag{6.10}$$

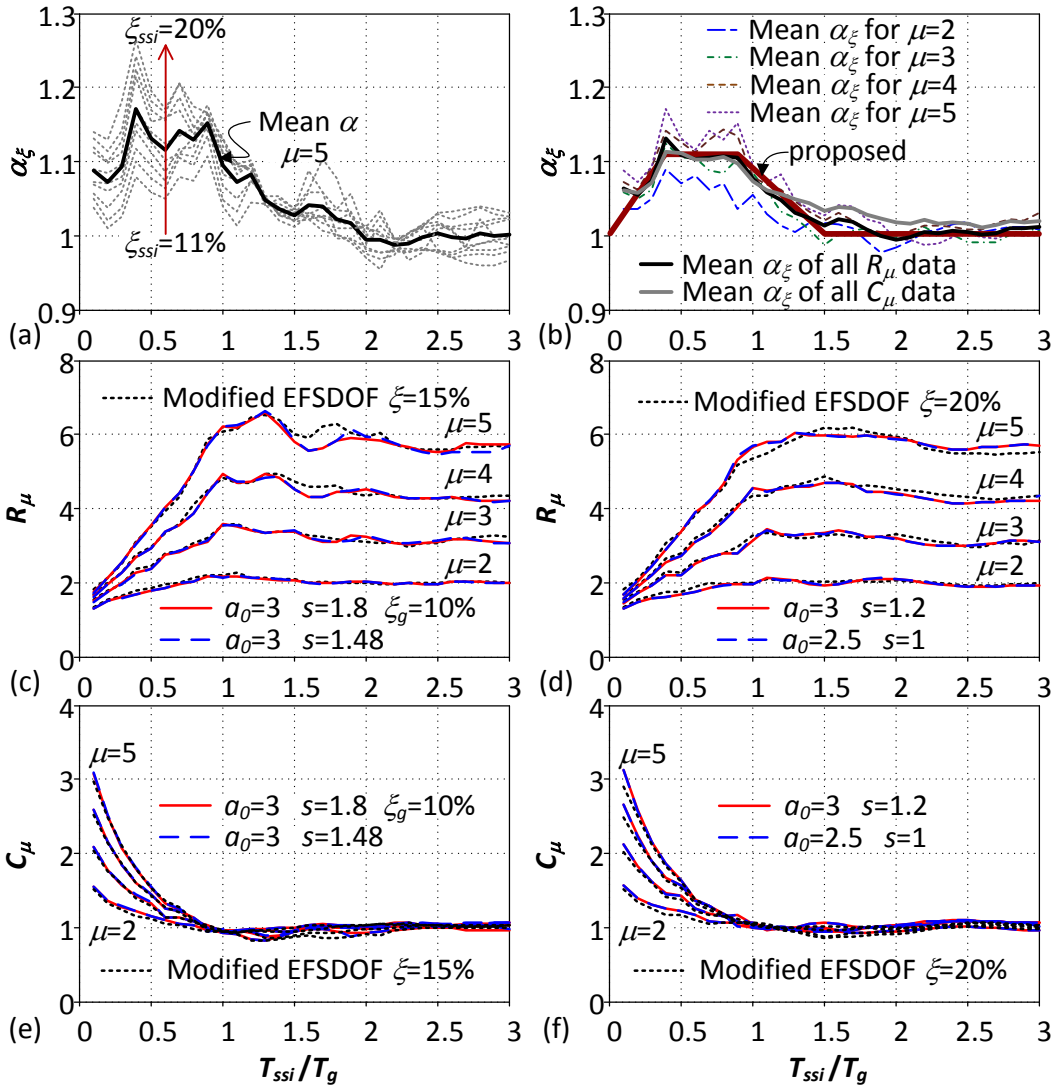

Figure 6.10: (a)-(b) Proposed correction factor α_ξ; and (c)-(f) improved performance of the EFSDOF oscillator approach for moderately to highly-damped SSI systems.

Figures 6.10 (c)-(f) demonstrate that R_μ and C_μ spectra derived using the correction factor α_ξ are in much better agreement with those for the actual SSI systems when compared to data in Figure 6.9.

The correction factor α_ξ proposed in this section provides a link between the R_μ and C_μ factors of the EFSDOF oscillators and those of the corresponding actual SSI systems. As mentioned in Section 6.3, Equation (6.5) may be used to calculated R_μ for the EFSDOF oscillator, and therefore C_μ can then be determined by Equation (5.7). To check the effectiveness of Equations (5.7) and (6.5), R_μ and C_μ spectra were derived using these equations for each of the selected 20 ground motions (Table 6.1) considering four values of ductility demand μ=2, 3, 4, 5 and three values of initial damping ratio ξ=5%, 10% and 20%. The mean response spectra are compared in Figure 6.11 with the results obtained by response-history analysis performed on EFSDOF oscillators, which were shown in Figures 6.7-6.9.

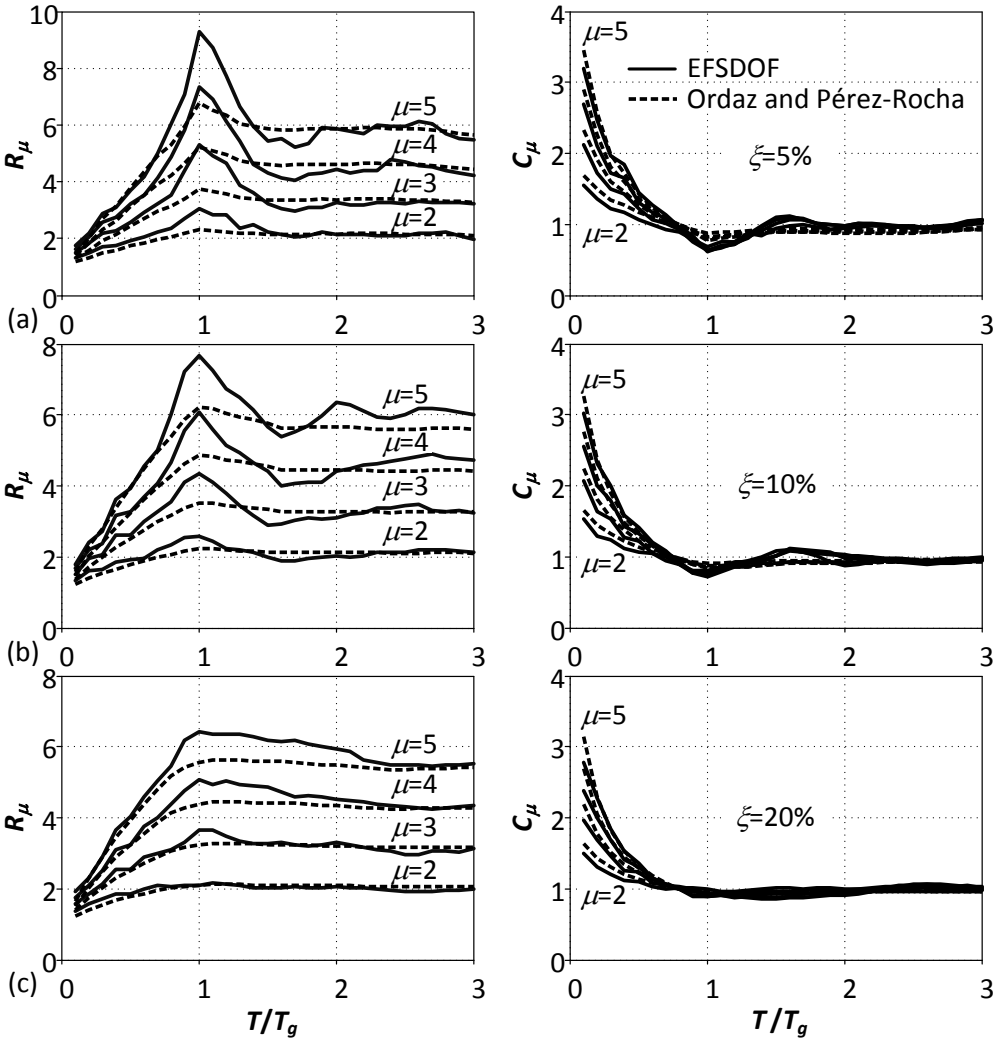

Figure 6.11: Comparison of normalised R_μ and C_μ spectra obtained using the EFSDOF oscillators with those derived by reduction rule proposed by Ordaz and Pérez-Rocha (1998) for initial damping ratios (a) ξ=5%, (b) ξ=10% and (c) ξ=20%.

Despite the fact that the peak responses of R_μ are not exactly reproduced (being underestimated), Equation (6.5) provides an excellent estimation of the variation of R_μ with the period ratio T/T_g. Although Equation (6.5) was suggested to be suitable for systems with an initial damping ratio less than 10%, it seems to work better for higher damping ratios (peaks are reduced) considering the 20 ground motions. Overall, Equation (6.5) is proved to be a useful reduction rule and can be applied in force-based design procedures. The under-prediction of the peak values of R_μ is in fact beneficial and conservative.

It should be mentioned that Ramirez et al. (2002) concluded that the effect of using different viscous damping ratios in the range of 5-30% on C_μ spectrum was insignificant. This conclusion seems to apply to the results for C_μ illustrated in Figure 6.11. However, the deviation of the 'valleys' in the C_μ spectra, as a result of variation of damping ratio, is not as visible as that of the 'peaks' in the R_μ spectra, due to the scale of the ordinate. For example, using 5% damping-based C_μ to calculate R_μ for a 20% damped system is unconservative (i.e., overestimate R_μ) for T/T_g close to one.

6.6 Structural and global ductility ratio

Although the global ductility μ_{ssi} relates the maximum displacement of an elastic SSI system to that of a yielding system, the structural ductility μ_s is sometimes more important since it directly reflects the expected damage in a structure (see Section 5.2). By using the global ductility μ_{ssi}, the structural ductility ratio μ_s can be calculated according to Equation (6.2). In order to evaluate the effectiveness of this Equation, the actual structural ductility ratios μ_s obtained by response-history analysis using the simplified SSI model (points) are compared with those calculated using Equation (6.2) (lines). The presented results are the average values for 20 earthquake records considering four global ductility values of μ_{ssi}=2, 3, 4, and 5.

In general, Figure 6.12 shows a good agreement between Equation (6.2) and the results of response-history analyses, especially for lightly-damped SSI systems whose

equivalent natural periods are close to their fixed-base systems (e.g., Figure 6.12(a)). For highly nonlinear structures, on the other hand, using Equation (6.2) leads to an overestimation of μ_s. This is in particular prominent for systems with a higher period lengthening effect shown in Figures 6.12(b), (c) and (e). However, it may not be important for common buildings that are usually designed for a structural ductility ratio less than 8. It should be noted that for a given global ductility value, the period lengthening effect is greater for structures with higher structural ductility ratio. Within the shaded areas representing the range of μ_s in design practice shown in Figure 6.12, μ_s correlates very well with μ_{ssi} by Equation (6.2).

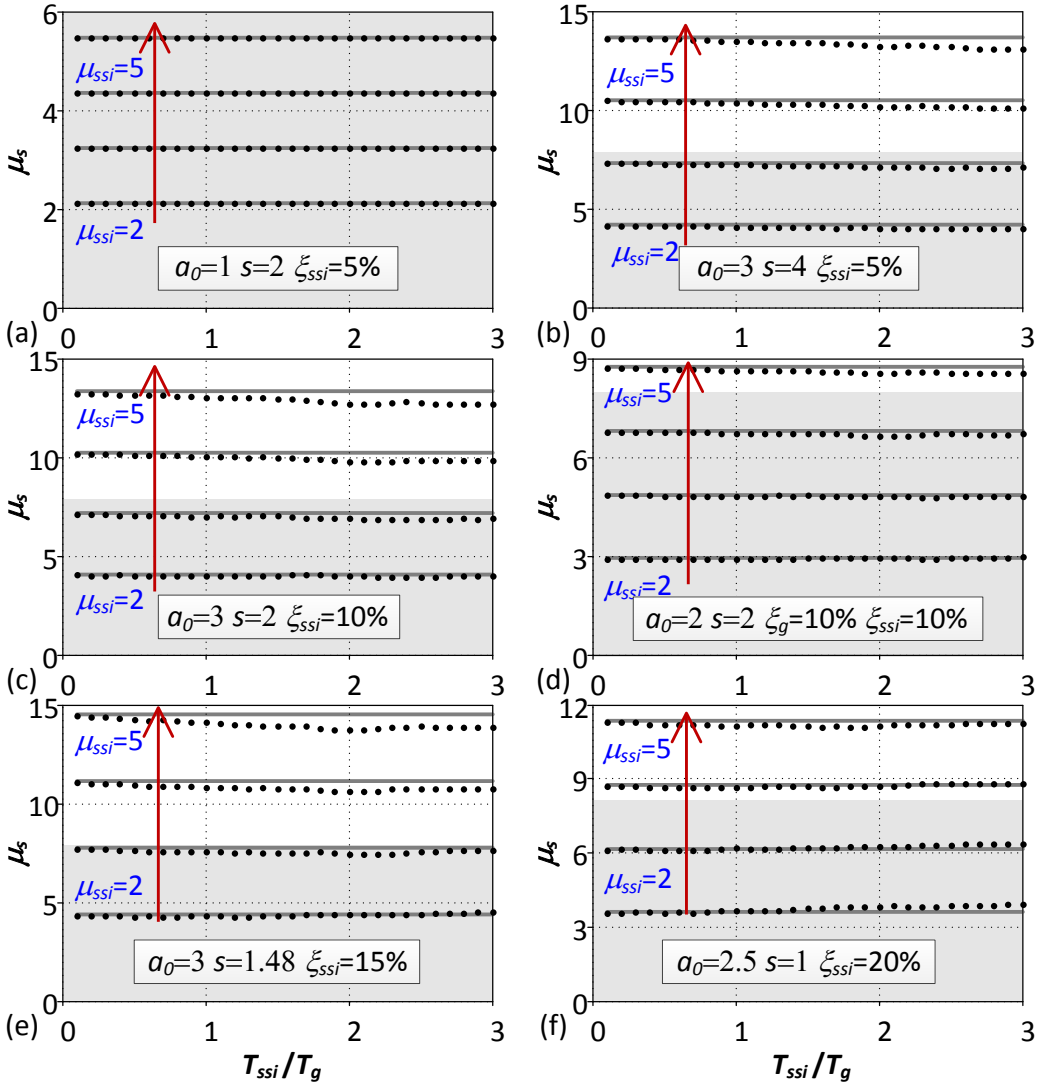

Figure 6.12: Comparison of structural ductility ratios μ_s obtained by response-history analysis using the simplified SSI model (points) with those calculated using Equation (6.2) (lines). Shaded areas represent the practical range of μ_s.

6.7 Summary

Several issues concerning the design of structures located on very soft soil profiles were investigated in this Chapter. A large number of response-history analyses were carried out by using a simplified soil structure interaction model to study the elastic and inelastic response spectra of buildings on soft soil profiles. Based on results for 20 ground motions recorded on very soft soil deposits, it was shown that normalising the equivalent period of an SSI system $T_{\rm ssi}$ by the corresponding predominant periods resulted in more rational spectra for seismic design purposes. In the elastic response spectra, $T_{\rm ssi}$ is normalised by the spectrum predominant period $T_{\rm P}$ corresponding to the peak ordinate of a 5% damped elastic acceleration spectrum, while for non-linear structures $T_{\rm ssi}$ should be normalised by the predominant period of the ground motion, $T_{\rm g}$, at which the relative velocity spectrum reaches its maximum value.

It was also shown that an actual SSI system could be replaced by an equivalent fixed-base SDOF (EFSDOF) oscillator having a natural period of $T_{\rm ssi}$, a viscous damping ratio $\xi_{\rm ssi}$ and a global ductility ratio of $\mu_{\rm ssi}$. The EFSDOF oscillator provided an excellent estimate of the elastic and inelastic spectra for lightly-to-moderately damped SSI systems. When using an EFSDOF oscillator, the actual acceleration should be considered for the response spectrum of flexible-base structures. It was shown that the EFSDOF oscillators, in general, overestimate the ductility reduction factor R_μ of SSI systems with high initial damping ratio (e.g. squatty structures founded on very soft soil profiles), which consequently leads to an underestimation of inelastic displacement ratio C_μ. Based on the results, a correction factor was proposed to improve the efficiency of replacement oscillators to predict the seismic response of SSI systems with effective damping ratio greater than 10%.

Finally, it was demonstrated that for any ground motion, the structural ductility demand of a nonlinear flexible-base structure can be calculated, with a desirable accuracy, from the global ductility demand of the whole SSI system. The EFSDOF oscillator can thus easily be implemented in the performance-based design of structures on soft soil with a target ductility ratio which is defined either for an SSI system or for the structure alone.

Chapter 7

A nonlinear sway-rocking model for seismic assessment of buildings on mat foundations

7.1 Introduction

Studies in Chapters 5 and 6 focused on the design of flexible-base nonlinear structures on the basis of the assumption that yielding in soil is not allowed to occur. However, nonlinearities in the soil (corresponding to large strains) and at the soil-foundation interface are almost unavoidable in strong seismic events. Moreover, a growing body of research suggests that soil nonlinearities may be beneficial to buildings and thus could be considered to be a design aspect (Anastasopoulos et al., 2010; Gazetas, 2015). It becomes increasingly important to incorporate this new concept into performance-based design methods. The objective of this chapter is to develop a nonlinear soil-foundation model that facilitates the analysis of soil-structure interaction in preliminary design stage. For this purpose, a simplified spring-type model is considered and its properties are calibrated against data obtained from a more comprehensive domain-type model.

7.2 Background and definition of the Problem

Recent studies on SSI have shown reduced seismic ductility demands of structures due to nonlinearity that arises mainly from the mobilisation of the ultimate capacity and the uplifting response of shallow foundations. These studies have mainly focused on stiff slender structures on small foundations, such as shear walls (e.g., Gajan et al., 2005), bridge piers (e.g., Ugalde et al., 2007; Anastasopoulos et al., 2013), and framed structures (e.g., Gelagoti et al., 2012; Chang et al., 2006) supported by spread footings. It has been found that the uplift of one side of the footing not only results in geometric nonlinearity at the soil-footing interface, but causes yielding of soil on the other side, which in turn increases the uplift. Allowing mobilisation of the foundation bearing capacity through soil yielding and foundation uplifting limits the maximum loads that can act on the superstructure, and also leads to a considerable amount of energy dissipation due to the hysteretic damping in the soil (Anastasopoulos et al., 2010).

On the other hand, structures supported on spread footings may experience unexpectedly high differential settlements during strong shaking. This phenomenon, induced by either heavy structural loads that are unevenly distributed across the footing, poor soil conditions, or the combination of both, can lead to failure of structural components and hence, non-repairable damage or collapse of structures (Anastasopoulos and Gazetas, 2007). Mat (or Raft) foundations, in these cases, are more suitable to spread the loads from the structure to the ground. Unlike the shear walls or bridge piers, structures supported on mat foundations are usually designed with a medium slenderness ratio. This leads to a strong interaction between the sway and rocking motions of the foundation when subjected to the horizontal component of strong ground motion.

It has been shown that nonlinearities in the soil (corresponding to large strains) and at the soil-foundation interface are almost unavoidable in strong seismic events (Figini et al., 2012). Performance-based seismic design methodology embraces these nonlinearities, provided that the responses of both structural and geotechnical components satisfy the performance targets. In this context, it is important to develop

reliable design tools that provide sufficient accuracy to assess the seismic performance of SSI while maintaining simplicity so as to be easily understood and accepted by engineers.

Using spring-type models to simulate the dynamic response of soil-structure systems is popular in design practice because of their ease of use and clear physical meaning (see Section 3.3). These models usually assume that the foundation soil is homogeneous, whereas in most cases the soil stiffness and strength increase with depth due to the effects of overburden stress. There is a lack of an effective and efficient spring-type model which is able to capture both nonlinear sway-rocking response of shallow foundations and soil non-homogeneity.

In view of developing a spring-type model for seismic design of buildings on soil that exhibits both nonlinearity and non-homogeneity, the problem should be well defined. The problem investigated in this chapter (Figure 7.1) is a seismically-excited building founded on a half-space consisting of saturated soft clay layers, where undrained shear strength s_u and stiffness G increase linearly with depth (Poisson's ratio ν and density ρ remain constant).

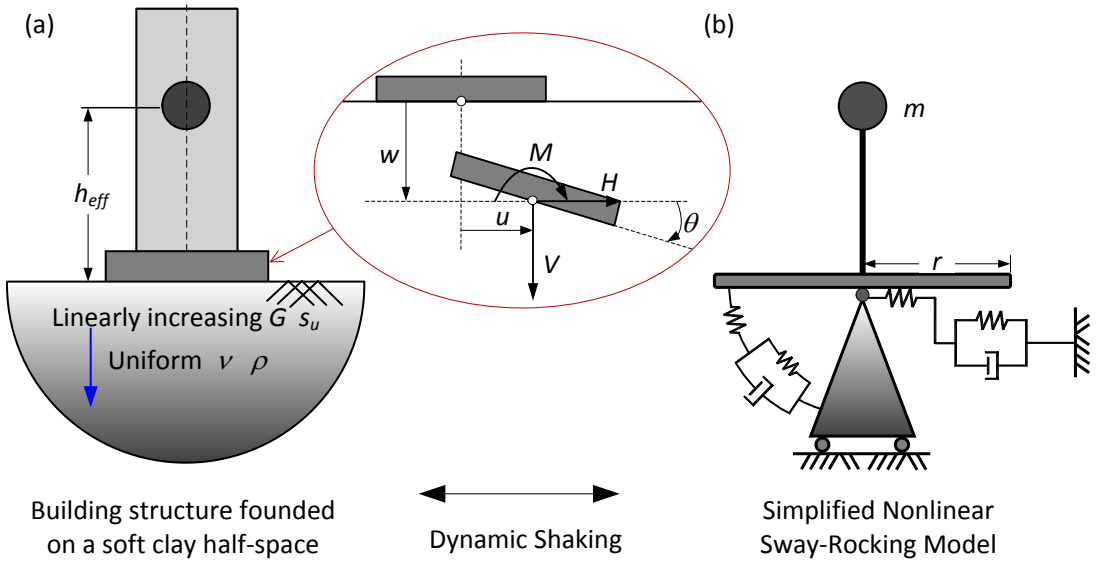

Figure 7.1: Problem illustration: (a) a seismically-excited building supported by a shallow foundation resting on a soil half-space; and (b) simplified nonlinear sway-rocking model consisting of an assemblage of springs and dashpots for simulating the seismic behaviour of the soil-foundation system.

The foundation is assumed to be rigid, which is appropriate for a mat foundation that is much stiffer than the soil. Foundation movements are described by the translations w (vertical) and u (horizontal) as well as rotation angle θ, which are correlated, respectively, with the forces V, H and moment M with respect to the base centre. The interface between the foundation and clay is assumed to sustain tension. This simplifying assumption is crude but uplifting will be left for future research. The overall SSI system is initially subjected to the self-weight V of the structure, followed by the radial load paths in the M-H plane representing the seismically loaded structures with a predominant mode of vibration.

Figure 7.1(b) displays the simplified nonlinear sway-rocking (NSR) model where the mass of the structure m is lumped at an effective height h_{eff} above a circular mat foundation with an equivalent radius $r{=}\sqrt{A/\pi}$, where A is the area of the foundation. In the NSR model, the soil half-space is replaced by an assemblage of springs and dashpots. The plastic spring (placed closer to the foundation) simulates the large-displacement behaviour of the soil-foundation system, whereas the spring and dashpot arranged in parallel are used to model, respectively, the small-displacement response and the radiation damping.

7.3 Modelling of a circular foundation on saturated clay under combined static loading

This section concentrates on modelling the static response of a circular foundation resting on an undrained clay deposit under combined loading. For this purpose, a three-dimensional finite-difference program FLAC^{3D} (2012) is used to simulate soil-foundation interaction. Data from analyses performed in this section will be used for developing the simplified NSR model in later sections.

7.3.1 FLAC^{3D} Model

FLAC^{3D} (2012) is a three-dimensional finite-difference program utilising an explicit Lagrangian scheme and the mixed-discretisation zoning technique that can be used to solve geotechnical problems where geo-materials undergo plastic flow.

In FLAC^{3D}, the basic calculation cycle involves iteration between solving the equations of motion at each grid-point (node) and the stress-strain constitutive equations for each zone (element). The finite difference method in FLAC^{3D} approximates each derivative in these equations using a fully explicit algebraic expression relating variables at specific locations in the coordinate system. At the beginning of each time step, the nodal velocities are derived based on the unbalanced forces and velocities calculated in the previous step, which are then used to derive new strain rates and stresses.

In a static problem, the final solution is obtained through a dynamic relaxation scheme where damping is introduced to absorb kinetic energy until the maximum unbalanced nodal force in the system falls below a limiting value, which implies that the system is in equilibrium or in steady-state flow. In FLAC^{3D}, the ratio of the maximum unbalanced force to the mean of applied total forces is used as the convergence criterion that allows users to define the desired tolerance of error.

FLAC^{3D} provides a built-in programming language (FISH) that enables users to write their own functions for the analysis. A variety of constitutive models are available in FLAC^{3D}, and in this study the linear-elastic perfectly-plastic model obeying the Tresca failure criterion (total stress analysis) and an associated flow rule were used to represent the saturated clay behaviour under undrained conditions.

As shown in Figure 7.2, the FLAC^{3D} model represents a circular foundation of diameter D resting on the surface of a cylindrical stratum of saturated clay defined by the undrained shear strength s_u, the shear modulus G=500s_u, and Poisson's ratio ν=0.49. Taking advantage of symmetry, only half of the model was considered in the analytical modelling. The undrained shear strength was assumed to increase

linearly with depth, which results in a profile described by:

$$s_{\mathrm{u}} = s_{\mathrm{u0}} + \kappa z \tag{7.1}$$

where s_{u0} is the shear strength at ground level and κ is the strength gradient with depth z. Note that G also increases at a gradient κ with depth, leading to a generalised 'Gibson' type stiffness profile (Gibson, 1967). The degree of non-homogeneity is measured by a dimensionless number:

$$\lambda = \frac{\kappa D}{s_{\mathrm{u0}}} \tag{7.2}$$

with λ increasing from 0 to 6, indicating a transition from homogeneous to increasingly heterogeneous soil conditions. Three values of λ were considered, with λ =0, 2 and 6 representing homogeneous, moderately non-homogeneous and highly non-homogeneous soil conditions, respectively.

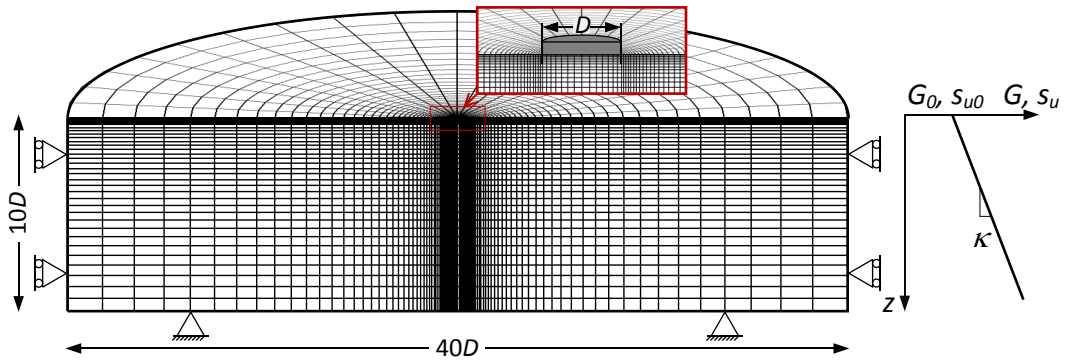

Figure 7.2: Finite-difference mesh showing a circular foundation resting on a saturated soil deposit having increasing shear modulus and undrained shear strength with depth.

The size of the soil grid (radius $20D$, depth $10D$) was selected in order to simulate a half-space condition of unbounded soil. Previous studies have shown that using dimensions which are just sufficient for predicting the foundation capacity (say, within 1% accuracy when estimating the vertical bearing capacity) may lead to 10-20% over-prediction of the initial foundation tangential stiffness (e.g., Bell, 1991; Gazetas et al., 2013). Therefore, the accuracy in prediction of the elastic foundation stiffness for homogeneous deposits was used as the criterion for selection

of appropriate grid dimensions. The static foundation stiffness (for uniform soil condition) in pure horizontal translation and rocking motions are respectively shown in Equations (3.11) and (3.12) while the vertical stiffness is given by (Poulos and Davis, 1974):

$$K_{\mathrm{v}} = \frac{2GD}{1-\nu} \tag{7.3}$$

Gazetas (1980) showed that soil non-homogeneity tends to reduce the 'depth of influence' in response to static vertical and horizontal forces as well as bending moment. This indicates that the grid size used for a homogeneous soil medium should also be valid for non-homogeneous conditions.

Both load-control and displacement-control methods were used to study the behaviour of the foundation using FLAC^{3D}. In the load-control analysis, the foundation was modelled with zones (Young's modulus E_{f}=$10^4 \times G$ and Poisson's ratio ν_{f}=0.2) that were separated from the soil using an interface modelled as a collection of linear spring-slider systems. To simulate a bonded interface, the tensile and shear strengths of the interface elements were assigned high values while the normal and tangential stiffness, k_n and k_t were calculated using the rule-of-thumb estimate recommended by Itasca (2012):

$$k_n = k_t = 10 \times \left[\frac{B + 4/3G}{\Delta w_{\min}}\right] \tag{7.4}$$

where B and G are the bulk and shear moduli of all zones adjacent to the interface and $\Delta w_{\min}$ is the smallest width of an adjoining zone in the normal direction. In this way, the relative displacement between the foundation and soil is mainly controlled by the stiffness and strength of the saturated clay. The load-control technique was used in the unidirectional loading tests to determine the load-displacement responses of the foundation under pure vertical or horizontal forces as well as bending moment.

Two sets of displacement-control tests were carried out in this study. In the first set of tests (referred to as DC-1), the foundation was not physically modelled but represented by the area of its base on the surface of the soil. Within the area, controlled displacements were applied to the nodes that were constrained in the horizontal direction to simulate the rigidity and roughness of the foundation. The

first set of displacement-control tests were used for identifying the load-displacement relations of the foundation in response to pure external loads and moments (results shown in Figure 7.4). The second set of displacement-control tests (referred to as DC-2) utilised the same foundation models used in the load-control tests (identical foundation and interface properties). In addition, in each of these tests, a stiff column was mounted on the foundation to simulate a relatively rigid superstructure, with a controlled horizontal displacement applied to the column at the effective height in accordance with a prescribed $M/(HD)$ ratio (Figure 7.3).

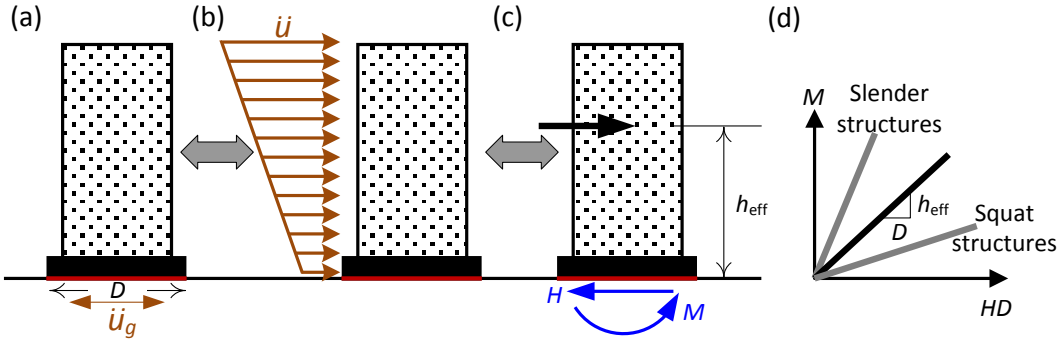

Figure 7.3: (a) Building subjected to horizontal varying ground acceleration; (b) induced acceleration in the building; (c) shear force and bending moment developed at base due to the equivalent seismic resultant inertial lateral force; (d) idealised seismic load paths.

When loaded to failure through a specific load path, the corresponding failure point of the foundation can be found. The failure envelope, defined as the closed surface where all possible failure points reside in the V:H:M space, can then derived from a number of tests conducted with different load paths.

7.3.2 Foundation force-displacement response

The tests to investigate the load-displacement characteristics of the foundation were first performed in a load-control fashion under a unidirectional loading condition. The controlled loading was specified by imposing nodal forces to the foundation at appropriate increments. The global forces V, H and moment M can be calculated

either by enforcing the equilibrium condition to the foundation or by evaluating the integral of the stresses over the area of the interface. Both approaches have been adopted to confirm consistency of results. A maximum allowable unbalanced force ratio of 1×10^{-6} was used as the convergence criterion.

To confirm the results of the load-control tests, an initial set of displacement-control tests (DC-1) was conducted in FLAC^{3D} by applying controlled uniform velocity (in order to simulate a rigid foundation) to the 'foundation nodes' on the surface of the soil half-space. The global forces were calculated as the integral of the accumulated unbalanced nodal forces, whereas the global displacements were evaluated as the integral of the velocity over the steps. A velocity of 3.3×10^{-8} D/step was used to obtain the vertical and horizontal response of the foundation while an angular velocity of 5×10^{-8} rad/step was used for analysing the rocking response. An advantage of using the displacement-control analysis is that there is no need to model the stiffness of the foundation or the interface, therefore the effect of these elements is not included in the DC-1 model results.

A good agreement between results from force- and displacement-control tests was found, as shown in Figure 7.4 which depicts the dimensionless load-displacement responses of the foundation on a homogeneous soil ($\lambda = 0$) under unidirectional loading. The dimensionless horizontal and vertical forces and the overturning moment are defined as $H/(As_{u0})$, $V/(As_{u0})$ and $M/(ADs_{u0})$, respectively. Numerical results shown in Figure 7.4 give a good match to the exact analytical values of 1.0, 6.05 and 0.67 (Gourvenec, 2007a). The dimensionless foundation stiffnesses for horizontal, vertical and rotational responses were calculated, using data from the DC-1 tests, to be: $H/(GDu)$=2.76, $V/(GDw)$=4.11 and $M/(GD^3\theta)$=0.68, which were within a 5% error compared with the exact analytical values of 2.65, 3.92 and 0.65 determined by Equations (3.11), (7.3) and (3.12), respectively. It was concluded that the parameters adopted for the foundation and interface stiffness in the load-control tests were appropriate given the good agreement obtained with the DC-1 results.

In a second set of displacement-control tests (DC-2), the path-dependent load-

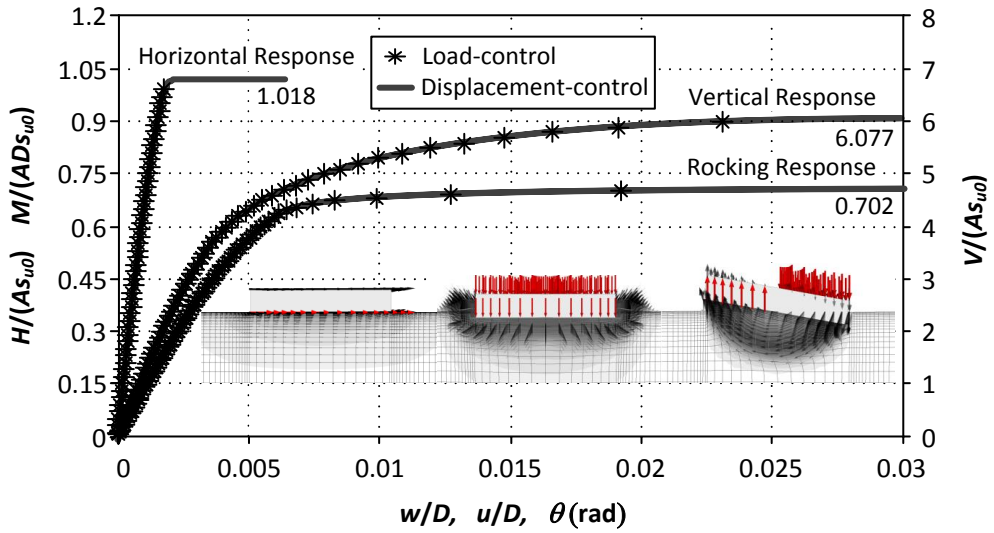

Figure 7.4: Force-displacement responses of a circular surface foundation on a homogeneous soil half-space under unidirectional loading in load-control and displacement-control (DC-1) tests.

displacement response was investigated through a series of push-over analyses. Letting V_{u}, H_{u} and M_{u} denote the ultimate foundation capacities due to the pure forces and moments in the load-control tests, the factor of safety against vertical bearing capacity failure FS_{V} is defined as the ratio V_{u}/V. In these displacement-control tests, a vertical downward velocity (1.6×10^{-8} D/step) was firstly applied to the nodes on the surface of the foundation and superstructure until the sum of the measured accumulated unbalanced nodal forces was, within 0.1% accuracy, equal to the desired vertical load level V for a given value of FS_{V}. Secondly, these unbalanced nodal forces were applied to the corresponding foundation nodes, whose degrees of freedom were then set free to achieve the load and stress state for the given FS_{V}. This was followed by the application of a horizontal displacement (at 3.3×10^{-9} D/step) to the height of the superstructure prescribed for a given moment-to-shear ratio $M/(HD)$.

Figures 7.5-7.7 present the push-over test results corresponding to different values of FS_{V}, moment-to-shear ratios and degrees of soil non-homogeneity. The tested range of moment-to-shear ratio $M/(HD)$ from 0.5 to 1.25 represents a typical building structure having a small-to-moderate slenderness ratio. It can be observed that the initial stiffness of the foundation (after applying the vertical load) reduces with

decreasing FS_V, especially for the rocking response (graphs (a)); whereas it is almost unaffected by the load ratio (graphs (b)). However, the variation of initial stiffness with FS_V is less significant when increasing the soil heterogeneity (i.e. increasing the λ value). The reduction of stiffness was the consequence of soil yielding during the first loading phase, where the penetration of the foundation into the underlying soil induced plasticity.

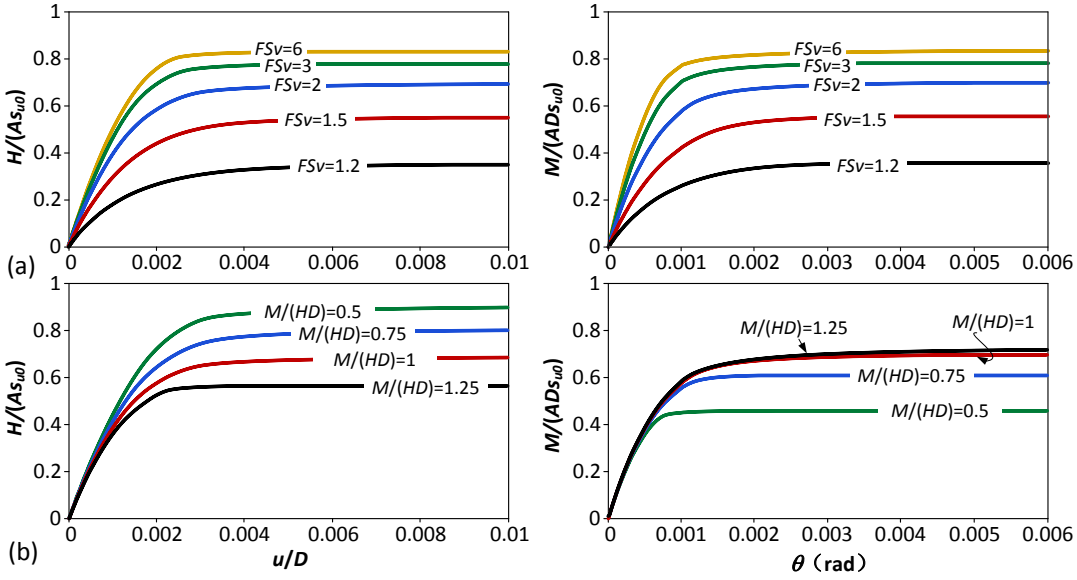

Figure 7.5: Push-over curves for the foundation on a homogeneous soil (λ=0) for (a) different FS_V with $M/(HD)$=1, and (b) different $M/(HD)$ with FS_V=2.

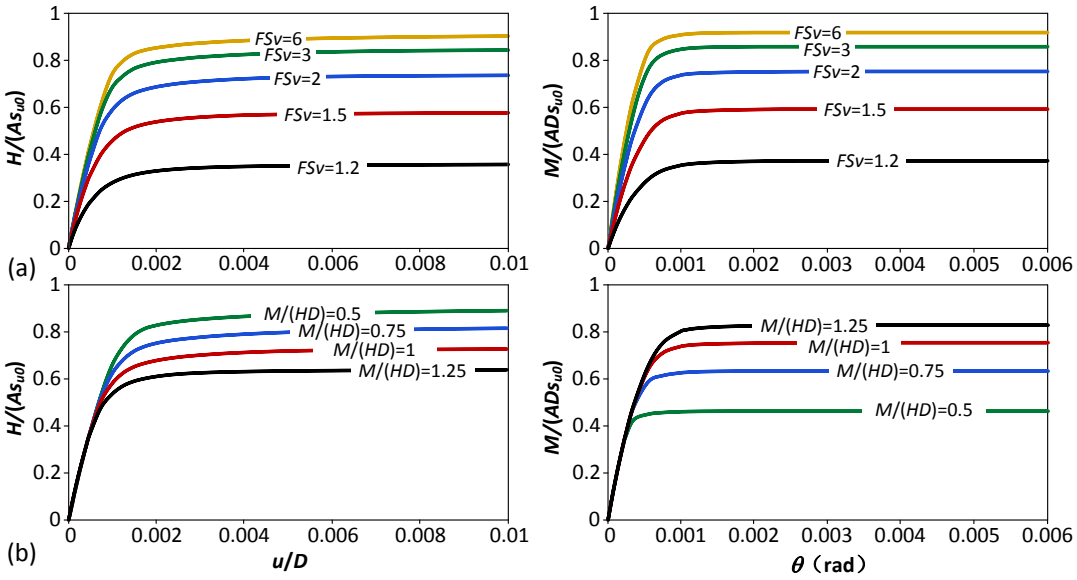

Figure 7.6: Push-over curves for the foundation on a homogeneous soil (λ=2) for (a) different FS_V with $M/(HD)$=1, and (b) different $M/(HD)$ with FS_V=2.

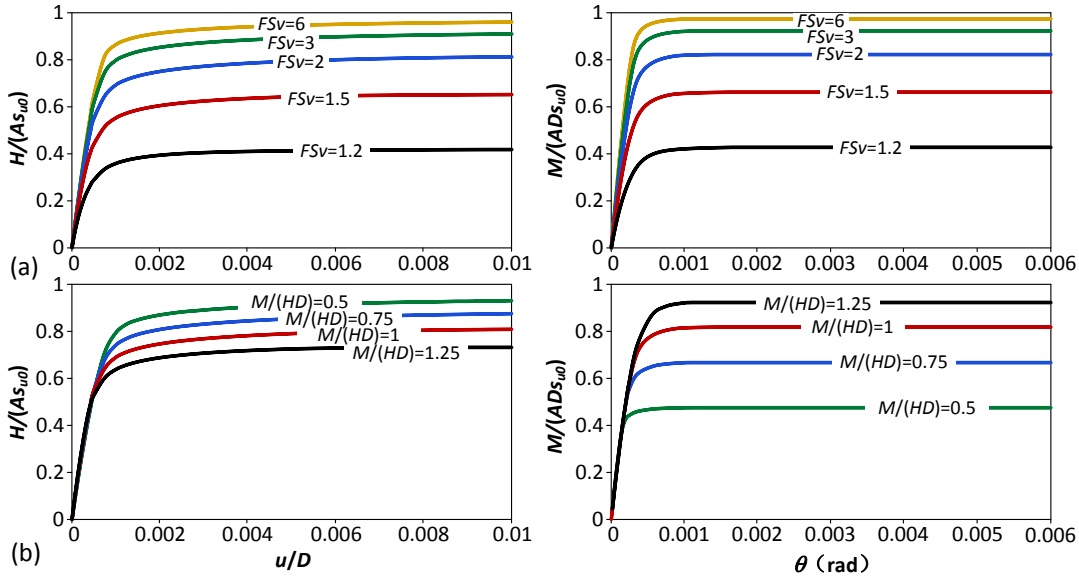

Figure 7.7: Push-over curves for the foundation on a homogeneous soil (λ=6) for (a) different FS_{V} with $M/(HD)$=1, and (b) different $M/(HD)$ with FS_{V}=2.

7.3.3 V:H:M Failure Envelope

Although the push-over tests enable the path-dependent load-displacement curve and the corresponding failure point to be obtained simultaneously, it is not a convenient way to develop the whole failure envelope representing the ultimate state of the foundation, simply due to the fact that each test can only determine a single point on the failure surface. Alternatively, a 'swipe' test may be introduced, where a single displacement-control test can yield a failure curve across the 3D failure surface. The 'side-swipe' test was proposed by Tan (1990) and has been adopted by various researchers to identify the failure envelope (e.g., Gourvenec and Randolph, 2003; Cassidy et al., 2002). This type of test is performed in the displacement space where the foundation is brought to failure by increasing the displacement in one direction u_1, followed by imposing displacement in the second direction u_2 while maintaining u_1 (i.e. Δu_1=0). During the second loading phase, the load in the first direction decreases with a reduction of the corresponding elastic displacement u_{1e}. This is accompanied by an increase in the plastic displacement u_{1p} to maintain the condition that Δu_1=0. As a result, the load path is believed to track close to the failure locus in the load space.

In order to evaluate the performance of the FLAC^{3D} model to predict the foundation ultimate capacity under combined loading, validation 'swipe' tests were carried out in the M:H plane. In these tests, the foundation was rotated to failure and then driven horizontally along the soil surface at a fixed angle of rotation. The general modelling considerations for the 'swipe' tests are similar to those described for the DC-1 tests. Figure 7.8(a) compares the 'swipe' test results with the finite-element results obtained by Gourvenec (2007a). The failure points obtained from the push-over analyses are also plotted to compare with the 'swipe' test results. The agreement between the three sets of results is fairly good. Figure 7.8(b) illustrates a 3D representation of the failure surface for the homogeneous soil condition, along with two of the preferred seismic load paths, in the normalised load space.

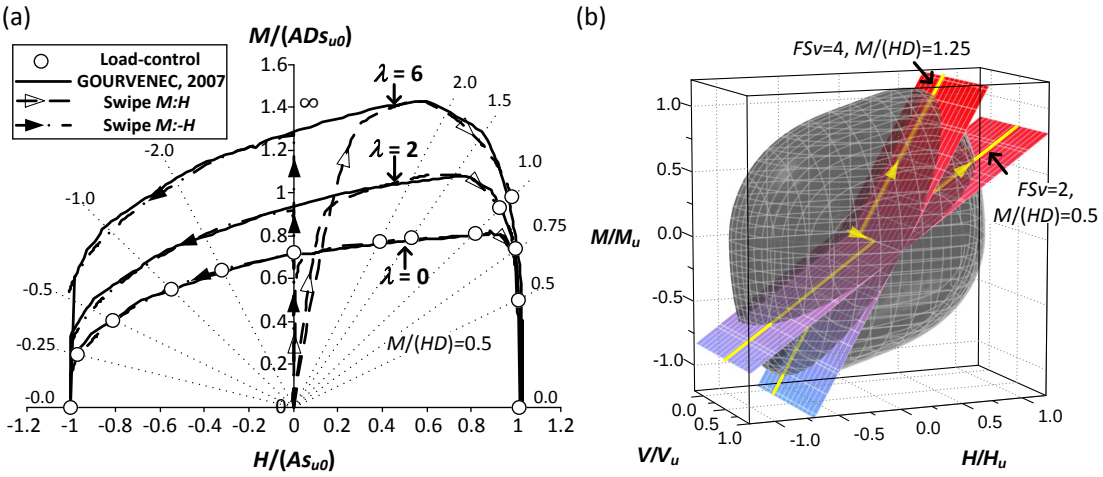

Figure 7.8: (a) Comparison of test results for the H-M interaction diagram of the failure envelope for FS_V=∞ and (b) 3D failure surface of the foundation (λ=0) and desirable load paths in the normalised V:H:M space.

Noting that the failure envelope shown in Figure 7.8 is not symmetric, a change in the sign of the gradients of the envelope in the H^+-M^+ (or H^--M^-) plane occurs at an abscissa that leads to the maximum moment capacity. According to the normality rule (associated flow rule), this change in the sign of $\partial M/\partial H$ at failure corresponds to a change of direction of the incremental plastic horizontal displacement of the foundation. This phenomenon is explained in Figure 7.9 that illustrates the foundation response under a constant load path of $M/(HD)$=1.25. Figure 7.9(a) shows a reversed (backward) translation at failure of foundations resting on a uni-

form soil deposit considering two safety factor values of FS_V=3 and 6; while for the non-homogeneous soil conditions, the foundation keeps moving forward at failure. Figure 7.9(b) depicts the flow directions of the foundation, which are normal to the failure envelope according to the normality rule. It should be mentioned that the 'zero gradient' abscissa is lower as a result of increased soil heterogeneity or reduced safety factor. In other words, lightly loaded slender structures on a homogeneous soil deposit are more prone to the reverse of foundation translation at failure. As a result, data for $M/(HD)$=1.25 with λ=0 and $FSv > 2$ have not been considered in developing the NSR model.

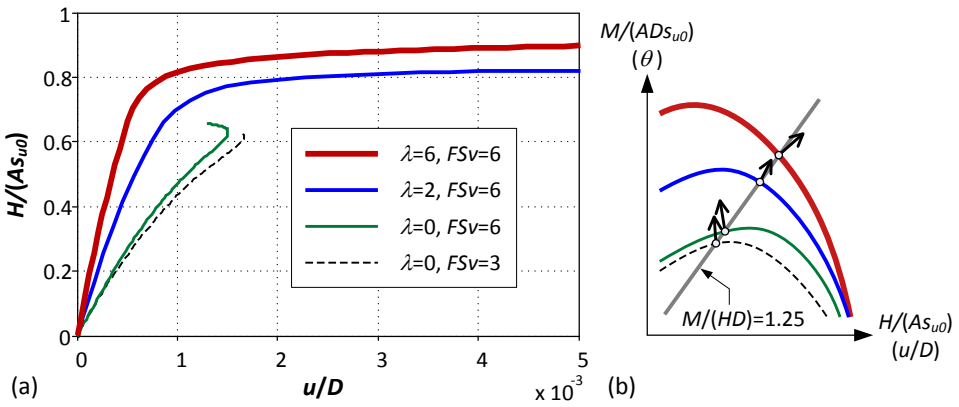

Figure 7.9: (a) Push-over curves showing the horizontal response of foundations loaded through a constant path of $M/(HD)$=1.25 and (b) flow directions of the foundations at failure.

7.4 Simplified NSR model

As described in Section 7.2, the NSR model consists of spring-dashpot systems capable of capturing the nonlinear sway and rocking responses of a shallow foundation. This section presents the mathematical formulations for characterising the behaviour of each model component as well as the model calibration procedures.

7.4.1 Model description

After reaching static equilibrium under vertical self-weight loading, the behaviour of the soil-foundation system in response to a small displacement is dictated by the initial stiffness k_{in}. Figures 7.5-7.7 showed that this stiffness drops as the safety factor FS_{V} decreases and that there is no significant degradation of the initial stiffness at low displacement levels. It is therefore assumed that the small-displacement response of the foundation, corresponding to either the sway or rocking degree of freedom, can be described using a linear relationship given by:

$$F = k_{\text{in}} u_{\text{e}} \tag{7.5}$$

where the global force F is calculated as the product of the initial stiffness k_{in} and the displacement u_{e}. The range of the linear portion of the load-displacement curve is defined by:

$$F_{\text{in}} = C_{\text{r}} F_{\text{c}} \tag{7.6}$$

where F_{in} is the global force when first entering the plastic cycle and C_{r} is the ratio of F_{in} to the capacity F_{c}.

The plastic component of the p-y springs developed by Boulanger et al. (1999) is adopted here to simulate the large-displacement response. The p-y springs were initially used in soil-pile interaction analyses to model the response of laterally loaded piles. In the NSR model, the plastic spring is assumed to be rigid when $|F| < F_{\text{in}}$ in virgin loading. This rigid range of $2F_{\text{in}}$ translates with plastic loading during which the nonlinear monotonic force-displacement curve of the plastic spring follows the relation:

$$F = F_{\text{c}} - (F_{\text{c}} - F_0) \left[\frac{c\, u_{50}}{c\, u_{50} + \left| u_{\text{p}} - u_{\text{p0}} \right|} \right]^n \tag{7.7}$$

where u_{p} is plastic displacement component; F_0 and u_{p0} are, respectively, the global force and plastic displacement at the start of the current plastic loading cycle; u_{50} is the total displacement (u_{e}+u_{p}) at which 50% of F_{c} is mobilised in monotonic loading; and c, n are constants that control the shape of the overall load-displacement curve of the foundation.

The radiation damping is assumed to be of viscous type and modelled through a

dashpot placed in parallel with the linear spring, while the hysteretic damping of the foundation is naturally accounted for by the nonlinearity embedded in the load-displacement behaviour during the loading-unloading-reloading cycles. Equation (3.15) may be used to calculate the upper-bound limit of the radiation damping coefficient. It should be noted that during strong shaking events, the radiation damping becomes negligibly small compared to hysteretic damping.

The global load-displacement behaviour of the foundation, shown in Figure 7.10, was implemented in OpenSees (2006) for each of the swaying (F, k replaced by H, k_{h}, respectively) and rocking (F, u, k replaced by M, θ, k_{θ}, respectively) responses. Detailed descriptions of the model components are provided by Boulanger et al. (1999) and Boulanger (2006).

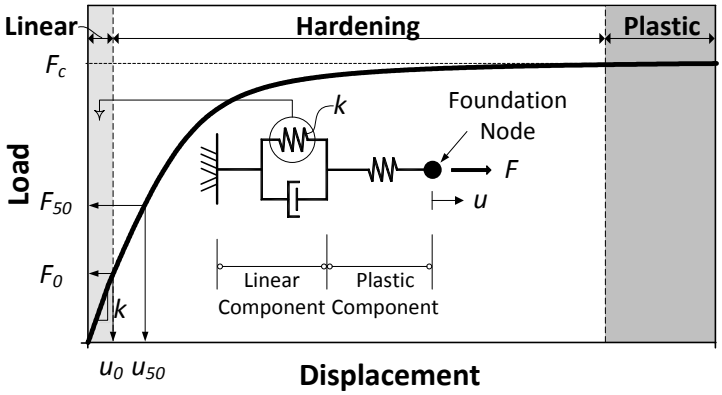

Figure 7.10: Nonlinear load-displacement response of a foundation modelled by the equivalent spring-dashpot system.

7.4.2 Model calibration

This section presents a description of the model calibration procedure that was performed utilising existing analytical and empirical expressions, as well as numerical results from the static FLAC^{3D} simulations. In practice, it is often required that a safety factor FS_{V} greater than 2 should be used to avoid excessive settlement; hence, results with FS_{V} less than 2 were not considered in the calibration.

7.4.2.1 Initial foundation stiffness

The initial swaying or rocking stiffness of the foundation corresponds to the condition where the vertical load V is fully developed during the construction and service period before any shaking takes place. It is convenient to express the initial stiffness k_{in} as a fraction of its purely elastic counterpart k (k_{h} and k_{θ} correspond to swaying and rocking degrees of freedom, respectively) as:

$$k_{\text{in}} = \alpha\left(FS\text{V}, \lambda\right) k \tag{7.8}$$

where α_{k} ($\alpha_{\text{k,h}}$ and $\alpha_{\text{k},\theta}$ correspond to swaying and rocking motions, respectively) is a stiffness loss factor which is a function of FS_{V} and λ. The variation of α_{k} with FS_{V} for different soil heterogeneity is depicted in Figure 7.11 for the swaying and rocking motions. The data shows that the rocking stiffness drops more significantly than the swaying stiffness when reducing the factor of safety FS_{V}.

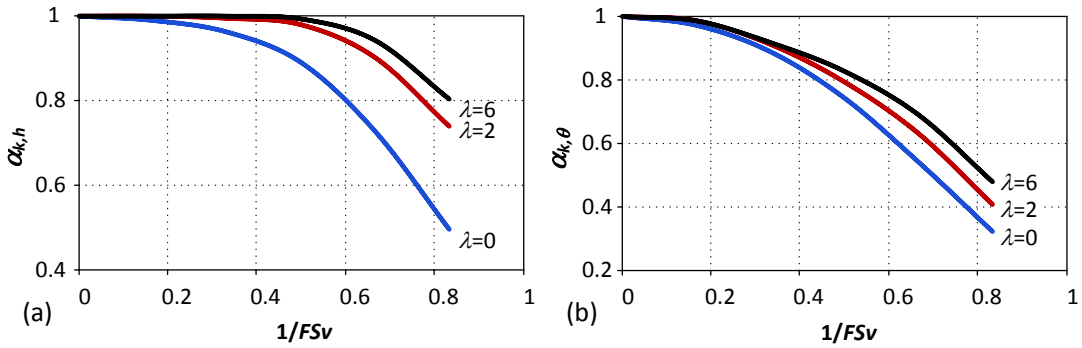

Figure 7.11: Variation of initial foundation stiffness with vertical load safety factor for (a) swaying and (b) rocking responses.

Considering the fact that the purely elastic foundation stiffness k in Equation (7.8) should also be a function of soil heterogeneity, k can be written as:

$$k_{\text{h}} = \chi_{\text{h}}\left(\lambda\right)\frac{4G_0 D}{2-\nu} \quad k_{\theta} = \chi_{\theta}\left(\lambda\right)\frac{G_0 D^3}{3\left(1-\nu\right)} \tag{7.9}$$

where G_0 is the small strain shear modulus of the soil at ground level and χ is a dimensionless influence factor that takes into account the effect of soil non-homogeneity. Note that for a uniform soil condition (i.e., λ=0), χ equals one and Equation (7.9) reduces to Equations (3.11) and (3.12). A number of investigations

have been carried out to study k_{h} and k_{θ} for surface foundations on non-homogeneous soil deposits (e.g., Gazetas, 1980; Wong and Luco, 1985; Waas et al., 1985; Waas et al., 1988; Hadjian and Luco, 1977; Booker et al., 1985). Some of these studies found that the swaying stiffness is more sensitive to the rate of non-homogeneity λ whereas the rocking stiffness is less affected (Gazetas, 1980; Waas et al., 1988; Hadjian and Luco, 1977). Based on these studies, Gazetas (1991) proposed the following empirical expressions for estimating χ, where the subscripts h and θ refer to swaying and rocking, respectively:

$$\chi_{\mathrm{h}}(\lambda) \approx 1 + 0.22\lambda \quad \chi_{\theta}(\lambda) \approx 1 + 0.15\lambda \tag{7.10}$$

It should be mentioned that most of the stated studies on which Equation (7.10) is based assumed a drained soil condition by using a constant Poisson's ratio of ν=0.25 or 0.33. Results from this study, however, show that under an undrained condition ($\nu \rightarrow$0.5), the rocking stiffness experiences a larger increase than the swaying stiffness when soil non-homogeneity increases. Figure 7.12 compares the variation of the influence factor χ predicted in this study with those estimated using Equation (7.10) for two values of Poisson's ratio ν=0.25 and 0.49.

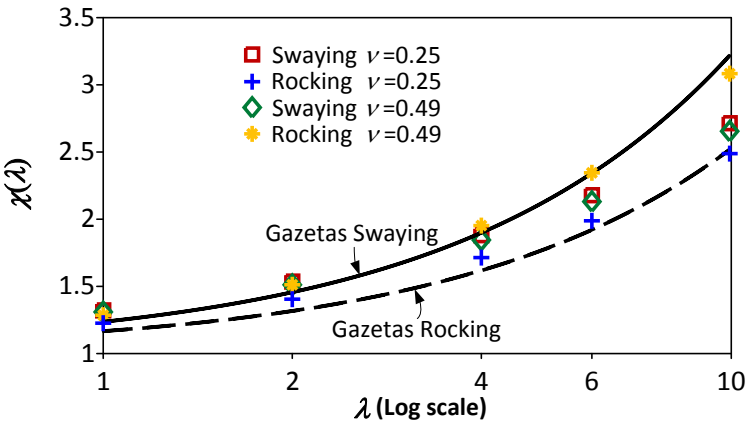

Figure 7.12: Effect of soil non-homogeneity and Poisson's ratio on elastic swaying and rocking stiffnesses.

The comparison demonstrates that for a wide range of heterogeneity ($1 < \lambda < 10$), the variation of the swaying stiffness is practically independent of Poisson's ratio ν, while the rocking stiffness increases more rapidly in an undrained condition than in a drained condition. Similarly, Carrier and Christian (1973) observed that for

a rigid circular surface foundation lying on a generalised 'Gibson' soil half-space, the vertical stiffness increases much faster with heterogeneity for higher values of Poisson's ratio. It can be concluded that the variation of foundation stiffness with soil heterogeneity for the vertical and rocking motions is much more sensitive to Poisson's ratio than for the swaying response. Figure 7.12 also illustrates that Gazetas's expressions for χ work reasonably well for estimating the swaying stiffness for $\lambda \leq 4$, while underestimating the undrained rocking stiffness. It should be noted that in application of the proposed model to dynamic loading, the frequency dependence of the stiffness and radiation damping was ignored since the emphasis was given to the post-yield response of the foundation where large displacements were expected to occur. In the developed NSR model, the initial foundation stiffness was evaluated by applying the values of α_{k} and χ obtained from the FLAC^{3D} analyses and illustrated in Figures 7.11 and 7.12, respectively, to Equations (3.11) and (3.12), that are the analytical solutions of k_{h} and k_{θ} for uniform soil conditions.

7.4.2.2 Coupled bearing capacity

The coupled shear and moment capacities H_{c} and M_{c} correspond to the intersection between the load path and the failure envelope in the load space. Gourvenec (2007a) proposed that the normalised moment capacity $M_{\mathrm{c}}/M_{\mathrm{u}}$ could be approximated as cubic or quartic polynomials with respect to $1/FS_{\mathrm{V}}$:

$$\frac{M_{\mathrm{c}}}{M_{\mathrm{u}}} = \sum_{i=1}^{p} c_i \left(\frac{1}{\mathrm{FSV}}\right)^{i-1} \tag{7.11}$$

where p=4 for $M_{\mathrm{c}}H_{\mathrm{c}} > 0$ and p=5 for $M_{\mathrm{c}}H_{\mathrm{c}} < 0$, c_i are polynomial coefficients given in Gourvenec (2007a) for a number of discrete values of normalised moment-to-shear ratios $M_{\mathrm{c}}/(N_{\mathrm{cM}}H_{\mathrm{c}}D)$ and non-homogeneity index λ. N_{cM} is the ultimate moment capacity coefficient defined as the ratio of $M_{\mathrm{u}}/(ADs_{\mathrm{u0}})$. Since the base shear and moment induced by the horizontal ground accelerations always act in the same direction (see Figure 7.1 for sign convention), only the cubic polynomial expression (p=4) in Equation (7.11) is necessary for calculating the moment capacity.

7.4.2.3 Hard-coded shape parameters

The shape of the nonlinear backbone curve for shallow foundations is mainly controlled by the parameters C_r, c and n, the initial foundation stiffness, ultimate capacity, and the displacement corresponding to 50% of the capacity (u_{50}). Although C_r specifies the range of the linear segment of a backbone curve, the push-over curves in the numerical tests do not possess a strictly linear portion. This scenario is shown in Figure 7.13, where secant foundation stiffness k_{sec}, normalised by its initial value, is plotted against the mobilised strength (H and M) normalised by corresponding ultimate values (H_c and M_c).

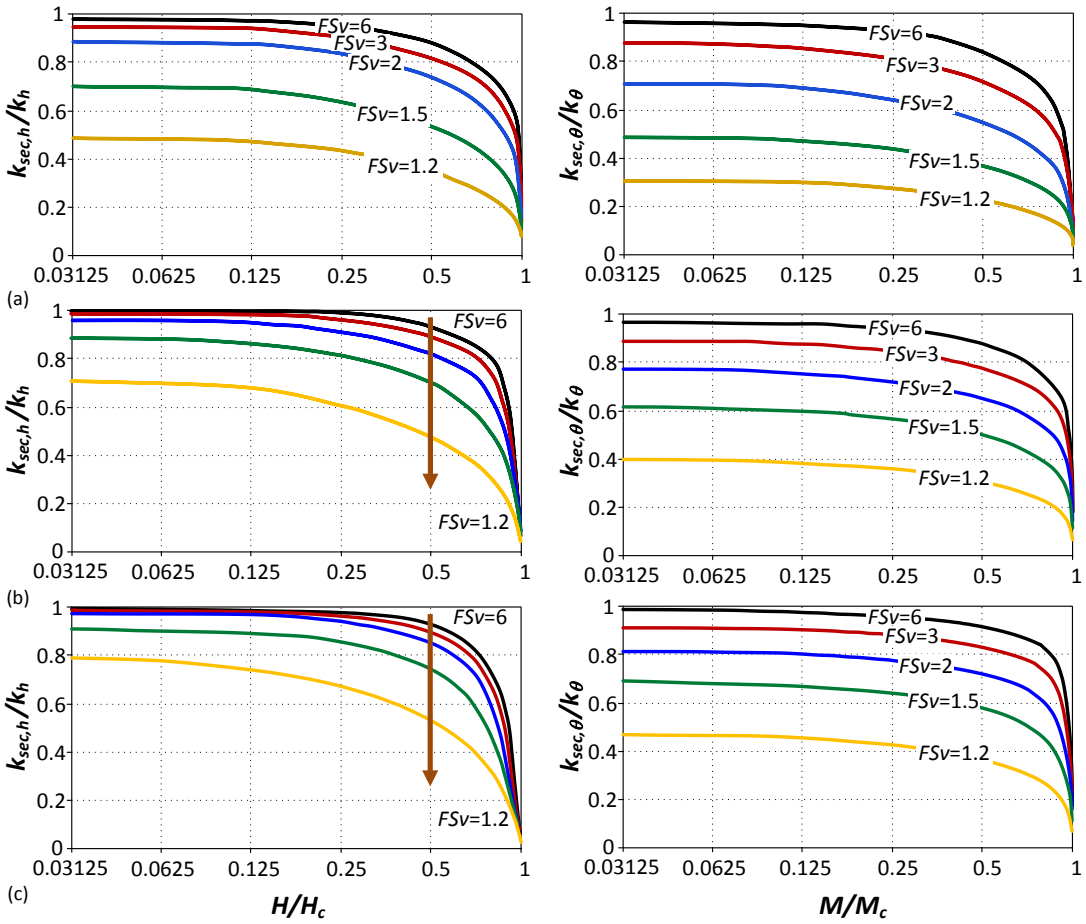

Figure 7.13: Variation of secant foundation stiffness with mobilised foundation load level for (a) λ=0, (b) λ=2 and (c) λ=6.

As seen in Figure 7.13, the foundation stiffness gradually reduces with increasing load level. This reduction, however, is not significant when the horizontal load and

moment are (approximately) lower than 0.125 of their ultimate values. Therefore, this value was used as the linear range for C_r in the current model. The reference displacement u_{50} can be related to a dimensionless parameter c_{50} defined as (Raychowdhury, 2008):

$$c_{50} = \frac{k_{in} u_{50}}{F_c} \tag{7.12}$$

c_{50} was calculated for each of the finite-difference push-over analyses (λ=0, 2, 6; FS_V=2, 3, 6; $M/(HD)$=0.5, 0.75, 1.0, 1.25) according to Equation (7.12) and are presented in Figure 7.14. It was found in this study that the calculated c_{50} values were not significantly affected by FS_V, $M/(HD)$ and λ. For example, the mean and standard deviation (SD) of c_{50} for the swaying response were 0.562 and 0.027; for the rocking response they were 0.561 and 0.042. Therefore, the mean values of c_{50} were hard coded into the model.

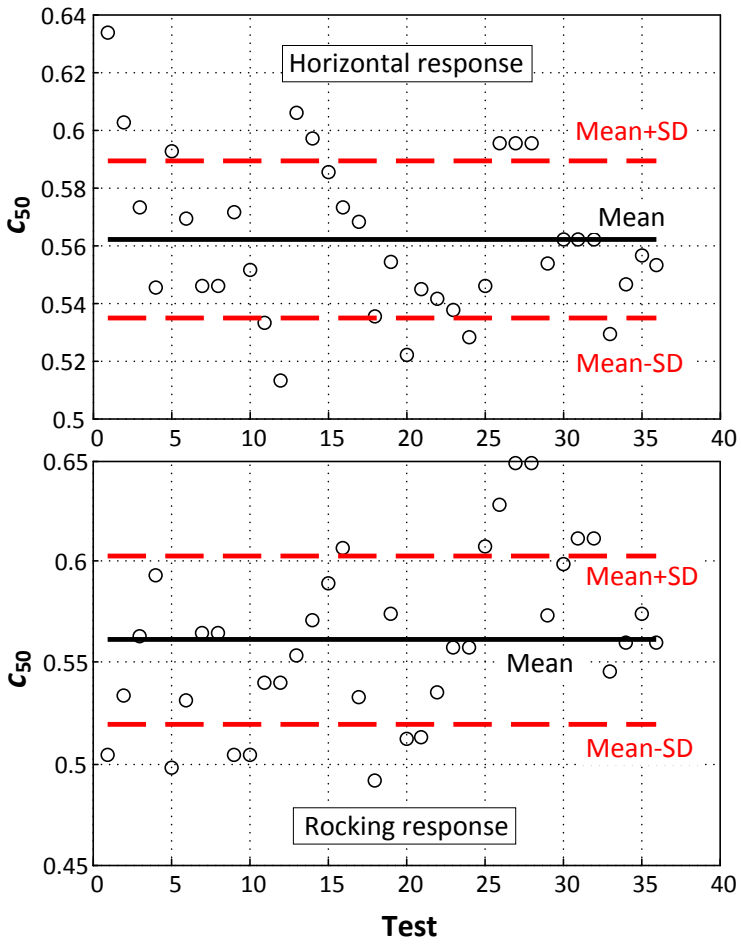

Figure 7.14: Scattering of c_{50} for various combinations of λ, FS_V and $M/(HD)$.

By normalising the load and displacement with respect to F_c and u_{50}, respectively, the data of the backbone curves for various λ, FS_V and $M/(HD)$ were narrow banded, as shown in Figure 7.15. Calibration of c and n were then carried out by identifying the 'best fit' values, which minimised the 'error' between the analytical (Equations (7.5) and (7.7)) and the numerical backbones. For this purpose, the force residuals were calculated over all displacement points and were squared to measure the error (Raychowdhury, 2008). It should be mentioned that when fitting the curves, the normalised displacements u/u_{50} from the FLAC^{3D} simulations were imported as the total displacements. If the calculated force F (Equations (7.5) and (7.6)) was greater than $C_r F_c$, F should be solved implicitly using Equation (7.7) where iterations were required. The 'best fit' values of c and n for the swaying response were identified to be 0.11 and 0.85, respectively; and for the rocking response, 0.35 and 1.9, respectively

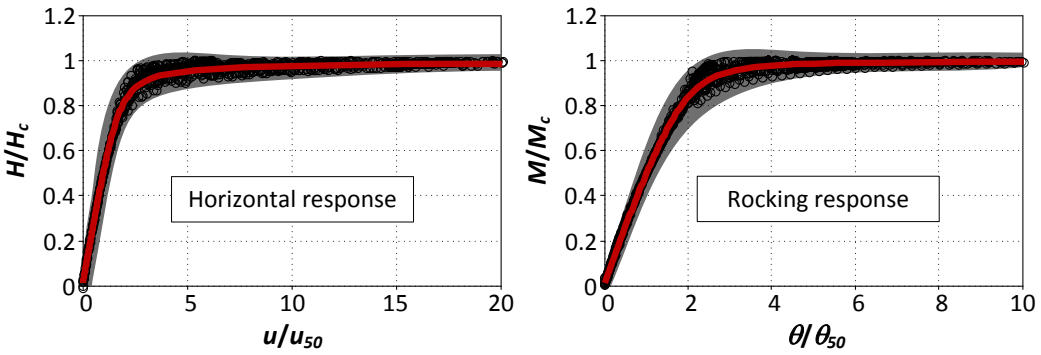

Figure 7.15: Normalised load-displacement curves for foundation swaying and rocking responses.

7.5 NSR model validation

In this section, results from nonlinear dynamic analyses performed using both rigorous FLAC^{3D} simulations and the simplified NSR model are compared to demonstrate the effectiveness and efficiency of the simplified model. Note that the FLAC^{3D} model used in this section differs from the static analysis model described previously.

7.5.1 Soil-structure model in dynamic analysis

The finite-difference grid of the soil-structure system used in the dynamic analysis is shown in Figure 7.16, where the superstructure is represented by a cylindrical aluminium column. A fine mesh was used close to the foundation and a coarser mesh was used near the sides and base of the soil domain. To avoid numerical distortion of the propagating wave, the maximum allowable mesh size was controlled within one-tenth to one-eighth of the wavelength associated with the highest frequency component of the input wave (Equation (3.4)).

In the dynamic analysis, the half-space condition of the unbounded soil was satisfied by applying appropriate boundary conditions. 'Free-field' boundaries were specified along the vertical sides of the soil grid to reproduce motions at infinity, whereas 'quiet' boundaries were imposed in between the 'free-field' and soil side boundaries, as well as at the bottom, to reduce the reflection of outward propagating waves back into the model. The 'quiet' boundaries are modelled using dashpots that are placed independently in the normal and tangential directions with respect to the soil boundaries. During the dynamic analysis in FLAC^{3D}, the motion within the model and the 'free-field' motion (in the absence of the structure and foundation) are calculated simultaneously, and the unbalanced forces at the 'free-field' grid-points are then applied to the soil-structure system through the corresponding grid-points at the soil boundaries (Itasca, 2012).

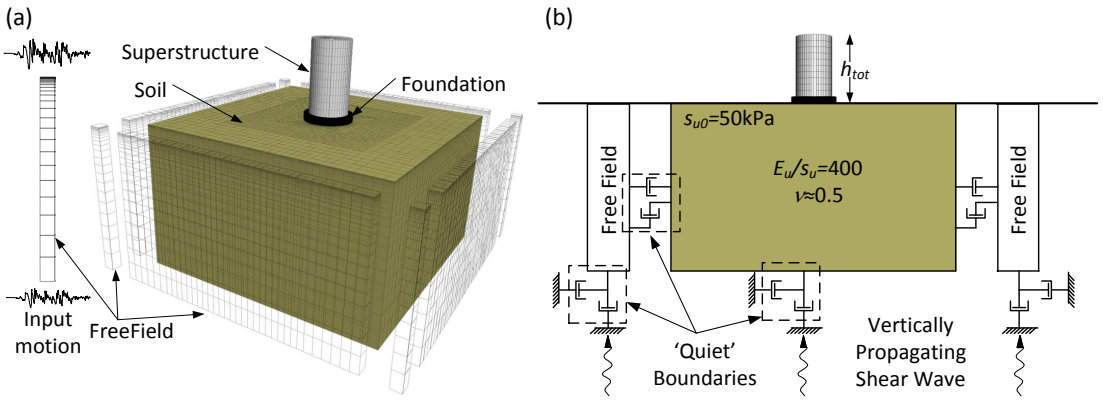

Figure 7.16: (a) Finite-difference grid and, (b) boundary conditions of the soil-structure model used in the nonlinear dynamic analysis.

It should be mentioned that the linear-elastic perfectly plastic soil model has a limitation in modelling dynamic soil behaviour, especially at small to medium strain levels. While the model cannot completely capture the hysteretic behaviour in response to the cyclic loading, FLAC^{3D} provides an optional 'hysteretic damping' model utilising a variety of stress-strain backbone curves and Masing rules (see Figure 3.5) to simulate the material damping at small strains. However, the use of this damping should be treated with care and justified when combined with a yield model. One issue with the 'hysteretic damping' model is that the stiffness degradation causes large strains, but the 'hysteretic damping' is not intended to simulate yielding at this strain level. Moreover, the reduction of stiffness with increasing strain may lead to unrealistic response as it modifies the dynamic properties of the system.

It is suggested by Itasca (2012) that a trial simulation should be run with an assumed linear material model to identify the large strain regions where the 'hysteretic damping' must be excluded. In other words, the use of the 'hysteretic damping' is subject to a case-by-case variability, which is a function of the stiffness, strength of the material, model geometry and applied load magnitude. Considering the generality of the proposed model, the 'hysteretic damping' model was therefore not adopted in this study. Instead, five percent Rayleigh damping was applied to the finite-difference model. As the focus of this study is on the mobilisation of foundation bearing capacity during strong shaking, the Tresca plasticity model is sufficient to model the large strain behaviour where a considerable amount of energy dissipation would occur during plastic flow.

The simplified NSR model, as illustrated in Figure 7.17, was constructed in the OpenSees (2006) platform. The lateral stiffness of the superstructure was modelled by an elastic beam-column element connecting the masses of the foundation and the structure at both ends, whereas the global force-displacement response of the foundation was simulated by the uniaxial material developed in Section 7.4 for both swaying and rocking motions. The NSR model requires an input of effective height for the structure, which was calculated based on a trapezoidal horizontal acceleration distribution that is made up of a uniform and a triangular pattern (Figure 7.17).

In order to give equal importance to each of the swaying and rocking responses, the rectangular and triangular patterns were devised such that each imparted the same lateral resultant force magnitude to the superstructure. The horizontal acceleration pattern illustrated in Figure 7.17 results in a value of h_{eff}=0.58h_{tot}.

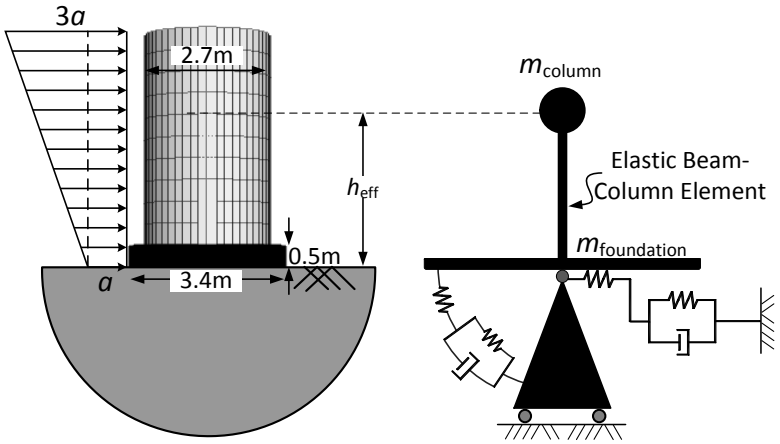

Figure 7.17: Simplified NSR model used in the dynamic analysis.

7.5.2 Methods and results

The analysis in FLAC^{3D} involved the following three steps: (1) the geo-static state is first achieved by bringing the soil grid to equilibrium under gravity with vertical-roller side-boundaries; (2) the circular foundation and the cylindrical column are then constructed on the soil surface and static equilibrium is solved for a given value of FS_{V}; (3) the roller boundaries are replaced by 'free-field' and the 'quiet' counterparts followed by dynamic analysis performed by subjecting the grid to the input ground motions applied at the base of the model. Two baseline-corrected artificial sinusoidal excitations and a real earthquake acceleration record, shown in Figure 7.18, were used as the 'free-field' horizontal motions recorded at the ground surface in the absence of the structure.

It should be noted that these 'design' acceleration records cannot be used as the input motions for the FLAC^{3D} model. Firstly, the input motions at the base of the FLAC^{3D} model should be determined in order that the motions measured at the ground surface in the 'free-field' are recovered as the 'design' motions. Secondly, the

grid-points on the base of the FLAC^{3D} model should be allowed to move according to the pattern of wave motions so that the 'quiet' dashpots can calculate the viscous forces. The former corresponds to the deconvolution process (see Section 3.2.2.2) whereas the latter requires the acceleration records to be transformed into stress records which can then be applied to the 'quiet boundary' at the base. It should also be mentioned that the input motion for a 'quiet' boundary refers to the upward propagating motion rather than the apparent (observed) acceleration within the base (Mejia and Dawson, 2006).

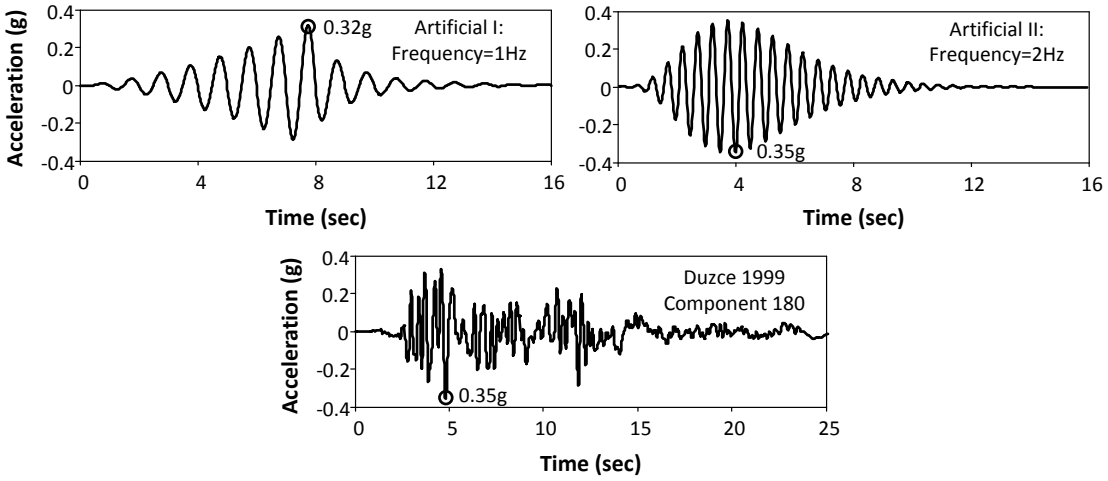

Figure 7.18: Artificial and real earthquake ground accelerations utilised as the 'free-field' motions recorded at the ground surface.

In FLAC^{3D}, Rayleigh damping is specified at a centre frequency at which mass damping and stiffness damping each supplies half of the total damping force. When subjected to the artificial ground motions, Rayleigh damping of the SSI system was specified at the frequencies of the excitations while for the real earthquake, the centre frequency was set equal to the middle frequency (1.8Hz) between the lowest and highest predominant frequencies, as suggested by Itasca (2012). In this way, the frequency-independent hysteretic damping could be approximated using Rayleigh damping.

The OpenSees (2006) analysis using the NSR model was used to study the inertial soil-structure interaction while effects of kinematic interaction were ignored, which is reasonable for shallow foundations subjected to coherent vertically propagating

shear waves. In this case, the 'design' motions shown in Figure 7.18 were directly applied as the 'free-field' motions to the model. The program SHAKE91 (Idriss and Sun, 1992) was used to calculate the base input motion of the FLAC^{3D} model from the 'design' motion (Mejia and Dawson, 2006). An example of the deconvolution process is illustrated in Figure 7.19 for a heterogeneous soil deposit. Both SHAKE91 and FLAC^{3D} models consisted of identical layers whose shear moduli were calculated based on λ=6. In addition, the SHAKE91 model had a 'half-space' which was assigned with the same shear modulus as that in the bottom layer whereas this 'half-space' condition was captured by the 'quiet' boundaries in the FLAC^{3D} model. The target motion (i.e., the earthquake ground motion shown in Figure 7.18) was applied at the top of the SHAKE91 model as an 'outcrop' motion. The upward propagating motion, extracted at the top of the half-space as half of the 'outcrop' motion , was regarded as the input motion for the FLAC^{3D} model.

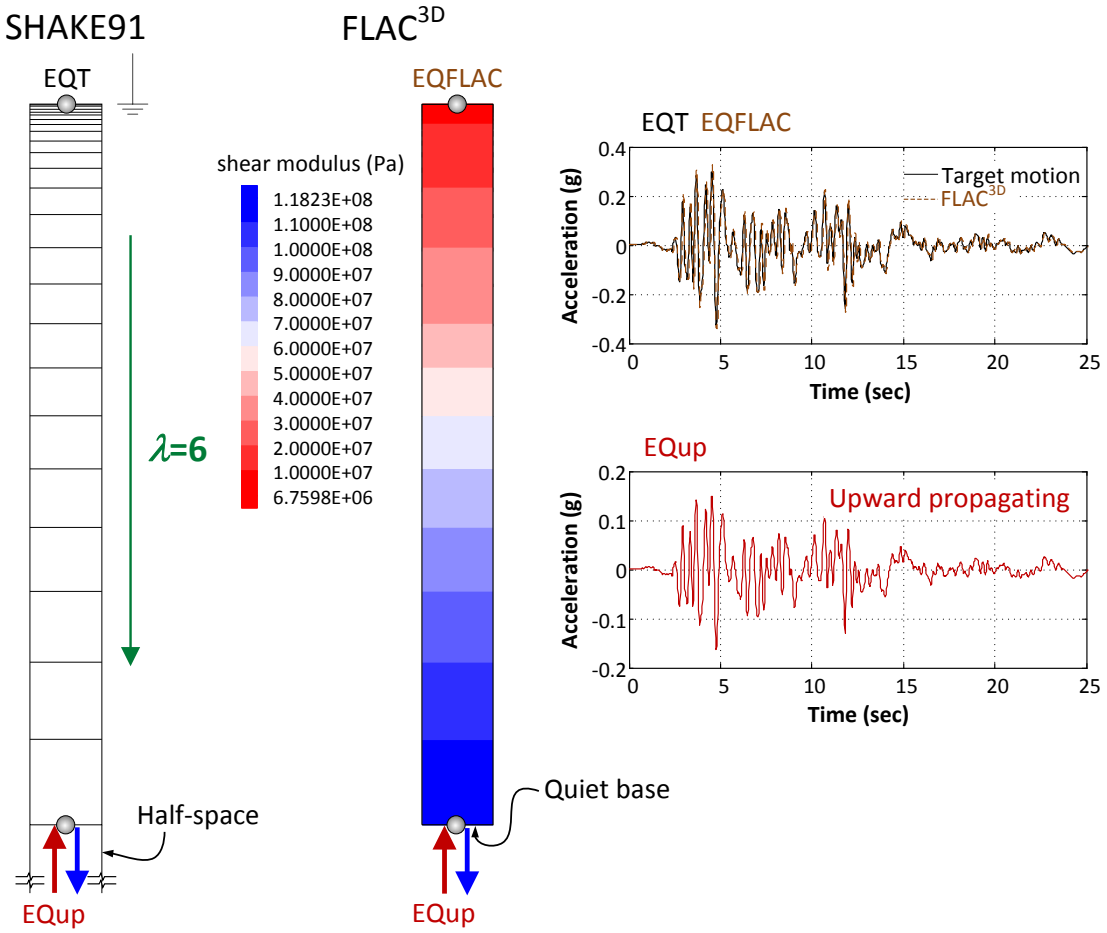

Figure 7.19: Deconvolution analysis using SHAKE91 for obtaining the input motion for the FLAC^{3D} model.

In order to apply the input motion at the 'quiet' base of the FLAC^{3D} model, the acceleration time-history was converted to a stress history given by (Itasca, 2012):

$$\tau = 2\rho V_s v_{inp} \tag{7.13}$$

where ρ is the soil mass density, V_s is the shear wave velocity calculated according to Equation (3.2) for the bottom layer, and v_{inp} is the input shear velocity time-history that can be determined from its acceleration history by the Newmark's integration method (see Section 4.5.2). Note that the factor of two in Equation (7.13) accounts for the fact that the applied stress must be double that which is observed in an infinite medium, since half the input energy is absorbed by the viscous boundary (Itasca, 2012). It is shown in Figure 7.19 that the ground motion of the FLAC^{3D} model computed following the deconvolution procedures compared very well with the target motion.

Despite the scattering of the data for the normalised foundation force-displacement backbone curve for various levels of soil heterogeneity, safety factor and moment-to-shear ratio (shown in Figure 7.15), the fitted curves were adopted for practical purposes.

Figures 7.20 compares the results predicted by both simplified NSR and more rigorous FLAC^{3D} models, in terms of shear-sliding and moment-rotation relations for the swaying and rocking motions of the foundation, respectively. The analyses were performed by using various combinations of different design parameters consisting of soil non-homogeneity index λ=0, 2, 6, safety factor FS_V=2, 3, 4, and slenderness ratio h_{tot}/r=2, 2.5, 3, where h_{tot} is the total height of the structure. Considering a typical five-bay building with a bay width of 6 meters and a storey height of 3.3 meters, h_{tot}/r=2, 2.5 and 3 approximately correspond to 10, 13 and 15 storeys, respectively, if the building is assumed to be symmetric.

The comparison shows that, in general, the simplified model is able to reproduce the foundation load-displacement response predicted using the FLAC^{3D} model. Maximum and residual foundation displacements, which are important parameters in a displacement design approach for structures, were also estimated by the simplified model with good accuracy. A significant advantage of the NSR model is that the

computational time for a dynamic time-history analysis is reduced from days (for running a FLAC^{3D} analysis) to seconds (when performing an OpenSees analysis). Another strength of the NSR model is its ability to approximate foundation force-displacement response, which is mainly affected by FS_V, $M/(HD)$ and λ, by using a single normalised backbone curve for each of the swaying and rocking degrees of freedom.

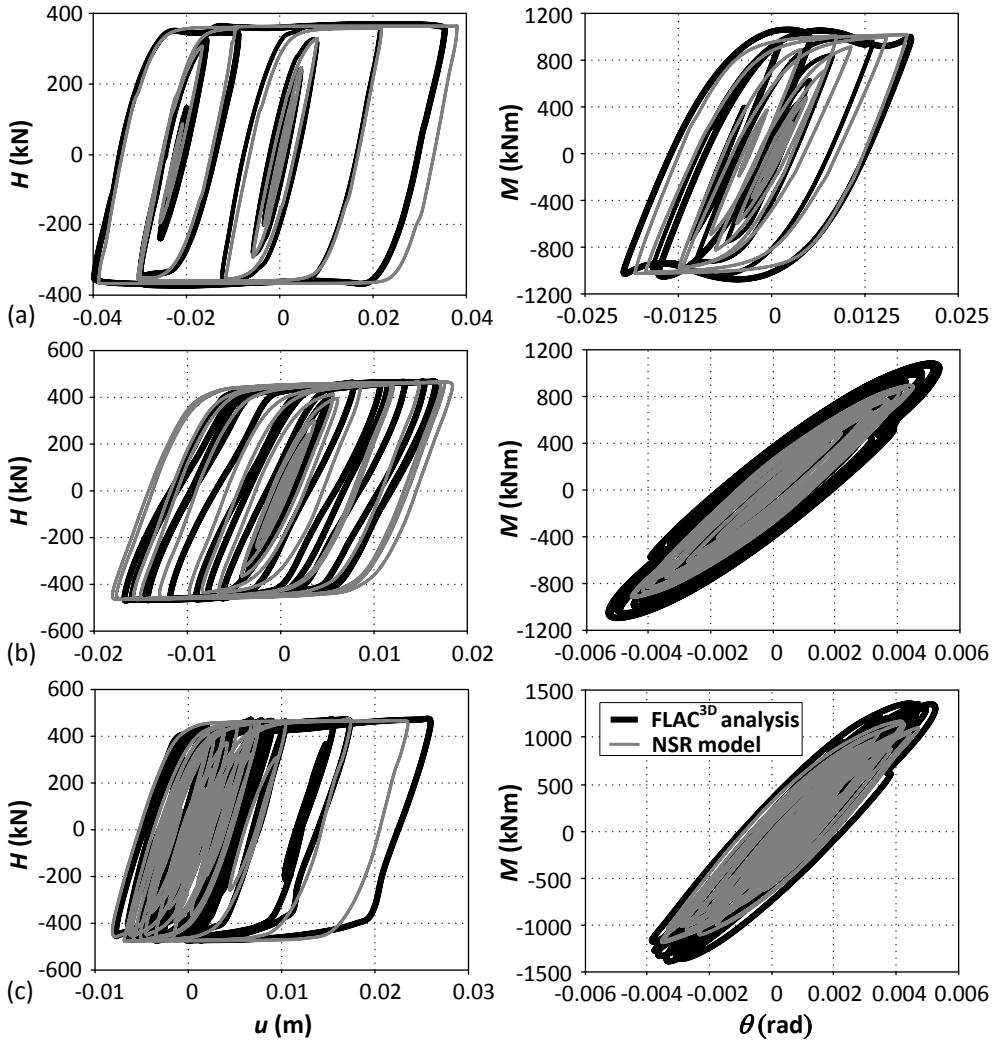

Figure 7.20: Comparison of the dynamic load-displacement and moment-rotation foundation responses computed with the FLAC^{3D} model (black lines) with those predicted by the NSR model (grey lines) for (a) artificial I ground motion with FS_V=2, h_{tot}/r=3, λ=0; (b) artificial II ground motion with FS_V=3, h_{tot}/r=2, λ=2; and (c) Duzce 1990 earthquake (component 180°) with FS_V=4, h_{tot}/r=2.5, λ=6.

For foundations resting on an elastic soil deposit having a generalised 'Gibson stiff-

ness profile' as illustrated in Figure 7.2, it is common in practice to calculate the foundation stiffness by assuming an equivalent homogeneous soil condition. This is usually done by selecting a representative soil element at an effective depth of the non-homogeneous soil profile such that the stiffness of the foundation on the uniform and non-homogeneous soil deposits is the same (Gazetas, 1980).

In the case of a yielding foundation, however, two issues arise in determining a uniform soil equivalent for a non-homogeneous soil deposit. Firstly, besides being a function of λ, the effective depth is also related to FS_{V}. Secondly, the effective depth is obtained by matching only the foundation stiffness while it is irrelevant to the post-yield response and bearing capacity of the foundation, both of which are strongly affected by the moment-to-shear ratio $M/(HD)$. Based on the assumption of a quasi-linear initial foundation stiffness (described in Section 7.4.2.1), a weak equivalence exists for the stated first issue and the effective depth can be calculated using Equations (7.8) and (7.9) with Figures 7.11 and 7.12. However, this equivalence fails to capture the nonlinear inelastic foundation response when moment and shear capacities are mobilised. On the contrary, in the proposed NSR model, the effects of soil non-homogeneity are inherently captured within the adopted normalised backbone curves.

7.6 Limitations of NSR model

The simplified NSR model is best suited for heavily-loaded structures where uplift is not expected to occur. The model is appropriate for buildings with a small to medium slenderness ratio (i.e., h_{eff}/D ranges from 0.5-1.25, except for the combination of $M/(HD)$=1.25 and $\lambda = 0$ with $FS_{\mathrm{V}} > 2$) under strong shaking and was developed for saturated clay conditions. In deriving the global force-displacement response, the nonlinear soil behaviour at small strains is neglected. As the focus of this study is seismic design for strong earthquakes where large strains dominate, it is believed that this feature has negligible impact on the overall behaviour of the soil-foundation-superstructure system. The model is not capable of predicting the

settlement of the foundation, however it is capable of capturing the maximum and residual differential settlements (indicated by the rotation θ), which are important displacement parameters that influence the design of superstructures.

7.7 Summary

A simplified nonlinear sway-rocking model has been developed in this chapter for nonlinear dynamic soil-structure interaction analysis. The proposed model is intended to simulate the nonlinear load-displacement response for the coupled sway-rocking behaviour of shallow mat foundations supporting heavily-loaded buildings under earthquake ground motions.

To simplify the model, the building is represented as an equivalent SDOF structure, whereas the soil-foundation system is replaced by an assemblage of springs and dashpots. While utilising independent springs to simulate each of the sway and rocking responses of the foundation, the coupling between the two motions is also accounted for by expressing the spring properties as a function of the load paths experienced by the foundation in the V:H:M space. Spring properties are controlled by the factor of safety against vertical bearing capacity failure FS_{V}, the moment-to-shear ratio M/HD, and the failure envelope defining the bearing capacities of the foundation in the V:H:M space. The effect of soil non-homogeneity on the stiffness and capacity of the soil-foundation system is also considered.

In order to identify the load-displacement responses and the coupled bearing capacities of the foundation, a series of static load-control and displacement-control finite-difference analyses were carried out by using the FLAC^{3D} program. The simplified model, developed in the OpenSees platform, was then calibrated against results from the static finite-difference analyses. The effectiveness and efficiency of the proposed model were validated against results from dynamic analyses performed using a FLAC^{3D} model by utilising two artificial input motions and one real earthquake acceleration record. The comparison of results predicted by both models demonstrates that the simplified model is capable of efficiently capturing

the foundation load-displacement behaviour, including the maximum and residual displacements, with good accuracy.

Although the proposed simplified model has some limitations, it is able to provide parameters necessary for preliminary design of buildings on weak soil while achieving a good balance between simplicity and accuracy. In addition, the concept of the model allows engineers to select appropriate model properties in accordance with specific site conditions.

Chapter 8

Conclusions and recommendations for future research

The aim of this research was to improve current procedures for soil-structure interaction in performance-based building design in earthquake engineering. Three main improvements have been made for this purpose. Firstly, the gap between code-specified design response spectra and base shear demands of inelastic flexible-base multi-storey buildings was bridged by introducing a strength reduction factor R_{F} and an MDOF modification factor R_{M} in Chapter 5. Secondly, the need and the way to consider the frequency content of ground motion in design of building located on very soft soil profiles were addressed in Chapter 6. Both stated improvements were based on results of a large number of analyses performed using a simplified SSI model where the foundation was assumed to behave linear-elastically. Finally, in view of taking into account foundation nonlinearity, a simplified nonlinear sway-rocking model was developed in Chapter 7. This chapter presents the general conclusions of the research (Section 8.1) and recommendations for future research (Section 8.2).

8.1 General conclusions

The discrete-element cone model (Figure 3.9) was proved to be a simple and reliable tool for simulating foundation vibration. This was verified by comparisons with exact solutions for displacement of linear systems obtained using Veletsos and Verbič (1973) impedance functions in both time and frequency domains. The cone model performed particularly well for higher values of soil Poisson's ratio (i.e., $\nu \rightarrow 0.5$).

For multi-storey buildings, the total strength demand (defined as the maximum value of the sum of the storey strengths), rather than the base shear demand (i.e., the maximum value of the strength of the first storey), should be used to indicate whether a design is economical. Using concentric, rectangular, trapezoidal, parabolic and code-specified design load patterns (i.e., CEN, 2004; IBC, 2012) to design flexible-base MDOF structures showed that the code-specified load patterns are, in general, more suitable for long period structures, whereas the trapezoidal pattern provides the best design solution for short period flexible-base structures.

For common building structures with low-to-medium ductility demands under spectrum compatible earthquakes, increasing structure-to-soil stiffness ratio a_0 could considerably reduce the structural strength demand in comparison to similar fixed-base structures. This implies that for most typical buildings considering SSI in the design process can lead to more cost-effective design solutions with less structural weight.

To satisfy a target ductility demand for SSI systems with similar fixed-base fundamental periods and structure-to-soil stiffness ratios, the total structural strength increased by increasing the slenderness ratio s, especially in the short period range (i.e., $T_s < 0.5$sec). This phenomenon was a result of a reduced initial damping ξ_{ssi} of the SSI systems due to an increase in structural slenderness s.

Applying conventional R_μ-T_s relationships for seismic design of flexible-base structures might not be appropriate, since the combined effects of a_0 and s could lead to inconsistent results in R_μ spectra. Replacing T_s with T_{ssi} could effectively solve the

problem.

SSI usually leads to increased period and damping in vibrating systems, which are very similar to the effects of yielding. These two scenarios (SSI and yielding) were considered simultaneously in design for inelastic flexible-base SDOF systems through a force reduction factor R_{F} that could be directly applied to code-design response spectra. The R_{F} spectra maintained the shape of the conventional ductility reduction factor spectra for fixed-base structures.

In general, SSI increased the values of the MDOF modification factor R_{M} which linked the base shear demand of an MDOF structure to that of its SDOF counterpart. The dependence of R_{M} on structural ductility demand μ was also manifested by SSI.

Based on results for 20 ground motions recorded on very soft soil deposits, it was shown that normalising the equivalent period of an SSI system T_{ssi} by the corresponding predominant periods resulted in more rational spectra for seismic design purposes. In the elastic response spectra, T_{ssi} is normalised by the spectrum predominant period T_P corresponding to the peak ordinate of a 5% damped elastic acceleration spectrum, while for nonlinear structures T_{ssi} should be normalised by the predominant period of the ground motion, T_{g}, at which the relative velocity spectrum reaches its maximum value.

An actual SSI system could be replaced by an equivalent fixed-base SDOF (EFSDOF) oscillator having a natural period of T_{ssi}, a viscous damping ratio ξ_{ssi} and a global ductility ratio of μ_{ssi}. The EFSDOF oscillator provided an excellent estimate of the elastic and inelastic spectra for lightly-to-moderately damped SSI systems. When using an EFSDOF oscillator, the actual acceleration should be considered for the response spectrum of flexible-base structures.

The EFSDOF oscillators, in general, overestimated the ductility reduction factor R_μ of SSI systems with high initial damping ratio (e.g. squatty structures founded on very soft soil profiles), which consequently led to an underestimation of inelastic displacement ratio C_μ. Based on the results, a correction factor was proposed to

improve the efficiency of replacement oscillators to predict the seismic response of SSI systems with effective damping ratio greater than 10%.

It was shown that, for any ground motion, the structural ductility demand of a nonlinear flexible-base structure could be calculated, with a desirable accuracy, from the global ductility demand of the whole SSI system. The EFSDOF oscillator can thus easily be implemented in the performance-based design of structures on soft soil with a target ductility ratio which is defined either for an SSI system or for the structure alone.

A simplified nonlinear sway-rocking model was developed to capture the coupled sway-rocking behaviour of shallow mat foundations supporting heavily-loaded buildings under earthquake ground motions. This spring-type model utilised a single normalised backbone curve for each of the swaying and rocking degrees of freedom. The normalised backbone curves were derived based on results of a series of static displacement-control finite-difference analyses carried out using the FLAC^{3D} program. The effect of soil non-homogeneity on the stiffness and capacity of the soil-foundation system was also considered.

The effectiveness and efficiency of the proposed model were validated against results from dynamic analyses performed using a FLAC^{3D} model by utilising two artificial input motions and one real earthquake acceleration record. The simplified model was capable of efficiently capturing the foundation load-displacement behaviour, including the maximum and residual displacements, with good accuracy.

Although the proposed simplified model has some limitations, it is able to provide parameters necessary for preliminary design of buildings on weak soil while achieving a good balance between simplicity and accuracy. In addition, the concept of the model allows engineers to select appropriate model properties in accordance with specific site conditions.

8.2 Recommendations for future research

- Results in Section 6.4 showed that response spectra for very soft soil profiles exhibited sharp peaks rather than flat shapes. These response spectra for flexible-base buildings depended on the initial damping level of the SSI system. It is desirable to introduce damping-dependent bi-normalised spectra into current code design procedures. One possible way to achieve this purpose is to derive equations for 5% damped bi-normalised spectra and apply damping reduction factors to these spectra. There is a need to investigate the effect of frequency content of ground motion on this damping reduction factor.

- Although the predominant period T_g for normalising periods in the R_μ and C_μ spectra (See Section (6.5)) was based on the peak spectral velocity for a corresponding damping ratio, it might not be a perfect normalising parameter for highly-damped systems. According to Ordaz and Pérez-Rocha (1998), T_g coincided well with the period that led to the maximum spectral displacement. Further study should be conducted concerning the selection of appropriate T_g for systems with various damping levels.

- Soil 'failure' has been recognised as a viable solution to reduction of force demand of structures. The degree of nonlinearity of the soil-foundation system is closely related to the intensity of the excitation and the relative 'strength' of the superstructure to that of the soil-foundation system. The latter is mainly affected by the factor of safety against vertical load FS_v and structural slenderness ratio s, as shown in Chapter 7. The combined effect of structural inelasticity and soil yielding on seismic response of an SSI system should be further examined.

- While using a simplified SSI model in this research to look at seismic response of isolated buildings considering a wide range of soil-structure interaction scenarios in earthquake engineering, further studies can be extended to (1) more complex structural systems with various foundation types and (2) structure–soil–structure interaction.

References

Adamidis, O. et al. (2014), 'Equivalent-linear stiffness and damping in rocking of circular and strip foundations', *Bulletin of Earthquake Engineering* **12**(3), pp. 1177–1200.

Allotey, N. and El Naggar, M. H. (2003), 'Analytical moment–rotation curves for rigid foundations based on a Winkler model', *Soil Dynamics and Earthquake Engineering* **23**(5), pp. 367–381.

Anastasopoulos, I. and Gazetas, G. (2007), 'Foundation–structure systems over a rupturing normal fault: Part I. Observations after the Kocaeli 1999 earthquake', *Bulletin of Earthquake Engineering* **5**(3), pp. 253–275.

Anastasopoulos, I. et al. (2010), 'Soil failure can be used for seismic protection of structures', *Bulletin of Earthquake Engineering* **8**(2), pp. 309–326.

Anastasopoulos, I. et al. (2013), 'Shaking Table Testing of Rocking—Isolated Bridge Pier on Sand', *Journal of Earthquake Engineering* **17**(1), pp. 1–32.

Apostolou, M. (2011), 'Soil–structure interaction under strong seismic moment: material and geometric nonlinearity', PhD thesis, PhD Thesis. National Technical University of Athens, Greece.

Apsel, R. J. and Luco, J. E. (1987), 'Impedance functions for foundations embedded in a layered medium: an integral equation approach', *Earthquake Engineering & Structural Dynamics* **15**(2), pp. 213–231.

ASCE (2010), Minimum design loads for buildings and other structures. *ASCE/SEI 7-10*, American Society of Civil Engineers, Reston, Virginia.

ASCE (2013), Seismic evaluation and retrot of existing buildings. *ASCE/SEI 41-13*, American Society of Civil Engineers, Reston, Virginia.

ATC (1978), Tentative Provisions for the Development of Seismic Regulations for Buildings. *ATC-3*, Applied Technology Council, Washington DC.

ATC (1996), Seismic evaluation and retrofit of concrete buildings. *ATC-40*, Applied Technology Council, Washington DC.

ATC (2005), Improvement of nonlinear static seismic analysis procedure. *FEMA 440*, Applied Technology Council, Washington DC.

ATC (2012), Soil-structure interaction for building structures. *NIST GCR 12-917-21*, prepared by the Applied Technology Council (*Rep. ATC-83*) and the Consortium of Universities for Research in Earthquake Engineering for the National Institute of Standards and Technology, Gaithersburg, MD.

Avilés, J. and Pérez-Rocha, L. E. (2003), 'Soil–structure interaction in yielding systems', *Earthquake Engineering & Structural Dynamics* **32**(11), pp. 1749–1771.

Bell, R. W. (1991), 'The analysis of offshore foundations subjected to combined loading', *M. SC, University of Oxford*.

Bielak, J. (1974), 'Dynamic behaviour of structures with embedded foundations', *Earthquake Engineering & Structural Dynamics* **3**(3), pp. 259–274.

Bielak, J. (1976), 'Modal analysis for building-soil interaction', *Journal of the Engineering Mechanics Division* **102**(5), pp. 771–786.

Bland, D. R. (1960), *The theory of linear viscoelasticity*, International series of monographs in pure and applied mathematics, Pergamon Press.

Booker, J. R., Balaam, N. P., and Davis, E. H. (1985), 'The behaviour of an elastic non-homogeneous half-space. Part II–circular and strip footings', *International journal for numerical and analytical methods in geomechanics* **9**(4), pp. 369–381.

Boore, D. M. (2001), 'Effect of baseline corrections on displacements and response spectra for several recordings of the 1999 Chi-Chi, Taiwan, earthquake', *Bulletin of the Seismological Society of America* **91**(5), pp. 1199–1211.

Boore, D. M. and Bommer, J. J. (2005), 'Processing of strong-motion accelerograms: needs, options and consequences', *Soil Dynamics and Earthquake Engineering* **25**(2), pp. 93–115.

Borowicka, H. (1939), 'Druckverteilung unter elastischen Platten', *Archive of Applied Mechanics* **10**(2), pp. 113–125.

Boulanger, R. W. (2006), The PySimple1, TzSimple1, and QzSimple1 material models, documentation for the OpenSees platform, URL: http://opensees.berkeley.edu.

Boulanger, R. W. et al. (1999), 'Seismic soil-pile-structure interaction experiments and analyses', *Journal of Geotechnical and Geoenvironmental Engineering* **125**(9), pp. 750–759.

BSSC (2000), Prestandard and commentary for the seismic rehabilitation of buildings. *FEMA 356*, Federal Emergency Management Agency , Building Seismic Safety Council, National Institute of Building Sciences Washington, DC.

BSSC (2009), NEHRP recommended seismic provisions for new buildings and other structures. *FEMA P-750*, Report prepared for the Federal Emergency Management Agency, Building Seismic Safety Council, National Institute of Building Sciences Washington, DC.

Carrier, W. D. and Christian, J. T. (1973), 'Rigid circular plate resting on a non-homogenous elastic half-space', *Géotechnique* **23**(1), pp. 67–84.

Cassidy, M. J., Byrne, B. W., and Houlsby, G. T. (2002), 'Modelling the behaviour of circular footings under combined loading on loose carbonate sand', *Géotechnique* **52**(10), pp. 705–712.

CEN (1998), 'Eurocode 8: Design of Structures for Earthquake Resistance-Part 2: Bridges', *PrEN*.

CEN (2004), Design of structures for earthquake resistance. Part 5: Foundations, retaining structures and geotechnical aspects. *EC8*, EN 1998-5:2004 Comité Européen de Normalisation, Brussels, Belgium.

Chang, B. J. et al. (2006), 'Centrifuge testing of combined frame-wall-foundation structural systems', in: *Proceedings of the 8th US national conference on earthquake engineering*.

Chopra, A. K. (2012), *Dynamics of Structures*, Pearson Education, ISBN: 9780133072693.

Cremer, C., Pecker, A., and Davenne, L. (2001), 'Cyclic macro-element for soil–structure interaction: material and geometrical non-linearities', *International Journal for Numerical and Analytical Methods in Geomechanics* **25**(13), pp. 1257–1284.

Crouse, C. B. (2002), 'Commentary on soil-structure interaction in US seismic provisions', in: *Proceedings of the 7th US national conference on earthquake engineering, Boston, Massachusetts*.

Cundall, P. A. et al. (1980), 'NESSI—soil structure interaction program for dynamic and static problems', *Norwegian Geotechnical Institute, Report*, pp. 51508–9.

Dafalias, Y. F. and Popov, E. P. (1975), 'A model of nonlinearly hardening materials for complex loading', *Acta Mechanica* **21**(3), pp. 173–192.

Diaz, O., Mendoza, E., and Esteva, L. (1994), 'Seismic ductility demands predicted by alternate models of building frames', *Earthquake Spectra* **10**(3), pp. 465–487.

Dobry, R. and Gazetas, G. (1986), 'Dynamic response of arbitrarily shaped foundations', *Journal of geotechnical engineering* **112**(2), pp. 109–135.

Ehlers, G. (1942), 'The effect of soil flexibility on vibrating systems', *Beton und Eisen* **41**(21/22), pp. 197–203.

Elsabee, F. and Morray, J. P. (1977), *Dynamic behavior of embedded foundations*, Massachusetts Institute of Technology, Department of Civil Engineering, Constructed Facilities Division.

Figini, R., Paolucci, R., and Chatzigogos, C. T. (2012), 'A macro-element model for non-linear soil–shallow foundation–structure interaction under seismic loads: theoretical development and experimental validation on large scale tests', *Earthquake Engineering & Structural Dynamics* **41**(3), pp. 475–493.

FLAC^{3D} (2012), Fast Lagrangian Analysis of Continua in 3 Dimensions, Version 5.0, Minneapolis, Minnesota, Itasca Consulting Group.

Gajan, S. and Kutter, B. L. (2009), 'Contact interface model for shallow foundations subjected to combined cyclic loading', *Journal of Geotechnical and Geoenvironmental Engineering* **135**(3), pp. 407–419.

Gajan, S. et al. (2005), 'Centrifuge modeling of load-deformation behavior of rocking shallow foundations', *Soil Dynamics and Earthquake Engineering* **25**(7), pp. 773–783.

Ganjavi, B. and Hao, H. (2012), 'Effect of structural characteristics distribution on strength demand and ductility reduction factor of MDOF systems considering soil-structure interaction', *Earthquake Engineering and Engineering Vibration* **11**(2), pp. 205–220.

Ganjavi, B. and Hao, H. (2014), 'Strength reduction factor for MDOF soil–structure systems', *The Structural Design of Tall and Special Buildings* **23**(3), pp. 161–180.

Gasparini, D. A. and Vanmarcke, E. (1976), *SIMQKE: A Program for Artificial Motion Generation: User's Manual and Documentation*, MIT Department of Civil Engineering.

Gazetas, G. (1980), 'Static and dynamic displacements of foundations on heterogeneous multilayered soils', *Géotechnique* **30**(2), pp. 159–177.

Gazetas, G. (1991), 'Foundation vibrations', in: *Foundation engineering handbook*, Springer, pp. 553–593.

Gazetas, G. (2015), '4th Ishihara lecture: Soil–foundation–structure systems beyond conventional seismic failure thresholds', *Soil Dynamics and Earthquake Engineering* **68**, pp. 23–39.

Gazetas, G. et al. (2013), 'Nonlinear rocking stiffness of foundations', *Soil Dynamics and Earthquake Engineering* **47**, pp. 83–91.

Gelagoti, F. et al. (2012), 'Rocking isolation of low-rise frame structures founded on isolated footings', *Earthquake Engineering & Structural Dynamics* **41**(7), pp. 1177–1197.

Ghannad, M. A. and Ahmadnia, A. (2002a), 'The effect of soil structure interaction on ductility demand of structure', in: *12th European Conference on Earthquake Engineering, London.*

Ghannad, M. A. and Jahankhah, H. (2007), 'Site-dependent strength reduction factors for soil-structure systems', *Soil Dynamics and Earthquake Engineering* **27**(2), pp. 99–110.

Ghannad, M. A. and Ahmadnia, A. (2002b), 'The effect of soil structure interaction on ductility demand of structure', in: *Proceedings of the 12th European Conference on Earthquake Engineering, London.*

Ghobarah, A., Abou-Elfath, H., and Biddah, A. (1999), 'Response-based damage assessment of structures', *Earthquake Engineering & Structural dynamics* **28**(1), pp. 79–104.

Gibson, R. E. (1967), 'Some results concerning displacements and stresses in a non-homogeneous elastic half-space', *Géotechnique* **17**(1), pp. 58–67.

Gourvenec, S. (2007a), 'Failure envelopes for offshore shallow foundations under general loading', *Géotechnique* **57**(9), pp. 715–728.

Gourvenec, S. (2007b), 'Shape effects on the capacity of rectangular footings under general loading', *Géotechnique* **57**(8), pp. 637–646.

Gourvenec, S. and Randolph, M. (2003), 'Effect of strength non-homogeneity on the shape of failure envelopes for combined loading of strip and circular foundations on clay', *Géotechnique* **53**(6), pp. 575–586.

Hadjian, A. H. and Luco, J. E. (1977), 'On the importance of layering on impedance functions', in: *Proc. 6th WCEE*, pp. 1675–1681.

Hajirasouliha, I. and Doostan, A. (2010), 'A simplified model for seismic response prediction of concentrically braced frames', *Advances in Engineering Software* **41**(3), pp. 497–505.

Hajirasouliha, I. and Pilakoutas, K. (2012), 'General seismic load distribution for optimum performance-based design of shear-buildings', *Journal of Earthquake Engineering* **16**(4), pp. 443–462.

Harden, C. et al. (2005), *Numeical Modeling of the Nonlinear Cyclic Response of Shallow Foundations*, Pacific Earthquake Engineering Research Center, College of Engineering, University of California.

Hardin, B. O. and Drnevich, V. P. (1972), 'Shear modulus and damping in soils: measurement and parameter effects (terzaghi leture)', *Journal of the soil mechanics and foundations division* **98**(6), pp. 603–624.

Houlsby, G. T. and Cassidy, M. J. (2002), 'A plasticity model for the behaviour of footings on sand under combined loading', *Géotechnique* **52**(2), pp. 117–129.

Houlsby, G. T., Cassidy, M. J., and Einav, I. (2005), 'A generalised Winkler model for the behaviour of shallow foundations', *Géotechnique* **55**(6), pp. 449–460.

IBC (2012), 2012 International Building Code. Country Club Hills, Ill: ICC.

Idriss, I. M. and Sun, J. I. (1992), 'SHAKE91: A computer program for conducting equivalent linear seismic response analyses of horizontally layered soil deposits', *Center for Geotechnical Modeling, Department of Civil and Environmental Engineering, University of California, Davis, CA*.

Iguchi, M. and Luco, J. E. (1982), 'Vibration of flexible plate on viscoelastic medium', *Journal of the Engineering Mechanics Division* **108**(6), pp. 1103–1120.

Ishibashi, I. and Zhang, X. (1993), 'Unified dynamic shear moduli and damping patios of sand and clay.' *Soils and Foundations* **33**(1), pp. 182–191.

Ishihara, K. (1996), *Soil Behaviour in Earthquake Geotechnics*, Oxford engineering science series, Clarendon Press.

Itasca (2012), Fast Lagrangian Analysis of Continua in 3 Dimensions, Version 5.0, manual, Minneapolis, Minnesota, Itasca Consulting Group.

Iwan, W. D. (1967), 'On a class of models for the yielding behavior of continuous and composite systems', *Journal of Applied Mechanics* **34**(3), pp. 612–617.

Jarenprasert, S., Bazán, E., and Bielak, J. (2006), 'Inelastic spectrum-based approach for seismic design spectra', *Journal of Structural engineering* **132**(8), pp. 1284–1292.

Jarernprasert, S., Bazan-Zurita, E., and Bielak, J. (2013), 'Seismic soil-structure interaction response of inelastic structures', *Soil Dynamics and Earthquake Engineering* **47**, pp. 132–143.

Kausel, E. (1988), 'Local transmitting boundaries', *Journal of Engineering Mechanics* **114**(6), pp. 1011–1027.

Kausel, E., Roesset, J., and Waas, G. (1974), *Forced vibrations of circular foundations on layered media*, Department of Civil Engineering, School of Engineering, Massachusetts Institute of Technology.

Khoshnoudian, F., Ahmadi, E., and Nik, F. A. (2013), 'Inelastic displacement ratios for soil-structure systems', *Engineering Structures* **57**, pp. 453–464.

Kramer, S. L. (1996), *Geotechnical Earthquake Engineering*, Upper Saddle River, New Jersey, USA: Prentice Hall.

Kramer, S. L. and Stewart, J. P. (2004), 'Geotechnical aspects of seismic hazards', *Earthquake Engineering: from Engineering Seismology to Performance-Based Engineering, Y. Bozorgnia, V. Bertero (Eds.), CRC Press* **4**, p. 85.

Krawinkler, H. and Nassar, A. A. (1992), 'Seismic design based on ductility and cumulative damage demands and capacities', *Nonlinear seismic analysis and design of reinforced concrete buildings*, pp. 23–39.

Krieg, R. D. (1975), 'A practical two surface plasticity theory', *Journal of applied mechanics* **42**(3), pp. 641–646.

Kuhlemeyer, R. L. and Lysmer, J. (1973), 'Finite element method accuracy for wave propagation problems', *Journal of Soil Mechanics & Foundations Div* **99**(Tech Rpt).

Lee, M. K. W. and Finn, W. D. L. (1978), *DESRA-2: Dynamic effective stress response analysis of soil deposits with energy transmitting boundary including assessment of liquefaction potential*, Department of Civil Engineering, University of British Columbia.

Lindman, E. L. (1975), '"Free-space" boundary conditions for the time dependent wave equation', *Journal of computational physics* **18**(1), pp. 66–78.

Liou, G. S. and Huang, P. H. (1994), 'Effect of flexibility on impedance functions for circular foundation', *Journal of engineering mechanics* **120**(7), pp. 1429–1446.

Luco, J. E. and Westmann, R. A. (1971), 'Dynamic response of circular footings', *Journal of the engineering mechanics division* **97**(5), pp. 1381–1395.

Lysmer, J. and Kuhlemeyer, R. L. (1969), 'Finite dynamic model for infinite media', *Journal of the Engineering Mechanics Division* **95**(4), pp. 859–878.

Lysmer, J. and Waas, G. (1972), 'Shear waves in plane infinite structures', *Journal of Engineering Mechanics* **98**(1), pp. 85–105.

Maravas, A., Mylonakis, G., and Karabalis, D. L. (2007), 'Dynamic characteristics of structures on piles and footings', in: *Proceedings of the 4th International Conference on Earthquake Geotechnical Engineering, Thessaloniki, Greece.*

Maravas, A., Mylonakis, G., and Karabalis, D. L. (2008), 'Dynamic soil-structure interaction for SDOF structures on footings and piles', in: *Proceedings of the 4th Geotechnical Earthquake Engineering and Soil Dynamics Conference (GEESD IV), Sacramento, USA.*

Maravas, A., Mylonakis, G., and Karabalis, D. L. (2014), 'Simplified discrete systems for dynamic analysis of structures on footings and piles', *Soil Dynamics and Earthquake Engineering* **61**, pp. 29–39.

Masing, G. (1926), 'Eigenspannungen und verfestigung beim messing', in: *Proceedings of the 2nd international congress of applied mechanics*, vol. 100, sn, pp. 332–5.

MATLAB (2011), *version 7.12.0 (R2011a)*, Natick, Massachusetts: The MathWorks Inc.

Meek, J. W. and Veletsos, A. S. (1973), 'Simple models for foundations in lateral and rocking motion', in: *Proceedings of the 5th World Conf. on Earthquake Engineering*, pp. 2610–2631.

Meek, J. W. and Wolf, J. P. (1992a), 'Cone models for homogeneous soil. I', *Journal of geotechnical engineering* **118**(5), pp. 667–685.

Meek, J. W. and Wolf, J. P. (1992b), 'Cone models for soil layer on rigid rock. II', *Journal of geotechnical engineering* **118**(5), pp. 686–703.

Meek, J. W. and Wolf, J. P. (1994a), 'Cone models for embedded foundation', *Journal of geotechnical engineering* **120**(1), pp. 60–80.

Meek, J. W. and Wolf, J. P. (1994b), 'Material damping for lumped-parameter models of foundations', *Earthquake Engineering & Structural Dynamics* **23**(4), pp. 349–362.

Mejia, L. H. and Dawson, E. M. (2006), 'Earthquake deconvolution for FLAC', *FLAC and Numerical*.

Meyerhof, G. G. (1953), 'The bearing capacity of foundations under eccentric and inclined loads', in: *Proceedings, 34th International Conference on Soil Mechanics and Foundation Engineering*, pp. 440–445.

Miranda, E. (1991), 'Seismic evaluation and upgrading of existing buildings', PhD thesis, University of California, Berkeley.

Miranda, E. (1993), 'Site-dependent strength-reduction factors', *Journal of Structural Engineering* **119**(12), pp. 3503–3519.

Miranda, E. (1997), 'Strength reduction factors in performance-based design', in: *Proceedings of EERC-CUREe Symposium, Berkeley, CA*.

Moghaddam, H. and Hajirasouliha, I. (2006), 'Toward more rational criteria for determination of design earthquake forces', *International journal of solids and structures* **43**(9), pp. 2631–2645.

Moghaddam, H. and Mohammadi, R. K. (2001), 'Ductility reduction factor of MDOF shear-building structures', *Journal of earthquake engineering* **5**(03), pp. 425–440.

Mroz, Z. (1967), 'On the description of anisotropic workhardening', *Journal of the Mechanics and Physics of Solids* **15**(3), pp. 163–175.

Muller, F. P. and Keintzel, E. (1982), 'Ductility requirements for flexibly supported antiseismic structures', in: *Proceedings of the 7th European conference on earthquake engineering.*

Muskhelishvili, N. I. (1966), 'Some basic problems of the mathematical theory of elasticity', *Nauka, Moscow* **1**(966), p. 2.

Nassar, A. A. and Krawinkler, H. (1991), *Seismic demands for SDOF and MDOF systems*, 95, John A. Blume Earthquake Engineering Center, Department of Civil Engineering, Stanford University.

Newmark, N. M. (1959), 'A method of computation for structural dynamics', *Journal of the Engineering Mechanics Division* **85**(3), pp. 67–94.

Nova, R. and Montrasio, L. (1991), 'Settlements of shallow foundations on sand', *Géotechnique* **41**(2), pp. 243–256.

OpenSees (2006), Open System for Earthquake Engineering Simulation: OpenSees, Pacific Earthquake Engineering Research Center (PEER), University of California, Berkeley.

Ordaz, M. and Pérez-Rocha, L. E. (1998), 'Estimation of strength-reduction factors for elastoplastic systems: a new approach', *Earthquake Engineering & Structural Dynamics* **27**(9), pp. 889–901.

Oztoprak, S. and Bolton, M. D. (2013), 'Stiffness of sands through a laboratory test database', *Géotechnique* **63**(1), pp. 54–70.

Paolucci, R. (1997), 'Simplified evaluation of earthquake-induced permanent displacements of shallow foundations', *Journal of Earthquake Engineering* **1**(03), pp. 563–579.

Pecker, A. (2008), *Advanced earthquake engineering analysis*, vol. 494, Springer Science & Business Media.

Pender, M. J. et al. (2006), 'Approaches to design of shallow foundations for low-rise framed structures', in: *Proceedings of the 8th U.S. National Conference on Earthquake Engineering*, pp. 9789–9798.

Poulos, H. G. and Davis, E. H. (1974), *Elastic solutions for soil and rock mechanics*, John Wiley.

Prévost, J. H. (1977), 'Mathematical modelling of monotonic and cyclic undrained clay behaviour', *International Journal for Numerical and Analytical Methods in Geomechanics* **1**(2), pp. 195–216.

Pyke, R. (1979), 'Non-linear soil models for irregular cyclic loadings', *Journal of the Geotechnical Engineering Division* **105**(6), pp. 715–726, ISSN: 1090-0241.

Pyke, R. (2004), 'Evolution of soil models since the 1970s', in: *International Workshop on the Uncertainties in Nonlinear Soil Properties and their Imp act on Modeling Dynamic Soil Response*.

Ramirez, O. M. et al. (2002), 'Elastic and inelastic seismic response of buildings with damping systems', *Earthquake Spectra* **18**(3), pp. 531–547.

Raychowdhury, P. (2008), *Nonlinear winkler-based shallow foundation model for performance assessment of seismically loaded structures*, ProQuest.

Roesset, J. M. and Ettouney, M. M. (1977), 'Transmitting boundaries: a comparison', *International Journal for Numerical and Analytical Methods in Geomechanics* **1**(2), pp. 151–176.

Ruiz-Garcıa, J. and Miranda, E. (2006), 'Inelastic displacement ratios for evaluation of structures built on soft soil sites', *Earthquake Engineering & Structural Dynamics* **35**(6), pp. 679–694.

Santa-Ana, P. R. and Miranda, E. (2000), 'Strength reduction factors for multi-degree-of-freedom systems', in: *Proceedings of the 12th world conference on Earthquake Engineering*, Auckland, New Zealand.

Schnabel, P. B., Lysmer, J., and Seed, H. B. (1972), 'SHAKE–A computer program for response analysis of horizontally layered site', Report No. EERC 72-12, University of California, Berkeley.

Seed, H. B. and Idriss, I. M. (1970), 'Soil moduli and damping factors for dynamic response analyses', UCB/EERC-70/10, Earthquake Engineering Research Center, University of California, Berkeley.

Seed, H. B. et al. (1986), 'Moduli and damping factors for dynamic analyses of cohesionless soils', *Journal of Geotechnical Engineering* **112**(11), pp. 1016–1032.

Silva, W. (1988), 'Soil response to earthquake ground motion', EPRI Report NP-5747, Electric Power Research Institute, Palo Alto, California.

Smith, W. D. (1974), 'A nonreflecting plane boundary for wave propagation problems', *Journal of Computational Physics* **15**(4), pp. 492–503.

Stewart, J. P. et al. (2008), *Benchmarking of nonlinear geotechnical ground response analysis procedures*, Pacific Earthquake Engineering Research Center.

Sun, J. I., Golesorkhi, R., and Seed, H. B. (1988), 'Dynamic moduli and damping ratios for cohesive soils', UCB/EERC-88/15, Earthquake Engineering Research Center, University of California, Berkeley.

Takewaki, I. (1998), 'Equivalent linear ductility design of soil-structure interaction systems', *Engineering structures* **20**(8), pp. 655–662.

Tan, F. S. C. (1990), 'Centrifuge and theoretical modelling of conical footings on sand', *Ph. D thesis, Cambridge Univ.*

Ugalde, J. A. et al. (2007), 'Centrifuge modeling of rocking behavior of bridges on shallow foundations', in: *Proceedings of the 4th international conference earthquake geotechnical engineering. Thessaloniki, Greece, Paper*, 1484, pp. 25–28.

Veletsos, A. S. and Verbič, B. (1974), 'Dynamics of elastic and yielding structure-foundation systems', in: *Proceedings of the 5th world conference on Earthquake Engineering.*

Veletsos, A. S. and Meek, J. W. (1974), 'Dynamic behaviour of building-foundation systems', *Earthquake Engineering & Structural Dynamics* **3**(2), pp. 121–138.

Veletsos, A. S. and Nair, V. V. (1975), 'Seismic interaction of structures on hysteretic foundations', *Journal of the Structural Division* **101**(1), pp. 109–129.

Veletsos, A. S. and Prasad, A. M. (1989), 'Seismic interaction of structures and soils: stochastic approach', *Journal of Structural Engineering* **115**(4), pp. 935–956.

Veletsos, A. S. and Wei, Y. T. (1971), 'Lateral and rocking vibration of footings', *Journal of Soil Mechanics & Foundations Div.*

Veletsos, A. S. and Verbič, B. (1973), 'Vibration of viscoelastic foundations', *Earthquake Engineering & Structural Dynamics* **2**(1), pp. 87–102.

Verbič, B. and Veletsos, A. S. (1972), Impulse response functions for elastic foundations.*Structural Research at Rice, Report*, no. 15, Houston, Texas, Rice University. Dept. of Civil Engineering.

Vidic, T., Fajfar, P., and Fischinger, M. (1994), 'Consistent inelastic design spectra: strength and displacement', *Earthquake Engineering & Structural Dynamics* **23**(5), pp. 507–521.

Vucetic, M. (1990), 'Normalized behavior of clay under irregular cyclic loading', *Canadian Geotechnical Journal* **27**(1), pp. 29–46.

Vucetic, M. (1994), 'Cyclic Threshold Shear Strains in Soils', *Journal of Geotechnical Engineering* **120**(12), pp. 2208–2228.

Waas, G., Riggs, H. R., and Werkle, H. (1985), 'Displacement solutions for dynamic loads in transversely-isotropic stratified media', *Earthquake Engineering & Structural Dynamics* **13**, pp. 173–193.

Waas, G., Hartmann, H. G., and Werkle, H. (1988), 'Damping and stiffness of foundations on inhomogeneous media', in: *Proc. 9th World Conf. Earthquake Engng, Tokyo*, vol. 3, pp. 343–348.

Wolf, J. P. (1985), *Dynamic soil-structure interaction*, Prentice-Hall international series in civil engineering and engineering mechanics, Prentice-Hall.

Wolf, J. P. (1986), 'A comparison of time-domain transmitting boundaries', *Earthquake Engineering & Structural Dynamics* **14**(4), pp. 655–673.

Wolf, J. P. (1994), *Foundation vibration analysis using simple physical models*, Pearson Education.

Wolf, J. P. and Deeks, A. J. (2004), *Foundation vibration analysis: A strength of materials approach*, Butterworth-Heinemann.

Wong, H. L. and Luco, J. E. (1985), 'Tables of impedance functions for square foundations on layered media', *International Journal of Soil Dynamics and Earthquake Engineering* **4**(2), pp. 64–81.

Xu, L. and Xie, L. (2004), 'Bi-normalized response spectral characteristics of the 1999 Chi-Chi earthquake', *Earthquake Engineering and Engineering Vibration* **3**(2), pp. 147–155.

Zhang, J., Andrus, R. D., and Juang, C. H. (2005), 'Normalized shear modulus and material damping ratio relationships', *Journal of Geotechnical and Geoenvironmental Engineering* **131**(4), pp. 453–464.

Zienkiewicz, O. C., Emson, C., and Bettess, P. (1983), 'A novel boundary infinite element', *International Journal for Numerical Methods in Engineering* **19**(3), pp. 393–404.

Ziotopoulou, A. and Gazetas, G. (2010), 'Are current design spectra sufficient for soil-structure systems on soft soils?', in: *Advances in Performance-Based Earthquake Engineering*, Springer, pp. 79–87.

Appendix A

Effects of SSI on strength demands of buildings subjected to spectrum-compatible earthquakes

A.1 Base shear demands of flexible-base SDOF structures

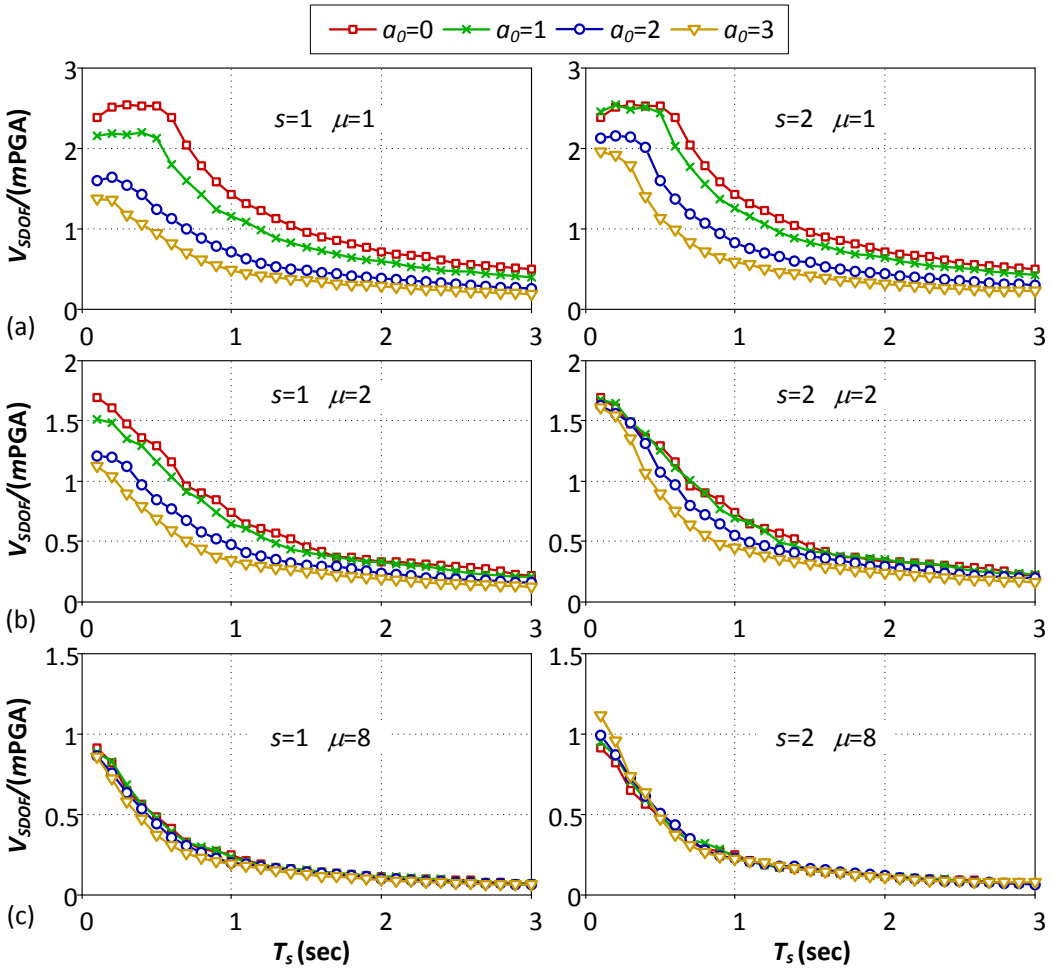

Figure A.1: Effect of structure-to-soil stiffness ratio a_0 on base shear demands of SDOF structures located on site class C.

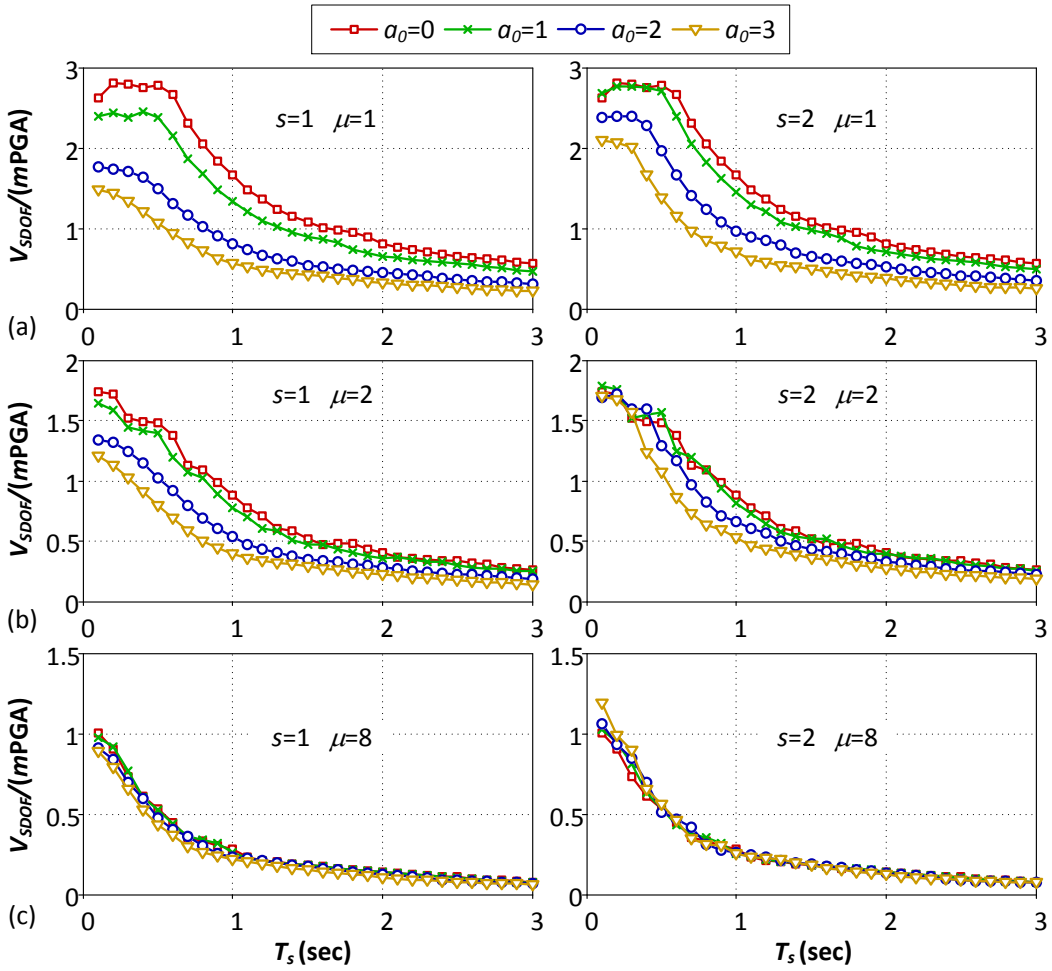

Figure A.2: Effect of structure-to-soil stiffness ratio a_0 on base shear demands of SDOF structures located on site class D.

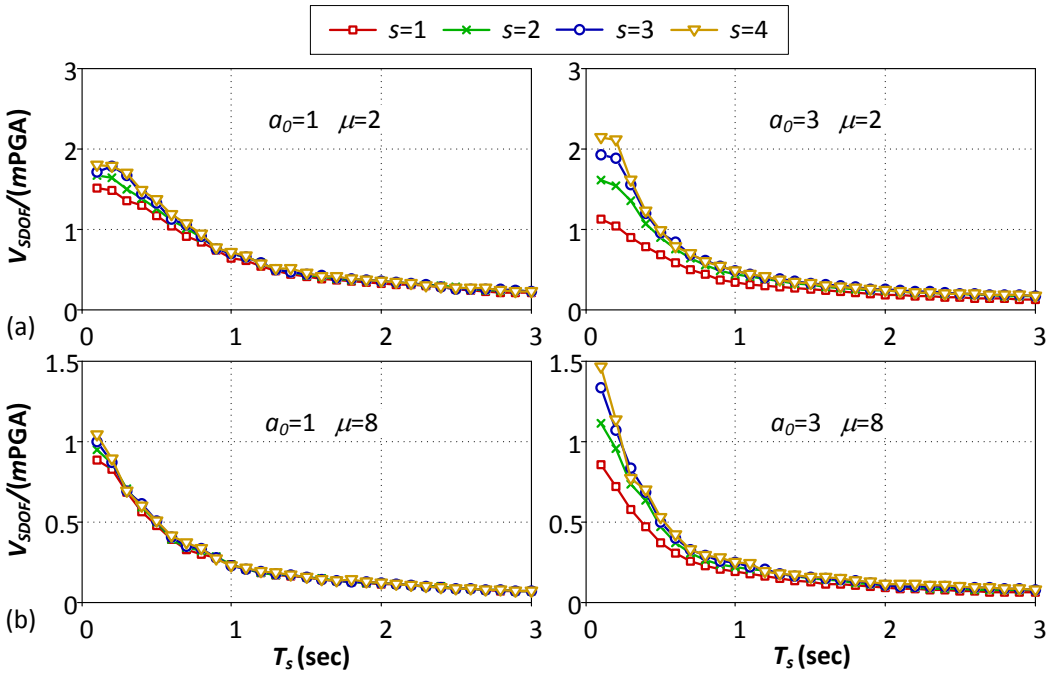

Figure A.3: Effect of structural slenderness s on base shear demands of SDOF structures located on site class C.

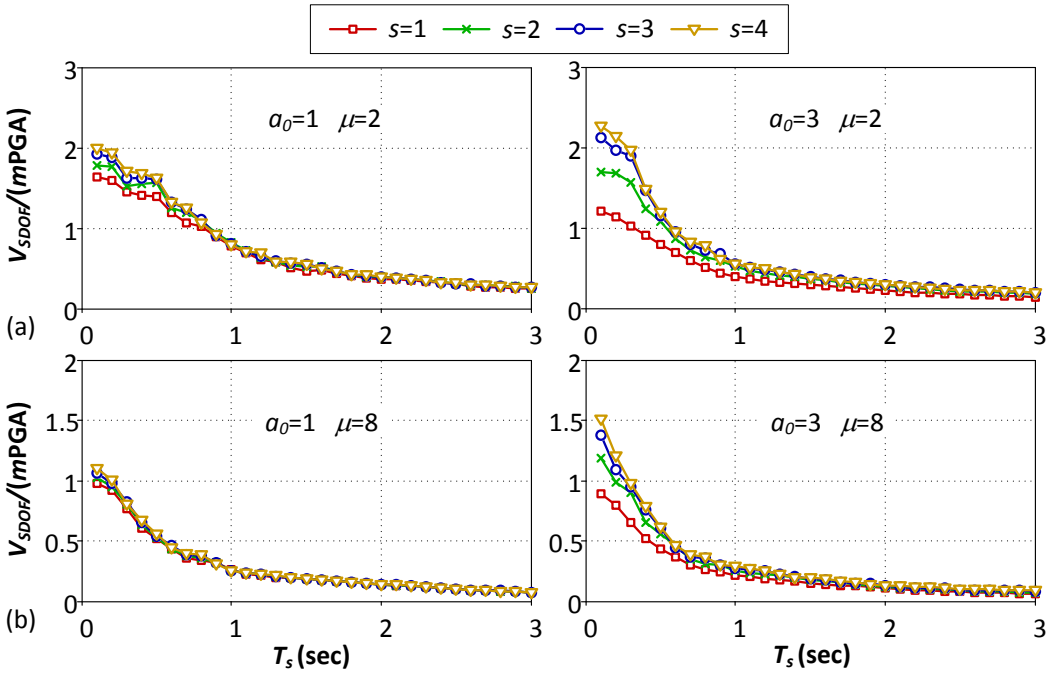

Figure A.4: Effect of structural slenderness s on base shear demands of SDOF structures located on site class D.

A.2 Base shear demands of flexible-base MDOF structures

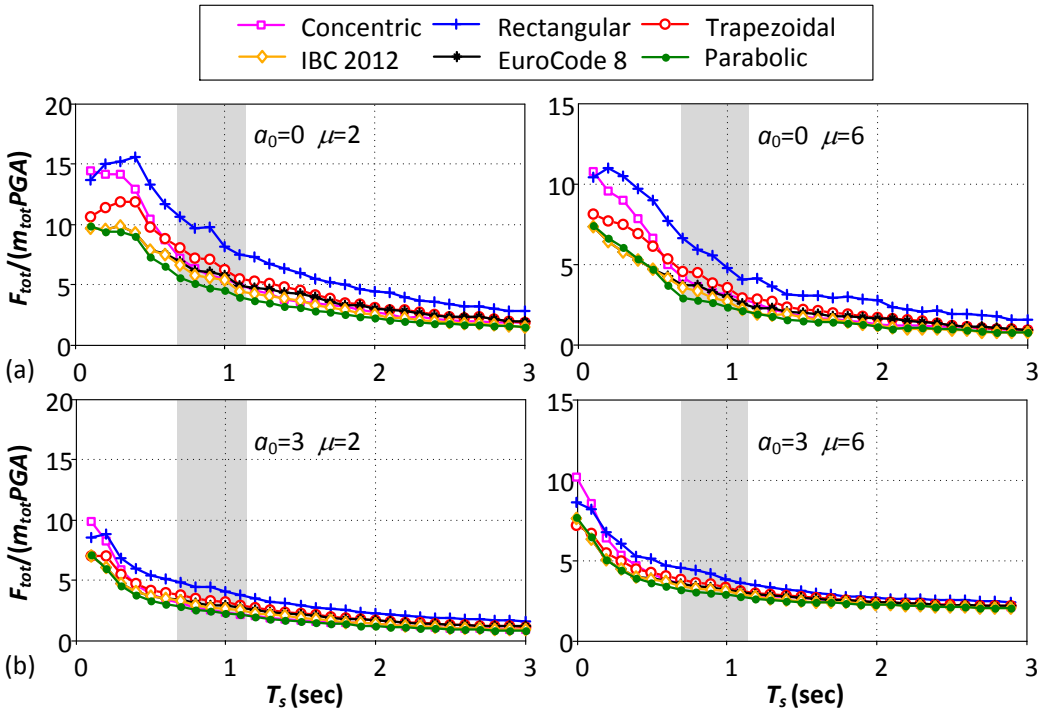

Figure A.5: Total strength demands of (a) fixed-base and (b) flexible-base 10-storey buildings designed according to different lateral load patterns, Soil Class C, s=2.

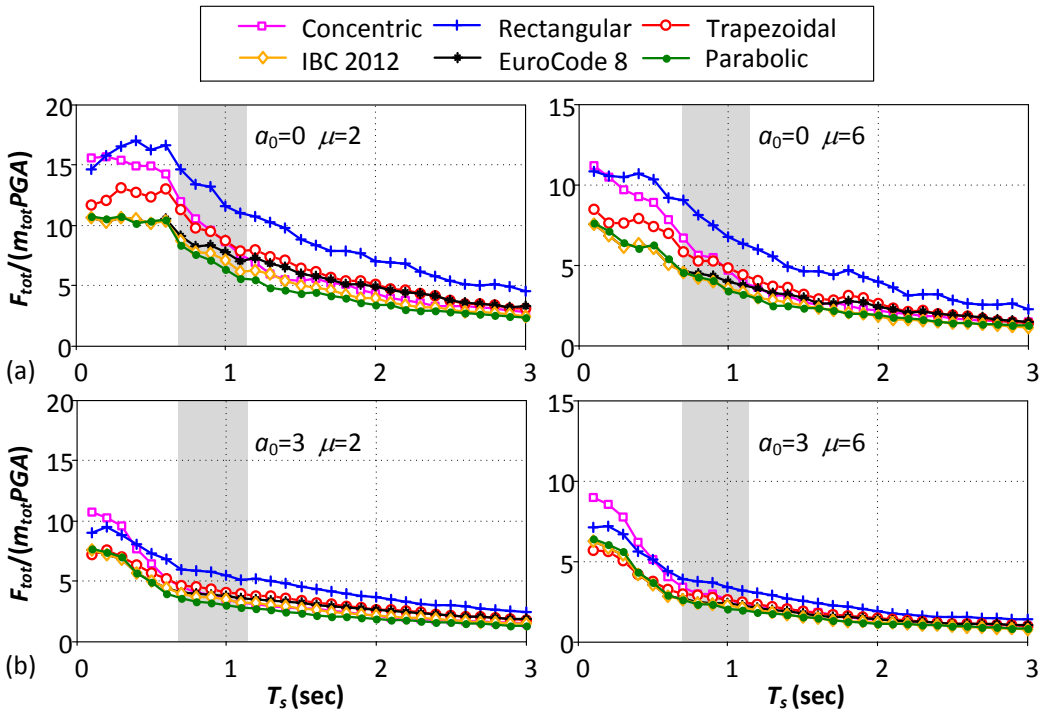

Figure A.6: Total strength demands of (a) fixed-base and (b) flexible-base 10-storey buildings designed according to different lateral load patterns, Soil Class D, s=2.

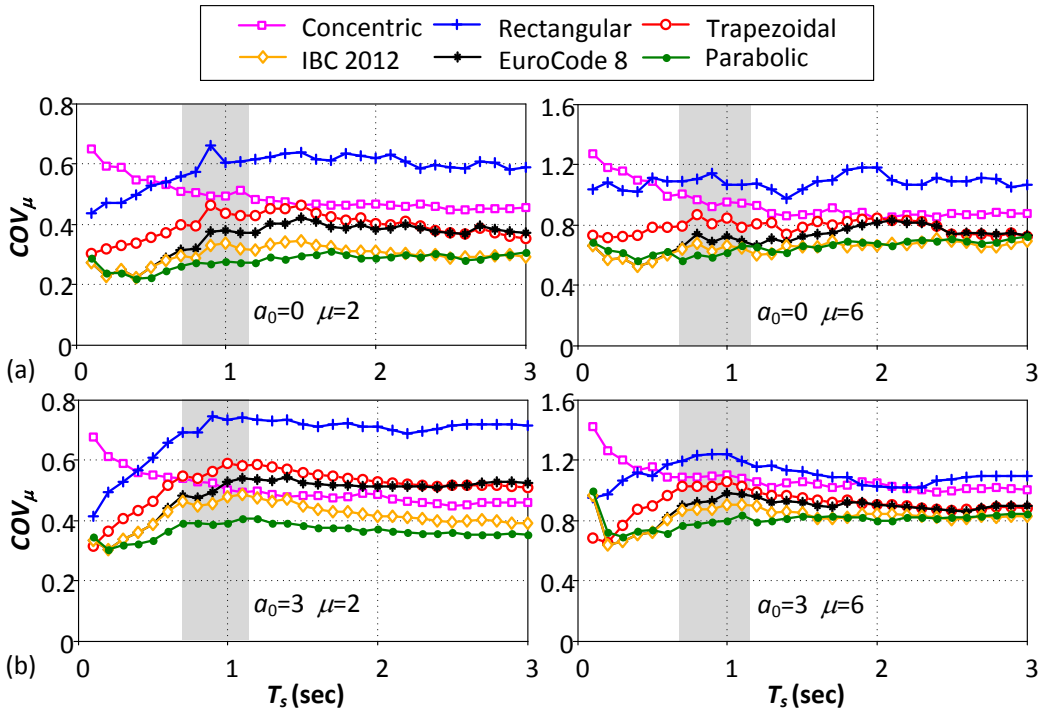

Figure A.7: Coefficient of variation of storey ductility for (a) fixed-base and (b) flexible-base 10-storey buildings designed according to different lateral load patterns, Soil Class C, s=2.

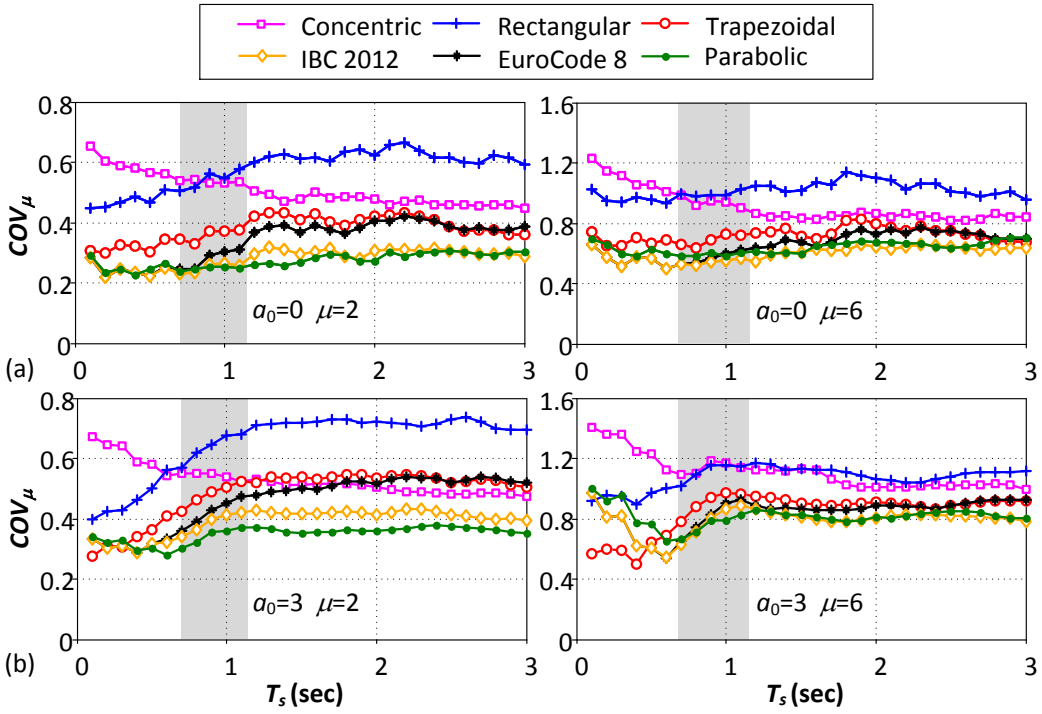

Figure A.8: Coefficient of variation of storey ductility for (a) fixed-base and (b) flexible-base 10-storey buildings designed according to different lateral load patterns, Soil Class D, s=2.

Appendix B

Constant-ductility spectra with normalised periods

B.1 Comparison between EFSDOF oscillators and actual SSI systems

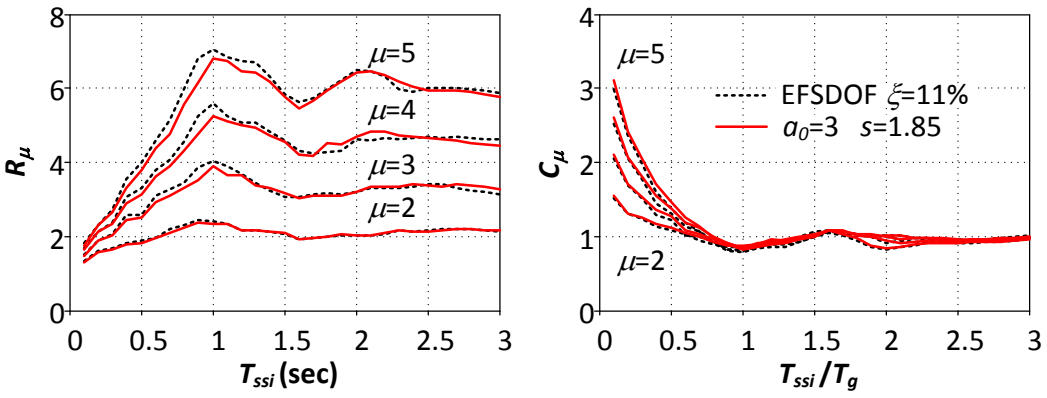

Figure B.1: Comparison of ductility reduction factor R_μ and inelastic displacement ratio C_μ spectra obtained by using the simplified SSI models and the EFSDOF oscillators having a 11% damping ratio.

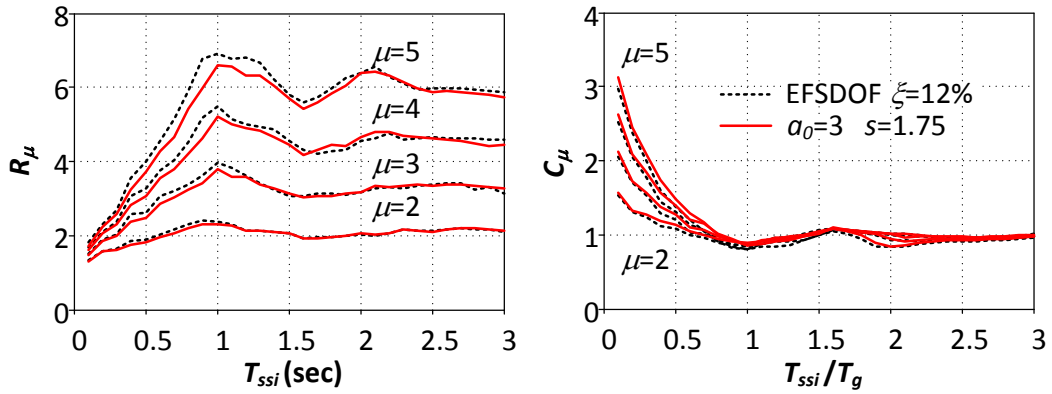

Figure B.2: Comparison of R_μ and C_μ spectra obtained by using the simplified SSI models and the EFSDOF oscillators having a 12% damping ratio.

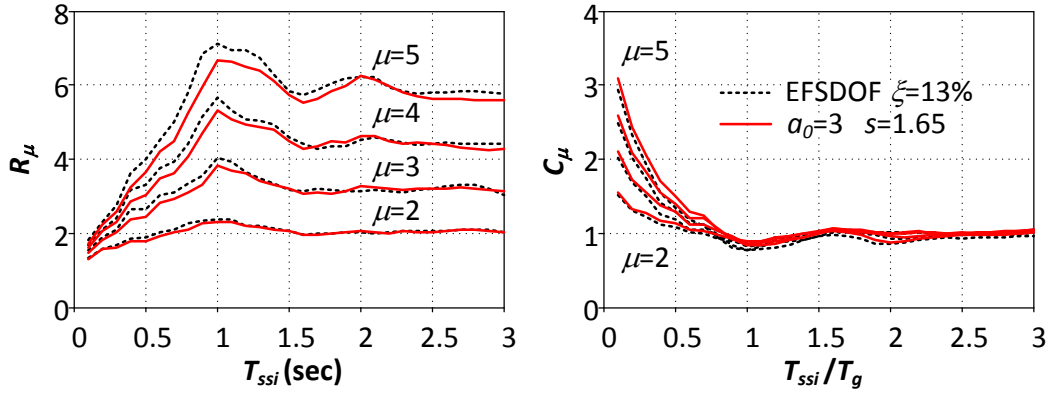

Figure B.3: Comparison of R_μ and C_μ spectra obtained by using the simplified SSI models and the EFSDOF oscillators having a 13% damping ratio.

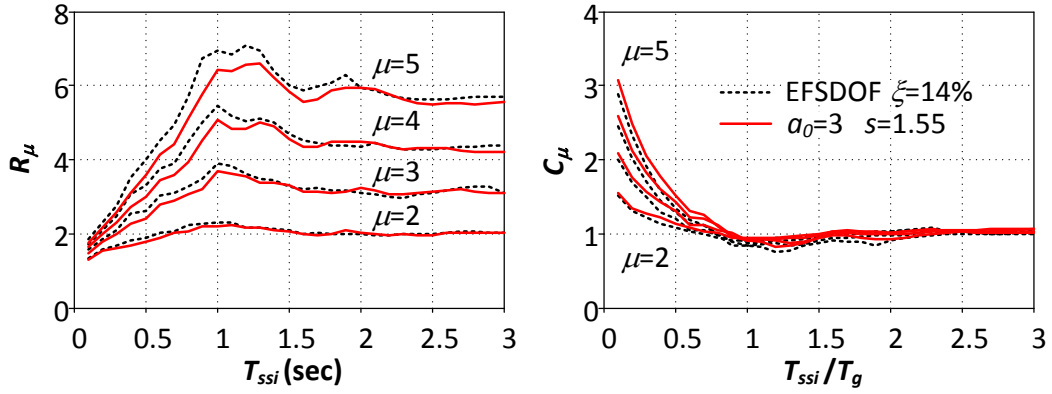

Figure B.4: Comparison of R_μ and C_μ spectra obtained by using the simplified SSI models and the EFSDOF oscillators having a 14% damping ratio.

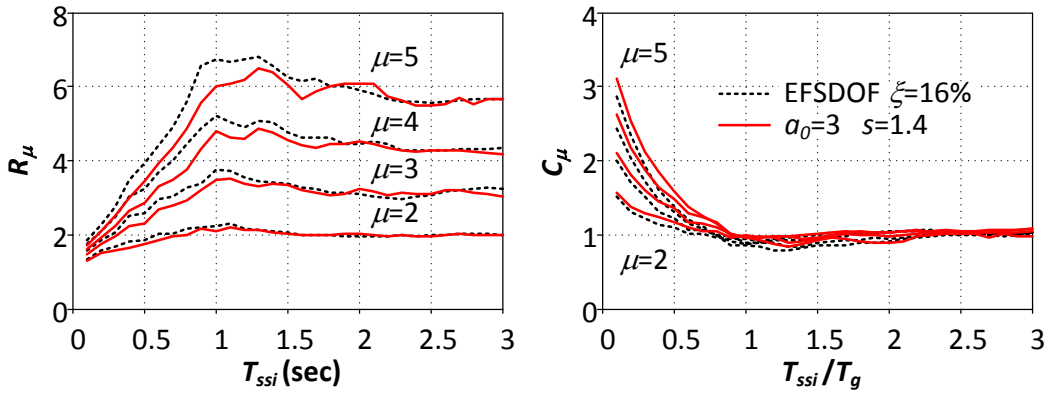

Figure B.5: Comparison of R_μ and C_μ spectra obtained by using the simplified SSI models and the EFSDOF oscillators having a 16% damping ratio.

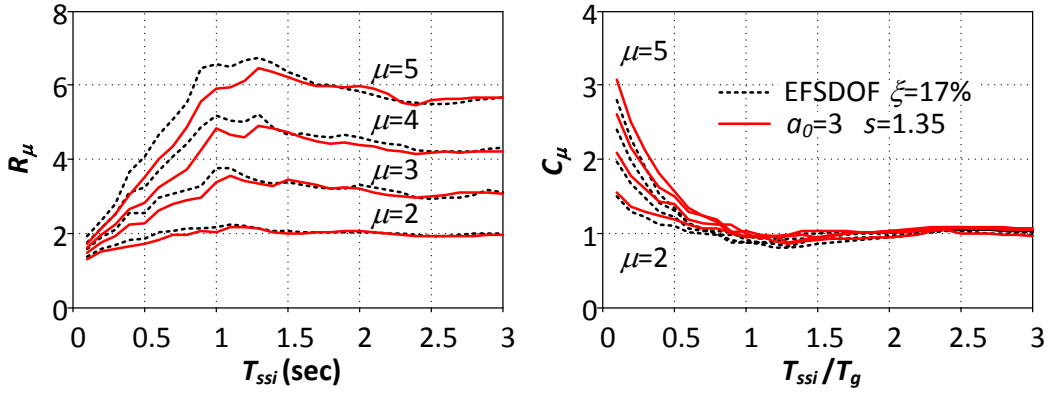

Figure B.6: Comparison of R_μ and C_μ spectra obtained by using the simplified SSI models and the EFSDOF oscillators having a 17% damping ratio.

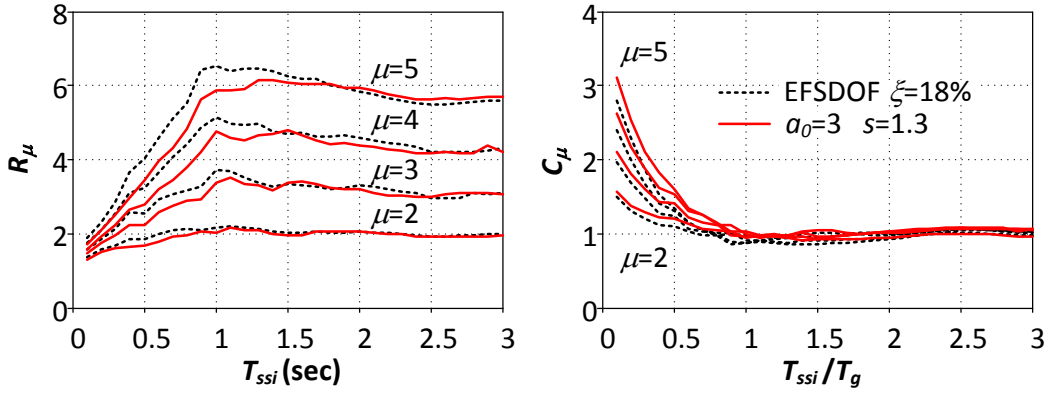

Figure B.7: Comparison of R_μ and C_μ spectra obtained by using the simplified SSI models and the EFSDOF oscillators having a 18% damping ratio.

Figure B.8: Comparison of R_μ and C_μ spectra obtained by using the simplified SSI models and the EFSDOF oscillators having a 19% damping ratio.

B.2 Improved performance of the modified EFS-DOF oscillators

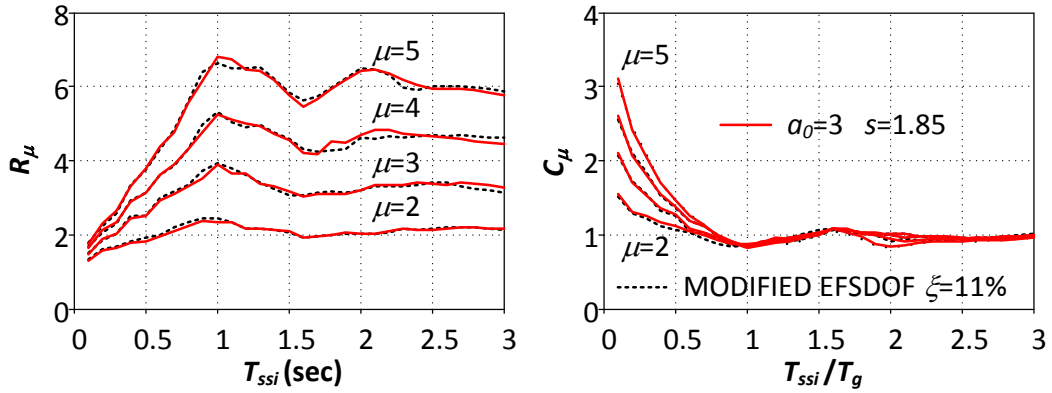

Figure B.9: Comparison of ductility reduction factor R_μ and inelastic displacement ratio C_μ spectra obtained by using the simplified SSI models and the modified EFSDOF oscillators having a 11% damping ratio.

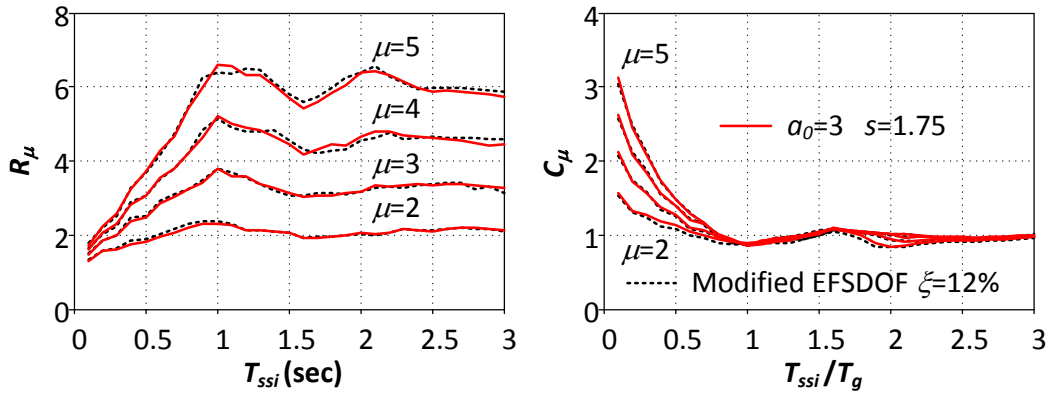

Figure B.10: Comparison of R_μ and C_μ spectra obtained by using the simplified SSI models and the modified EFSDOF oscillators having a 12% damping ratio.

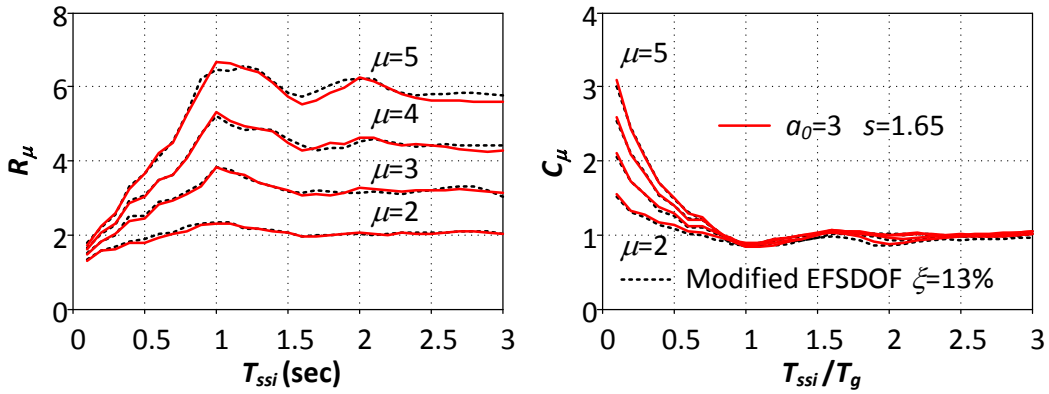

Figure B.11: Comparison of R_μ and C_μ spectra obtained by using the simplified SSI models and the modified EFSDOF oscillators having a 13% damping ratio.

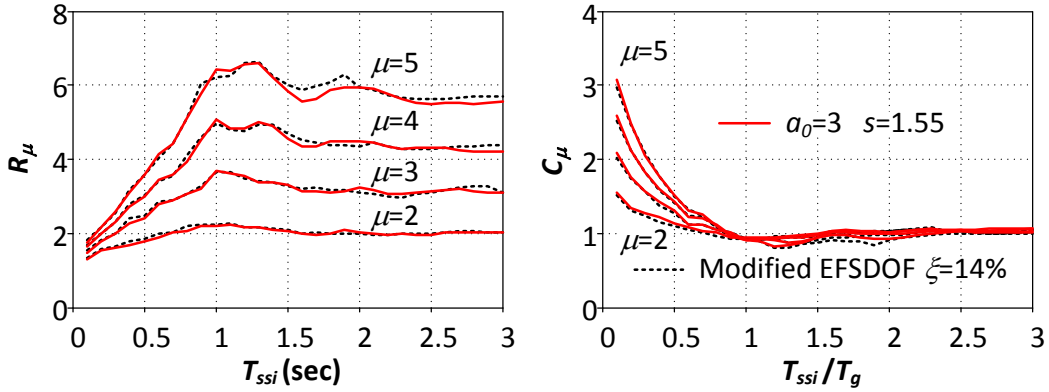

Figure B.12: Comparison of R_μ and C_μ spectra obtained by using the simplified SSI models and the modified EFSDOF oscillators having a 14% damping ratio.

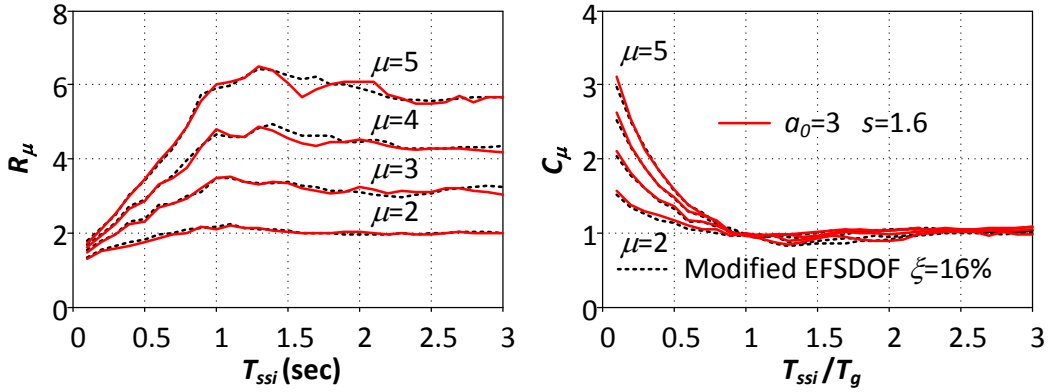

Figure B.13: Comparison of R_μ and C_μ spectra obtained by using the simplified SSI models and the modified EFSDOF oscillators having a 16% damping ratio.

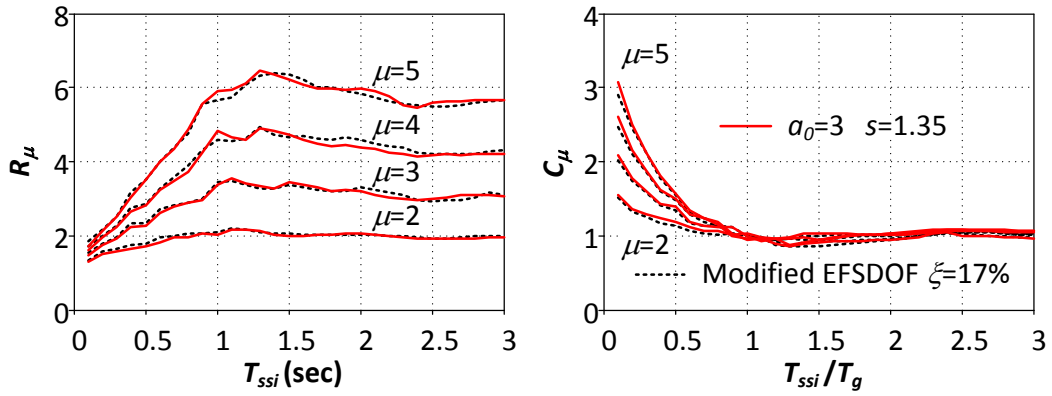

Figure B.14: Comparison of R_μ and C_μ spectra obtained by using the simplified SSI models and the modified EFSDOF oscillators having a 17% damping ratio.

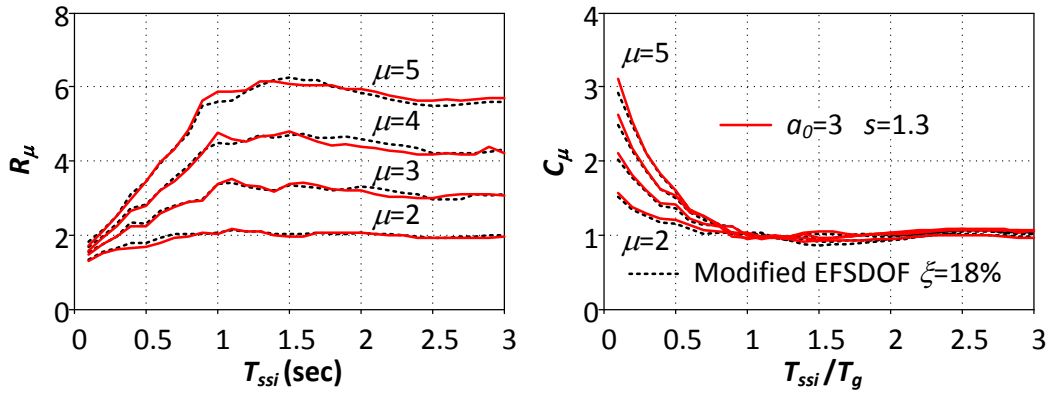

Figure B.15: Comparison of R_μ and C_μ spectra obtained by using the simplified SSI models and the modified EFSDOF oscillators having a 18% damping ratio.

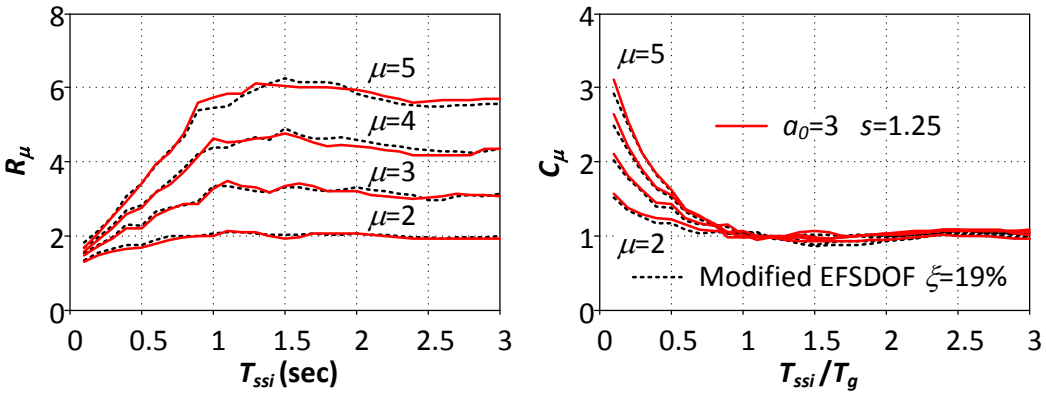

Figure B.16: Comparison of R_μ and C_μ spectra obtained by using the simplified SSI models and the modified EFSDOF oscillators having a 19% damping ratio.